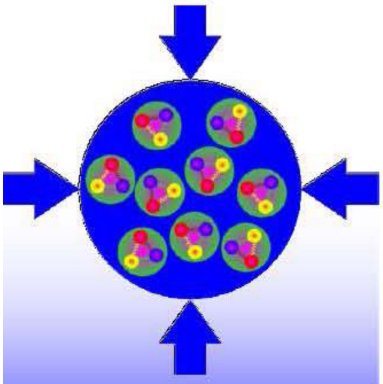

Compressed Baryonic Matter Experiment

Technical Design Report for the CBM

Micro Vertex Detector (MVD)

The CBM Collaboration

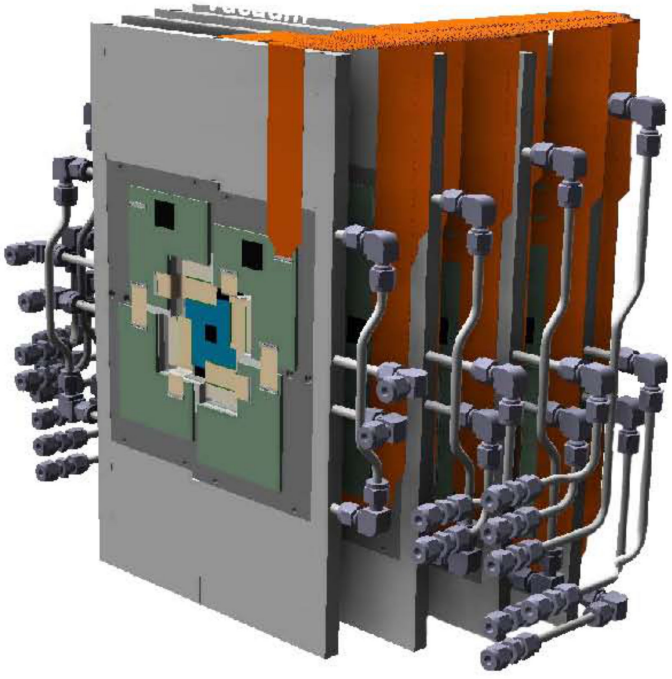

December 2021

The Micro-Vertex Detector of the CBM Experiment at FAIR

The CBM Collaboration*

Editors:
M. Deveaux, P. Klaus, M. Koziel, J. Michel,
C. Müntz and J. Stroth†

December 21, 2021

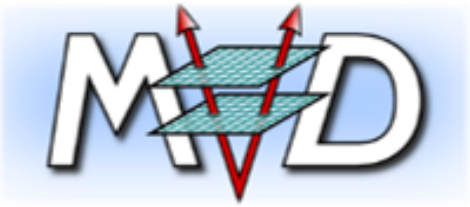

*The full list of the CBM members is given in A.2
†Corresponding author

The CBM-MVD Working Group

The MVD working group comprises participants from the CBM Collaboration and from the PICSEL group at IPHC Strasbourg (France), as of October 2020:

Institut für Kernphysik Frankfurt (IKF), Goethe-Universität Frankfurt, Frankfurt am Main, Germany
B. Arnoldi-Meadows, T. Bus, I. Fröhlich[1], P. Klaus, M. Koziel, J. Michel, C. Müntz, J. Stroth[1]

GSI, Darmstadt, Germany
H. Darwish[2], M. Deveaux[2]

PICSEL group, IPHC Strasbourg, France
J. Baudot, A. Besson, R. Bugiel, S. Bugiel, Z. El Bitar, M. Winter, G. Claus, M. Goffe, K. Jaaskelainen, M. Specht, G. Bertolone, C. Colledani, A. Dorokhov, G. Dozière, A. Himmi, C. Hu-Guo, F. Morel, H. Pham, I. Valin, Y. Zhao

The following persons (institutions) have expressed interest to formally join the MVD project:

Pusan National University (PNU), South Korea
In-Kwon Yoo

Institute of Modern Physics (IMP) of the Chinese Academy of Sciences, Lanzhou, China
N. Xu

Czech Technical University (CTU), Prague, Czech Republic
P. Chaloupka

Additional affiliations:
[1] GSI Helmholtzzentrum für Schwerionenforschung GmbH (GSI), Darmstadt, Germany
[2] Institut für Kernphysik, Goethe-Universität Frankfurt, Frankfurt, Germany

Acknowledgements

Editor team of the Technical Design Report for the CBM-MVD:
M. Deveaux, P. Klaus, M. Koziel, J. Michel, C. Müntz and J. Stroth.

We, the editors, grateful acknowledge important inputs of the following people and institutions to the MVD TDR:

The following former students have contributed to this document with their expertise in the framework of their Diploma-, Bachelor-, Master or PhD thesis:
S. Amar-Youcef, O. Artz, C. Deveaux, M. Domachowski, D. Döring, J. Enders, T. Galatyuk, E. Krebs, G. Kretzschmar, Q. Li, B. Linnik, D. Mijatovic, B. Milanovic, B. Neumann, S. Ottersbach, P. Scharrer, C. Schrader, S. Seddiki, P. Sitzmann, T. Tischler, C. Trageser, M. Wiebusch, A. Yazgili.

We want to emphasize the contributions and advises of (local) workshops to the MVD project:
The IKF mechanical workshops (heads: J. Kölichhaus, T. Schwab), the IKF Electronics Department with B. Bialas (head) with S. Schreiber, R. Weirich, and the GSI Detector Laboratory (head: C. Schmidt) with C. Simons.

We want to thank the following individuals for their advise and support during the years of R&D and preparing this document:
E. Anderssen, E. Bechtel, C. Blume, W. Dulinski^{+}, V. Friese, P. Gozik*, T. Galatyuk*, L. Greiner, J. Heuser, L. Musa, W.F.J. Müller*, H.G. Ritter, C.J. Schmidt*, R. Schmidt*, I. Selyuzhenkov*, A. Senger, P. Senger, W. Snoeys, F. Uhlig, I. Vassiliev*, H. Wieman, P. Zumbruch, M. Zyzak

We also would like to express our gratitude to the following facilities for granting access for test beam and irradiation campaigns on sensors and prototype module:
CERN, DESY, FRM II Garching and the Triga Reactor (Jozef Stefan Institute Ljubljana).

Funding agencies and supporting institutions:
This work was supported in part by the GSI Helmholtzzentrum für Schwerionenforschung, Darmstadt, the Facility for Antiproton and Ion Research (FAIR), The German BMBF-Verbundforschung (06FY173I, 05P09RFFC7, 05P12RFFC7, 05P15RFFC1 and 05P19RFFC1), IN2P3/CNRS and University of Strasbourg, the EU FP7 projects HadronPhysics2 (WP26 ULISI) and HadronPhysics3 (WP26 ULISINT), the Hessian LOEWE initiative HICforFAIR, and the ExtreMe Matter Institute EMMI at GSI.

* also serving as member of the internal CBM review committee for this TDR.
$^{+}$ deceased.

Contents

List of Figures

List of Tables

1 Executive Summary

1.1 Scientific motivation and the detector concept

The CBM collaboration proposes the construction of a dedicated Micro Vertex Detector (MVD) positioned in direct vicinity to the stationary target of CBM in vacuum, and in front of the STS, placed outside the vacuum. The interplay of the MVD and the STS allows for high-precision track reconstruction inside the magnetic field with a total of four MVD and eight STS planar tracking stations. Besides extending the acceptance to lower momenta down to about 300 MeV/c and assisting in background rejection, the MVD enables CBM performing particle identification via inspection of the track topology of daughter particles from weakly decaying charged hyperons produced in A+A collisions and open charm mesons in p+A collisions in the SIS-100 energy regime. The detector will allow for secondary vertex reconstruction for weak decays of charmed hadrons with a precision significantly better than 100 µm along the beam axis for decay products with laboratory momenta above 1 GeV/c. In dielectron spectroscopy the MVD contributes to improving the signal-to-background by identification of close pairs from conversion and π^0-Dalitz decays. The detector concept provides two different detector geometries, optimized for track (TR) and vertex (VX) finding. They detector geometry "TR" ("VX") consists of four planes of increasing size inside the CBM acceptance, placed equidistantly between 8 (5) and 20 cm downstream of the target and inside the target vacuum chamber. The "TR" detector geometry will represent the start version of the MVD. Each plane is made of four quadrants, called modules, arranged around and in close vicinity to the beam axis. Inside the acceptance of $2.5^\circ \leq \theta \leq 25^\circ$ in the full azimuth, these modules are equipped with radiation hard CMOS MAPS (aka CPS). The sensors are mounted on both sides of a thin support sheet of high-performance material to efficiently evacuate the heat. The MVD stations feature a material budget of $O(0.5\,\%)$ (x/X_0). However, the first station employed in the VX detector geometry offers $O(0.3\,\%)$ (x/X_0) to enable high-precision secondary vertex finding. The senors are connected with thin flexible flat cables to front-end electronics placed on the same support sheet but outside the acceptance. By means of dedicated, highly integrated vacuum feed-throughs and a second layer of readout electronics outside the target box, the detector is connected to the CBM data acquisition.

The detector employs MIMOSIS pixel sensors, which represent the state of the art of an ongoing development line, which has produced the ULTIMATE sensors used in the STAR HFT and the ALPIDE sensor for the upgraded ALICE ITS. In fact, MIMOSIS represents a dedicated CBM sensor, optimized to fulfill the challenging requirements of CBM *w.r.t.* interaction rate, radiation hardness and high (and non-uniform) hit occupancy. A sophisticated data buffering scheme will cope with the expected occupancy fluctuations due to beam micro spill-structure, as well as the large occupancy gradients in some sensors due to the strongly forward peaked particle emission and δ-electrons. In addition, the sensor features low power dissipation mandatory for vacuum operation and a very low material budget.

1.2 Organization of the Technical Design Report

The document is organized as follows: the following chapter (2) briefly introduces the CBM experiment, with a focus on the different detector subsystems and the baseline physics program to be studied with CBM. Chapter 3 gives an overview on MVD, emphasizing the operation environment of the detector, which drives its technical design. In addition, the resulting layout of the detector is introduced. The main chapter, 4, contains all technical details relevant for the technical design, comprising the sensor technology, sensor and detector integration, readout and services. These results have been reviewed, and iterated, during extensive prototyping, presented in chapter 5. The following chapter 6 takes the design of the MVD presented so far and studies its physics performance based on recent Monte Carlo simulations. The report is concluded by providing information on the project organization and costs, chapter 7.

2 The Compressed Baryonic Matter Experiment

2.1 Exploring the phase diagram of nuclear matter

Substantial experimental and theoretical efforts worldwide are devoted to the exploration of the phase diagram of nuclear matter. Fig. 2.1 illustrates the possible phases of nuclear matter and their boundaries in a diagram of temperature versus the baryon chemical potential. Cold nuclear matter - as found in normal nuclei with a net-baryon density equal to one - consists of protons and neutrons (*i.e.* nucleons) only. At moderate temperatures and densities, nucleons are excited to short-lived states (baryonic resonances) which decay by the emission of mesons. At higher temperatures, also baryon-antibaryon pairs are created. This mixture of baryons, anti-baryons and mesons, all strongly interacting particles, is generally called hadronic matter, or baryonic matter if baryons prevail. At very high temperatures or densities the hadrons melt, and the constituents, the quarks and gluons, form a new phase: the Quark-Gluon-Plasma (QGP). For very low net-baryon densities where the numbers of particles and anti-particles are approximately equal, Quantum Chromo-Dynamics (QCD) on the lattice predicts that hadrons dissolve into quarks and gluons above a temperature of about 160 MeV [1, 2]. The inverse process happened in the universe during the first few microseconds after the big bang: the quarks and gluons were confined into hadrons. In this region of the phase diagram the transition is expected to be a smooth crossover from partonic to hadronic matter [3]. Calculations suggest a critical endpoint at relatively large values of the baryon chemical potential [4]. Beyond this critical endpoint, for larger values of net-baryon densities (and for lower temperatures), one expects a phase transition from hadronic to partonic matter with a phase coexistence region in between. A new phase of so called quarkyonic matter has been proposed to exist beyond the first order phase transition at large baryon chemical potentials and moderate temperatures [5]. High-density but cold nuclear matter is expected to exist in the core of neutron stars. At very high densities correlated quark-quark pairs are predicted to form a color superconductor.

As illustrated in Fig. 2.1, it is expected that the QCD phase diagram exhibits a rich structure at finite values of baryon chemical potentials, such as the critical point, the predicted first order phase transition between hadronic and partonic or quarkyonic matter, and the chiral phase transition. The experimental discovery of these prominent landmarks of the QCD phase diagram would be a major breakthrough in our understanding of the properties of nuclear matter. Equally important is quantitative experimental information on the properties of hadrons in dense matter which may shed light on chiral symmetry restoration and the origin of hadron masses.

In the laboratory hot and dense nuclear matter is generated in a wide range of temperatures and densities by colliding atomic nuclei at high energies. The goal of the experiments at RHIC and LHC is to investigate the properties of deconfined QCD matter at very high temperatures and almost zero net-baryon densities. Several experimental programs are devoted to the exploration of the QCD phase diagram at high net-baryon densities. The STAR collaboration at RHIC scanned the beam energies in order to search for the QCD critical endpoint [7]. For the same reason, measurements are performed at the CERN-SPS with the upgraded NA49

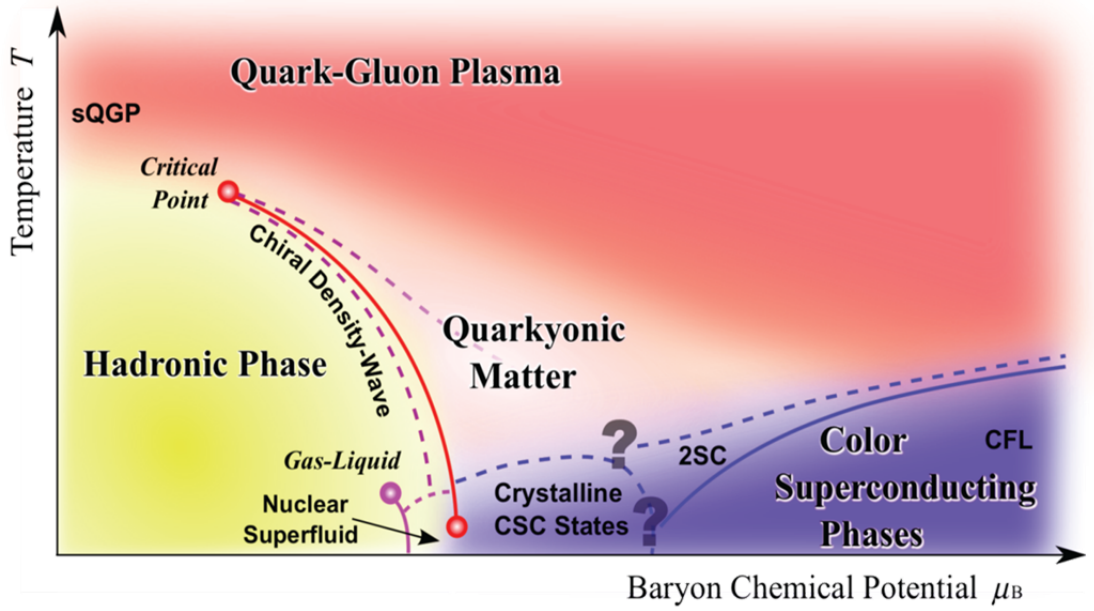

Figure 2.1: Sketch of the phase diagram for strongly-interacting matter (taken from [6]).

detector (NA61/SHINE) using light and medium size ion beams [8]. At the Joint Institute for Nuclear Research (JINR) in Dubna, a heavy-ion collider project (NICA) is planned with the goal to search for the coexistence phase of nuclear matter [9]. However, due to luminosity or detector limitations these experiments are constrained to the investigation of particles which are abundantly produced. In contrast, the Compressed Baryonic Matter (CBM) experiment at the Facility for Antiproton and Ion Research (FAIR) in Darmstadt is designed for precision measurements of multidimensional observables including particles with very low production cross sections using the high-intensity heavy-ion beams provided by the FAIR accelerators.

The SIS100/300 accelerators at FAIR are very well suited to create high net-baryon densities. This is illustrated in Fig. 2.2 which depicts results of transport code calculations for central Au+Au collisions. According to these calculations, densities of up to seven times saturation density can be produced already at beam energies of 10 A GeV. Under these conditions the nucleons overlap, and theory predicts a transition to a mixed phase of baryons and quarks.

2.2 Diagnostic probes of the high-density fireball

Fig. 2.3 depicts three snapshots of the evolution of a heavy-ion collision at FAIR energies as calculated with the UrQMD transport code [11], and illustrates the time of production and eventual emission of various particle species. Particles containing charm quarks are expected to be created in the very first stage of the reaction. D mesons and J/ψ mesons may serve as probes for the dense fireball and its degrees of freedom. Vector mesons like ω, ρ and ϕ mesons are produced continuously via $\pi\pi$ annihilation during the course of the reaction, and decay either again into mesons or into a pair of leptons. However, as leptons are not affected by final-state interactions, the dileptonic decay offers the possibility to look into the fireball. In particular, the short-lived ρ meson is a promising diagnostic probe of hot and dense nuclear matter. Due to

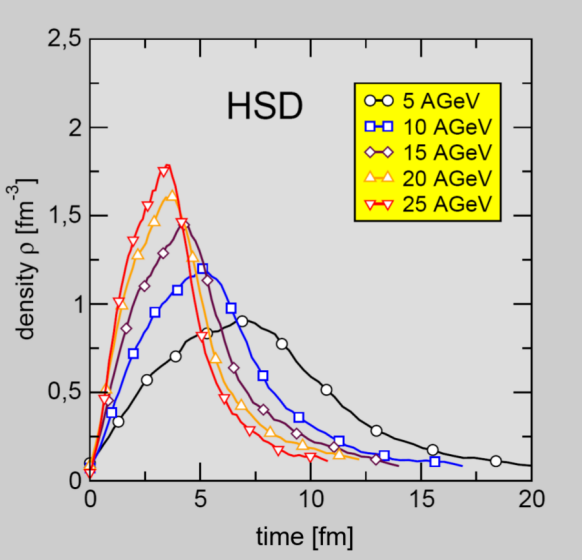

Figure 2.2: Baryon density as function of elapsed time for central Au+Au collisions at different energies as calculated with the HSD transport code [10].

their small hadronic cross sections, also multi-strange hyperons and ϕ mesons carry information on the dense phase of the collision, in particular via their collective flow. Finally, the bulk of the particles freezes out at densities below saturation density. Up to date, essentially only these bulk particles have been measured in heavy-ion collisions at beam energies between 2 and 40 A GeV (on stationary target). Diagnostic probes of the dense stage of the fireball such as multi-strange baryons, dilepton pairs and charmed particles will be measured for the first time by the CBM experiment in this beam energy range. Therefore, the CBM experiment has a unique discovery potential both at SIS100 and SIS300 energies.

The experimental challenge is to measure multi-differential observables and particles with very low production cross sections such as multi-strange (anti-)hyperons, particles with charm and lepton pairs with unprecedented precision. The situation is illustrated in the left panel of Fig. 2.4 which depicts the multiplicities for various particle species produced in central Au+Au collisions at 4 A GeV. The data points are calculated using the thermal model based on the corresponding temperature and baryon-chemical potential [12]. The dilepton decay of vector mesons, here illustrated for the ϕ meson, is suppressed by the square of the electromagnetic coupling constant $(1/137)^2$, resulting in a dilepton yield which is about six orders of magnitude below the pion yield, similar to the multiplicity of multi-strange anti-hyperons.

In order to produce high-statistics data even for the particles with the lowest production cross sections, the CBM experiment is designed to run at reaction rates of 100 kHz up to 1 MHz. For charmonium measurements - where a trigger on high-energy lepton pairs can be generated - reaction rates up to 10 MHz are envisaged. This exceeds the rate capabilities of other existing and planned heavy-ion experiments by orders of magnitude, as illustrated in the right panel of Fig. 2.4.

2.3 CBM physics cases and observables

The CBM research program is focused on the following physics cases:

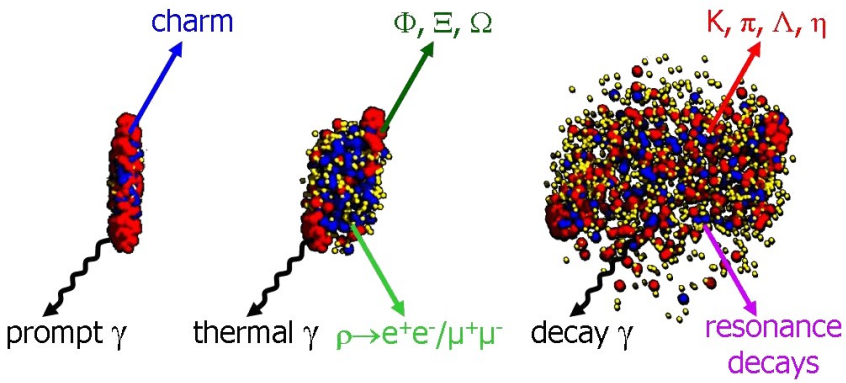

Figure 2.3: Three stages of a U+U *collision at a laboratory beam energy of 23 A GeV as calculated with the UrQMD model [11]: The initial stage where the two Lorentz-contracted nuclei overlap (left), the high density phase (middle), and the final stage ("freeze-out") when all hadrons have been formed (right). Different particles are created in different stages of the collisions or escape from the interaction region at different times (see text). Almost 1000 charged particles are created in such a collision, most of them are pions.*

The equation-of-state of baryonic matter at neutron star densities.
The relevant measurements are:

- The excitation function of the collective flow of hadrons which is driven by the pressure created in the early fireball (SIS100).
- The excitation functions of multi-strange hyperon yields in Au+Au and C + C collisions at energies from 2 to 11 A GeV (SIS100). At sub-threshold energies, Ξ and Ω hyperons are produced in sequential collisions involving kaons and Λ, and are therefore sensitive to the density in the fireball.

In-medium properties of hadrons.
The restoration of chiral symmetry in dense baryonic matter will modify the properties of hadrons. The relevant measurements are:

- The in-medium mass distribution of vector mesons decaying in lepton pairs in heavy-ion collisions at different energies ($2 - 45$ A GeV), and for different collision systems. Leptons are penetrating probes carrying the information out of the dense fireball (SIS100/300).
- Yields and transverse mass distributions of charmed mesons in heavy-ion collision as a function of collision energy (SIS100/300).

Phase transitions from hadronic matter to quarkyonic or partonic matter at high net-baryon densities.
Already at SIS100 energies densities of up to seven times of the normal nuclear density are reached in central collisions between heavy-ions. A discontinuity or sudden variation in the excitation functions of sensitive observables would be indicative of a transition. The relevant measurements are:

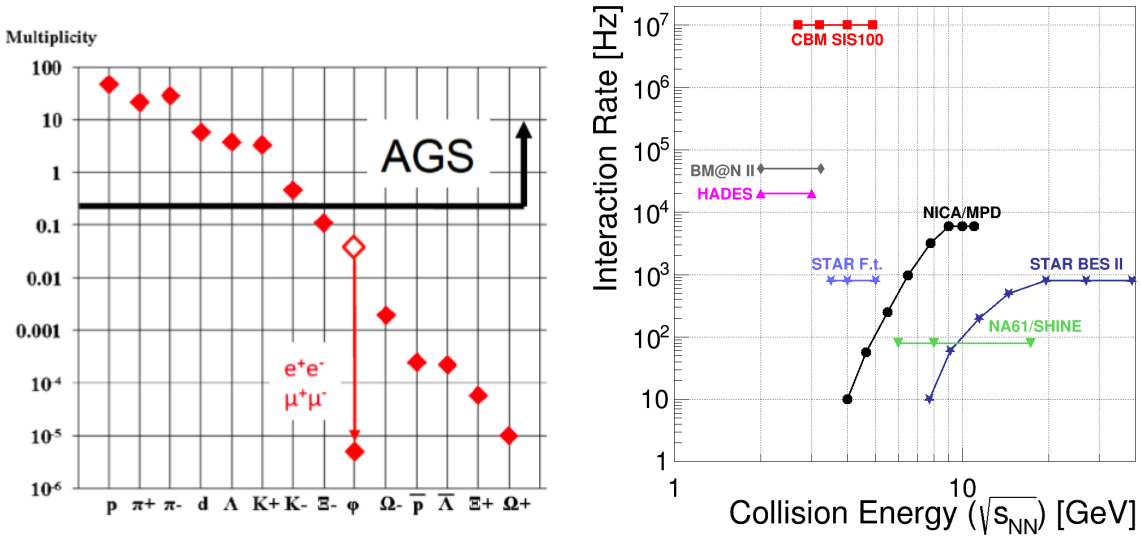

Figure 2.4: Left: Particle multiplicities for central Au+Au collisions at 4 A GeV as calculated with a statistical model [12]. For the ϕ meson also the branching fraction for the decay into lepton pairs is included (open symbol). The black line roughly indicates the multiplicities that were available to the AGS heavy-ion program at BNL at this energy. Right: Interaction rates achieved by existing and planned heavy-ion experiments as a function of center-of-mass energy [13]. "STAR F.T." denotes the fixed-target operation of STAR.

- The excitation function of yields, spectra and collective flow of strange particles in heavy-ion collisions from $6 - 45\,A\,\mathrm{GeV}$ (SIS100/300).
- The excitation function of yields, spectra and collective flow of charmed particles in heavy-ion collisions from $6 - 45\,A\,\mathrm{GeV}$ (SIS100/300).
- The excitation function of yields and spectra of lepton pairs in the intermediate mass region in heavy-ion collisions from $6 - 45\,A\,\mathrm{GeV}$ (SIS100/300).
- Event-by-event fluctuations of conserved quantities like baryons, strangeness, net-charge etc. in heavy-ion collisions with high precision as function of beam energy from $6-45\,A\,\mathrm{GeV}$ (SIS100/300).

Hypernuclei, strange dibaryons and massive strange objects.
Theoretical models predict that single and double hypernuclei, strange dibaryons and heavy multi-strange short-lived objects are produced via coalescence in heavy-ion collisions with the maximum yield in the region of SIS100 energies. The planned measurements include:

- The decay chains of single and double hypernuclei in heavy-ion collisions at SIS100 energies.
- Search for strange matter in the form of strange dibaryons and heavy multi-strange short-lived objects. If these multi-strange particles decay into charged hadrons including hyperons they can be identified via their decay products.

Charm production mechanisms, charm propagation and in-medium properties of charmed particles in (dense) nuclear matter.
The relevant measurements are:

- Cross sections and momentum spectra of open charm (D-mesons) in proton-nucleus collisions at SIS100/300 energies. In-medium properties of D-mesons can be derived from the transparency ratio $T_A = (\sigma_{pA} \rightarrow DX)/(A \times \sigma_{pN} \rightarrow DX)$ measured for different size target nuclei.
- Cross sections, momentum spectra and collective flow of open charm (D-mesons) in nucleus-nucleus collisions at SIS300 energies.
- Cross sections, momentum spectra and collective flow of charmonium (J/ψ) in proton-nucleus and nucleus-nucleus collisions at SIS100/300 energies.

As discussed above, a substantial part of the CBM physics cases can be addressed already with beams from the SIS100 synchrotron [13]. The intended measurements at SIS100 including the results of simulations and count rate estimates are described in [14]. A general review of the physics of compressed baryonic matter, the theoretical concepts, the available experimental results and predictions for relevant observables in future heavy-ion collision experiments can be found in the CBM Physics Book [15].

2.4 The Facility for Antiproton and Ion Research (FAIR)

The international Facility for Antiproton and Ion Research (FAIR) in Darmstadt will provide unique research opportunities in the fields of nuclear, hadron, atomic and plasma physics [16]. The research program devoted to the exploration of compressed baryonic matter will start with primary beams from the SIS100 synchrotron (protons up to 29 GeV, Au up to 11 A GeV, nuclei with $Z/A = 0.5$ up to 14 A GeV), and will be continued with beams from the SIS300 synchrotron (protons up to 90 GeV, Au up to 35 A GeV, nuclei with $Z/A = 0.5$ up to 45 A GeV). The layout of FAIR is presented in Fig. 2.5. The beam extracted to the CBM cave reaches intensities up to 10^9 Au ions per second.

2.5 The Compressed Baryonic Matter (CBM) experiment

The CBM experimental strategy is to perform systematic both integral and differential measurements of almost all the particles produced in nuclear collisions (i.e. yields, phase-space distributions, correlations and fluctuations) with unprecedented precision and statistics. These measurements will be performed in nucleus-nucleus, proton-nucleus, and - for baseline determination - proton-proton collisions at different beam energies. The identification of multi-strange hyperons, hypernuclei, particles with charm quarks and vector mesons decaying into lepton pairs requires efficient background suppression and very high interaction rates. In order to select events containing those rare observables, the tracks of each collision have to be reconstructed and filtered online with respect to physical signatures. This concept represents a paradigm shift for data taking in high-energy physics experiments: CBM will run without hierarchical trigger system. Self-triggered readout electronics, a high-speed data processing and acquisition system, fast algorithms, and, last but not least, radiation hard detectors are indispensable prerequisites for a successful operation of the experiment. Fig. 2.6 depicts the CBM experimental setup for SIS100. The CBM experiment comprises the following components:

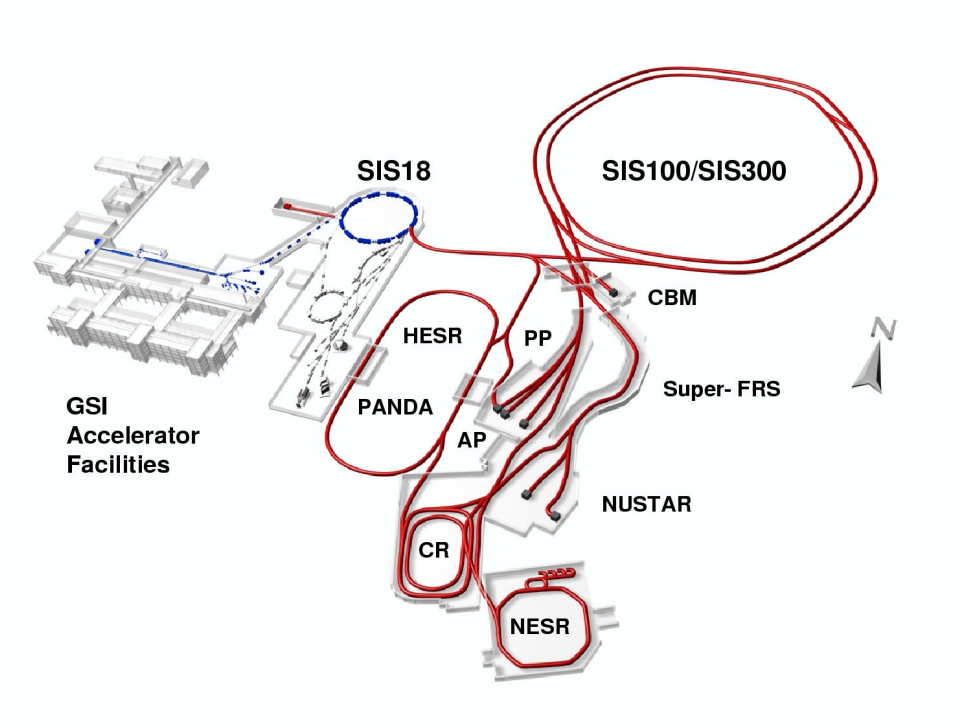

Figure 2.5: Layout of the Facility for Antiproton and Ion Research (FAIR) [16].

Dipole magnet
The dipole magnet will be superconducting in order to reduce the operation costs. It has a large aperture of $\pm 25^\circ$ polar angle, and provides a magnetic field integral of 1 Tm.

Micro-Vertex Detector (MVD)
The MVD will provide excellent spatial precision and low material budget as required for the identification of open charm particles and weakly decaying charged hyperons by the measurement of their displaced decay vertex. It consist of four planar stations equipped with thin and large-area Monolithic Active Pixel Sensor (MAPS) chips. The station's layout and distance from the target can be adopted to the needs of a specific run, *i.e.* optimized *w.r.t.* vertexing (VX) or tracking (TR) capability, respectively. They are located from 5(8) cm to 20 cm downstream of the target in vacuum, for the VX (TR) detector geometry. As a figure of merit, the VX detector geometry aims at a precision of secondary vertices determination of about $50 - 100\,\mu$m along the beam axis.

Silicon Tracking System (STS)
The task of the STS is to provide track reconstruction and momentum determination of charged particles. The system consists of eight tracking layers of silicon strip detectors, located downstream of the target at distances between 30 cm and 100 cm inside the magnetic dipole field, and provides a momentum resolution of about $\Delta p/p = 1.5\,\%$.

Ring Imaging Cherenkov Detector (RICH)
The RICH detector will provide the identification of electrons via the measurement of their

Cherenkov radiation. This will be achieved using a gaseous RICH detector build in a standard projective geometry with focusing mirror elements and a photon detector. The detector will be positioned behind the dipole magnet about 1.6 m downstream of the target. It will consist of a 1.7 m long gas radiator (overall length approximately 2 m) and two arrays of mirrors and photon detector planes. The design of the photon detector plane is based on MAPMTs in order to provide high granularity, high geometrical acceptance, high detection efficiency of photons also in the near UV region and a reliable operation.

Muon Chamber System (MUCH)
The concept of the muon detection system is to track the particles through a hadron absorber and thus perform a momentum dependent muon identification. The absorber/detector system is placed downstream of the STS, which determines the particle momentum. In order to reduce meson decays into muons the absorber/detector system is designed as compact as possible. It consists of six hadron absorber layers made of iron plates and 18 gaseous tracking chambers located in triplets behind each iron slab (SIS300 setup). The trigger concept is based on the measurement of short track segments in the last tracking station triplet, and extrapolation of these tracks to the target. For J/ψ measurements at SIS100 a MUCH start version with three chamber triplets is sufficient.

Transition Radiation Detector (TRD)
The Transition Radiation Detector, consisting of four detector layers grouped into one station in the SIS100 configuration (ten layers in three stations for SIS300), will serve for particle tracking and for the identification of electrons and positrons with $p > 1.0\,\mathrm{GeV}/c$ ($\gamma \geq 1000$). The detector layers are located at approximately 4.1 m to 5.9 m downstream of the target, the total active detector area amounts to about $114\,\mathrm{m}^2$ (SIS100). The TRD readout will be realized in rectangular pads giving a resolution of $\sim 300\,\mu\mathrm{m}$ across and $3 - 30\,\mathrm{mm}$ along the pad. Every second TRD layer is rotated by 90°.

Time-Of-Flight System (TOF)
An array of Multi-gap Resistive Plate Chambers (MRPC) will be used for hadron identification via TOF measurements. The TOF wall covers an active area of about $120\,\mathrm{m}^2$ and is located about 6 m downstream of the target for measurements at SIS100, and at 10 m at SIS300. The required time resolution is on the order of 80 ps. At small deflection angles the pad size is about $5\,\mathrm{cm}^2$ corresponding to an occupancy of below 5 % for central Au+Au collisions at 25 A GeV.

Electromagnetic Calorimeter (ECAL)
A "shashlik" type calorimeter as installed in the HERA-B, PHENIX and LHCb experiments will be used to measure direct photons and neutral mesons (π^0, η) decaying into photons. The ECAL will be composed of modules which consist of 140 layers of lead and scintillator sheets. The shashlik modules can be arranged either as a wall or in a tower geometry with variable distance from the target.

Projectile Spectator Detector (PSD)
The PSD will be used to determine the collision centrality and the orientation of the reaction plane. The detector is designed to measure the number of non-interacting nucleons from a projectile nucleus in nucleus-nucleus collisions. The PSD is a fully compensating modular lead-scintillator calorimeter which provides very good and uniform energy resolution. The calorimeter

comprises 44 individual modules, each consisting of 60 lead/scintillator layers.

Online event selection and data acquisition
High-statistics measurements of particles with very small production cross sections require high reaction rates. The CBM detectors, the online event selection systems and the data acquisition will be designed for event rates of 10 MHz, corresponding to a beam intensity of 10^9 ions/s and a 1 % interaction target, for example. Assuming an archiving rate of 1 GByte/s and an event volume of about 10 kByte for minimum bias Au+Au collisions, an event rate of 100 kHz can be accepted by the data acquisition. Therefore, measurements with event rates of up to 10 MHz require online event selection algorithms (and hardware) which reject the background events (which contain no signal) by a factor of 100 or more. The event selection system will be based on a fast online event reconstruction running on a high-performance computer farm equipped with many-core CPUs and graphics cards (GSI GreenIT cube). Track reconstruction, which is the most time consuming combinatorial stage of the event reconstruction, will be based on parallel track finding and fitting algorithms, implementing the Cellular Automaton and Kalman Filter methods. For open charm production the trigger will be based on an online search for secondary vertices, which requires high speed tracking and event reconstruction in the STS and MVD. The highest suppression factor has to be achieved for J/ψ mesons where a high-energetic pair of electrons or muons is required in the TRD or in the MUCH. For low-mass electron pairs no online selection is possible due to the large number of rings/event in the RICH caused by the material budget of the STS. In the case of low-mass muon pairs some background rejection might be feasible.

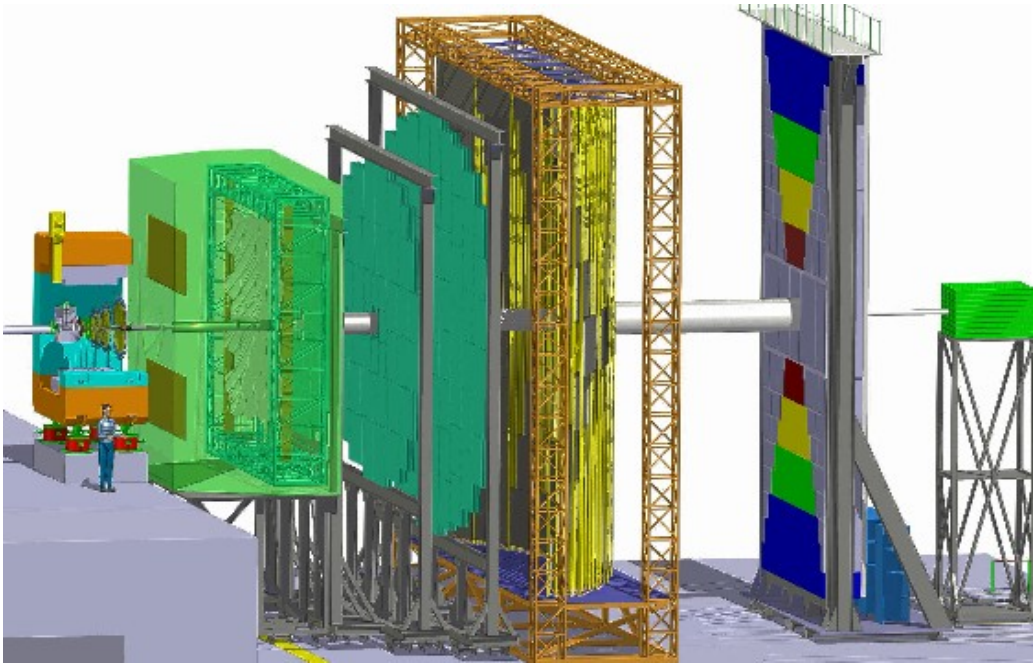

Figure 2.6: Drawing of the experimental setup of CBM (so-called electron setup with the RICH detector) for the SIS100.

3 Overview of the Micro Vertex Detector

3.1 Basic considerations

The role of the Micro Vertex Detector is to provide tracking with highest precision in the high track density environment very close to the interaction region. The four-station detector setup matches the geometrical acceptance of the main tracking detector STS of the CBM experiment of $2.5° \leq \theta \leq 25°$ in the full azimuth. The first station of the detector features a quadratic beam hole of a minimum clearance of 5.4 mm with respect to the beam axis[1], which is to accommodate the anticipated 1 mm radius pencil beam [17, 18] reaching the experiment. The MVD will extend the momentum reconstruction for charged particles down to about 300 MeV/c and enable secondary vertex reconstruction for weak decays of charmed hadrons with a precision significantly better than 100 µm for decay products with laboratory momenta above 1 GeV/c, benchmarked by the D mesons (lab) live time. The detector will be sandwiched between the target and the STS. It will be located at 5–20 cm from the target and consist of four planar detector stations. This number is the result of a compromise between tracking precision and material budget and is also dictated by the available space. While the fixed-target geometry (and high interaction rates) will give rise to a harsh radiation environment, it will, on the other hand, provide rather easy access to the the detector system. The detector concept will therefore rely on a high degree of modularity, optimized in a way as to ease the exchange of damaged detector elements typically within a scheduled maintenance process after one year of operation. The MVD-stations will be equipped with 50 µm thin CMOS Monolithic Active Pixel Sensors, which will provide a spatial precision of ~ 5 µm. A single sensor will provide a sensitive area of $30.1 \times 13.5\,\mathrm{mm}^2$ with a 3.6 mm wide insensitive region at one long-side containing the data processing circuitry. To provide a fill factor of close to 100% for the active area of a station, sensors will be placed on either side. Each detector station will be composed of two separable halves which can be moved out by about 5 cm to either side of the acceptance region during beam manipulation or in case of insufficient beam conditions.

3.2 Running environment

The anticipated vertexing and tracking precision prohibits using a vacuum window between the target and the MVD. The detector will have to be operated in the ~ 1 T magnetic field of the CBM dipole (see Fig. 3.1) and in a moderate $\sim 10^{-4}$ mbar target vacuum. While the sensors are intrinsically immune to both, magnetic field and vacuum, both create a substantial constraint for the general system integration. It is assumed that no RF-fields from the synchrotron have to be considered and no shielding is foreseen.

Due to the small separation between the MVD and the target, the detector will be exposed to exceptional track densities above 3 tracks per mm^2 (see Fig. 3.2), translating in a harsh radiation dose environment, *cf.* Sec. 3.2.3. In case of an operation with heavy ions, the dominating source

[1] driven by radiation hardness constraints, see below.

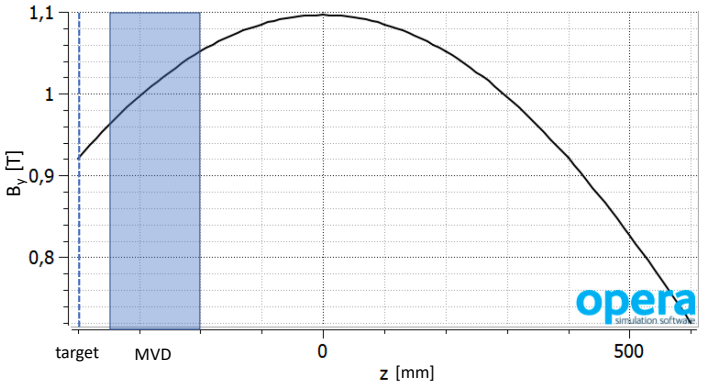

Figure 3.1: Magnetic flux density in the vertical direction along beam axis for the maximum current possible. For measurements with lower beam rigidities, the field will be scaled down accordingly.

of charged particles are δ-electrons which are expelled out of the target by the primary beam ions. Due to the $\propto 1/T^2$ (T = kinetic energy) spectral distribution of the δ-electrons, the most of them are trapped in the magnetic field at the target. Instead of reaching the first station they spiral until they are absorbed by any material in the target chamber. The remaining energetic fraction of the δ-electrons is directed essentially on one side of the detector stations, thereby forcing high occupancies (*cf.* Fig. 3.4). The situation is different in experiments with proton beam. While δ-electrons do not play a significant role, (quasi) elastically scattered protons provide an extra load to the detector region *i.e.* at the smallest polar angles (*cf.* Fig. 3.3).

Details on the beam parameters required by CBM are documented in Ref. [18], which remains a document under discussion, but gives important guide lines for both, accelerator and detectors, for reference modes of the Modularized Start Version of FAIR.

3.2.1 Vacuum operation and magnetic field

For most of the particle momenta expected to occur in the CBM experiments the tracking precision will be dominated by multiple scattering. For maximum magnetic field setting, the bending power between two MVD station amounts to

$$B\mathrm{d}\ell \approx 0.05\,\mathrm{Tm}\,, \tag{3.1}$$

from station to station, which modifies the momentum of single-charged particles by adding a $p_\perp \approx 150\,\mathrm{MeV}$.

As placing a vacuum windows between the MVD and the target would cause unacceptable multiple coulomb scattering and thus deteriorate the pointing precision of the detector, the MVD has to be operated in the about 10^{-4} mbar vacuum of the target chamber. The target chamber vacuum will be separated from the vacuum of the high energy beam transport line by differential pumping or possibly in addition by a thin foil placed upstream of the target. This installation is not part of the MVD system and is therefore not discussed further in this document. The so-called target box is presently (fall 2020) being designed.

The requirement of vacuum compatibility leads to harsh consequences for the MVD operation, both w.r.t. construction and operation. Most importantly, active cooling has to be provided for the sensors and near detector electronics without introducing significant extra material

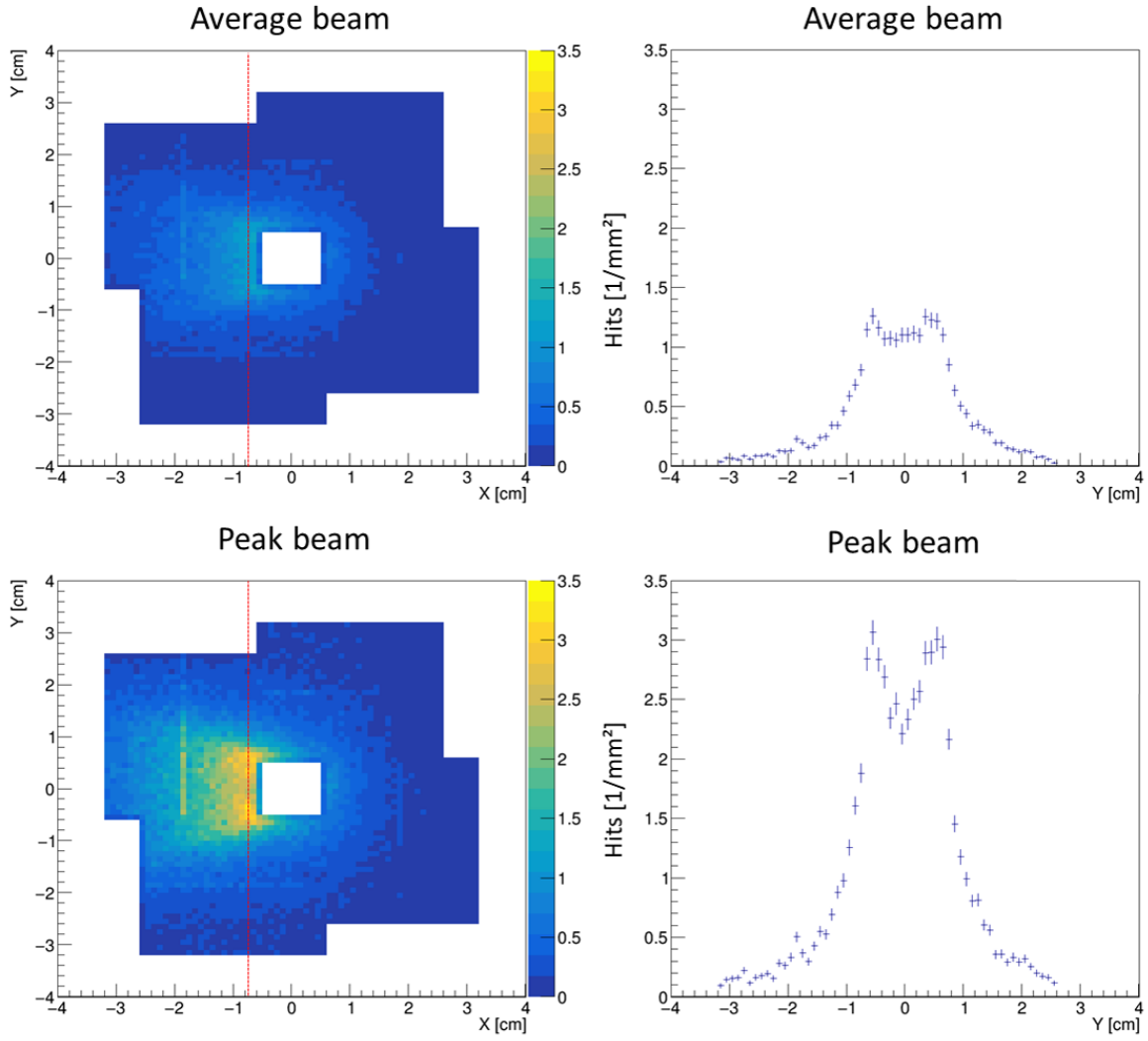

Figure 3.2: Hit Occupancy of the first station of the MVD assuming 100 kHz Au-Au collisions at 12 AGeV beam energy and a sensor integration time of 5 µs. Values for the average occupancy are shown in the upper panels, the lower panels anticipate peak beam intensities (3× average, see Section 3.2.6 and 6.4.1 for details). The right panels represent a projection of the data along the red lines in the two-dimensional histograms.

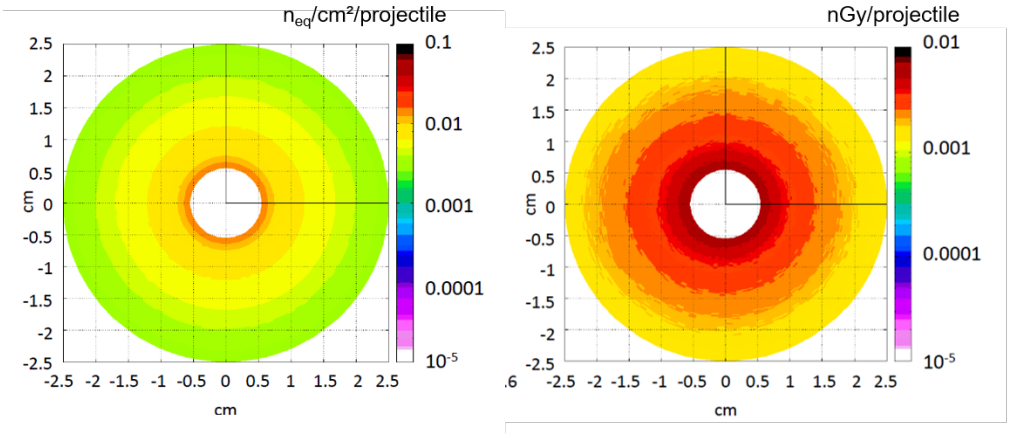

Figure 3.3: Non-ionizing (left) and ionizing (right) radiation dose per projectile in a p-A collision system on the first detector station located at $z = 5\,cm$ (VTX) computed with FLUKA.

budget. Other design aspects are low out-gassing rates, vacuum-compatible gluing techniques and dedicated feed-throughs for cooling liquid, power and signal transmission are needed. Last not least, precautions have to be taken to avoid glow discharges or arcs in case of vacuum degradation as well as charging-up effects due to the numerous δ-electron production.

3.2.2 Radiation doses due to reactions in the target

The MVD is designed to operate at average collision rates of of 100 kHz Au+Au or 10 MHz p-A collisions, which represents only a fraction of the maximum collision rate of CBM. The radiation doses of the MVD are computed under the assumption that the detector will be installed only during beam times respecting these limited rates and fully removed prior to CBM runs requiring full beam intensity. Moreover, we anticipate it will be possible to replace the small and most exposed, first detector station after one year of operation. Despite doing so would extend the lifetime of the MVD by up to a factor of two, we do not consider to change the polarity of the magnetic field within one yearly beam. While the MVD will be designed to cope with a field inversion, we do not wish to require it. This is as it remains to be shown that the fully constructed CBM detector may carry out this step with negligible efforts and impact on an ongoing physics program.

The expected radiation doses per CBM year for the MVD were computed with FLUKA based on the following assumptions. A single Au target with 1% interaction probability and the maximal magnetic field of 1.1 T. The beam intensity is assumed to be 10^7 projectiles per second (average) as minimally required to reach the nominal goal of 100 kHz interaction rate with the MVD built in. It is anticipated that the MVD will be fully removed during high intensity runs exceeding this limit. All integral doses, here and in the following section, are evaluated for a so-called CBM year, *i.e.* for 2 months beam on target without any break (5×10^6 s). Based on this definition the lifetime of a detector element can be evaluated by simple scaling. We anticipate that after one year of running, all components which have reached the end of their life time, can be maintained or replaced. We evaluate the doses in the station nearest to the target only as secondary particle production is not contributing to the total dose at a visible level. The radiation doses are observed to scale at most proportional to $1/z^2$ (z distance from

the target) as expected from a simple scaling assuming flux conservation. Therefore, the more downstream stations are unlikely to suffer from decisive radiation damage within a reasonable time scale.

Radiation doses were derived from two running scenarios: 30 GeV p+Au and 10 A GeV Au+Au. The running scenario of 3.5 A GeV Au+Auwith 30% relative field strength was confirm to yield less radiation damage than the above cases. The respective results for the case of proton beam is shown in Fig. 3.3. The left panel refers to the non-ionizing radiation dose on the first station at a position of 5 cm downstream the target. The dose is given in units of n_{eq}/cm^2 per beam ion traversing the target. The simulation results were normalized to an anticipated running time of CBM of 5×10^6 s per year. Based on this assumption, one computes a maximum annual dose for non-ionizing radiation of $7 \times 10^{13}\, n_{eq}/cm^2$. This is reached at smallest polar angels and does not show substantial deviation from azimuthal symmetry since the dose is primarily due to beam protons with high rigidity scattered under small forward angles. The right panel of Fig. 3.3 displays the related ionizing radiation dose in units of nGy per ion (projectile). The maximum ionizing dose in one year CBM running amounts to 5 MRad.

Unlike to the radially symmetric case for proton induced reactions, the radiation field experienced in Au+Au experiments is very asymmetric. Fig. 3.4 shows respective radiation doses for the same station. Now the maximum appears on the side to which the δ electrons are deflected to. It is evident that the ionizing radiation dose is dominantly due the δ electrons. Those electrons dominate both the ionizing dose and the occupancy of the MVD, and add also a sizable contribution to the non-ionizing dose. The maximum doses located along the white line shown in the right panel of Fig. 3.4 are depicted in the left panel of the figure. Based on these arguments, we conclude that the sensors have to withstand during an Au+Au beam time an ionizing radiation dose of 5 MRad and a non-ionizing radiation dose of $2 \times 10^{13}\, n_{eq}/cm^2$. Note that only one of these two running scenarios will only apply. Therefore, the doses for p + Au, and Au + Au do not add and only the higher of both numbers for ionizing and non-ionizing radiation, respectively, have to be considered.

Due to the complex radiation field, the sensors will be exposed to radiation gradients of more than one order of magnitude over the surface of a single sensors. Therefore, they have to withstand the radiation doses without a need of tuning device parameters out of the range suited for operating the non-irradiated device.

3.2.3 Radiation effects due to beam ions passing the detector

Relativistic heavy ions are known to form a serious thread to all kinds of semiconductor devices. This is as those particles cause a large number of ionizations and atom displacements when penetrating silicon.

The ionization damage induced by heavy ions is calculated assuming that it scales with the specific energy loss. Based on this approach and by assuming for the sake of simplicity that the momentum per nucleon of the beam ions is reasonably close to the one of minimum ionizing particles, the radiation dose D_{ion} can be approximated by

$$D_{ion} \approx \Phi \cdot z^2 \cdot k_{mip}\,. \tag{3.2}$$

Here, Φ represents the particle flux in units of particles/cm^2 and z the atomic number of the projectile. The constant $k_{mip} = 2.89 \times 10^{-11}\, krad \cdot cm^2$ [19] represents the radiation dose caused by the individual minimum ionizing particle. It was indeed observed during the operation of MIMOSA-26 sensors in NA61/SHINE that the impact of a heavy ion (Pb) in the active area of the sensor leads to substantial charge generation forming clusters of active sensors comprising

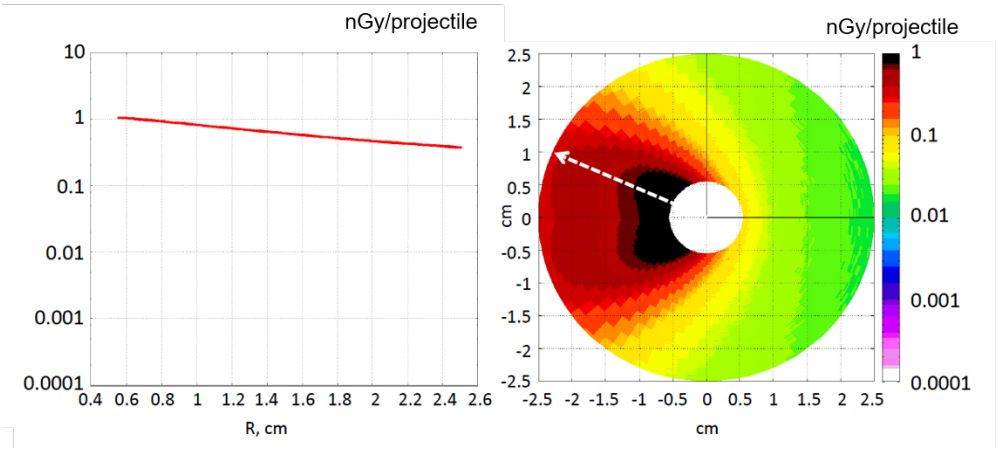

Figure 3.4: Ionizing radiation dose per projectile for a Au+Au collision system as simulated with FLUKA for a first detector station located at $z = 5\,\mathrm{cm}$. The left panel indicates the doses along the arrow indicated in the distribution plot shown in the right panel. The non-ionizing radiation doses show a similar distribution (not shown).

	Protons	Au-ions
Max. flux (ionizing dose)	$60\,\mathrm{kHz/mm^2}$	$10\,\mathrm{Hz/mm^2}$
Max. flux (non-ionizing dose)	$1.8\,\mathrm{Hz/mm^2}$	$60\,\mathrm{Hz/mm^2}$
Max. flux	$1.8\,\mathrm{Hz/mm^2}$	$10\,\mathrm{Hz/mm^2}$

Table 3.1: Maximum tolerable heavy-ion flux in the beam halo at $r > 5$ mm in the MVD area. See text.

up to $\sim$ 200 pixels. Yet, the MIMOSA-26 sensor did not have a depleted epitaxial layer and charge collection was almost entirely due to diffusion.

Concerning the integrated non-ionizing dose, one anticipates that the hardness factor of a heavy beam ion amounts roughly to $300\,\mathrm{n_{eq}/cm^2}$. This is suggested by the extrapolation of related theoretical studies [20] and supported by the preliminary results of irradiation studies with $30\,A\,\mathrm{GeV}$ Pb ions, which were carried out at the CERN-SPS together with the NA61 collaboration [21].

3.2.4 Integrated radiation damage caused by the beam halo

The MVD detector is not only near to the target but reaches also very close to the nominal beam axis, cf. Tab. 3.2. Hence, a crucial operational condition is the transverse beam profile in the region of the MVD detector and the stability of the beam.

To assess the level of tolerable beam halo quantitatively, we took into account information obtained with the operation of MIMOSA-26 sensors in the NA61/SHINE setup as well as experiences with beam halos made in HADES experiments. Requirements for the beam conditions are derived from the assumption that the integrated radiation load caused by beam ions must not exceed one third of the nominal radiation tolerance of the MIMOSIS sensors which translates to a maximum tolerable dose due to ion impact of 1MRad and $10^{13}\,\mathrm{n_{eq}/cm^2}$ within a CBM year.

Based on this assumption, we derive a maximum tolerable heavy-ion flux at a radial distance

of 5 mm from the nominal of 10 Hz/mm^2 and of 1.8 kHz/mm^2 for Protons (*cf.* Tab. 3.1). Note that the limits have also to be kept in case the beam is not ideally centered or moving within a spill. An appropriate monitoring of the beam halo with a slow feed back to the operating is needed for safe operation of the MVD.

3.2.5 Coasting beams

A direct impact of the beam into the MVD might be caused by i) errors during the beam tuning procedure and ii) failure of the beam steering during regular operation. To avoid the first scenario, the MVD will be mounted on moving tables, which allow to move it into a safe position during beam tuning. Due to mechanical constraints, this safe position cannot be further than 4 cm from the beam center. Suited collimators are required in order to dump the beam in case it leaves this allowed radius around the nominal beam center.

In the second scenario, the MVD will be in its measuring position, which will likely not be fully protected by collimators. Therefore, a direct beam impact is not excluded and a fast beam abort system is required to prevent permanent damage in the detector. To estimate the reaction time required, we considered permanent damage due to integrated radiation doses and to Single Event Effects (SEE). Based on the arguments discussed in the previous chapter, one concludes that the detector would withstand the beam $\mathcal{O}(1 - 10$ s) before its tolerance to integrated radiation damage is exhausted.

Damage by SEE include for example the destruction of the vulnerable transistor gates of CMOS sensors. This would turn into an immediate and permanent destruction of the sensors. The conditions under which CMOS sensors would suffer from such damage have so far not been studied in a systematic way. For a rough assessment, we rely on the observation that no such effect was observed when exposing the sensors to the NA61/SHINE beam. Based on this observation, we anticipate with caution that individual relativistic Pb ions do not create permanent damage in the sensors. A damage by the summed charge of several ions cannot be excluded as the beam intensity of NA61/SHINE is considered as too low to trigger this scenario. From this consideration, we derive the requirement that, to prevent damage, each unit of surface should be hit in average by less than one heavy ion before a successful beam stop. The allowed number of impinging ions per unit surface is then given by:

$$N_{\text{ion}}^{\text{max}} = \frac{1}{\pi r^2} \tag{3.3}$$

The radius of the volume, in which $> 99\%$ of the ionization is taking place, was found to be $r = 5\,\mu$m for Au-ions [22]. From this we derive a maximum tolerable integrated ion flux of $N_{\text{ion}}^{\text{max}} \approx 6 \times 10^4$ ions/mm^2. Assuming an beam ion flux of $\sim 10^7$ Hz/mm^2, this value is reached within ~ 100 µs. Therefore, a reaction time of $\lesssim 100$ µs of the beam stop system seems required.

3.2.6 Beam intensity fluctuations

Slowly extracted beams from synchrotrons exhibit temporal variations of beam intensities on basically all time scales. From experiments at the SIS18 it is known that the ratio of average beam intensities evaluated for short periods of some 10 µs during the flat top of a spill (called peak), relative to the mean over the full flat-top of the spill (average), can reach values as large as ten, even after dedicated optimization of the slow extraction. Such fluctuations are referred to as spill micro-structures and the peak-to-average values are used as indicators for the beam quality. In the context of the MVD, intensity fluctuations evaluated for time bins in the order of

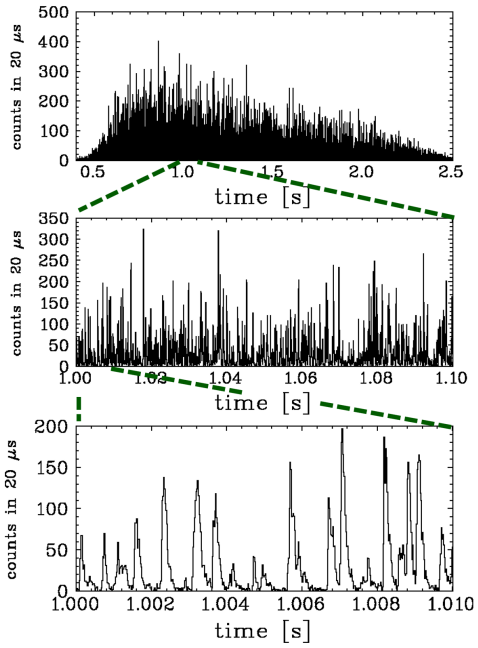

Figure 3.5: Instantaneous beam flux of a slow-extracted beam from SIS18 measured with a scintillation detector. The flux is given in counts per 20 µs. Three different scales are used (from top to down), 2 s (full spill length), 100 ms and 10 ms. The rate average over 10 ms (lowest panel) amounts to 29 per 20 µs bin. Note that instantaneous rates can exceed the average by more than a factor 10. Picture taken from [23].

the integration time of the sensors are most important. Fig. 3.5 shows such intensity fluctuations for a beam extracted from the SIS18.

The quality of the extracted beam, the SIS100 will provide, is at this time not known. It has, however, to be assumed that the peak-to-average will never be even close to unity. In the conception of the MVD we therefore evaluated the occupancy, buffer sizes and band width of the data transmission assuming that the detector should handle a peak beam intensity of a factor of three above the spill-average for at least 50 µs. In case the instant beam flux exceeds the spill-average by more than this factor, or for a longer duration, data taking with the MVD will remain possible but the local efficiency is reduced by a controlled truncation of the recorded data.

3.3 Detector geometries

In order to fulfill specific performance requirements for different physics cases, two main MVD (detector) geometries have been investigated and technically evaluated, based on four detector stations each:

- **VX**: This geometry focuses on the identification of secondary vertices of decaying open charm D mesons. This aspect was originally driving the need and the first design of the MVD. Given the D mesons' lifetime of $c\tau \simeq 100 - 300\,\mu\text{m}$ and the moderate γ factors at SIS100 energies, the first station has to be positioned as close as possible to the target, employing as little material budget as technically feasible. On the other hand, such a placement poses high demands on the radiation hardness of the respective sensors.
- **TR**: This geometry focuses on track reconstruction of mainly low-momentum particles, which, due to their track curvature, do not or only partly reach the STS detector. Such a capability is of primary interest *e.g.* for dilepton spectroscopy where it significantly contributes to background reduction. In the meanwhile, reconstructing hyperons decaying in the volume of the MVD, together with STS, was recognized as another valuable physics

Station geometry	Inner radius (mm)	Active area (cm^2)	no. of sensors front+back side	Module carrier dimensions (mm^2)	Carrier material
a	5.4	33.0	4+4	51.0 × 59.6	CVDD
b	5.4	130.6	16+16	81.9 × 85.7	CVDD/TPG
c	10.4	455.1	64+48	124.9 × 143.9	TPG

Table 3.2: Geometrical parameters of the 3 MVD station geometries a, b, and c: inner radius (distance beam - edge of first sensor), active area (front-/back-side, minus sensor overlap), number of sensors, dimensions of the planar carrier housed by a module, representing a station quadrant, and the carrier bulk material Thermal Pyrolytic Graphite (TPG) or pCVD Diamond (CVDD).

case, also for MVD. To improve detection capability for such observables, single detector stations have to cover a larger geometrical acceptance compared to the VX geometry. Moreover, the first station need not be placed as close as possible to the target, a situation mitigating radiation damage as well.

The detailed description and code references of the different MVD detector geometry versions have been made available to the CBM members in an internal CBM computing note [24]. Both detector geometries are based on three module (*i.e.* quadrant) geometries (called a, b and c), which differ in the active area covered. Table 3.2 summarizes the geometrical parameters of these three MVD station geometries. Note, each sensor ladder (*i.e.* row of adjacent sensors) of a given station geometry counts the same number of sensors. As a consequence, the MVD geometrical acceptance at large polar angles exceeds the nominal geometrical acceptance of CBM. Table 3.3 summarizes the main geometrical parameters of the two detector geometries, composed of station geometries a-c, placed at different distances from the target ($z = 0\,\mathrm{cm}$). Figure 3.6 compares the two MVD detector geometries VX and TR (lateral dimension not to

Station no./ Geometry	0	1	2	3	total active area (cm^2)	total no. of sensors
VX	a (5)	b (10)	c (15)	c (20)	1073.8	264
TR	b (8)	b (12)	c (16)	c (20)	1171.4	288

Table 3.3: Geometrical parameters and the total number of sensors mounted of the two MVD detector geometries VX and TR. Stations are positioned at given z-position, given in brackets in units of cm (target position $z = 0$ cm). Module geometries a,b and c refer to table 3.2.

scale), comprising 4 planar detector stations built of 3 different station geometries a, b, c, which are positioned between $z = 5$ (8) and 20 cm for VX (TR) downstream the target. Figure 3.7 compares both detector geometries in 3-D.

3.3.1 Building blocks

The underlying concept of the detector design is modularity and scalability. In this way, we want to minimize design effort and reduce the number of individual solutions to mechanical and electrical challenges. W.r.t. maintenance between runs it also allows to reduce the number of "hot spare modules" needed to exchange broken detector stations. Fig. 3.8 depicts the resulting MVD detector concept, represented by a CAD model view (left). It shows the VX geometry

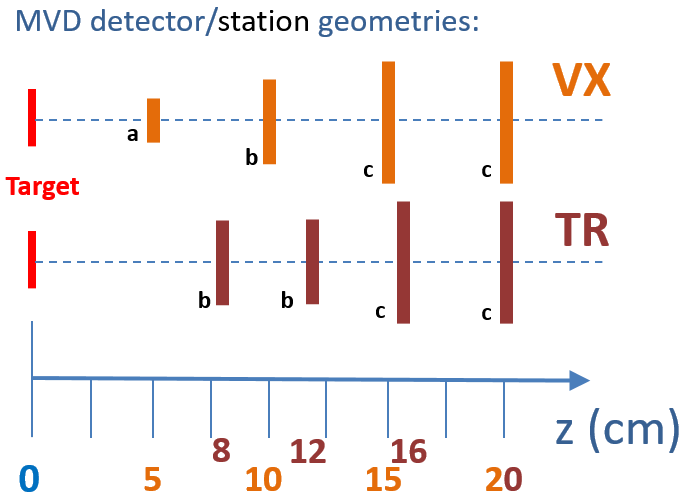

Figure 3.6: Illustration of the two MVD detector geometries VX and TR (lateral dimension not to scale), comprising 4 planar detector stations built of 3 different station geometries a, b, c, positioned between $z = 5$ (8) and 20 cm for VX (TR) downstream the target.

comprising four planar stations. The model is based on building blocks defined in the following (ordered in a top-down approach). A detailed description of each building block follows in Chapter 4.

- **MVD**: MVD denotes the complete vertex detector comprising four detector stations located inside the target vacuum vessel. To allow for moving the sensors away from the beam axis during beam tuning, each station is composed of two half-detectors, left and right of the beam axis.
- **Half-detector**: Each of the two half-detectors comprises four half-stations, which share a common base plate. This table can be remotely moved perpendicular to the beam axis in the horizontal plane.
- **Station**: A station is the combination of two half-stations place at the same distance to the target. It refers to an entity mostly relevant for track reconstruction package dealing with hit points in a plane. It is rather not a self-contained hardware device, due to the split of the detector in two halves.
- **Half-station**: A half-station comprises two detector modules, spliced together during assembly. Both heat sinks, part of the modules, can be connected to the a single cooling pipes either parallel (outer stations) or serial (inner stations), depending on the amount of heat to be extracted. The half-stations are mounted in dedicated C-shaped Aluminum structures which are fixed to the half-detector base plate.
- **Stand**: A mechanical stable vertical holding structure (B)elow and on (T)op of the half-station. (B) comprises a stand with slides to mount the half-station to the rails fixed on the half-detectors base plate. (T) extends the half-station to the top allowing for linking all half-stations together after integration. Both stands are made of Aluminum and eventually feature a thin vertical interconnecting brace for mechanical stabilization, constrained by space restrictions on both sides due to cables and pipes.
- **Module**: A module denotes one quadrant of a station, *i.e.* sensor ladders, carrier and heat sink, and it represents the smallest functional and self-contained unit of the MVD,

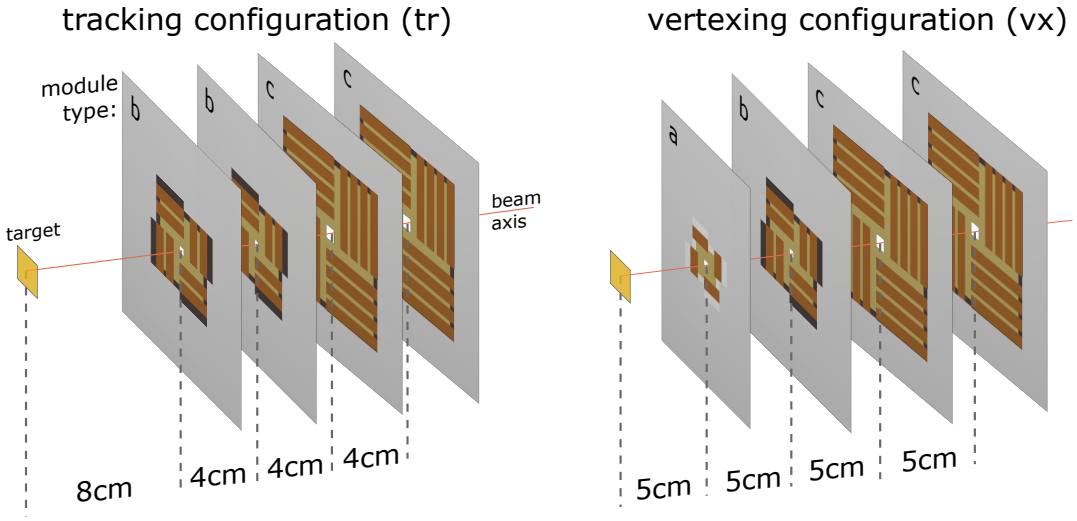

Figure 3.7: 3-D illustration of the two MVD detector geometries TR (left) and VX (right), comprising 4 planar detector stations built of 3 different station geometries a, b, c, positioned between $z = 5$ (8) and 20 cm for VX (TR) downstream the target (z=0).

i.e. it has been subject to performance studies during the prototype phase. Each (planar) module houses sensors and flex cables on both sides, as well as the first stage of the front-end electronics, which is directly attached to the heat sink.

- **Heat Sink**: This component represents the Aluminum structural element which holds the sensor carrier by clamping it with a dedicated clamp to a cold plate. The latter contains the coolant pipe and also serves as holding structure for the front end electronics.
- **Carrier**: A carrier holds the sensor ladders and guides the dissipated heat to the heat sink. It is made of thin, high performance thermal materials (pCVD diamond or Thermal Pyrolytic Graphite TPG) and represents the best compromise between cooling performance, material budget and mechanical stability. The dimensions of the carriers are large enough to include keep-out areas without sensors needed to clamp the carrier to the heat sink, a minimum gap between the sensors and the heat sink of 10 mm and a gap for mounting the (outer) flex cable. Both gaps are required to minimize residual forces to the part of the flex cables housing the wire bonds.
- **Ladder** The sensors are arranged in rows, called ladders, with sensors butt-joint at the short sides, respectively. Two sensors share one Flex cable providing the electrical connectivity. Note that a module can house several ladders on each side of the carrier.
- **Sensor**: High-granular CMOS monolithic pixel sensor sensitive to charged particles (see Chapter 4.1), the MIMOSIS chip.
- **Flex cable**: Flexible, thin cables, attached to the ladders, are used to connect the sensor to the read-out. The final layout of the different flex cables needed is presently under evaluation and is driven by the design of the MIMOSIS sensor. Since the flex cables are partly placed inside the acceptance, their material budget has to be minimized. Currently, a flex cable serves two sensors.

Note, holding structures of different sizes, indicated with light gray in Fig. 3.8, are not considered in this list of building blocks.

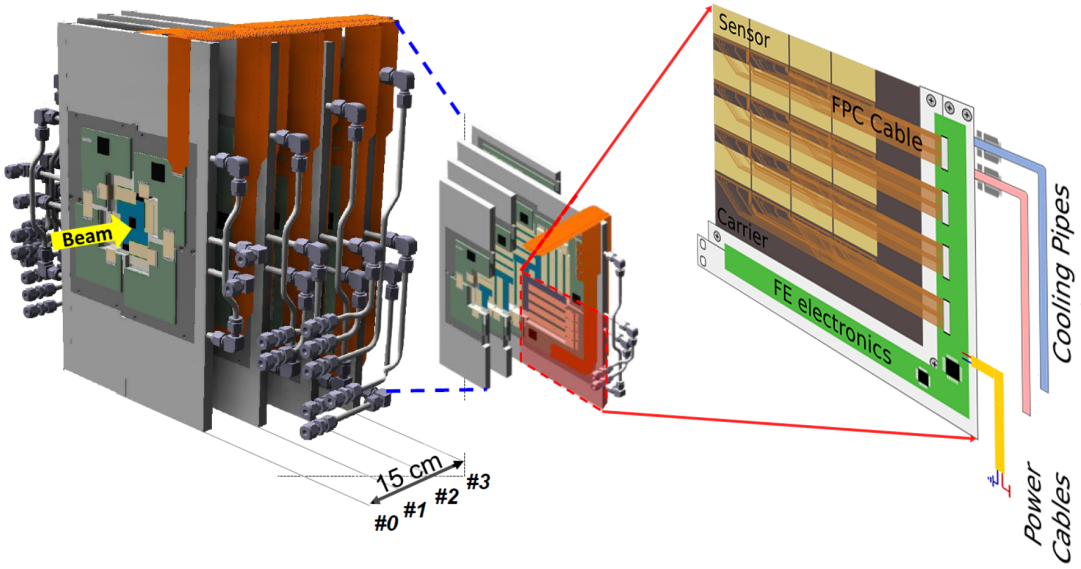

Figure 3.8: Left: CAD views of the 4-station MVD (VX geometry) with services, beam from the left. Middle: Station 2 (geometry b) with service lines and flexible readout cables, stations 0,1 and 3 shown as half stations only. Right: Sketch of a MVD module, representing a quadrant of station 2. The active part (geometrical acceptance) with sensors is indicated, as well as flex cables and carrier, fixed to the heat sink, which supports the front-end electronics (R/O) and houses cooling channels.

3.3.2 Station layout

The "heart" of each station is the MIMOSIS sensor, shown in the left panel in Fig. 3.9. It is arranged side by side touching each other on the short sides. One row of placed sensors is called a ladder. Depending on the acceptance to be covered, a ladder contains up to four sensors and a carrier is populated with up to four or three ladders on either the front or back side, respectively. This leads to three different module and station layouts used for the TR and VX detector geometries. To account for the insensitive area of a sensor, ladders are glued on both sides of the module carrier. To achieve full acceptance in the active area sensors are placed with a slight overlap even of the sensitive areas to prevent dead areas even for inclined tracks, cf. Sec. 4.2.2.1. A sketch of the concept is shown in the right panel of Fig. 3.9. To provide full azimuthal coverage within the requested polar angle region, four nearly identical modules are arranged in a 90° rotational symmetry around the beam axis as shown in Fig. 3.10. Note that the coverage eventually extends to outside the polar region of the nominal geometrical acceptance. Adding extra sensors at the periphery of stations has a negligible impact on the project costs and has no impact on the design of the read-out and integration procedures. However, the extended acceptance provides extra space points for tracking of in particular low-momentum particles. The total number of sensors needed to build the MVD in the given geometries VX and TR are summarized in Tab. 3.3. The current installations plan of CBM envisages employing the "TR" detector geometry for the starting phase of the experiment. Our concept would allow for re-using individual modules in the "VX" detector geometry in a later phase, depending on their performance parameters after operation in CBM.

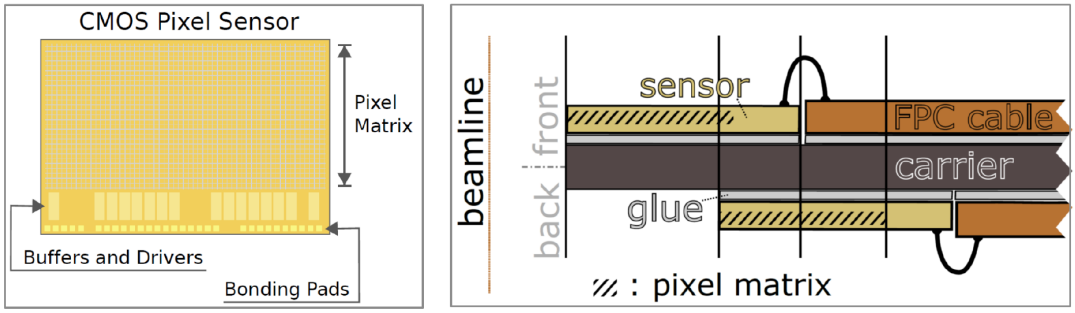

Figure 3.9: Left: MIMOSIS geometry, indicating the sensitive (pixel matrix) and insensitive (buffers and drivers, pads) sensor area. Left: Schematic cross section of the inner part (next to the beam axis) of a MVD module, demonstrating the relative sensor arrangement on the front and back side of the carrier.

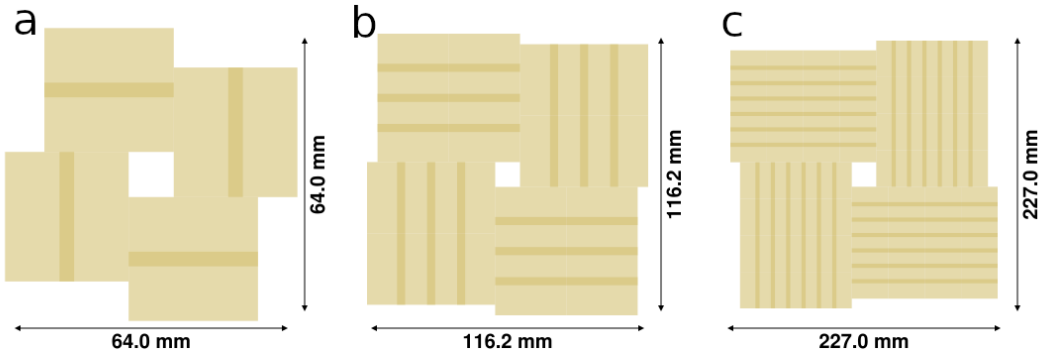

Figure 3.10: A top view, looking downstream from the target, of the sensor (MIMOSIS) arrangement of module and stations geometries a, b and c. For simplicity, only sensors (a) and ladders of sensors (b, c) are shown, mounted on both sides of the carrier, visualizing the actively covered area per station. The darker structures indicate overlapping sensors (ladders).

4 Technical Design

4.1 Sensor Technology

4.1.1 Sensor requirements

The choice of the sensor technology for the MVD was initially driven by the physics case of open-charm reconstruction, which required to focus in particular on the secondary vertex resolution. Accounting for the lifetime $c\tau \approx 100$ µm of those particles, a precision of the reconstructed secondary vertex along the z-axis of $\sigma_z \approx 70$ µm for particles with $p > 1\,\mathrm{GeV}/c$ is required. Additional constraints were obtained from the need to withstand the harsh and strongly inhomogeneous radiation field found in the vicinity of the target. Moreover, the design aims to obtain – within reasonable limits – a homogeneous and symmetric distribution of the material budget. This consideration was based on the assumption that "heavy" structures would locally deteriorate the sensitivity of the detector and consequently complicate efficiency and acceptance corrections.

The studies of technology requirements were started with a simplified detector geometry, which represented the MVD as three silicon discs located at $z = 5\,\mathrm{cm}$, $z = 10\,\mathrm{cm}$, and $z = 15\,\mathrm{cm}$ downstream the target. A number of alternative and refined geometry options were also simulated for SIS100 and SIS300 beam energies. The results vary slightly, depending on the detailed assumptions made, but provide a common overall conclusion. A representative outcome of the simulations on the relation between the secondary vertex precision, spacial resolution, and material budget is shown in Fig. 4.1. The former simulation was carried out for a beam energy of 25 A GeV and central Au+Au collisions. It can be considered, besides the much different apparent charged particle multiplicities, as representative for p+A collision systems with similar beam energy as foreseen for open-charm studies at SIS100. One observes that reaching the targeted secondary vertex resolution requires a combination of extremely granular pixels with a spatial resolution of ~ 5 µm and a material budget of only few $0.1\,\%\,X_0$. These requirements hold, first of all, for the most upstream station. More detailed simulations showed that the material budget of the more downstream stations can be relaxed to $\sim 0.5\,\%\,X_0$ without a sizable loss of sensitivity. A fourth station located at $z = 20$ cm is required to solve issues of bad track matching between the MVD and the STS [26].

Additional requirements were obtained from the envisaged rate capability of the detector. Operating the MVD at the nominal collision rate of CBM (10 MHz Au+Au peak rate) is found to turn into unrealistic requirements. It was therefore decided to design the MVD for a collision rate of ~ 100 kHz Au+Au or 10 MHz p+A and to remove it for CBM physics cases, which do not require the MVD but higher rates. As discussed in more detail in Sec. 3.2.2, the latter collision rate turns into radiation doses of ~ 5 MRad and $\sim 7 \times 10^{13}\,\mathrm{n_{eq}}/\mathrm{cm}^2$. The peak counting rate of the most exposed sensor was found to amount to $70\,\mathrm{MHz}/\mathrm{cm}^2$, which includes a margin for beam fluctuations of a factor three.

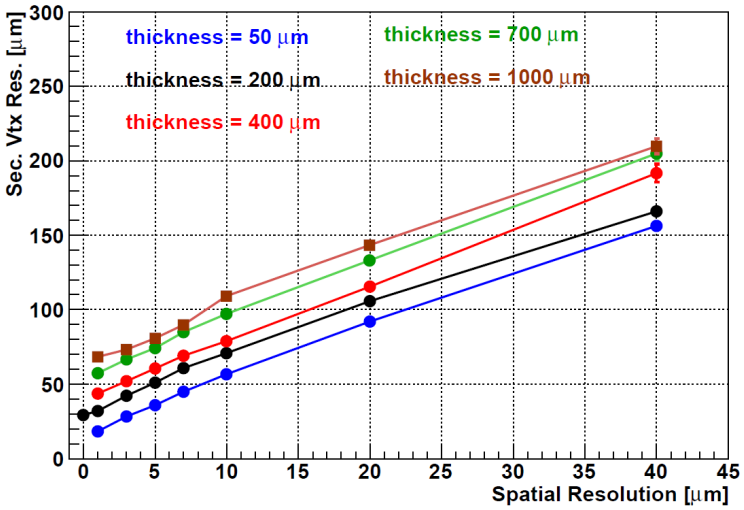

Figure 4.1: Secondary vertex resolution for daughter particles of a $D^0 \rightarrow K^+\pi^-$ *decay along the z-axis, for an early MVD geometry with a first station at* $z = 5\,\mathrm{cm}$*, as a function of the spatial resolution of the sensor and various thickness' of the MVD station.* $1\,\% X_0 \approx 1000\ \mu\mathrm{m}$ *Silicon. The early study relied on a simplified geometry and anticipated a 25 A GeV Au+Au collision system. From [25].*

4.1.2 Technology choice

During the first phase of the technology choice, the requirements of the MVD were compared with the capabilities of different silicon pixel sensor technologies including CCDs, hybrid pixels, DepFET and CMOS-sensors. The first round of technology choices were done by exclusion and accounting for the features of the technologies.

For hybrid pixels, it was acknowledged that this technology provides an exceptional time resolution, and radiation tolerance. However, the pixels, as prepared for the first generation LHC, did not provide the fine pixel pitch and low material budget required for reaching requirements. CCDs were found to match our requirements in granularity and material budget but their tolerance to non-ionizing radiation missed our specifications by orders of magnitude. DEPFET pixels are considered to provide a much better compromise between these parameters. However, they are restricted to a common roller shutter readout, which is limited in time resolution. Moreover, it was questioned if the pixels would be suited to be operated in strongly non-homogeneous radiation fields. This is, as DEPFETs reach their good tolerance to ionizing doses only if the radiation damage is compensated by tuning reference voltages. Doing this in a complex, two dimensional topology seemed out of reach. CMOS Monolithic Active Pixel Sensors demonstrated an excellent granularity, light material budget, and good time resolution in combination with an advanced radiation tolerance. They were, therefore, considered as baseline technology for the CBM-MVD. This was done knowing that specific R&D on CPS was needed to meet all requirements simultaneously.

4.1.3 An introduction into CMOS pixel sensors

CMOS Monolithic Active Pixel Sensors (CPS or MAPS) are silicon pixel sensors, which are produced with standard CMOS processes. This approach allows to integrate sensing element

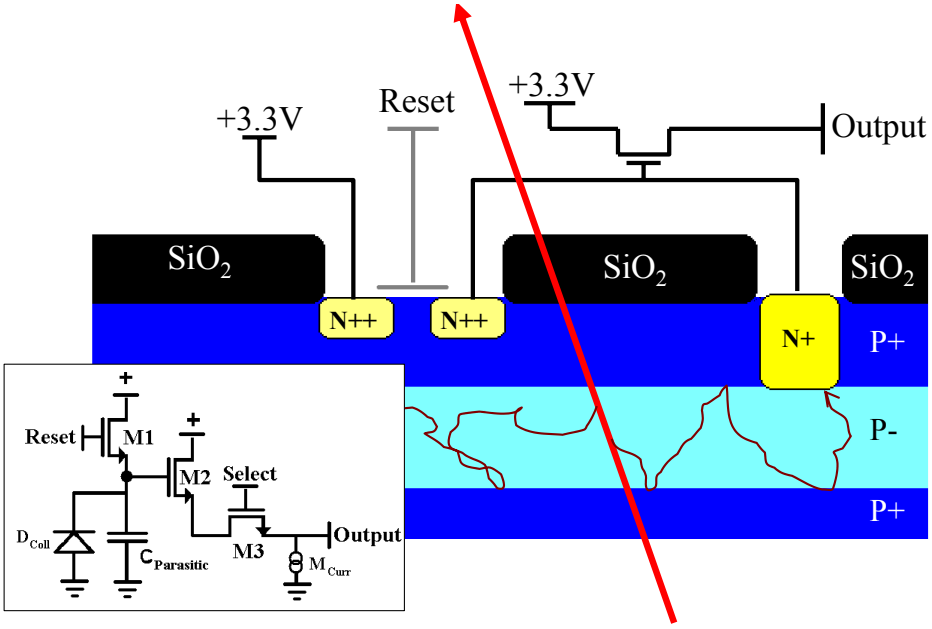

Figure 4.2: Fundamental layout of a CMOS-sensor. The trajectory of an impinging minimum ionizing particle and the diffusion paths of two free electrons in the active volume, the epitaxial layer, is shown. The figure presents a cross-section of the most traditional pixel design relying on a standard collection diode and a preamplifier with reset-transistor and source follower (see schematics in the lower left box).

as well as analog and digital signal processing circuits on a sole chip, which may be produced in cost efficient commercial CMOS foundries. Moreover, the approach eliminates the need for building separate sensor and front-end chips and for interconnecting both. This reduces both, the material budget and the complexity of the detector, in addition to benefits in terms of cost and production yield. The missing optimization of the production processes forced initially to accept compromises, namely in terms of reduced rate capability and radiation tolerance of the devices. However, this issue is increasingly being solved thanks to the constant evolution of commercial CMOS processes used for digital imaging sensors from which CPS are derived.

Already short time after the invention of CPS, their potential for charged particle tracking was recognized [27]. First CPS prototypes showed a single point resolution of 1–2 µm and a detection efficiency close to 100% [28] in a $\sim 100\,\mathrm{GeV}/c$ pion beam at the CERN-SPS. Those excellent results were reproduced with a full reticle size CPS up to 10^6 pixels on active areas as large as 4 cm^2 [28, 29]. Soon after, the feasibility of thinning the sensors to a thickness of 50 µm without loss of performance was demonstrated. A review of the technology of CPS with a focus on radiation tolerance can be found in [30].

The design of the sensing element of a CPS was guided by the need to remain compatible with non-optimal, double well CMOS processes relying on wafers with low resistivity epitaxial layer. A simplified sketch of a CPS implemented in this process is shown in Fig. 4.2. The lowest layer of the device is formed from a highly doped silicon wafer. On top of this wafer, a lowly doped epitaxial layer is implemented, which (P− in the figure) represents the active volume of the sensor and may show a typical thickness of 20 µm. Above, a highly doped layer is added,

which is typically realized by a P-well (P+ in the figure). The collection diode is implemented as an N-well/P-epitaxial junction.

For a long period of time, the possibility to deplete the sensitive volume of CPS was very limited. The signal electrons generated by impinging particles are collected by thermal diffusion, which is guided by repulsive potentials created by the P−/P+ interfaces at the borders of the epitaxial layer. This collection process is almost 100% efficient. The charge is distributed over a cluster of several neighboring pixels. While the signal amplitude in the individual pixel is reduced, the particle's impact position can be reconstructed with improved precision by employing center-of-gravity methods. In the meanwhile, the option of using fully depleted pixels is available. It provides substantially improved radiation tolerance, potentially with draw backs in terms of spatial resolution.

The small thickness of the sensing element of CPS allows for very light material budget but otherwise translates to moderate signal charges, subject to large Landau fluctuations. Depending on details of the design and process the signal charges can range from some 100 to 1000 electrons per pixel. To distinguish this signal from noise very low-noise preamplifiers are needed. Moreover, they must be suited for integration into the small area of individual pixels. The preamplifier of the future sensor for the CBM-MVD is an extension of the SB-pixel amplifier (see box in Fig. 4.2). This amplifier is composed of the collection diode and a high resistivity, forward-biased biasing diode. The signal is generated by collecting the signal charge in the tiny (few fC) parasitic capacity of the collection diodes and by buffering the resulting voltage drop using an impedance converter (in the most simple case the source follower shown in Fig. 4.2). The biasing diode compensates the static leakage current of the collection diode and clears the signal charge after a hit occurred.

4.1.4 The MIMOSIS sensor - design goals

4.1.4.1 Introduction

The MVD will be equipped with a customized sensor labeled MIMOSIS, which is being developed within the CBM collaboration by the IPHC Strasbourg. The sensor will rely on the positive experience collected with the ULTIMATE sensor [31] used in the STAR HFT and the ALPIDE sensor [32] used for the ALICE ITS upgrade [33]. It will be engineered in the Tower/Jazz 180 nm CMOS process, which comes with a quad-well technology and a certain flexibility in terms of the thickness and doping of the epitaxial layer.

The in-pixel preamplifier was derived from the successful solution found for the ALPIDE sensor [34], which incorporates a discriminator in each pixel and a pixel readout based on a fast priority encoder. It is considered to combine this amplifier with fully depleted sensing layers using a novel top bias scheme [35]. Such a configuration allows to apply a depletion voltage of up to 40 V. It is expected to extend the tolerance of the sensors to non-ionizing radiation by up to one order of magnitude, a comfortable safety margin with respect to the environment expected in CBM runs. This advantage has to be traded against a potential loss in spatial resolution from 5 µm to ∼ 8 µm. The optimum may be chosen at run-time accounting for the physics goals of the run and the radiation damage of the sensors by tuning the high voltage.

The internal data processing chain of MIMOSIS will be modified with respect to the one of ALPIDE with focus on two major concerns. Firstly, unlike to ALICE, CBM relies on a continuous readout. Therefore, the trigger-oriented data reduction circuits of ALPIDE have to be replaced by a high bandwidth readout which also allows to cope with the occupancy fluctuations introduced by the beam fluctuations, and the strong occupancy gradients. Moreover,

MIMOSIS will have to satisfy higher requirements in respect to radiation tolerance. Besides the higher integrated ionizing and non-ionizing doses, the sensor will be exposed to sizeable dose gradients over its surface. As the sensor will be installed very close to the beam axis, it will be continuously exposed to direct impacts of heavy ions from the beam halo. Therefore, it has to be protected against SEE's like bit flips and potential latch ups.

Realising the MIMOSIS sensor requires several prototyping steps. It started with a validation of the pixel array sensing system and read-out architecture, followed by a progressive validation of the newly designed data processing and sensor steering circuitry implemented on the sensor edge. The first step was completed with a small sensor (called MIMOSIS-0) encompassing a section of the full pixel array composing the final sensor. The next step necessitates full scale prototypes. The first of them, MIMOSIS-1, incorporates nearly all functionalities of the final sensor and explores alternative pixel array variants to seek for an optimized detection performance. Currently being characterised, The tests of MIMOSIS-1 will yield design optimisations integrated in the next prototype, MIMOSIS-2, which will incorporate the complete circuitry of the final sensor and exploit the test results of MIMOSIS-1. The performance assessment of MIMOSIS-2 is expected to provide the necessary understanding for deriving the optimised design of the final MIMOSIS sensor.

4.1.4.2 MIMOSIS: Global layout

The detailed optimisation of the MIMOSIS sensor design is currently being studied with a full size prototype sensor, called MIMOSIS-1, featuring several alternative designs of the in-pixel circuitry. It hosts a ~ 4 cm^2 active pixel matrix consisting of 504×1024 pixels with a height of 26.88 µm and a width of 30.24 µm. As discussed in more detail later-on, each pixel incorporates a full amplifier-shaper-discriminator chain similar to the one used in ALPIDE. The on-pixel digital front-end is modified and relies on a non-triggered, frame based readout. The start and end time of a frame is set by an end-of frame signal, which is generated by an internal sequencer. The frame length may be set in multiples of the 20 MHz clock cycle of this sequencer by means of detector control and will amount to 5 µs by default. In case the on-pixel discriminator detects a hit, this information is stored in an on-pixel memory cell and forwarded to the pixel's output buffer at frame end. Hereafter, the pixel may resume with hit detection. An edge detection circuit is used to avoid a double/multi-counting of analog hit signals with a time-over-threshold spanning over two or more frames.

Each pixel features a pulse injection system, and a disabling circuit. The latter allows to switch off pixels individually by detector control. This feature will presumably help to reduce the dark rate of the sensors, which is typically dominated by few individual hot pixels. The pixel masking capability is also expected to extend the sensor lifetime as it suppresses the impact of a potentially rising number of hot pixels during data taking, consecutive to the steadily increasing radiation load.

As depicted in the block diagram shown in Fig. 4.3, the 1008 pixels of two neighboring columns are read out by a common priority encoder, which is operated at a nominal clock frequency of 20 MHz. The data obtained is first fed into a simple cluster finder, which is suited to identify sets of up to four consecutive active pixels in the sense of the serpentine shaped readout. This allows to recognize 2D-clusters of up to 2×2 pixels, provided they are located in a single double column. The 16-bit data words generated by the cluster finder are forwarded to a so-called region buffer, which is suited to hold a maximum of 100 data words as provided by a total of 16 columns. This turns into a theoretical maximum pixel occupancy of 2.5% at this level. A 16-bit header holding the number of the region is added to the data of each frame and complements

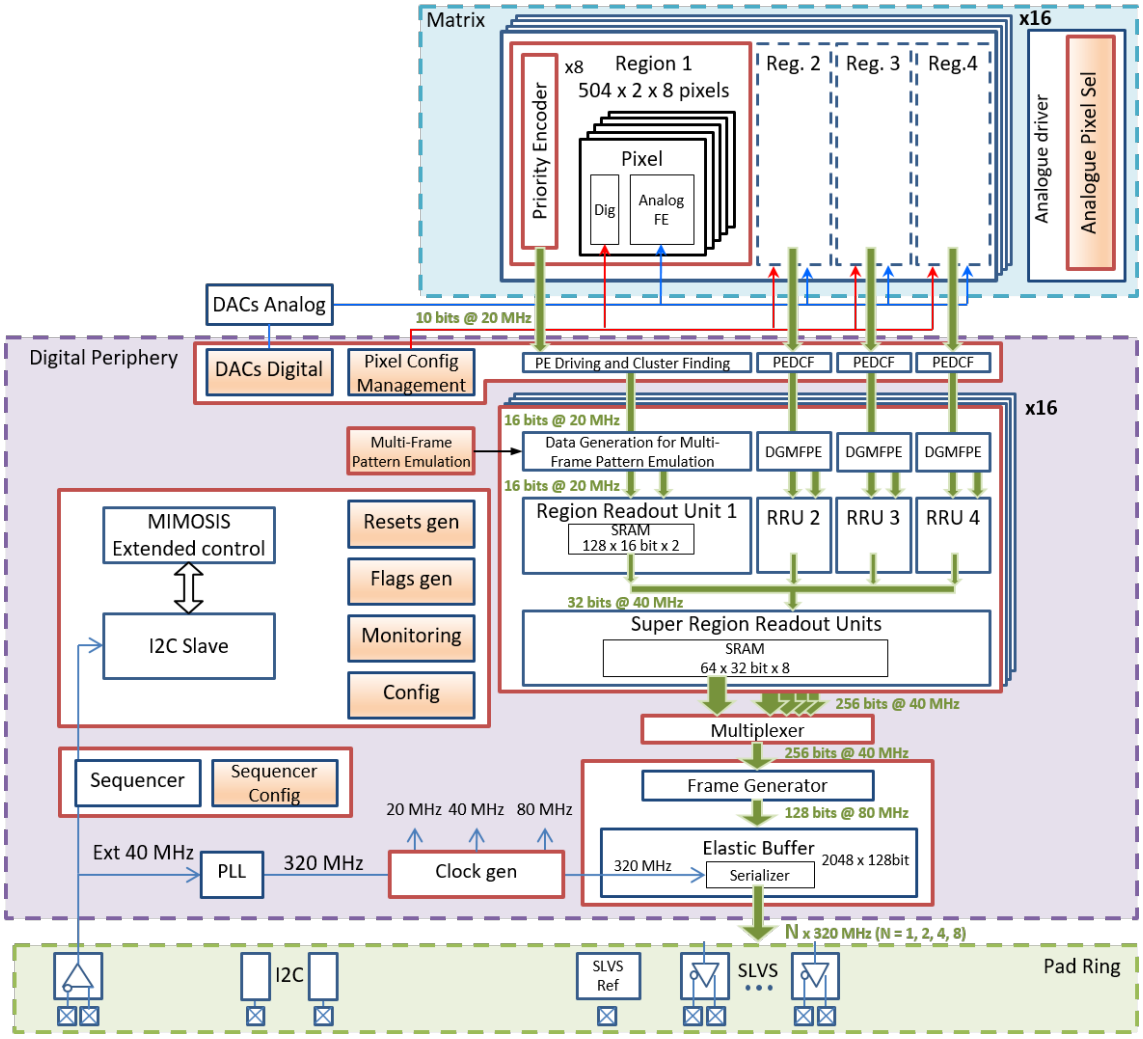

Figure 4.3: Block diagram of MIMOSIS as projected in 2021.

the otherwise insufficient position information stored in the individual data words.

The data from four region buffers are concentrated via a priority-encoded 40 MHz, 32-bit data bus to the so-called super region buffer. After this first step of data concentration, the data of the 16 super region buffers is sent to a common and priority-encoded 256-bit-wide, second data concentrator bus, which provides its output via a so-called frame generator to an elastic output buffer. The frame generator adds header and trailer information indicating, among others, the frame number and as such a time stamp. Moreover, idle words, which are required to fill up the transmission of the wide data busses, are removed. The elastic buffer holds a maximum of 16384 data words. It sends the data to the outside world via up to eight 320 Mbps differential data links.

The design approach reflects our need for handling data rate fluctuations, and reducing the data at the earliest possible stage as follows: The three consecutive data concentration stages allow to average out hot spots in occupancy as much as the non-negligible local Poisson fluctuations of this occupancy. The internal buffers and the data busses are optimized to handle a burst occupancy which corresponds to three times the nominal occupancy of the MVD. This

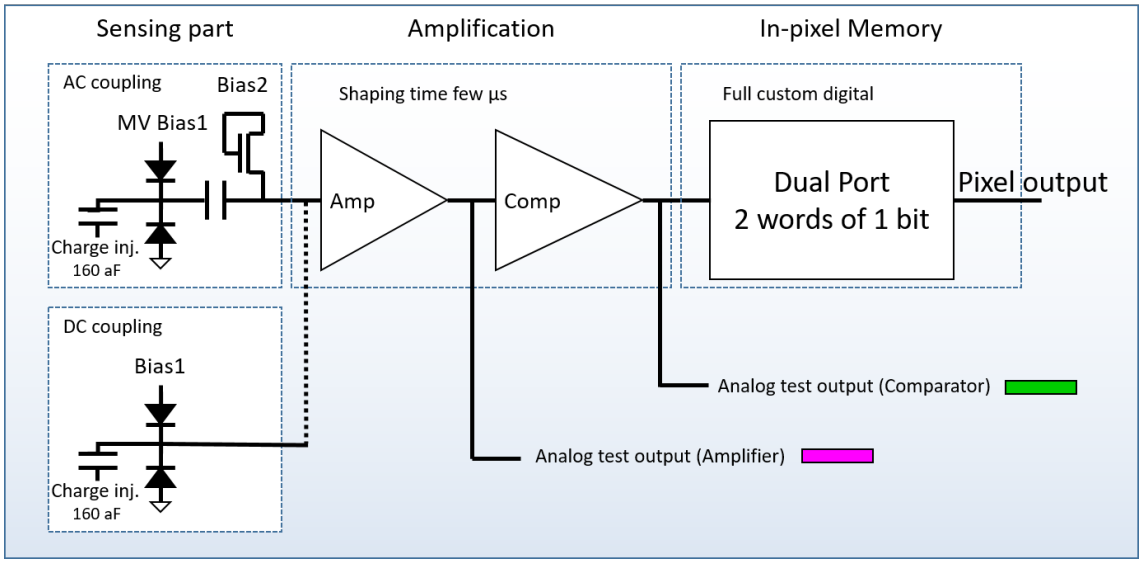

Figure 4.4: Block diagram of the AC- and DC- sensing element proposed for MIMOSIS. From [36].

is to accommodate beam intensity spikes which exceed the average beam intensity by this factor (see section 3.2.6).

However, providing this extended bandwidth for the external communication would require additional data lines and power/cooling, which would both increase the material budget of the MVD. Instead, the elastic buffer is to average out the data flow in time and only about the average data rate is required for the external links. While the precise properties of the beam spikes of the SIS100 is unknown at this stage, the depth of the elastic buffer was designed to hold the data of a maximum 50 µs (10 frames) long, rectangular beam spike of three times the nominal beam intensity. Given that most sensors will face a strongly reduced data load, the number of active data links can be reduced by detector control to one, two, and four. Simulations confirming the validity of the readout concept are shown in Sec. 6.4.1.

The decisive building blocks of MIMOSIS will be carried out in a triple-redundant logic. This is to compensate for potential bit flips, as introduced by direct heavy-ion hits. This feature is considered for the steering logic and the related configuration registers of the chip. The data memories are not protected as space constraints have to be respected and as individual bit flips in the data stream are considered to have only marginal impact on the data quality. The memory cell related to the disabling of the individual pixels cannot be protected due to space constraints. It was checked and confirmed that a reset of those cells during the spill breaks is sufficient to secure a stable device operation.

4.1.4.3 MIMOSIS: Sensing element

The details of the sensing element of MIMOSIS are not yet finally decided. At the time given, we follow up two pixel options as displayed in Fig. 4.4. The first option is a DC-coupled pixel diode, as known from ALPIDE. This pixel is suited for a biasing voltage of 1.8 V only. However, a moderate back bias of up to 6 V can be applied. Alternatively, the use of an AC-coupled sensing element is considered. This sensor may top-bias the collection diode with up to 40 V depletion voltage while the sensitive amplifier structures are exposed to a maximum of 1.8 V,

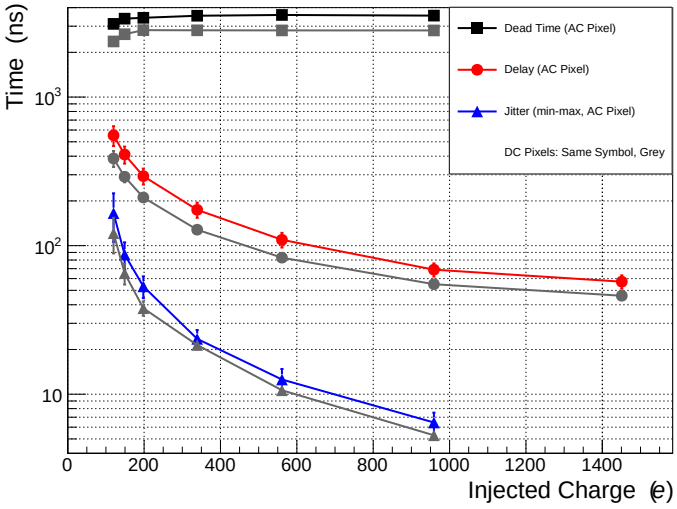

Figure 4.5: Delay, jitter and dead-time of the response of the AC- and DC- pixel of MIMOSIS-0 as obtained from injecting a charge pulse to the primary pixel node and measuring the response of the discriminator output of the pixel.

thanks to the decoupling capacitor.

Both biasing schemes may be combined with different diode layouts. Besides standard diodes, which would most likely be sufficient to obtain the targeted radiation tolerance, advanced diode structures engineered in the so-called double modified 0.18 µm Tower/Jazz process may be used. It has been shown that related sensors may fully deplete the active medium and have thus the potential to reach a tolerance to $\sim 10^{15}\,\mathrm{n_{eq}/cm^2}$ [37, 38]. Possible drawbacks of a fully depleted AC pixel consist in a reduction of charge sharing, which may worsen the spatial precision of the device from ~ 5 µm to the digital resolution of ~ 8 µm. This is not expected to affect significantly the tracking performance of the MVD and it is considered that the impact on the vertexing resolution will remain acceptable (see Fig. 4.1). Moreover, fully depleted pixels generate a higher leakage current than partially depleted pixels thus requiring moderate additional cooling in a very high radiation-dose scenario.

4.1.5 Status of the sensor R&D

4.1.5.1 Observations on MIMOSIS-0

The first MIMOSIS prototype, MIMOSIS-0 [39], was submitted in 2018. The sensor consists of 16 double columns with 2×504 pixels each. Half of the pixels were realized each with AC and DC coupling. The priority encoder used for the pixel readout as well as the DACs, required for steering the pixels, were implemented. A selected number of pixels were realized with a dedicated analogue readout lines shown in Fig. 4.4, which allow to observe the analogue signals within the in-pixel amplification chain directly.

The response of the AC- and DC-pixels of the sensor were measured by means of the in-pixel pulse injection circuits. The response of the amplifier was found to be mostly linear in a range between $150\,e$ and $600\,e$. As planned, it saturates at higher values. The timing of the pixel response was measured by means of the analog outputs and first results are displayed in Fig. 4.5. The delay is defined as the time between the moment of the pulse injection and the

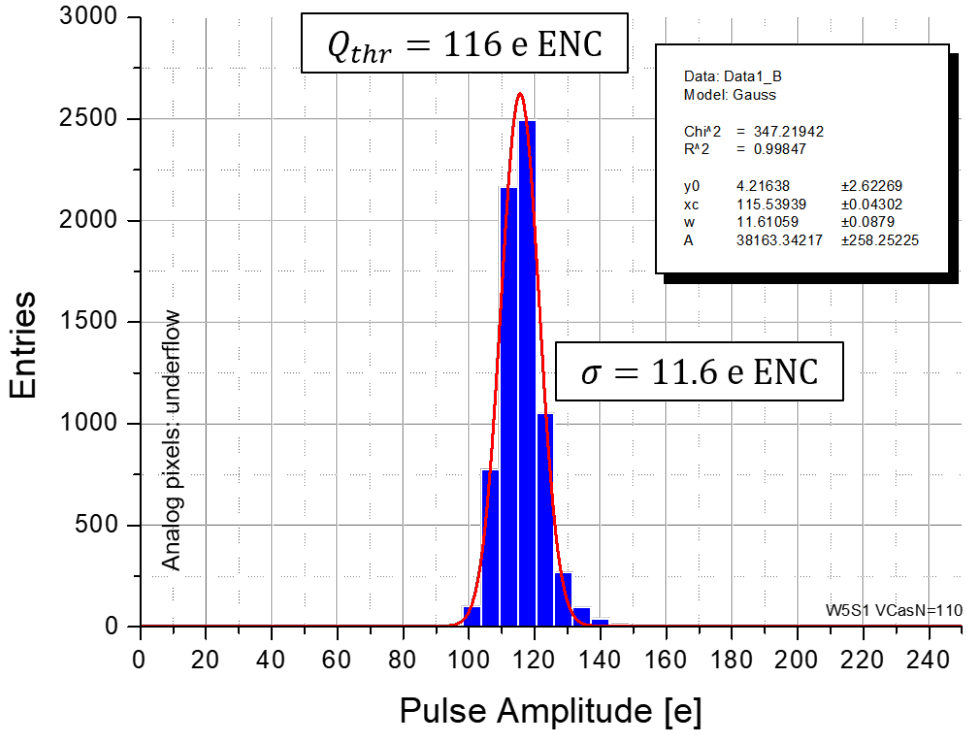

Figure 4.6: Results of the S-curve scans of the DC-pixels of MIMOSIS-0. The pixel threshold as obtained from tests with pulse injection is shown. The width of the distribution is identified with the fixed pattern noise of the pixel matrix.

moment, the analog output signal of the in-pixel discriminator exceeds 80% of the maximum value. The jitter is given as the full width of the related distribution over 10k injected pulses. The time-over-threshold or dead-time denotes the time, this signal remained above 20% of the maximum value. One observes that, with suited settings, the dead-time remains below 4 µs while the delay amounts less than 500 ns even for the lowest signal amplitudes. The jitter remains well below 200 ns under most unfavorable conditions. From this, one concludes that the analog time resolution is fast as compared to the foreseen frame time of 5 µs and that at the nominal heavy ion collision rate of 100 kHz, mostly no event pile-up is to be expected. The results also suggest that a time resolution of $\lesssim$ 1 µs might be reached with MIMOSIS in case the frame time is reduced by a factor of about five by means slow control. This procedure is however only suitable for sensors located in low occupancy regions as the maximum occupancy per frame of the sensor is reduced (due to additional overhead) by a slightly higher factor. It remains to be studied, to which degree this option can be exploited during real detector operation.

The noise of the sensors was studied by means of S-curve scans. The sensors were operated at non-controlled room temperature and a back bias of 1V was applied. The settings including threshold were kept constant and signal pulses with increasing signal amplitude were injected to the sensor. The probability $P(A)$ of a given pixel to detect this signal amplitude A as a function of the pulse amplitude was measured. The step size of $\sim$ 6 e reflects the resolution of the injector DACs. The S-curve obtained was differentiated ($dP(A)/dA$) and the mean value of the Gaussian-like derivative was defined as the detection threshold of the specific pixel. The related standard deviation was identified as thermal noise. Only data from the digital outputs of the

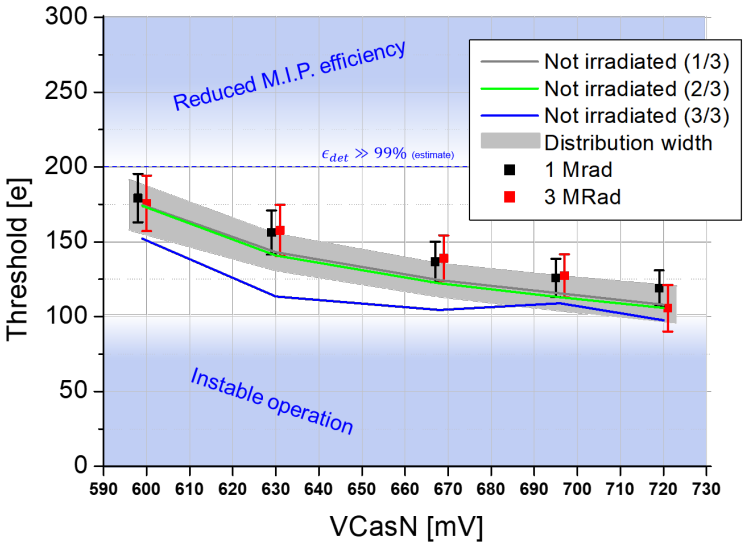

Figure 4.7: Histogram of the electronic noise of many DC-pixels of MIMOSIS-0 measured through S-curve studies. The threshold is plotted as function of the steering voltage VCasN. Results from 3 non-irradiated and two X-ray irradiated sensors are given. The grey surface represents the fixed pattern noise of the non-irradiated sensors. For the irradiated sensors, this information is encoded in the error bars. The X-position of the points related to the irradiated sensors was slightly shifted for clarity.

DC-pixel matrix of the sensors could be used as the priority encoder of the AC-pixels injected noise to those pixels. Tests with the analog output suggest however that the results are also reasonably representative for the corrected AC-pixels designed for MIMOSIS-1. The thermal noise of the individual pixels was indicated as amounting typically a fraction of a DAC step of the charge injection system. No precise measurement of this noise could thus be performed. The upper limit of this noise amounts $\ll 6\ e$ ENC for all individual pixels measured.

An example of the distribution of the pixel thresholds is shown in Fig. 4.6. Pixels featuring a complementary analog output were removed from the distribution as they required slightly different threshold settings. The remaining distribution shows a fairly Gaussian shape. Its mean and width represent the average threshold and the fixed pattern noise of the sensor and amount 116 e and 11.6 e respectively in the example.

As shown in Fig. 4.7, the measurement was repeated for three different non-irradiated sensors for different threshold values as steered by the control voltage VCasN. To compensate for the tolerances of the internal DACs, all steering voltages were controlled by external voltmeters. It is found that two of the three non-irradiated sensors show very similar performances. The fixed pattern noise remains mostly constant over a wide range of relevant thresholds. A slight increase is only seen for the highest threshold applied. The results of the third sensor differs moderately from the previous results but the differences could be compensated by applying appropriate voltage settings. Over all it is concluded that the sensors tested show excellent performances.

4.1.5.2 Observations on MIMOSIS-1

The consecutive prototype MIMOSIS-1 was designed as a full size prototype and in contains all features of the final sensor apart from the on-chip cluster finding and some triplication of its

logic. The sensor hosts two flavours of each, AC and DC pixels. Those differ in particular by the size of the entrance transistor of the pre-amplifier as this parameter is known to trade the random telegraph signal of this amplifier against its gain. Increasing its size comes typically with a reduced number of hot pixels on expense of a higher thermal pixel noise.

MIMOSIS-1 was realized with four different wafer/diode flavours. The traditional diode design (called Split 1 hereafter) was expected to provide fewest depletion and radiation tolerance but best spatial precision. Two additional flavours extend the collection diode by a wide, very deep N-implantation. While this implantation formed a layer in the related MIMOSIS-0, it was segmented in MIMOSIS-1 in order to generate lateral drift fields in the periphery of the pixel. This was once done by removing the very deep N-implantations such that a few µm wide ring without implantation is formed around each pixel (Split 3). In a second design, this ring was moreover filled up with a very deep p-implantation (Split 4).

Split 3 and split 4 were designed for improving the depletion and thus the radiation hardness of the sensing node on expense of reducing the charge sharing of the pixels. This reduced charge sharing was expected to deteriorate the spatial resolution of the sensor moderately. This is as the spatial resolution is improved if the information on the multiplicity and shape of the pixel clusters can exploited for improving the spatial resolution, which works best in case the multiplicity is high.

MIMOSIS-1 was commissioned and a dedicated beam telescope comprising 6 sensors (*i.e.* planes) was designed. In this telescope, 4 sensors (Split 1) formed reference planes and two additional sensors in the middle could be tested. The sensors were mounted in dark chambers on cooling plates, which were cooled by means of a chiller providing a coolant with $T = 15\,^{\circ}\mathrm{C}$. The sensors of the reference planes were operated by default at $V_{bb} = -3$ V and $HV = 10$ V while those voltages were varied for the devices under test (DUT).

The telescope was operated in the ~ 5 GeV electron beam of DESY and in the ~ 100 GeV pion beam of the CERN-SPS. The data was analyzed with the IPHC TAF software. At the time of the submission of this report, the tests and their analysis were ongoing. All preliminary results discussed in the following are subject to change and represent the status of the analysis of Dec. 17th 2021.

4.1.5.3 Sensor commissioning (preliminary)

The sensors were operated with a dedicated readout system relying on a so-called S3 board hosting an Arduino micro processor and a FPGA-board controlled by a NI-PXI readout crate. The Arduino processor generated the I2C signals required to slow control the sensors via a a standard output. The build-in I2C output was not used at this stage. The FPGA-board operated the sensors continuously and received the data. As the data bandwidth of the build-in Windows computer controlling the crate was insufficient for writing the full data stream, typically blocks of 1000 frames were recorded and a controlled dead time to the consecutive block was accepted.

The sensor commissioning revealed a number of weak points, which did not prevent the successful operation of the device and will be fixed in the consecutive MIMOSIS-2 prototype: The sensor was successfully steered by its nominal 40 MHz clock but the stability of the on-chip PLL transforming this signal to the internal 320 MHz clock signal of the sensor did not show fully satisfactory stability. Therefore, most results were obtained by the related backup system, which allows for injecting directly a 320 MHz clock. The edge of the I2C clock and of this 320 MHz system clock had to be synchronized by external measures to avoid occasional bit errors in the slow control. The analog output was found unavailable thus no measurements on the signal timing could be performed. S-curve scans revealed that the pixel threshold varied by some tens

of electrons over the full surface of the pixel matrix due to ohmic losses in some in-chip power lines.

Moreover, it was found that performing an S-curve scan required for the commissioning of the sensor may take up to several days with the present procedure. While this could be accepted during the present prototyping phase, improvements will be required for performing those scans for threshold tuning prior and during the full MVD operation.

4.1.5.4 Results from S-curve scans (preliminary)

S-curve scans were performed to measure the thermal noise and the fixed pattern noise of the sensor. It was found that the sensors can be operated at thresholds below 120 electrons. The fixed pattern noise was found to amount $5 - 17$ e ENC depending on the pixel flavour and the setting of the steering voltages. In general, it was observed that this noise decreased with increasing back bias (V_{bb}). As suggested already by the results of MIMOSIS-0, the thermal noise was observed to amount $3 - 5$ e for non-irradiated sensors at a coolant temperature of 15 °C. As mentioned previously, the threshold of the pixels was found to vary by about 50 e over the sensor matrix. According to simulations, this was as ohmic losses in the power distribution net of MIMOSIS-1, which was shared by the pixels and some power consuming DAC blocks. Separating them in MIMOSIS-2 is expected to further reduce the fixed pattern noise. The stability of the thresholds was checked at temperatures from −7 °C to 35 °C as recorded with a PT100 sensor mounted nearby the sensor. Preliminary observations suggest that the threshold shifts generated by those different temperatures remains below few 10 e ENC. Therefore, it seems be feasible to operate the sensors with temperature gradients far beyond the so far required 5 K.

A comparison of the thresholds of sensors before and after irradiation suggests that X-ray doses may generate a threshold shift of the pixels. Due to the small number of irradiated sensors studied so far, this effect is not yet fully understood. First estimates suggest that the pixels of sensors, which were exposed to a sizeable radiation gradient of $\gtrsim 1$ MRad over the sensor's surface, cannot be operated with a common setting of their steering voltages. However, the threshold shifts appear to saturate toward higher doses. Therefore, it is likely possible to alleviate the effect by irradiating sensors exposed to such extreme conditions with a moderate ionizing dose prior to installation.

4.1.5.5 Detection efficiency and spatial precision (preliminary)

During the analysis of the beam test data, it was observed that the time walk of the pixel signal as depicted in Fig. 4.5 is not negligible. This is as occasionally a particle is detected in different frames by the telescope and in the DUT due to different signal delays. Time walk effects are also expected and observed in hit clusters as the seed pixel of the cluster senses the particle with higher amplitude and thus faster than the peripheral pixels. Therefore, the data of two neighboring pixels has to be accounted for during cluster and track finding. A preliminary analysis suggests that a failure to do so reduces the detection efficiency of the sensors by roughly 1% and their spatial resolution by a sizeable fraction of a micrometer.

As time walk effects were negligible in earlier and slower CPS versions, the analysis software used is not yet suited for handling them in a reliable way, which biases the results reported here toward lower performances. Still it is found that MIMOSIS-1 shows typically a detection efficiency of $\gtrsim 99\%$ in combination with a dark rate of $\lesssim 10^{-7}$ at suited settings. To reduce the impact of hot pixels, typically few 10 pixels (fairly below 10^{-4} of the total) were masked during the dark rate measurements.

The mean pixel multiplicity amounts slightly below three at the most favourable conditions (Split 1, DC pixel with low V_{bb}, ~ 120 e threshold) and slightly above one (Split 3/4, AC pixel after massive neutron radiation damage, high threshold). The non-corrected spatial resolution scales between roughly 4.2 µm/5.2 µm (for the short/long side of the pixel, respectively) at highest pixel multiplicities and 6.8 µm/7.8 µm for low pixel multiplicities.

4.1.5.6 Radiation tolerance (preliminary)

MIMOSIS-0 was not primarily designed for performing radiation tolerance tests. This holds in particular for testing the response of the sensor to non-ionizing radiation doses, which cannot be mapped out due to the strongly non-linear properties of the preamplifier. However, the response of the sensing element has been intensely studied with previous sensor generations [30] and valuable complementary information is obtained from the tests of the mostly identical sensing element of the ALPIDE sensor [32].

Both lines of study confirm that no crucial trapping of signal charge is to be expected for doses well above $10^{13}\,\mathrm{n_{eq}/cm^2}$ even if no explicit depletion voltage is applied. ALPIDE is reported to withstand $1.7 \times 10^{13}\,\mathrm{n_{eq}/cm^2}$, which was the highest NIEL doses applied, without relevant loss in performance. A next generation sensing element [40], which was kindly made available for a use in MIMOSIS-1 by its inventors, has demonstrated the potential to withstand non-ionizing doses of up to $10^{15}\,\mathrm{n_{eq}/cm^2}$ without crucial loss in charge collection efficiency (CCE). Therefore, reaching the targeted tolerance of the CCE to non-ionizing radiation appears well feasible nowadays.

Besides signal charge recombination, radiation induced leakage currents I_L of the charge collection diode are of worry. An upper limit on this current is given by the need to control the injected shot noise and to avoid a premature clearing of the pixel signal charge. I_L is known [41] not to depend on the silicon doping and to scale like:

$$I_L = I_L(0) + \alpha(T) \cdot \Phi_{eq} \cdot V \tag{4.1}$$

Here, $I_L(0)$ is the negligible leakage current of the non-irradiated device, $V = 2 \times 10^{-8}\,\mathrm{cm^3}$ is the depleted volume of a fully depleted MIMOSIS pixel with an anticipated 25 µm thick epitaxial layer, $\alpha(20°\mathrm{C}) = 4 \times 10^{-17}$ A/cm and Φ_{eq} the equivalent neutron dose. For the target dose of $\phi_{eq} = 7 \times 10^{13}\,\mathrm{n_{eq}/cm^2}$, one obtains a leakage current of $I_L(20°\mathrm{C}) = 57$ pA. This theoretical value compares with a measured leakage current of ~ 50 pA and ~ 100 pA for pixels irradiated with $3 \times 10^{13}\,\mathrm{n_{eq}/cm^2}$ and $10^{14}\,\mathrm{n_{eq}/cm^2}$ respectively.

The magnitude of the shot noise in electron equivalent units is given [30] with:

$$Q_{\mathrm{Noise}} = \sqrt{2e \cdot I_L \cdot t_{int}} \tag{4.2}$$

The equation accounts for the fact that the forward-biased biasing diode of the sensing element adapts its current dynamically to I_L. Therefore, the average collected charge in the absence of a signal is zero but the fluctuations from both, I_L and the identical biasing current contribute. In conventional pixels with well defined frame readout, t_{int} is identified with the time between two readout cycles and thus the frame time. In MIMOSIS, the amplifier/shaper operates independently of the frame readout. Again, t_{int} is identified with the time needed to clear the response of the pixel to an signal electron, which is now about the time-over-threshold or dead-time of the shaper and amounts $t_{int} \lesssim 4\,\mu\mathrm{s}$ according to the results shown in Fig. 4.5. Thanks to this fast shaping, the shot noise remains below a value of $2e$ ENC and may thus be neglected.

The clearing of the signal charge Q_S is described with:

$$Q_S(t) = Q_S(t=0) \cdot \exp\left(-\frac{t}{\tau}\right) \tag{4.3}$$

In this equation, t is the time after the particle impact (assuming a negligible charge collection time) and τ the time constant of the clearing process, which is given with:

$$\tau \approx \frac{n \cdot k_B \cdot T \cdot C}{e} \cdot \frac{1}{I_L} \tag{4.4}$$

Here, $1 < n < 2$ represents the emissivity of the biasing diode, k_B the Boltzmann constant and $C \approx 5$ fF the capacity of the pixel diode. At room temperature and with the above mentioned leakage current, on obtains $\tau \approx 4\,\mu$s. This is to be compared with a delay of at worst 0.6 µs between the pulse injection into the particle and the response of the comparator. Accounting for Eqn. 4.3, this turns into a 13% drop of the signal or equivalent into a ~ 20 e raise of the detector threshold, which appears tolerable. The planned cooling of the sensor to $T = -20$°C reduces the leakage current by a factor of roughly 45, which provides a comfortable safety margin.

The pixel-to-pixel dispersion of the thresholds was measured with CE18 test sensors hosting the same analog readout chain as MIMOSIS but no potentially vulnerable internal trim DACs. A tuning of the pixel's reference voltages for each radiation step was applied, which represents the dominating source of uncertainty of the study. The width of the threshold distribution was found insensitive to radiation doses of up to $10^{14}\,\mathrm{n_{eq}/cm^2}$ within the few e ENC uncertainty.

Beam tests with MIMOSIS-1 suggest that the sensor may reach an detection efficiency of $\gtrsim 99\%$ in combination with a dark rate $\lesssim 10^{-7}$ after being irradiated to the end-of-lifetime dose of $10^{14}\,\mathrm{n_{eq}/cm^2}$ at a coolant temperature of 15 °C. To reach the dark rate, a $\lesssim 10^{-4}$ fraction of pixels showing an individual dark rate above 10^{-3} were masked at ~ 130 e thresholds.

4.1.5.7 Ionizing radiation (preliminary)

Imager sensors of the MIMOSA family have been found to resist to doses of 10 Mrad [42], which exceeds the requirements of the MVD . However, the additional complexity of MIMOSIS with respect to those simple devices may come with additional vulnerabilities. Three major radiation effects are to be expected for MIMOSIS due to ionizing radiation doses. Those are a radiation induced increase of the leakage currents of the collection diode, a shift of the thresholds of the in-pixel discriminators and finally issues with the trim DACs. While the prior effect is well understood, the two latter effect are specific to the MIMOSIS design and were previously reported from related studies with ALPIDE.

Preliminary tests with MIMOSIS-0 and CE18 sensors indicate that radiation doses of 10 Mrad turn into an increase of I_L, which ranges between 50 and 100 pA per pixel for a depletion voltage of 1 and 20 V, respectively at room temperature. Those currents were reduced by a factor of two after five days of room temperature annealing. As pointed out in the previous section, this level of leakage currents is still acceptable and may be further reduced by exploiting the option of cooling the sensors.

The shift of the thresholds was studied by irradiating two individual MIMOSIS-0 sensors to a dose of 1 and 3 Mrad respectively. Their performances were compared with the ones of non-irradiated devices (see Fig. 4.7). Due to an undetected issue with the test protocol, valid data could only be recorded one year after the irradiation. The results represent thus the status of the sensor after one year of room temperature annealing, which is at the end somewhat representative for the slow irradiation expected in the experiment. One observes a significant

shift, which amounts less than 20 electrons w.r.t the regular, non-irradiated sensors. Both, the thermal and the fixed pattern noise of the irradiated sensors is found to increase significantly. However, the increase remains in the order of few electrons, which is not considered to endanger the sensor operation. Despite additional tests are required, the results obtained show a first evidence that MIMOSIS will tolerate ionizing radiation doses without worrying increases of noise or relevant threshold shifts. The latter is of particular relevance for sensors, which have to operate with common pixel settings in the strongly non-homogeneous radiation field found on the first MVD station. To further mitigate this issue, MIMOSIS will be subdivided into four zones with individual threshold setting. Moreover, complementary measurements made with analog CE18 sensors hosting the same pixels suggest that the radiation damage goes mostly into saturation for doses above 1 Mrad. Therefore, one may consider to precondition the sensors by irradiating them with dose of $\sim$ 1 Mrad. This would substantially improved uniformity of the response of sensors being exposed to non-homogeneous radiation fields while the modest radiation damage effects caused by the conditioning should be rather tolerable.

Particular care was undertaken to test the response of the on-chip DACs to radiation damage. The sensors were irradiated to up to 10 Mrad while applying a nominal bias and a back bias of 1 V. The linearity of the DACs was recorded prior to the irradiation, few minutes after the irradiation was completed and some days after irradiation. The characteristic curve of the DACs was found to show specific steps after irradiation, which were substantially reduced by few days room temperature annealing. The origin of the steps was studied and associated to radiation damage in the linear transistors switching the individual current sources of the DACs. It was concluded that using an ELT-transistor for switching transistor of the current would overcome the issues observed while the digital logic steering this transistor may remain unprotected. A related modification was made and implemented into MIMOSIS-1 and will presumably solve the issue.

Beam tests with MIMOSIS-1 suggest that the sensor may reach an efficiency of $\gtrsim$ 99% in combination with a dark rate $\lesssim 10^{-6}$ after being irradiated to the end-of-lifetime dose of 5 MRad at a coolant temperature of 15 °C. Again, up $\lesssim 10^{-4}$ of all pixels showed an individual dark rate of $> 10^{-3}$ at lowest thresholds and they were masked for determining the dark rate.

4.1.5.8 Tolerance to heavy ions (preliminary)

The operation of CPS in the presence of heavy ion beams was studied within the NA61/SHINE Small Acceptance Vertex Detector project. Within this project, MIMOSA-26 sensors were exposed to a direct 30 AGeV/c Pb beam of the CERN-SPS and operated in this beam. The sensor was found to operate and to record the beam particle impacts. Three mild latch-up events were observed within 24 hours of beam operation but no permanent damage was caused. In a next step, the same sensors were operated within NA61/SHINE in position similar to the one foreseen for the sensors of the CBM-MVD. No harmful effects like latch-up or sensor damage were reported. In contrast to this, MIMOSA-28 (ULTIMATE) sensors were reported to exhibit permanent damage due beam incidents at the STAR-experiment. Post incident checks revealed an overheating of sensor components as caused by latch-up. The overheating occurred because the "latch-up watch-dog" foreseen to detect and prevent it was controlling variations of the total current of 10 sensors. The solution came out to feature an insufficient sensitivity to react to the behaviour change of a single sensor. Reducing the reaction threshold of the system solved the problem.

The risk of latch-ups will be controlled by installing an improved latch-up protection system based on the experiences made with the previously mentioned system. If necessary, it is

considered to routinely power cycle the sensors during spill breaks. This in combination with the robust sensor cooling system should alleviate the consequences of a possible, undetected latch-up.

As mentioned above, MIMOSIS will be equipped with a triple redundant digital logic, which is intended to compensate single event effects like bit flips. Despite no issues of this kind are reported from previous heavy ion experiments using CPS and this redundancy is considered as additional safety measure, it remains to be rigorously shown that MIMOSIS will be stable against SEE under CBM beam halo conditions.

It is anticipated that it is not feasible to improve the radiation tolerance of the MVD such that it would be able to tolerate the integrated radiation damage caused by a dense halo of the CBM primary beam (see Sec. 3.2.3 for details). Therefore, quantitative requirements on the beam focusing were worked out and communicated to the SIS100 beam division. It was stated that the requirements would be fulfilled by means of installing a suited collimator / scraper system into the CBM beam extraction line.

MIMOSIS-1 was operated in an ~ 1 AGeV Xe- and Pb- beam of the GSI SIS-18 synchrotron to test its vulnerability to single event effects caused by heavy ion impacts. The study targeted initially the cross-section for single event latch-ups (LU), which were detected based on an increase of the current consumption of the sensor. The data readout circuits of the proximity boards holding the sensor were removed as they were not expected to withstand the radiation load related to the experiment. Thus, no data readout was available and, the study restricted itself to monitoring the sensors by means of slow control and by measuring significant changes of their current consumption.

During the experiment it got clear that bit flips in the steering registers of the sensor may cause increases of the current consumption similar to what one expects from a LU. This complicates at present a quantitative assessment of the experimental results. As an upper limit, we expect that the number of LUs will remain below 1 per hour for the sensors closest to the beam pipe under CBM-MVD conditions, which is considered as an acceptable rate. Moreover, the study revealed an issue with the bit-flip compensation of the steering registers, which will be fixed in MIMOSIS-2. To simulate a beam loss scenario, MIMOSIS-1 was exposed to 10 s spills with up to 3×10^9 heavy ions. The sensor did not show fatal damage and still responded to slow control after several spills.

4.2 Sensor Integration

4.2.1 Design constraints

The MVD layout is based on dedicated modules, representing a quarter of a given station. Each module comprises the sensor chips, the mechanical support, read-out FPC cables, and the heat sink which also serves for holding and cooling the front end electronics. The choice of materials and technologies is mainly constrained by:

- **Material budget:** There, we are guided by the benchmark of an overall thickness of the first station and the following stations in units of the radiation length of 0.3 and 0.5%, respectively.
- **Vacuum operation and cooling:** Vacuum operation requires an effective cooling of the sensors. For MIMOSIS-1 we have specified a power consumption of below $300\,\mathrm{mW/cm^2}$ [43] and recent studies indicate a value below $50\,\mathrm{mW/cm^2}$ [44].
- **Mechanical stability:** Mechanical stability in a planar disk-geometry is mandatory for

high-precision and time-invariant alignment, which allows to take profit from the intrinsic sensor spatial resolution of a few µm.

- **Integration procedures:** The procedures are supposed to ensure a high yield during assembly. Most challenging here is the front-/backside sensor integration. Reworking and low-risk module exchange with hot spares is desirable.
- **Electrical sensor insulation:** To increase the sensor performance, mainly the charge collection process, the sensor's bulk is polarized with a potential up to several volts. Consequently, sensors should be electrically insulated from their carriers, in case the latter are electrically conductive, e.g., TPG.

This list defines the main guideline for the construction of the MVD module and the integration of the sensors. Motivated by results from simulation and prototyping, we are following a conservative approach of sensor integration. We employ a cooling concept based on extracting the heat load by means of a combination of lateral conductive cooling in the acceptance and an actively cooled heat sink outside. Sensors are connected via wire wedge-bonding to dedicated thin FPC cables.

4.2.2 Module constituent parts

This section discusses the major building blocks of the MVD module with a particular emphasis on support and cooling, FPC cables, selection of suitable glues and assembly procedures as well as the electric connections of the sensor chips. Based on experiences with MIMOSA-26 sensors employed during the prototyping phase, we rely on wire bonding for connecting the MIMOSIS sensors to the FPC cable. Alternative techniques like TAB or laser bonding do not contradict with the integration strategy discussed here, but would eventually require different approaches *w.r.t.* sensor-FPC cable alignment, order of the integration steps and FPC cable design. During tests with MIMOSA-26, the FPC design has been optimized *w.r.t.* transmission properties, mechanical reliability and material budget during several iterations. The sensor and FPC cable properties relevant for the concept of the sensors' integration are as follows:

- **Sensor material and thickness:** The sensors are manufactured in CMOS technology (Si) and are thinned down to 50 µm. The presently observed bending after thinning with a radius of 20-30 cm (intrinsic feature of the MIMOSA-26 sensors [43]) can be tolerated, and it might in the future be avoided by better process control.
- **Sensor dimensions:**
  - The external dimensions of the sensor chip after dicing: $31.150 \times 17.250\,\mathrm{mm}^2$,
  - The area occupied by pixels is $30.935 \times 13.520\,\mathrm{mm}^2$,
  - The area occupied by digital circuits and bonding pads is $30.935 \times 3.560\,\mathrm{mm}^2$.
- Thickness of the FPC cables: 63 µm, based on the commercially available technology with Copper traces. [1]
- Two sensors are read-out by one FPC cable.

To limit the amount of glue and to allow for a smooth overhang of a FPC over the next sensor, it is aimed to glue the FPC mostly underneath the bonding pads and reinforce the FPC cable

[1] This thickness holds for the flex cable developed for the MIMOSA-26 sensor. Since the final MVD sensor MIMOSIS (-3) does not exist yet, we cannot give any details on the final flex cable *w.r.t.* material budget and technology. However, we consider the existing cables as baseline and would have to counterbalance a significant increase in thickness by employing Aluminum instead of Copper traces, as it was developed for the STS system. For details on the material budget see Sec. 4.2.5.1.

mostly outside of the geometrical acceptance. The placement of FPC cables on modules with more than two sensors in a ladder follows the same concept, with two FPC cables staggered on top of each other.

4.2.2.1 Sensor arrangement

The MVD will be equipped with CMOS pixels sensors of the same type and hence, all stations feature the same pixel dimensions and sensor form factor. This offers many advantages, both in the sensor integration as well as in the read-out architecture. As discussed in Sec. 4.1, the state-of-the-art sensor developed at IPHC Strasbourg is defined by the ALPIDE family based on the TowerJazz 180 nm CMOS process. The ALPIDE is used for the ITS upgrade for the ALICE experiment [43]. It is also the basis for the first generation of CBM sensors named MIMOSIS. To arrive at a suitable arrangement of sensors for the different stations, the following assumptions were made:

- Sensor geometry: 31.150×17.250 mm^2, thickness of 50 µm.
- Active sensor area of 30.935×13.520 mm^2 and 30.935×3.560 mm^2 of in-active area occupied by digital circuits and pads.
- No in-active area is assumed on the three remaining sides next to the active area. Sensor dicing quality, sensor-sensor positioning by butting (including 50 µm gap between the sensors for electrical and mechanical separation) and residual in-active area on the sides will typically lead to a minimum distance of active Si area of about 315–365 µm.
- The relative alignment of sensors assumes edge to edge positioning (butting) of rectangular objects.
- To maximize the geometrical acceptance, the in-active area of a given sensor needs to be covered by active volume of a second sensor mounted on the backside of the planar carrier. To regard inclined tracks, adjacent front- and backside sensors feature an overlay of their active volumes of 500 µm. This value is obtained by maximizing the acceptance for inclined tracks, as suggested by simulations [45], and (ii) by enabling a relative alignment of front and backside sensors.
- The distance between the beam and the digital part of the sensor is maximized to reduce the impact of radiation-caused failures (*e.g.* latch-up).

Following these rules, sensors can be arranged to ladders, which are placed on the front- and back side of a module. Fig. 4.8 depicts the resulting sensor arrangement for station 1, together with the FPC cables attached to the sensors.

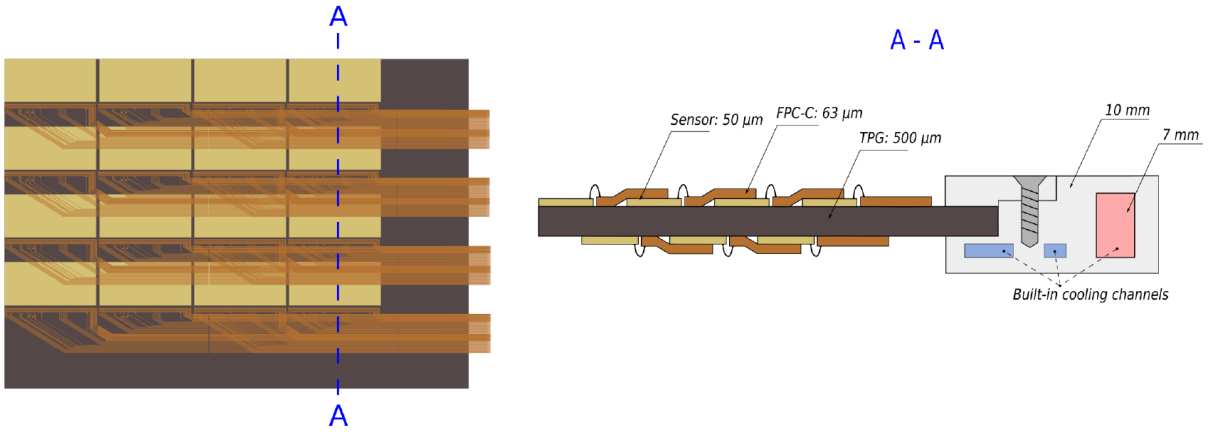

Figure 4.8: Sensor arrangement in the quadrant of station 2 and 3 (module geometry c). Left: Schematic front view of the station formed out of four modules, upper right: detailed front view with sensors and FPC cables attached, lower right: cross section perpendicular to the ladder orientation. Note the zoomed-in z-coordinate, material thickness is indicated.

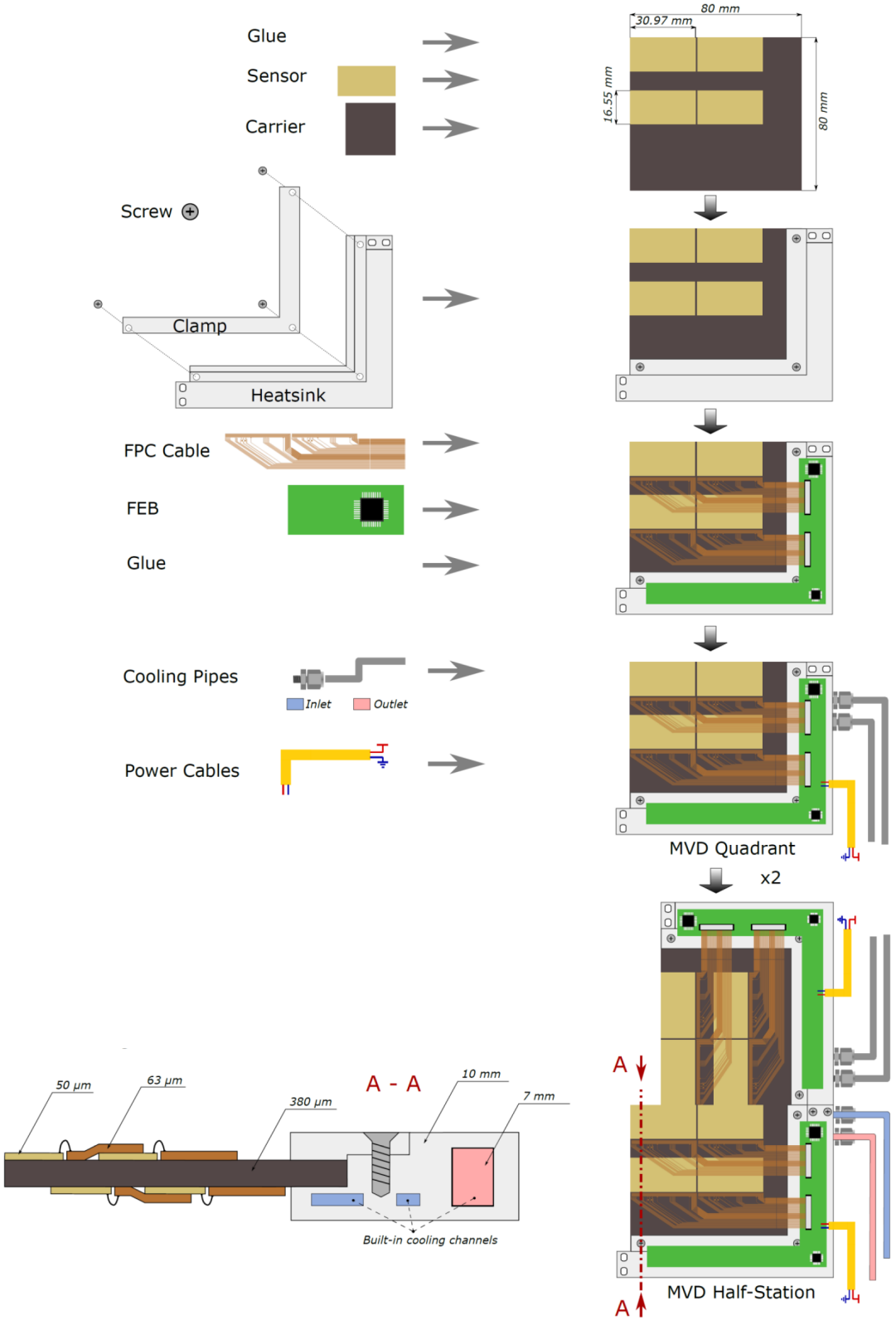

Figure 4.9: The MVD integration flow (right). Left: Components to be provided, lower left: sketch of a cross section of a MVD module, thicknesses indicated, axes not to scale.

4.2.2.2 Mechanical support of sensors

This section discusses the selection of carrier materials. It is obvious to focus on materials with high specific stiffness and high thermal conductivity. Respective installations in detectors with collider geometry use light-weight support structures arranged as ladders, which are actively cooled with flowing media inside the geometrical acceptance. They are placed outside the beam pipe and are arranged as cylinders or planes to cover the mid or forward rapidity region, respectively. In contrast, the CBM-MVD is optimized for the fix-target geometry of CBM requiring acceptance in the the forward polar angle region only and a placement in near vicinity of the stationary target. Hence, the detector is being realized with planar, disk-like stations placed inside the target chamber. To guarantee the optimum thermal performance, the sensors are glued directly on the support material, respecting the need to electrically insulate the sensors from the carrier material, as discussed in Sec. 4.2.1. The supports (carriers) are mounted, moderated by thermal grease [2], in actively cooled heat sinks outside the geometrical acceptance. Apart from cost and availability of the form factor needed, the choice of carrier materials is mainly driven by the following constraints:

- The MVD disk geometry relaxes the requirements regarding the stiffness of the (elastic) carrier material in contrast to *e.g.* long ladders.
- Radiation hardness should significantly exceed the one reached for the pixel sensors, *i.e.* $10^{13}\,\mathrm{n_{eq}/cm^2}$ and Mrad radiation.
- The thermal expansion coefficients (CTE) of the components should not differ beyond a tolerable amount[3].
- The material budget should be as little as possible (large radiation length).
- Material should have a high heat conductivity.

Trading these requirements, carbon-based high-performance materials are recommended, while two materials are of particular interest as carrier bulk material: pCVD-Diamond (poly-crystalline Chemical Vapor Deposition) and TPG (Thermal Pyrolytic Graphite). The optimum material with respect to thermal performance and mechanical properties is pCVD diamond. However, it cannot be used for all module geometries due to its high cost and restricted availability in terms of thickness. Therefore, both materials diamond and TPG have been studied in great detail by implementing them in several prototypes, see Sec. 5.

pCVD Diamond: Synthetic poly-crystalline (p) diamond, grown by means of Chemical Vapor Deposition (CVD), features unsurpassed hardness, and extremely high thermal conductivity of up to five times that of copper. Table 4.1 summarizes the main properties of pCVD diamond. The following conclusions were drawn from experiences with prototypes:

- **Cost**: The high price of poly-crystalline CVD diamond, optical grade, recommends its use for smaller station geometries a and b only, where also material budget is of primary importance, *i.e.* the first station in the VX detector geometry.
- **Material budget**: Trading mechanical stability, handling and material budget, a carrier thickness between 150 and 200 µm is recommended.

[2] The need of thermal grease to optimize the heat contact is presently under study, and might depend on the carrier material and constraints *w.r.t.* quality of the vacuum.

[3] The CTE mismatch can be relaxed by using a dedicated glue with remaining flexibility after curing. Instead, the absolute CTE can be minimized, emphasizing the overall thermal-mechanical stability during temperature cycles.

Property of pCVD diamond	Value
Young's modulus	1050 GPa
Density	3.51 g/cm^3
Radiation length X_0	12.22 cm
Surface roughness	< 20 nm
Thermal expansion coefficient	$(1.0 \pm 0.1) \times 10^{-6}$/K at 25 °C
Thermal conductivity	> 1800 W/mK at 25 °C
	> 2300 W/mK at -20 °C
Electrical Resistivity	$10^{13} - 10^{16}$ Ωcm
Price tag	18 €/mm^3

Table 4.1: Properties of poly-crystalline CVD diamond (polished surface) used during prototyping the MVD, see also [46]. The radiation length is calculated with the Dahl fit formula to data [47],price in 2020 [46]).

- **Electrical properties**: Its high resistivity guarantees that sensors attached to a CVD diamond carrier are electrically insulated with respect to each other.
- **Other properties**: Thin pCVD diamond wafers of several cm diameter are technically hard to produce. A high risk of damage during processing remains as a consequence of internal stress built up during deposit.
- **Vendors of choice**: Diamond Materials [46], Element 6 [48] or DIDCO [49].

Presently, only Diamond Materials offers solutions for our application - mainly constrained by the limitations of the wafer diameter in combination with its thickness. During prototyping we have ordered many carriers from Diamond Materials and have also explored the maximum lateral dimensions realizable as thin pCVD diamond. In 2014, Diamond Materials succeeded in producing two 126 mm diameter wafers of pCVD-diamond with 150 µm thickness. One of them was cut to 80×80 mm^2 without visible problems[4]. We are confident that the form factor needed for MVD station geometry b can be realized with pCVD diamond. Fig. 4.10 shows both, a carrier with a cut-out (left) used for our MIMOSA-26 pixel telescope, and the first large-diameter wafer of pCVD-diamond (middle), and the resulting carrier of station geometry b (right) together with the CAD drawing of the sensors to be positioned on this carrier. pCVD diamond will be the carrier material employed for the station geometry a, used exclusively in the MVD geometry version VX, and with the available large wafer diameters it remains an option for the station geometry b, *e.g.* in the position of MVD station 0.

Thermal Pyrolytic Graphite: TPG (Thermal Pyrolytic Graphite, or TCPG Thermal Conductive Pyrolytic Graphite) is a unique form of Pyrolytic Graphite (PG) manufactured by thermal decomposition of hydrocarbon gas in a high temperature chemical vapor deposition reactor. It represents a highly oriented graphite, with anisotropic material properties. It features a high in-plane thermal conductivity of better than 1500 W/mK, which is indeed comparable to pCVD diamond. However, the out-of-plane thermal conductivity is lower by approximately one order of magnitude. This material is heavily used in industry for dedicated heat spreaders, as well as in detectors [50]. Due to its diamagnetism, pyrolytic graphite repels magnetic field.

[4] Meanwhile (February 2020), Diamond Materials has announced having successfully produced a disk with 150 mm diameter, 150 µm thickness, however with a residual non-planarity, suggesting further process optimization.

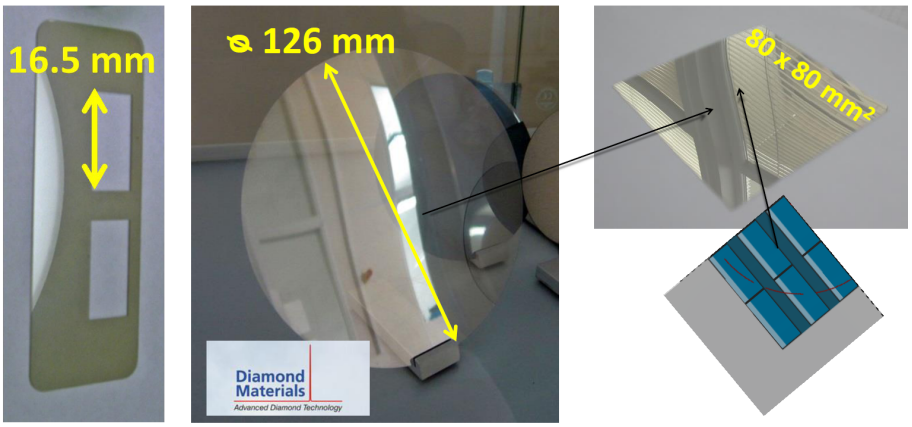

Figure 4.10: Pictures of a pCVD diamond carrier with cut-out (left) for our MIMOSA-26 pixel telescope, and the first polished pCVD diamond wafer with a diameter of 12.6 cm (middle), and the carrier (right) for station geometry b (one quadrant), which has been cut-out (thickness of 150 µm). The CAD drawing (lower right) indicates the positions of the sensors to be integrated on this carrier. Picture of the wafer: by courtesy of Diamond Materials.

However, inside the CBM magnet any effect on the sensor carriers made of TPG is negligible due to the strength of the magnetic field, its gradient and orientation. Table 4.2 summarizes the main features of TPG. Our assessment of TPG as carrier material is summarized in the following:

- **Material budget:** Trading mechanical stability, handling and material budget, a carrier thickness of 300 µm is recommended. A thickness of minimum 254 µm for sheets [5] can be ordered for all sizes relevant for the MVD, but handling becomes very difficult due to the softness of the material. Hence, it is not recommended to be used in a self-supporting geometry.

[5] TPG foils with thicknesses of 20 µm are available as heat spreader, but require a substrate for mechanical stability. In this respect, we are evaluating Carbon foams sandwiched with TPG foils.

Property of TPG	Value
Young's modulus	1050 (36) GPa
Density	2.26 g/cm^3
Radiation length X_0	19.03 cm
Surface roughness	not specified
Thermal expansion coefficient	$-1.0...0$ (25) $\times 10^{-6}$/K
Thermal conductivity	1500 ($<$ 20) W/mK
Electrical Resistivity	1×10^{-4} (Ω cm)
Price tag (2020)	0.15 €/mm^3

Table 4.2: Properties of Thermal Pyrolytic Graphite (TPG) at room temperature, see also [51]. The electrical resistivity refers to Pyrolytic Graphite. Numbers in brackets refer to the orientation out-of-plane. The radiation length is calculated with the Dahl fit formula to data [47]. Price in 2015 [51]

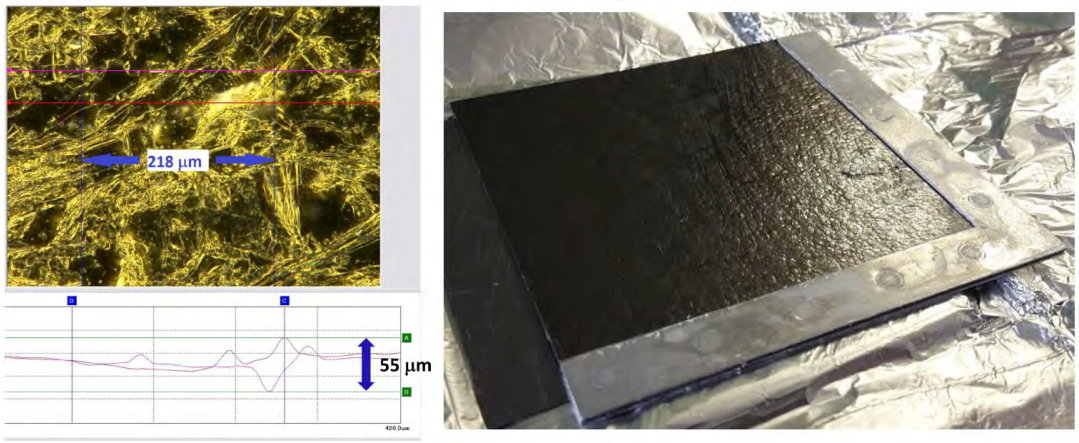

Figure 4.11: Left: Picture of bare Thermal Pyrolytic Graphite (TPG) taken with a dedicated microscope, which allows for measuring the surface profile, as indicated next to the picture. The color is caused by the illumination, bare TPG is dark-grey/black. Right: A TPG carrier (size of module geometry b, Parylene coated) sandwiched by Aluminum holding structures from Optigraph.

- Other properties:
  - The bare TPG surface is textured like slate. Hence, very small pieces of TPG can splinter off while handling, and dedicated coating is required. See for example Fig. 4.11 depicting a close-up view of a TPG surface (left side) compared a (Parylene-coated[6]) TPG carrier (right side), which is on two adjacent sides sandwiched by 0.3 mm thick Aluminum stripes. This carrier was used to study options of mounting the carrier in the heat sink.
  - The (measured) surface roughness of several 10 µm (see Fig. 4.11, left) is sizable. Parylene-coating will improve the surface quality in general. However, we have not experienced problems when gluing thinned sensor chips even to bare TPG.
  - Since TPG features a moderate electrical conductivity, additional measures are required to electrically insulate the sensors, *i.e.* coating with Parylene.
  - When delivered, TPG sheets revealed a bending of typically 1 mm over 80-100 mm. Due to the inherent flexibility we have not experienced any problem when clamping the carrier with two adjacent sides in the heat sink. However, the optical survey of the assembled module is mandatory to provide input to the alignment procedure.
- **Vendors of choice:** Momentive [51], Optigraph [52] or Panasonic [54] for pyrolytic graphite foils.

TPG is currently considered as baseline material for the module geometry versions b and c of the MVD.

[6] To prevent de-laminating and improving the surface quality w.r.t. electrical insulation, We are evaluating TPG samples Parylene (C)-coated by Optigraph [52] and IGB Fraunhofer (Stuttgart) [53] with a maximum thickness of 10 µm. The surface quality, the adhesion properties of dedicated glues as well as possible degradation of the thermal performance are subject of systematic assessments as well as the option of surface treatment, *i.e.* activation, of TPG prior to and after coating.

Adhesives: This section refers to the glue being used to fix the pixel sensor on the carrier, based on either pCVD diamond or (Parylen-coated or bare) TPG. The selection of the glue is driven by the following constraints:

- Low out-gassing and avoiding bubbles during preparation (vacuum operation).
- Sufficient radiation tolerance, *i.e.* better than the limits stated for the pixels sensors (5 Mrad/year and 7×10^{13} n_{eq}/a for ionizing and non-ionizing radiation, respectively).
- A high thermal conductivity. This could be relaxed if the glue properties would allow for preparing thin layers (50 µm), *e.g.* low viscosity before curing.
- A residual flexibility after curing to compensate the mismatch of thermal expansion between the carrier and the sensor.
- A curing time which fits to the time scale of assembling a module.

Furthermore, it is known that silicone-based glues, which would provide the residual flexibility, show pronounced out-gassing. Glues with improved thermal conductivity compared to standard glues contain impurities of silver, giving rise to an additional entry in the material budget. On the other hand, epoxy-based glues do not provide residual flexibility after curing and hence would lead to internal mechanical stress when cooling down from room temperature (assembly environment) to operation temperatures around −20 °C.

During prototyping (Prototype 1) the epoxy-based resin Epotecny E501 [55] was evaluated, featuring a viscosity of only 0.1 to 0.2 Pa s before curing, and hence it was easy to dispense. The prototype was operated in the temperature range from 5 up to 25 °C and we found no hint, both from visual inspection and data analysis, that the rigid link between sensor and carrier has triggered problems due to internal mechanical stress. For the CBM-MVD we are currently following two further options:

- A custom made glue by RAL (Advanced Materials Group, STFC, UK) [56], formulations 245, 246 and 247. They feature a low viscosity of about 0.1 Pa s before curing, and become stiff at around −45 °C. The tolerance against radiation is currently being studied.
- Hysol Eccobond 45/Catalyst 15 (now Loctite Ablestik 45 from Henkel) [57], Epoxy-based, being evaluated by ALICE. It features a residual elasticity after curing down to −55 °C. The viscosity of 36 Pa s, however, asks for a detailed study of dispensing techniques to allow for preparing thin layers.

Our studies regarding the selection of glues are guided by the corresponding activities for LHC detector upgrades. Locally, we are focusing on providing thin, still flexible layers of glue between sensor and carrier, and test regarding radiation hardness and compatibility with moderate vacuum. To do so, we have selected a custom made two compound adhesive by RAL [56], RAL-247. The glue has a glass temperature of −45 °C, a viscosity of below 100 mPa s and a curing time of 48 h at +50 °C. To investigate its radiation hardness, RAL-247 samples were irradiated with X-rays to 100 Mrad and exposed to a proton dose of about $10^{15} n_{eq}/cm^2$, see Fig. 4.12. The irradiated samples were sent to RAL for further Dynamic Mechanical Analysis tests, which revealed no significant change of properties. It confirmed the expected radiation hardness in the range of the radiation doses and temperatures expected for the MVD. The glue was deployed during the assembly of prototype 2 (PRESTO, sensors glued to bare TPG). Both, tests before assembly, focusing on processing the glue without air bubbles, thickness and out-gassing, and with PRESTO (a glue layer of 15 µm thickness) did not reveal any problems for long-term operation in moderate vacuum.

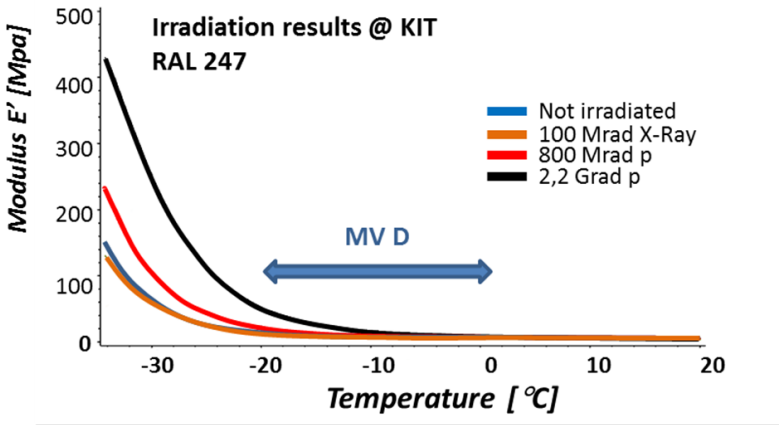

Figure 4.12: Measured dependence of the Modulus of adhesive samples RAL-247 on the irradiation level, plotted a a function of the temperature, provided by RAL

4.2.2.3 The heat sink

The heat sinks are made of bulk Aluminum alloy, comprising a hidden channel structure for the cooling fluid with two connections for in- and outlet at the long side. The cooling channel runs parallel and close by the interface to the carrier plates to allow for most effective heat transfer. In view of the system's moderate heat load of well below 50 W per module (quadrant), it is optimized for mono-phase cooling with high-performance heat transfer coolants. So far, alcohol mixtures or silicone oil [7] have been explored. With NOVEC^{TM} 649 (3M^{TM}) [58] a modern coolant is available and it is currently being characterized. The heat sink comprises dedicated structures to position and mechanically clamp the sensor carrier as well as to fix the sink itself to outer supporting structures, that are mounted on the common base plate. The interface between the carrier and the heat sink has to fulfill both, a reliable mechanical fixation of the carrier, as well as an efficient heat transfer. Systematic tests with mock-up samples in the vacuum, employing flexible Kapton heaters (OMEGA Engineering INC) to mimic the areal heat dissipation of sensors, and monitored in vacuum by a network of Pt-100 temperature sensors and IR visualization, helped to optimize the heat sink design used for the MVD. Presently, we are characterizing heat sinks manufactured at "Cool Tec Electronic GmbH" [59], depicted in Fig. 4.13 for module geometry b, and CTX Thermal Solutions GmbH" [60], with the following specifications and procedures:

- Material: AlMgSi0,5 Al-alloy, featuring a heat conductivity of about 210 $\frac{W}{mK}$ and a CTE of 23.4×10^{-6} K^{-1}.
- Minimizing the distance between pipe structures and heat contact to the carrier, while maximizing the cross sections of the pipe to decrease pressure drops and allow for laminar flow of the coolant.
- The cooling pipes are milled into the cold plate, which then is closed by welding a cover plate on top, specified for a maximum pressure of 5 bar.
- Together with Cool Tec we have conducted thermal simulations to optimize the design,

[7] Bi-phase cooling with CO_2 is currently not considered and would require a complete redesign of the cooling system.

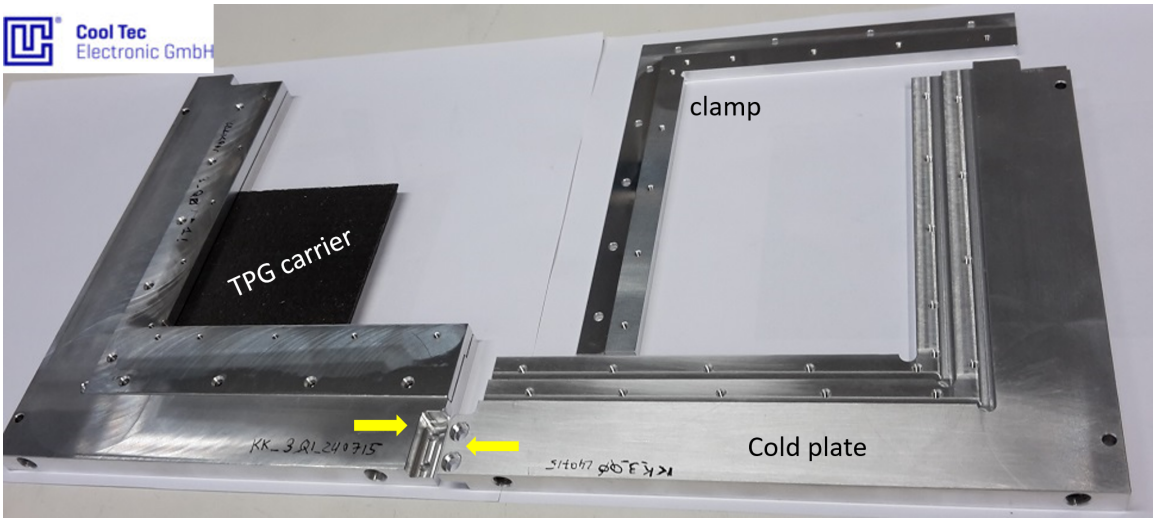

Figure 4.13: Heat sinks (version 2, two quadrants) of module geometry version 2.0, manufactured at Cool Tec Electronic GmbH. Cooling pipe structures are buried in the Aluminum bulk of the cold plate. The clamp (right) fixes the carrier (as example a smaller-size TPG carrier) to the heat sink (left).

based on the use of Silicon-Oil M80.055.03, 7.33 l/min, at −50 °C.

Employing modern techniques of welding and gluing, both companies can offer dedicated, customer-specific affordable solutions for complex geometries. With version 2.5 the design of the heat sink is largely fixed. Fig. 4.14 depicts technical views of this latest version of the heat sink. Note that the cooling channel reaches underneath the contact area of the carrier and features variable aspect ratios to minimize the pressure drop over the channel while optimizing the heat transfer from the carrier. Its present dimensions are driven by the maximum thickness of the heat sink (10 mm, allowing for a minimum station-two-station distance of 40 mm for the TR detector geometry), minimum distance to the carrier and the minimum thickness of bulk Aluminum walls required by the manufacturer (1.5 mm). The dimensions of the heat sink challenges the welding procedure of the channel's cover plate w.r.t planarity. Only CTX was able, so far, to provide adequate planarity needed to avoid residual mechanical tension in the carrier once clamped to the heat sink. Presently, studies are in progress to characterize the thermal performance of the carrier–heat sink unit in the temperature of interest with alcohol-mixtures and NOVEC^{TM}-649 (see Sec. 4.5.2 and 4.2.5.2.).

4.2.3 Module assembly

Module assembly has been exercised during prototyping, see Sec. 5. The prototype PRESTO-1, employing MIMOSA-26 sensors, has been finalized in 2019 and is being successfully evaluated in vacuum since then. Issues w.r.t. the sensor integration yield have been resolved by identifying a problem with the calibration of the bonding machine used. However, the assembly procedure as well as the tools being developed and used for integration have been validated during the PRESTO-1 work package. We are currently developing the tools compatible with new sensor form factor (MIMOSIS-1) and upgrading the integration procedures that will then be used

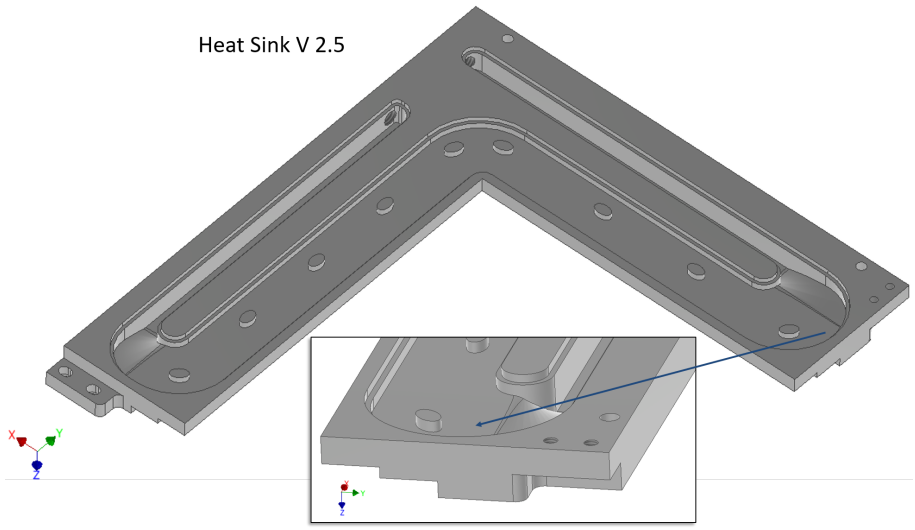

Figure 4.14: CAD view of the latest heat sink version 2.5. The zoomed insert details the cooling channel. Not shown: the cover plate welded on top of the heat sink closing the cooling channel.

to assembly PRESTO-3 module[8]. Therefore, we will confirm the improved sensor integration yield, and study the option to integrate sensors on two separate, but thinner (254 µm) TPG sheets Sec. 4.2.4.4 (instead of the baseline concept where sensors are integrated on both sides of one sheet) within PRESTO-3 project. If successfully demonstrated, we would trade sensor integration yield against material budget, *cf.* section 4.2.4.4. Lessons learned with PRESTO-3 project will be then applied for the final sensor integration concept with the first generation of full-size MIMOSIS sensors.

4.2.3.1 Gluing sensors on the carrier

Fixing the thin CMOS sensors onto their carrier material is based on the following steps (see Fig. 4.15). The precision of this method is of about 100 µm.

- **Placement of the carrier on the carrier jig:** Fig. (4.15a) - in this step, the "c-frame" with defined 90° corners is used. C-frame is mounted in its desire position with pins that fit to the holes drilled inside the carrier jig. Then, the TPG plate is aligned with the "c-frame" and held at its position by means of vacuum channels built in the carrier jig (Fig. 4.15b). The "c-frame" is removed (Fig. 4.15c).
- **Placement of sensors on the sensor jig:** in this step one ladder of sensors is aligned with respect to predefined points on the sensor jig (Fig. (4.15d)). To do that, the "c-frame" is first aligned with respect to the sensor jig. Next, the first sensor is aligned with respect to the "c-frame" 90° corner. The next sensor is aligned with respect to the edge of the c-frame and the edge of the predeceasing sensor (Fig. 4.15e). The "c-frame" is removed.
- **Adhesive deposition:** A drop of a low viscosity adhesive (RAL-247) is deposited at the center (back side) of each sensor (Fig. 4.15f). In case of CVD-diamond carrier the adhesive drop amounts 5 µl, which translates to a 16 µm thin layer of adhesive between the sensor and the carrier. In case of the uncoated TPG-carrier an amount of 9 µl is needed, since a

[8]PRESTO-2 is skipped due to the availability of the MIMOSIS-1 sensors.

part of it is absorbed by the carrier material.

- **Joining of jigs:** In this step the sensor and the carrier jigs are aligned with respect to each other and connected together such that the sensors are in contact with the carrier (Fig. 4.15g). The sensor jig is removed (4.15h) and the next row of sensors can be mounted.

4.2.3.2 Mounting and routing of FPC cables

Currently, the design of the FPC cable allows to host services for two MIOMSA-26 sensors in parallel. In case the ladder is composed of three or four sensors, one more FPC is added on top of the previous one. This procedure is shown in Fig. 4.16. In the first step, a mask made out of a 25 µm-thin double-sided adhesive Kapton tape is applied. The mask has a size of 45×2 mm and is placed at 1 mm distance from the cable edge (Fig. 4.16a). Next, an adhesive is deposited and the mask is removed (Fig. 4.16b). In the next step, a spacer cable (66 µm thin), limiting the lateral flow of glue, is added between the two FPC cables that are being connected (Fig. 4.16c). Both FPC cables and the spacer are aligned on a jig, clamped together and place inside an oven for curing (Fig. 4.16d). After 20 hours the final product is visually examined and electrically tested.

We consider two types of two-components epoxy-based adhesives to serve as an adhesion layer between the two FPC cables: RAL-247 and Loctite Ablestik 45 W1. Both of them are sufficiently radiation tolerant and stay flexible after curing. The RAL-247, due to its very long curing time (3 days at +50 °C) and very low viscosity, is difficult and time consuming to work with but allows to achieve a layer that is about 10 µm thick. This is three to five times less than what can be achieved with the Loctite adhesive that, on the other hand, needs only 8 hours to cure at room temperature.

We also investigated the feasibility of using a 25 µm thin 3M$^{\text{TM}}$ double-sided adhesive transfer tape 9460PC as joint between the sensor and the carrier. It was concluded that the tape cannot be used for bringing together non-planar objects. Multiple tiny voids of air between objects are created since the tape does not stick to these objects across the whole area. There is, therefore, a risk of creating a object not compatible with vacuum operation.

4.2.3.3 Bonding of FPC cables to sensors

The sensors are electrically connected to the FPC cables by wire bonds made of 25 µm aluminum wire. The pull tests revealed that the bonds can withstand 7 ± 2 g force, which is considered an acceptable value. To keep the material budget low, we do not foresee a full bond encapsulation. If any, the encapsulation will be limited to the bond feet only.

4.2.3.4 Mounting the carrier to the heat sink

The concept of clamping (instead of gluing or screwing) the assembled carrier to the heat sink was proven to be safe, placing a low risk to the bonded sensors. However, with the currently studied prototype PRESTO-3 we are as well studying the option to first clamp the carrier to the heat sink before gluing the sensors. This might even further improve the integration yield since the heat sink serves as both, integration jig and tool to safely handle the object after sensor integration. The decision on the final method will be taken after prototyping the proposed new assembly order, and evaluating the option of employing two instead of one carrier sheet, as outlined in the introduction of this section.

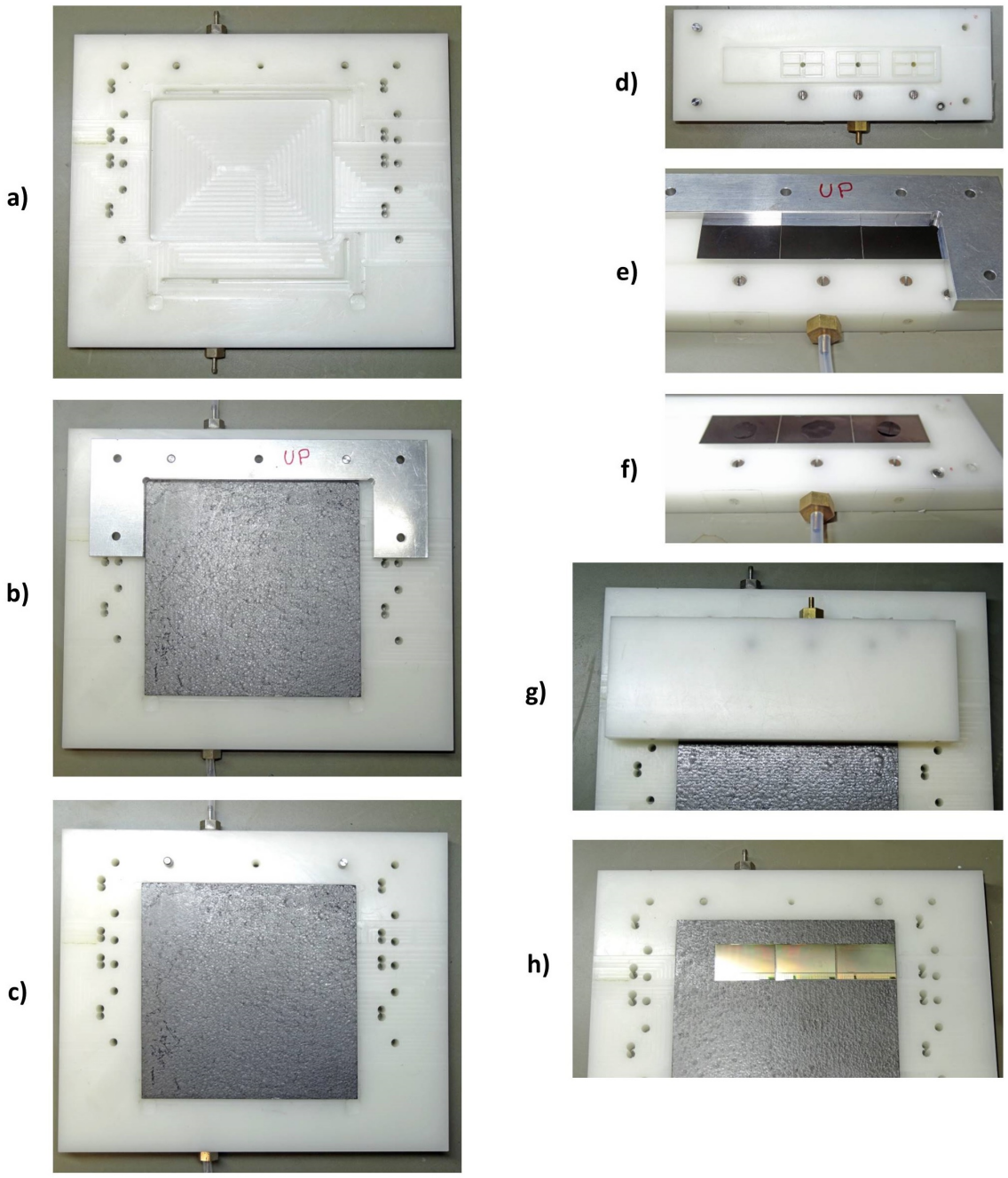

Figure 4.15: Sensor assembly onto its carrier: a) Carrier jig, b) a carrier is aligned with the jig by the means of a c-frame, c) TPG carrier aligned with respect to the carrier jig and kept at the desire position by under-pressure, d) sensor jig, e) sensors are aligned on a sensor jig by the means of the c-frame and kept at the desire position by under-pressure, f) sensors on a jig with RAL-247 deposited in the middle of each one, g) the carrier and sensor jigs are aligned by the mean of holes (carrier jig) and pins (sensor jig), h) the under-pressure from the sensor jig is released and the jig is removed - final product.

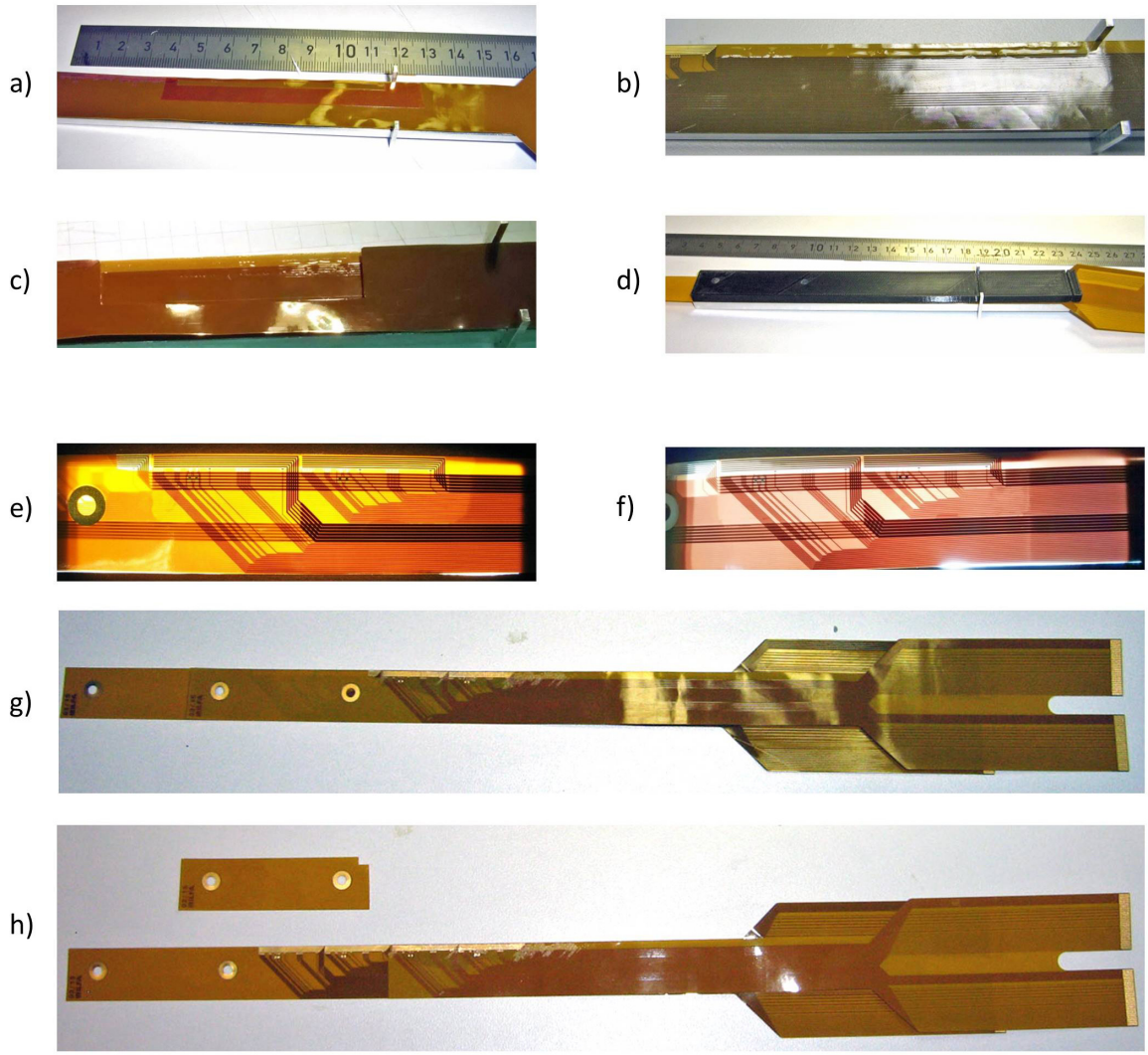

Figure 4.16: Step-by-step assembly of a double FPC: a) Mask for depositing an adhesive is placed onto the FPC cable, b) adhesive is deposited and the mask is removed, c) a spacer cable is added to control the glue flow, d) two cables and a spacer are aligned by means of an aluminum jig and pressed together with a black plastic clamp, e) and f) after curing for 20 hours, cables are visually inspected in front of a strong light source, g) the not needed pieces are removed, including a spacer, h) final product.

4.2.3.5 Attaching and connecting FEE boards

During prototyping the length of the FPC cables was not optimized, since the receiving FEE boards were mounted slightly displaced from the sensors. However, we made sure that no residual force was acting on the carrier assembled with sensors and FPC cables when connecting to the FEE. Hence, in the final setup, loops of FPC cables will be avoided by optimizing their length fitting to the place to be mounted. In addition, the mechanical decoupling of sensors and FEE will be ensured by a proper fixation of the FPC cables prior to connecting.

We currently plan to place all passive components for power filtering was as well as GBT-SCA ASICs for sensor control and monitoring inside the MVD vacuum box. The connection between these elements and the rest of associated electronics, placed outside the vacuum chamber, will be done by means of dedicated feedthroughs, as described in Sec. 4.3.1.2 and in Fig. 4.27.

4.2.4 Procedures

4.2.4.1 Survey and alignment

The knowledge of the absolute position and orientation of the pixel sensors in the CBM coordinate system, called sensor alignment in the following, is the prerequisite for high-precision tracking and vertexing with the MVD. For sensors with a single hit spatial precision of about 5 µm, and aiming at a secondary vertex precision of several 10 µm with the MVD alone, a sensor-to-sensor alignment precision of 5 µm and better is mandatory. Achieving this level of precision is only possible by employing high-statistics analysis of (straight) tracks, predominantly delivered by runs without magnetic field taking place on a regular basis to assess and correct for long-term variations[9]. Typically, alignment parameters are the result of iterative minimization algorithms, such as the established Millipede code [61] or Minuit (ROOT). However, to assure reliable convergence, starting positions (x, y, z-position of the fiducial marks) have to be known with a precision of about 100 µm or (preferably) better. Therefore, the fiducial marks are directly implemented on the surface of the CMOS sensors. Accessing their positions will most probably rely on 3D optical survey techniques, *e.g.* presently being developed for the CBM-STS [62], or on photogrammetry[10], resulting in metrological parameters for each sensor, and comprising the position of its reference points relative to the carrier and heat-sink and its individual 3D surface.

The alignment strategy based on Root (TMinuit) with start values given by measured sensor positions on a given carrier and station positions during assembly in a 5-station DUT (so-called prototype 1)/telescope setup has been successfully exercised for our CERN test beam campaign in 2012, see [63, 64] and Sec. 5.2.1. We were able to demonstrate a spatial precision (per sensor) in the order of 4 µm by referencing the detector under test (DUT, 4 thinned MIMOSA-26 pixel sensors, mounted back-to-back on a pCVD diamond carrier) with a compact 4-station telescope setup (MIMOSA-26). We did not experience a measurable impact of vibrations caused by the cooling system, *e.g.* moderated by the cooling fluid, on the setup. Mechanical decoupling of pumps from the setup is, however, advised and is currently being exercised in our vacuum chambers.

Results from prototype 1, featuring 2 sensors mounted back-to-back on both sides of a thin

[9] Whether cosmic rays might supplement the high-precision sensor alignment in our compact geometry has not yet been explored.

[10] The precision of this method depends crucially on the quality and number of the fiducial marks, number of pictures (cuttings per module) taken and the resolution of the camera system employed. An evaluation of options to place fiducial marks by lithographic means directly on the sensors or use other high-contrast sensor structures as fiducial marks is under investigation.

carrier (cf. Sec. 5.2.1), respectively, suggest another method of aligning sensors on the front and the back side of a given MVD module relative to each other. As discussed in Sec. 4.2, we provide a front-to-back sensor (*i.e.* ladder) overlap of the active pixel area of 500 µm, yielding more than 15 mm^2 per sensor overlap with its proximate partner on the other carrier side. This overlay allows for a high-precision sensor-to-sensor alignment by means of straight track (no field) measurements.

4.2.4.2 Quality assurance

A fine-pitch grid of quality assurance (QA) steps will be applied to the individual components of the produced MVD modules, before and after each integration step. Controlling the quality of individual as well as assembled components, including assessment and documentation, is of utmost importance during production. The following QA measures have been invented and applied for the needs of prototyping (*e.g.* PRESTO-1) as well as to provide a reliable Small Acceptance Vertex Detector (SAVD) for the NA61 collaboration (see Sec.A.1). However, a final QA plan is to be further optimized and set up prior to production. Aiming at fully functional detector modules, ready for being integrated on detector half stations, the proposed QA measures are[11]:

- Probe-testing of the sensors (exercised with MIMOSA-26 sensors during several prototype studies).
- Visual inspection of the carriers w.r.t. surface damages, irregularities, geometrical properties. In the case of TPG before and after Parylen-coating.
- Visual inspection and electrical functionality tests of the FPC cables.
- Tests with the glue (bubbles, viscosity at a given temperature and humidity) after opening of the container, just before application.
- Verifying (and documenting) each sensors position on the carrier relative to carrier intrinsic coordinates after positioning, and after curing.
- Conducting an optical survey of the sensors on the carrier (3D), for each side, respectively.
- In case of integrating on two separate TPG sheets: Additional QA measures before and after mounting both sheets back-to-back.
- Verifying (and documenting) of the FPC cable position after gluing the FPC to the carrier.
- Visual inspection of bonds after bonding the sensors to the FPC cables.
- Connecting to the FEE and running first (smoke) tests of the MVD module, *e.g.* threshold setting, measurement of fake hit rates and identification of dead pixels.
- Environmental tests, *i.e.* running individual modules in vacuum at the anticipated operation temperature. This includes temperature and pressure cycles with powered modules.

We have not yet defined binding criteria to reject components for module integration, *e.g.* depending on the number of pixels to be masked or dead, assembly precision reached or noise immunity in a well-defined (and closed) setup. For example, the fraction of dead pixels for a given sensor (position), which still can be tolerated for a given physics case, depends *e.g.* on where the senors is going to be mounted (station, distance from beam axis), or whether dead pixels are randomly distributed or adjacent. This has to be assessed by means of detailed physics simulations. It is obvious that all (quantitative) results from QA steps will be documented together with unique ID tags of the component in a dedicated component database, taking

[11] assuming that all tools and jigs have been validated before.

profit of similar tools used for the CBM STS detector [65].

4.2.4.3 Repair strategies

In a dense, highly integrated object like a MVD module, the possibility of repairs is rather limited. In fact, having bonded sensors on both sides of a thin carrier makes repair almost impossible. On the other side, the components itself are rather inexpensive. This does not hold for modules (stations) employing CVD diamond carriers. Module geometry "a" will use CVD diamond as carrier material, but only a few sensors are attached, which can be (all) taken off again to re-use the carrier. Module geometries "b" and "c" will employ TPG. Hence, the strategy is to replace complete units (*e.g.* carriers equipped with sensors) rather than trying to rework individual sensors. Obviously, this concept drives our attempt to trade integration yield against material budget for station geometries "b" and "c" by studying the option of integrating sensors on two thinner TPG sheets with PRESTO-3, which will then be linked together in one module. Nevertheless, during prototyping some repair options have been successfully conducted: Gluing and bonding a second sensor on top of a broken one (not considered as solution for "good" MVD modules), and repairing individual bond wires. Removing and replacing sensors after gluing is not advised. Besides risking damage to adjacent sensors and bonds, in the case of TPG the carrier's surface does delaminate. In conclusion, our primary goal must be to produce many modules of each geometry (focus "b", "c"), out of which we then select the best ones for the detector and the hot spare modules.

4.2.4.4 Alternative sensor integration concept

A conceptional drawback of the sensor integration concept discussed so far is the large number of sensors to be integrated on one module on both sides of a given carrier. Station geometry "c" calls for 16 (front) and 12 (back) sensors. In contrast to ladder-based geometries, the sensors have to be placed in a 2-dimensional grid, which represents an additional risk during handling and assembly, further reducing the integration yield. Employing ladders instead of (quadratic) discs, fixed on one side only to the heat sink, would add additional temperature gradients between 5 and 10 K and hence degrade the module's thermal performance. The increased temperature gradients are caused by a reduced heat contact area between ladder and heat sink for those ladders clamped only on one side to the heat sink.

The only practical way to reduce the overall sensor integration risk is separating front- and backside integration by using two instead of one sheet of TPG. However, the material budget (for details see Sec. 4.2.5.1 of station geometries "b" and "c" will suffer, since the minimum thickness of TPG sheets in the size required is around 250 µm [12], which is more than half of the current baseline thickness of 380 µm. Fig. 4.17 compares different thicknesses (material budget) of carrier options to the baseline for station geometries "b", "c". Integrating the sensors on two thin TPG sheets would add 20% additional material budget compared to the baseline. Multiple scattering would increase by 9%. Spacers are not taken into account, yet. Gluing large-area TPG sheets together would endanger vacuum compatibility. Whether or not employing one-sided integration of two TPG sheets will depend on the results of the ongoing prototype studies with PRESTO-3 and physics performance studies.

[12] Handling of 254 µm thick TPG sheets was exercised during prototyping and it was concluded that double-sided integration of sensors is too risky due to handling issues. One-sided integration, with the TPG sheet placed on a planar layer seems, however, possible.

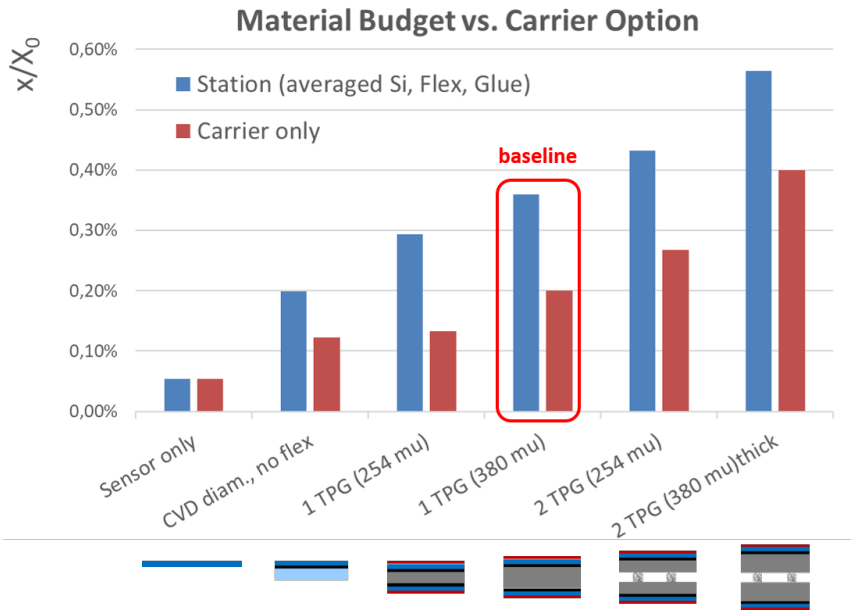

Figure 4.17: Comparison of the material budget of MVD detector stations of different carrier thickness options. The current baseline layout of station geometries "b" and "c" is indicated.

4.2.5 Module performance

The sensor integration and module design is driven by meeting requirements w.r.t. thermal performance and material budget, both reviewed in the following.

4.2.5.1 Material budget

The precision in determining primary or secondary vertices represents the driving force in designing a vertex detector. Following a simplistic approach of a 2-layer vertex detector, *e.g.* given in [66], the vertex-finding performance, which can be quantified by the pointing precision of a reconstructed track to the vertex, is mainly given by

- (Geo) The spatial precision of the pixel sensor, i.e. pixel pitch and charge sharing.
- (Geo) The distance of the first detector station to the vertex.
- (Geo) The distance between both detector stations.
- (MS) The multiple scattering of the particle before being detected in the second station.

Assuming the first three geometrical items (Geo) defined by constrains of the setup (target chamber dimensions) and the sensor technology employed (*e.g.* pixel size and radiation hardness), the contribution of multiple scattering (MS) is given by (i) the momentum, velocity and charge of the daughter particles and (ii) the material budget of detectors in the geometrical acceptance. The particle's average (lab) momenta result from the physics cases and are typically in the GeV/c-range in the SIS100 energy range. With a material budget of a few per mill only, but in the momentum region below approximately 2 GeV/c, the vertex finding precision is driven by multiple scattering. The contribution of the detector (sensor and station geometry) to the pointing precision becomes dominating above 2 GeV/c for our setup, depending on the detector

geometry VX or TR. Hence, it is advised to place the MVD in vacuum[13] and to employ detector stations as thin as technically possible[14]. This translates in three main frontiers of technical development w.r.t. the material budget:

- Sensor: With an epitaxial layer of about 10-20 µm thickness, CMOS monolithic active pixel sensors are thinned down to about 50 µm.
- Carrier: Operation in vacuum calls for trading between cooling performance and material budget. Inside the acceptance we opt for passive cooling by means of heat conduction. Hence, materials with maximum thermal performance (CVD diamond, TPG) are employed, featuring thicknesses which are mainly defined by mechanical stability during handling (both during production and assembly) and operation .
- Sensor readout cables FPC : Minimizing material calls for dedicated thin and flexible cables, with thin copper, better aluminum traces.

Based on the design decisions given above the material budget inside the geometrical acceptance can be assessed, as detailed in a CBM Technical Note [67]. The minimum thickness of the pixel Si sensors (50 µm) is given by the process employed and cannot substantially be reduced. Hence, the material budget is mainly driven by the supporting carrier and the readout cables (if placed inside the acceptance), where special attention has to be paid to the first station once the detector operates in vacuum, driving the vertexing precision along the beam axis (see Sec. 6.4.2). As a baseline, a material budget of $x/X_0 < 0.3\%$ is envisaged of this first station (detector geometry VX, station geometry "a" only). This value follows from what is technologically possible without placing too high risk to production yield and performance, and the required precision in secondary vertex determination of below 70 µm (σ). This value represents a cutting-edge performance parameter for Si-pixel based tracking stations operated in vacuum. For the two other station geometries "b" and "c" this baseline can be relaxed for detector geometry VX and it is $x/X_0 < 0.5\%$. For station geometry "b", used as first station in detector geometry TR at $z = 8$ cm, it might be advised to use CVD Diamond ($x/X_0 = 0.12\%$) instead of TPG ($x/X_0 = 0.2\%$) as carrier material, see Sec. 4.2.2.2. However, a substantial cost increase compared to TPG and additional risk w.r.t the production yield has to be traded against the increase in multiple scattering.

Fig. 4.18 depicts the 2-dimensional representation of the three module types "a", "b", and "c". The module employing CVD diamond stays well below the limit ($x/X_0 = 0.3\%$, first row/column). The same holds for the baseline TPG carrier thickness (380 µm), first column, second and third row ($x/X_0 = 0.5\%$). Only the $2 \times 250 = 500$ µm TPG module of type "c" (second column, last row) exceeds this limit mainly where the FPC cables overlap, visible as distinct parallel patterns. This can be better seen in Fig. 4.19 by comparing the left and the right plot. The MVD baseline concept for FPC was developed during the construction phase of prototype 1, cf. 5.2.2.4, and relies on (robust) flex cables with copper traces, featuring a material budget x/X_0 of 0.051%, cf. Tab. 5.1 and depicted in Fig. 4.16. Replacing Cu by Al traces of the FPC cables would push the material budget below the limit everywhere again. However, this non-standard technology would add risks and costs into the project, which we want to avoid compared to the little gain in the (average) material budget. Fig. 4.20 demonstrates that these spikes in x/X_0, caused by overlaying FPC, are averaged out once integrated over the azimuth,

[13] To be more specific, avoiding material from a vacuum window between the vertex and the first detector station, and assuming that the target is positioned in vacuum.

[14] The quest of employing low-Z materials while minimizing the material budget close to the target in order to reduce γ-conversion is not discussed here. It is, however, decisive for the physics case of dielectron spectroscopy with CBM.

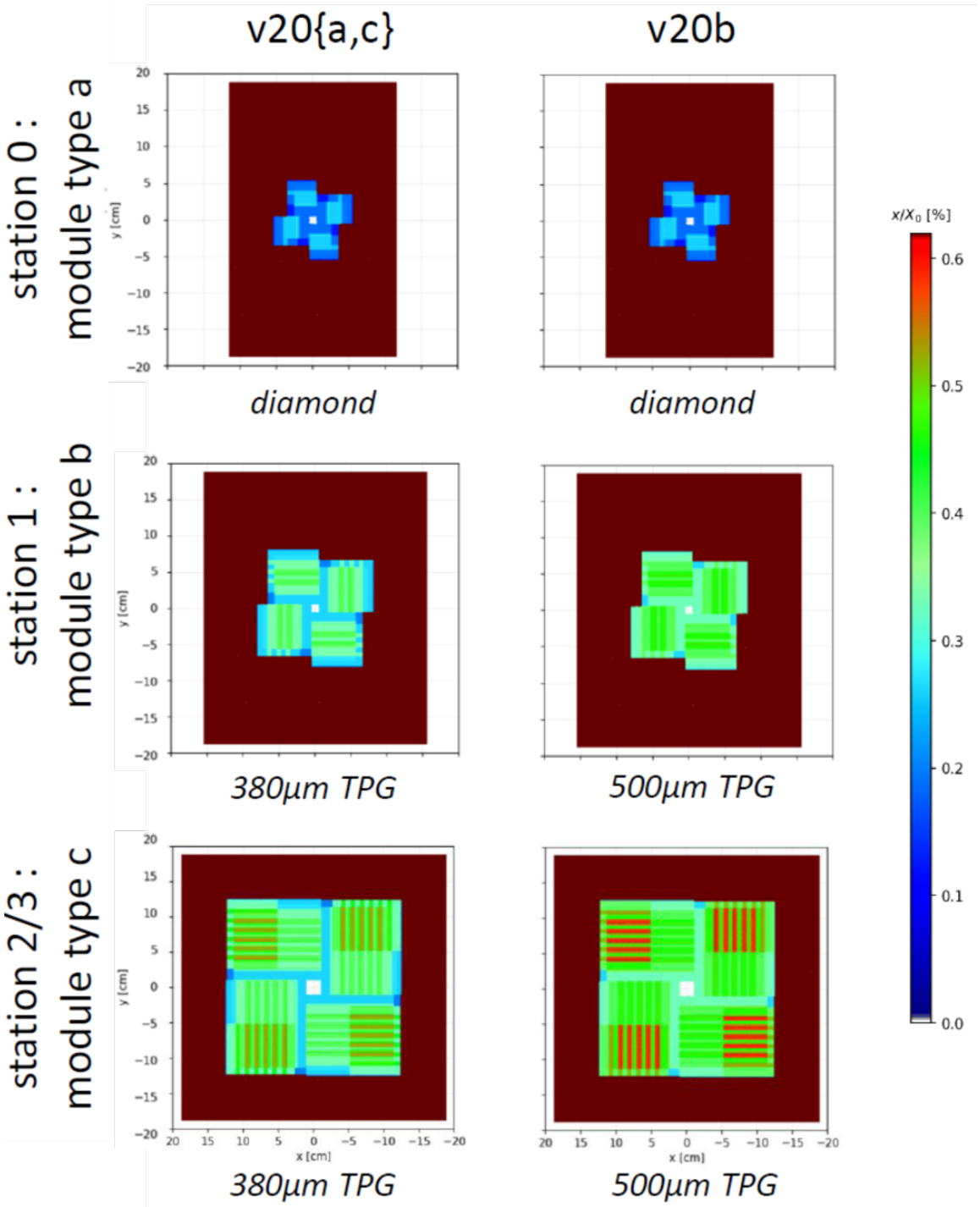

Figure 4.18: 2-D-representation of the station's material budget (top view), comparing different module types "a", "b" and "c" (rows) employed in the VX detector geometry (station 0 - 3), and comparing the baseline thickness of the TPG carrier (left column) with the version proposed for sensor integration on two 250 µm thick TPG sheets (together 500 µm), right column."v20a,b,c" correspond to the geometry version names used in simulation.

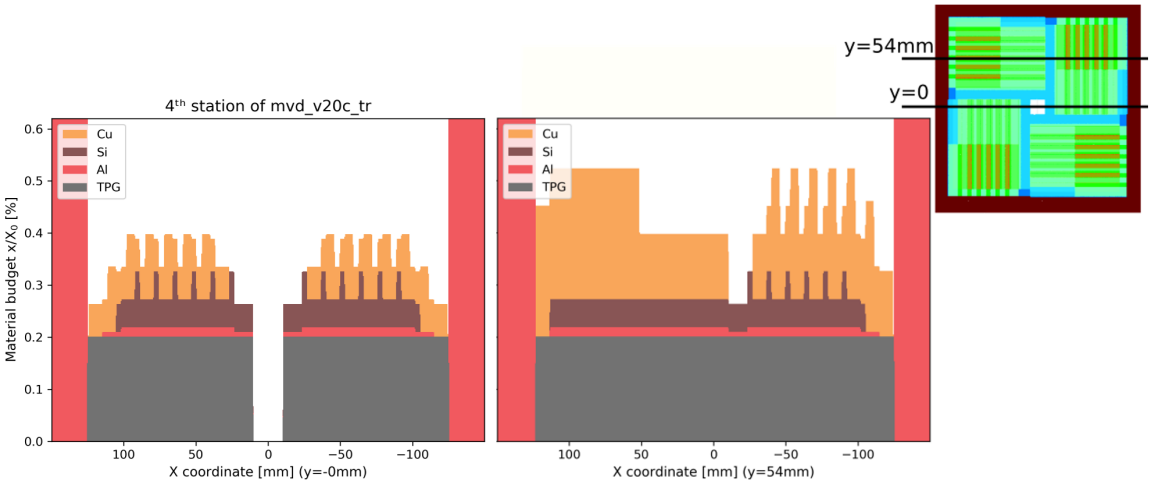

Figure 4.19: Material budget vs. x of the module geometry "c" for two cuts in y, indicated in the inlay in the upper right corner. Cu: FPC cables, Si: sensors, Al: heat sink (outside acceptance) and glue inside, and TPG: carrier.

staying below 0.5% X_0 thickness.

4.2.5.2 Thermal management

As detailed above, the obvious contradiction between effective cooling and low mass detector stations operating in vacuum is resolved by employing high performance heat conduction in the geometrical acceptance, where minimal material budget is essential for the tracking performance, and effective heat evaporation by means of actively cooled, dedicated heat sinks outside the acceptance. The main source of heat are the sensors, comprising active sensing pixels and digital structures for data handling. The power dissipation for the CBM-MVD pixels sensor MIMOSIS was originally specified as (average numbers) between 200 and 350 mW/cm^2, depending on the number of active links needed to cope with the expected range of occupancy. The updated predicted power consumption per sensor is 230 mW per sensor (corresponding to about 45 mW/cm^2) at maximum load [44]. This power is reduced by up to 50 mW if the sensor runs idle. Due to the efficient cooling of the sensors, and the heat capacities and contacts involved, this power swing, which would *e.g.* occur during spill on/off, results in a temperature swing of the sensor of about 1.7 K, on a time scale of 0.01 s. All these numbers, however, have to be confirmed with MIMOSIS-1, as soon as the sensor is being integrated in a module prototype (PRESTO-3).

To accommodate the heat dissipation by additional components mounted on the module, the following power loads have been estimated [15]: 0.2 W per FPC cable (one cable serves 2 sensors), and 4 (2) W per r/o board FEB (one FEB per module) for stations 0, 1 (2, 3 respectively), both detector geometries VX and TR. Fig. 4.21 shows for the VX detector geometry the resulting dissipated power per station, adding up to 135 W grand total for 264 sensors. The TR detector geometry with 288 sensors yields 143 W grand total. In-situ measurements (thermal mock-ups

[15] DC-DC conversion will, if at all placed inside the vacuum, not affect the module's thermal performance discussed here.

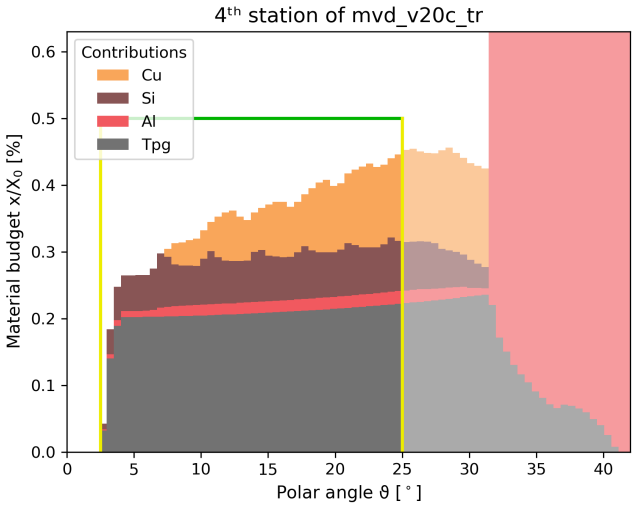

Figure 4.20: Estimation of the material budget of module geometry "c" (fourth MVD station in both detector geometries), integrated over azimuth. Lines to guide the eye w.r.t. the material budget (horizontal/green) and geometrical acceptance limit (vertical/yellow). Cu: FPC cables, Si: sensors, Al: heat sink (outside acceptance) and glue inside, and TPG: carrier.

characterized by PT100 sensors and IR survey) with detector and heat sink prototypes, back-on-the-envelope assessments addressing heat transfers and temperature differences as well as simulations based on dedicated software packages which make use of the detector CAD design help to characterize the thermal performance of the proposed concept.

The driving forces for optimizing the thermal management of the MVD are

- **temperature differences** across the sensor sub structures, to ease finding of optimum sensors setting for keeping the detection efficiency high while minimizing the fake rate. The typical scale (sub-matrices of the sensor) with the same threshold setting is 1 cm or less.
- **temperature differences** across the carrier inside the acceptance, to allow for sensor operation well below 0 °C for all sensors, which has positive influence on the pixel signal-to-noise, especially after having accumulated dose.

In an early stage of developing the MVD conceptual design [45] the thermal performance of the MVD stations was assessed by means of simulations based on *Autodesk Inventor Professional (2012/13)*. At this time, the dissipated power of the sensor was estimated to be 350 mW/cm^2, which is about a factor of 7 higher compared to the recent specifications. Nevertheless, Fig. 4.22 exhibits the temperatures across the carrier of station geometry "c", representing the worst case w.r.t. temperature differences. For the critical sensors at $x = 0$ the maximum temperature difference across 1 cm is close to 5 K (sensor close to the heat contact to the heat sink), and the temperature difference to the heat sink temperature is close to 40 K (sensor close to the beam), assuming 350 mW/cm^2 power dissipation[16]. As stated above, recent estimates driven by the MIMOSIS-1 design suggest only close to 45 mW/cm^2, which is a factor of about 7

[16]This value represents the original estimate for the CBM dedicated pixel sensor. Taking profit of recent progress in developing low-power MAPS, the state-of-the-art performance in power dissipation is more than welcome.

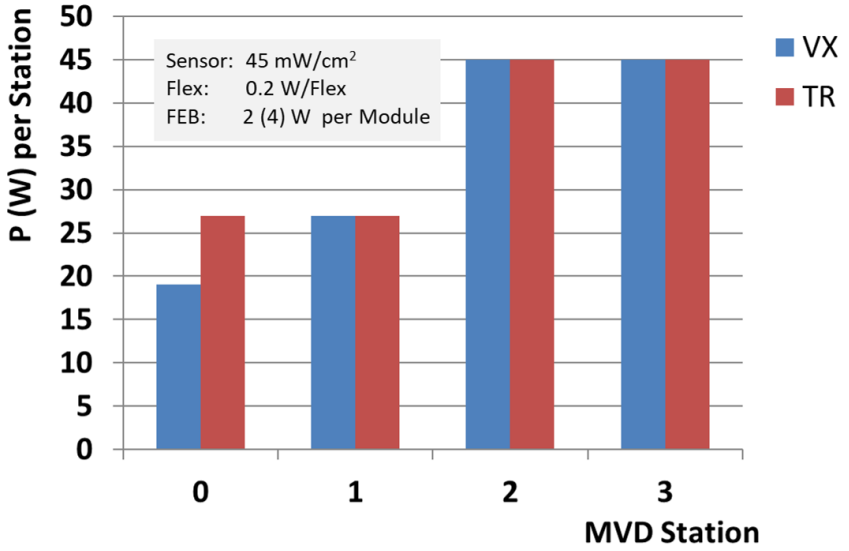

Figure 4.21: Estimated dissipated power of the MVD stations (VX and TR detector geometries), considering power dissipated by the sensors (MIMOSIS-1 specifications), FPC cables and FEBs (both estimated) inside he vacuum.

reduction in dissipated power. The law of heat conduction gives a linear relation between temperature differences and power, suggesting negligible temperature differences across the sensor, and maximum temperature differences between the hottest sensor and the contact area at the heat sink of about 6 K.

The total temperature difference between the hottest sensor and the cooling fluid can be estimated based on the numbers taken from Fig. 4.22 and applying the law of heat conduction to the different heat transfers in the module. To do so, realistic heat transfer numbers have to be derived, es detailed in [68], for heat contacts and the heat transfer to the cooling fluid. Here, we assumed, besides average dimensions for the cooling channels in the heat sink, already NOVEC-649 as high performance cooling fluid [58] with its physical parameters valid at -40°C. Fig. 4.23 shows the result on estimating temperature differences for the different detector station geometries. It is important to note that a safety factor of 2 was assumed regarding the sensor power dissipation (45 mW/cm^2 baseline), and that the warming up of the cooling fluid was limited to 1 K. The latter defines the individual flow of the coolant through the heat sinks as well as the heat transfer between the heat sinks bulk material and the coolant. The results, indicating maximum temperature differences between the hottest sensor and the cooling fluid of about 12 K, suggest a comfortable temperature operation regime of the cooling system with a total flow below 10 l/min.

Employing our test stand for thermal performance characterization we have gained insights from systematic measurements on the two dominating sources of temperature gradients, (i) the sensor carrier and (ii) the heat transfer between the heat sink bulk material and the coolant, corresponding to the red- and grey-shaded boxes in Fig. 4.23. The heat entry was simulated by dedicated heat foils.

The temperature differences on the **sensor carriers** with a lateral size of 80×80 mm^2 and a thickness of 380 (TPG) and 150 µm (pCVD diamond) have been studied. Fig. 4.24 compares for TPG measurements to simulations results from ThSim [69], a software which translates thermal

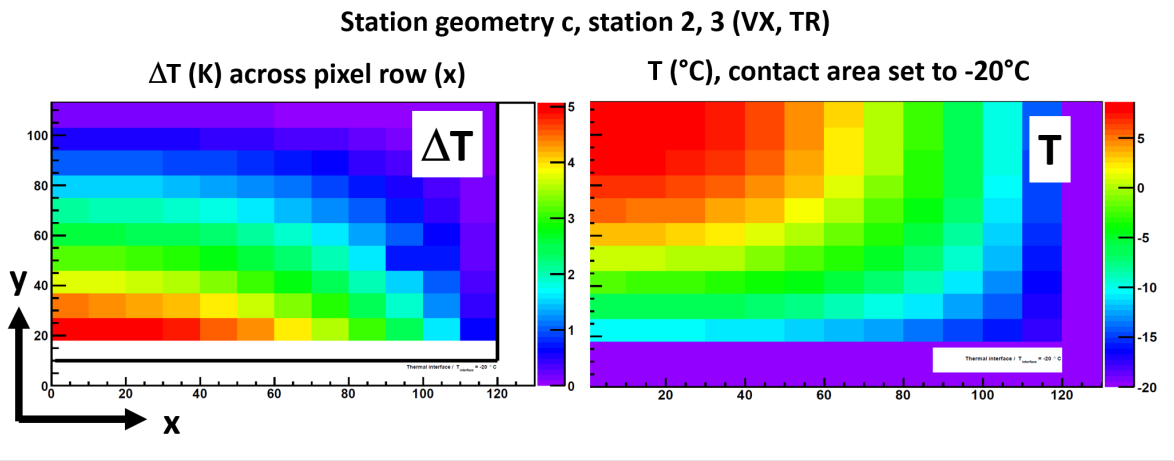

*Figure 4.22: Simulated temperature differences across station geometry "c". The beam is located at the upper left corner. Left: temperature difference (*K*) along x (along pixel rows), $\Delta x = 1$ cm. Right: Absolute temperature [°C], contact area to the heat sink set to $-20\,°C$, conservative sensor power dissipation of 350 mW/cm^2.*

to electrical properties to allow for (Lt)Spice evaluation. The match between measurement and simulation for both, pCVD diamond (not shown) and TPG is almost perfect. For TPG, a 2-dimensional material with outstanding heat conduction in lateral dimensions only, the worse heat conduction into the bulk does obviously not play a sizable role due to the thickness.
The **heat converters (sinks)** extract the heat of one station quadrant, respectively, and are made of Aluminum with customized buried heat channels. Fig. 4.25 depicts a performance plot based on the temperature difference between Aluminum bulk and the coolant, a measure of how efficient heat is extracted. The measurements are compared to calculations (formulas) based on assessing the convective and conductive heat transfer properties of the system (geometry and coolant specifications), detailed above. Both exhibit a linear dependence on the power. Deviations as a function of coolant flow indicate that the complicated cooling channel geometry cannot be easily described with linear equations. However, the deviations are below 1 K in the region of interest.

Both simulating the heat conduction on the thin sensor carriers as well as assessing the heat sink performance with dedicated formulas, which calculate the temperature difference between bulk (*i.e.* cooling pipe) and the coolant based on the known specification of the coolants, yield realistic results. The results gained so far suggest that the projected operation temperature range of the sensors below 0 °C can be guaranteed with the proposed MVD cooling concept. Moreover, operation studies with NOVEC-649 as coolant are in progress at temperatures above 0 °C and first preliminary results confirm the expected performance. Below 0 °C operation with NOVEC-649 requires a reconfiguration of the cooling system which is currently in preparation. Here, we take profit of similar activities based on NOVEC-649 mono-phase cooling within the CBM-STS sub-detector.

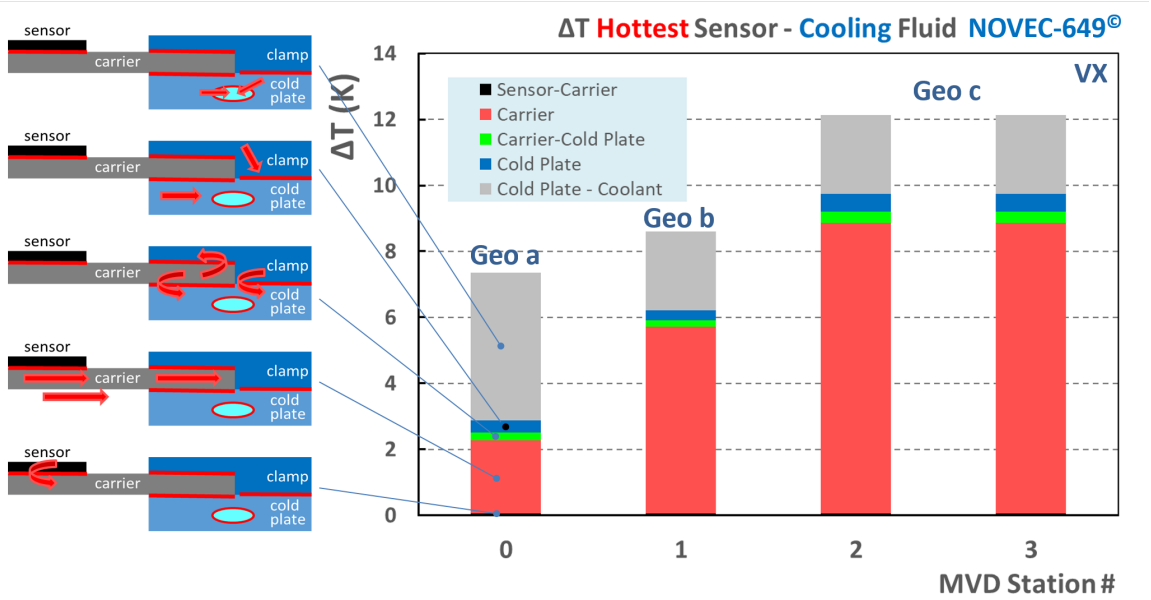

Figure 4.23: Estimated temperature differences between the hottest sensor and the cooling fluid NOVEC-649, see text. The heat path is composed of 5 different parts, as schematically indicated on the left side. Numbers are shown for the detector geometry VX, station geometries are indicated accordingly. Power dissipation of the sensor: 45 mW/cm^2.

4.3 Detector Integration

The MVD is a bench-top detector system which fits in a volume defined by 62 × 52(lateral) × 22.5(depth) cm^3, and a total weight of below 50 kg. The integration concept takes profit of this compact setup in many respects:

- Detector integration and commissioning takes place at a remote place (dedicated laboratories at the University Frankfurt), not at the FAIR/CBM site.
- The detector integration comprise mounting of the detector components, all cables for operating the MVD, all cooling pipes, and all modules housing the sensors. Note, that electrical signal cables and cooling pipes are connected to several feedthrough plates mounted on the front plate.
- Detector integration relies on the modular structure of the MVD and starts from integrating fully commissioned MVD modules (quadrants).
- Detector modules and stations are fully accessible during mounting and (first) commissioning, enabling step-by-step integration, testing and alignment, metrology.
- Having completed the detector integration, the setup (*i.e.* the master table attached to the front plate, which houses all feedthroughs) can be mounted into the target chamber (or a clone) for commissioning at below zero temperatures in vacuum.
- The final detector will be transported to the CBM site and integrated into CBM in front of the STS detector cool-box inside the magnet.

The unique advantage of this concept is, that all integration steps can be conducted in a single off-site laboratory, including detector commissioning under realistic environmental conditions. It is not yet decided, whether the final target chamber can be used for detector integration.

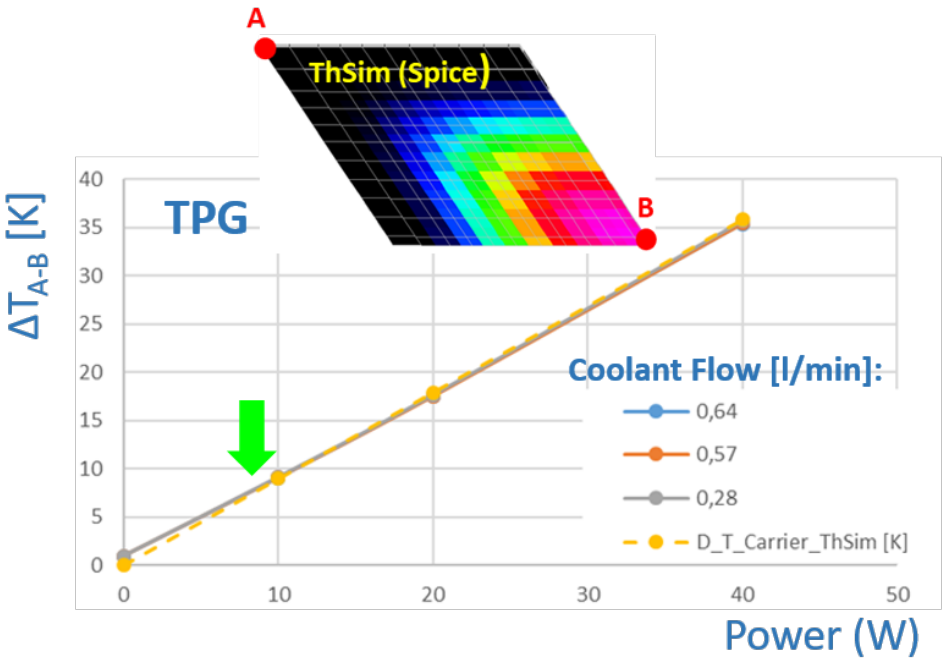

Figure 4.24: Temperature difference between the hottest and coldest point of a TPG carrier vs. the total power, produced by a dedicated heat sheet covering approximately the same area as occupied by the MVD sensors, aligned to the corner B. Point A was kept at −10 °C. The inlay exhibits the temperature distribution simulated by the ThSim package (based on Spice), the dashed line in the diagram indicates the simulation results, compared to measurement (symbols). Green arrow: MVD operation region.

off-site [17]. In both cases we consider it as important to have the master table, which supports the MVD inside the target chamber, firmly attached to the front plate to avoid disconnecting cables and pipes after commissioning when mounting and closing the target chamber both off or on-site CBM. A mechanical solution is currently being assessed.
Note, during the prototype phase prior to finalizing this document detector integration has not been exercised, due to the focus on developing the MVD modules as smallest self-contained unit. Hence, the final installation sequence has not been fine-tuned, yet, and is subject of ongoing optimization.

4.3.1 Mechanical and electrical integration

Detector integration starts from fully integrated and tested modules, *i.e.* sensors glued from both sides to a carrier, which is clamped to an actively cooled heat sink. The heat sink houses as well the first stage of FEE, which is connected to the sensors by dedicated flex cables bonded to the senors and mechanically reinforced. Since the integration concept relies on commissioning and approving the detector step-by-step in its final position next to the front plate, the front

[17] This is due to open technical questions regarding connecting the upstream beam pipe to the target chamber and vacuum window

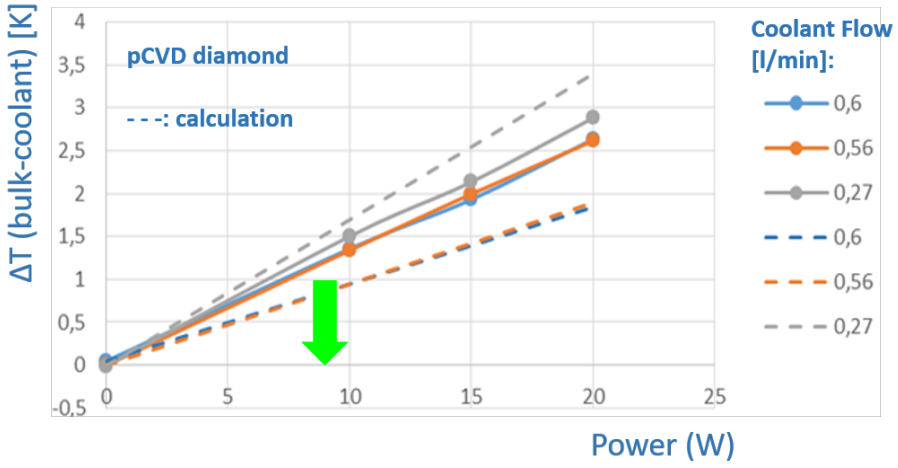

Figure 4.25: Measured (symbols) and calculated (dashed lines) temperature difference between heat converter bulk and coolant (Glycol:water = 1:1) for different flows, employing a pCVD diamond carrier. Temperature at point A (Fig.4.24) is −10 °C. Green arrow: MVD operation region.

plate with all feedthroughs, the master table, the remote positioning system for left and right half stations, and their individual base plates have to be prepared (and tested) prior to detector integration which progresses as follows:

- The station will be set up starting from station number 0, then 1 etc., since all cables and cooling pipes are guided (and reinforced) in layers towards the front plate containing all feedthroughs. The space restrictions in the target box do unfortunately not allow for a fully independent installation and access of the individual stations. However, we will try to minimize interference between stations, *e.g.* during service and repair.
- Left and right half-detectors will be setup (and commissioned) independently from each other, half station by half station, according to the following sequence:

  1. The C-frame containing both modules of a given half station is mounted on the half-detector's rail system, which is mounted on the common base plate.
  2. Both modules are fixed to each other by dedicated joints provided on the heat sinks.
  3. The modules linked to each other are inserted and fixed to the C-frame.
  4. Services (cooling, cables) are installed, *i.e.* the half-station is connected to the front plate feedthroughs. At this point it is important to reinforce cables and pipes accordingly. Hence the stations have to be at or close to their final position on the rails.
  5. The half station is set into operation and electrically tested (biasing, grounding, r/o tests) at room temperature.

- Eventually, half-station to half-station joints have to be established to enhance mechanical stability.
- The detector, mounted to the front plate, is ready to be moved in the (clone) target chamber to continue commissioning under vacuum conditions and at targeted operation

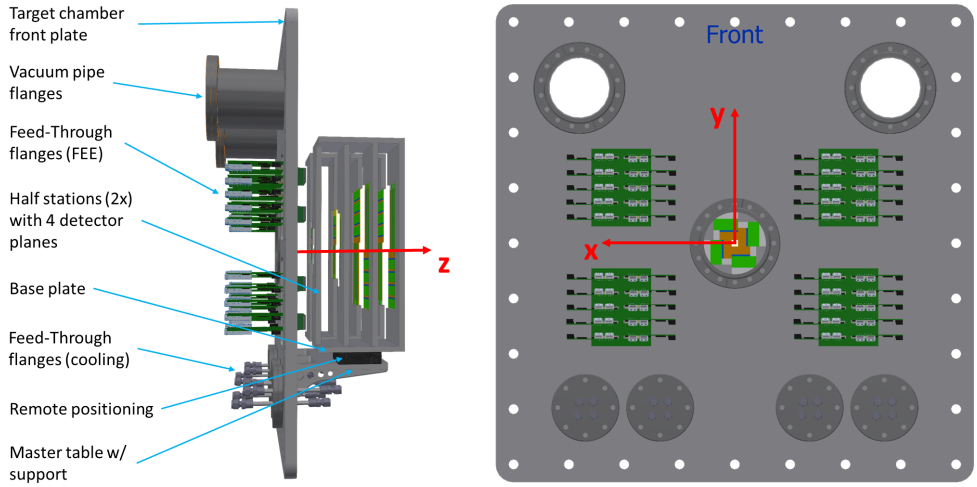

Figure 4.26: The MVD mounted inside the target chamber. Left: Side view of the MVD mounted on the target chamber front plate and of dedicated feedthroughs connecting the MVD through the front plate. Right: Front view of the target chamber front plate, indicating feedthroughs for electrical signals, cooling fluid and (optional) vacuum pumping.

temperatures.

4.3.1.1 Remote positioning

Remote positioning of the half stations is required to move the detector halves to a safe position during beam tuning to minimize radiation-caused damage on the detector. Hence, the detector halves move horizontally perpendicular to the beam by about 5 cm (targeted distance). The reproducibility of better than 50 µm can be easily realized by dedicated stops. The system has to work in a moderate vacuum and a magnetic field of up to 1 T. We estimate a total weight to be moved assuming a weight of 3 kg/station, piping (cooling) about 1 kg/station, plus 1 kg per half station base plate. This adds up to less than 10 kg per half station to be remotely positioned. Technical solutions are offered by industry (*e.g.* "PI"), but details have not yet been worked out.

4.3.1.2 Feedthroughs

A schematic and preliminary overview on the MVD position inside the target chamber box, with a focus on the required feedthroughs both for electrical signals and cooling fluid, is depicted in Fig. 4.26. The arrangement and final number of vacuum and fluid feedthroughs is subject of further planning, since the engineering of the target holder box has not yet been concluded. To assist this activity, a dedicated CBM Technical Note has been filed [70], defining those volumes to be exclusively reserved for housing the MVD and its infrastructure.

Cooling: As detailed in Sec. 4.5.2 the layout of the station cooling requests 5 feedthroughs for the cooling fluid, with 2 (in/out) cooling pipes each (diameter of 6 mm). These pipes should be thermally insulated from the flange itself. Hence, existing standard solutions for *e.g.* liquid nitrogen offered by many providers would be recommended.

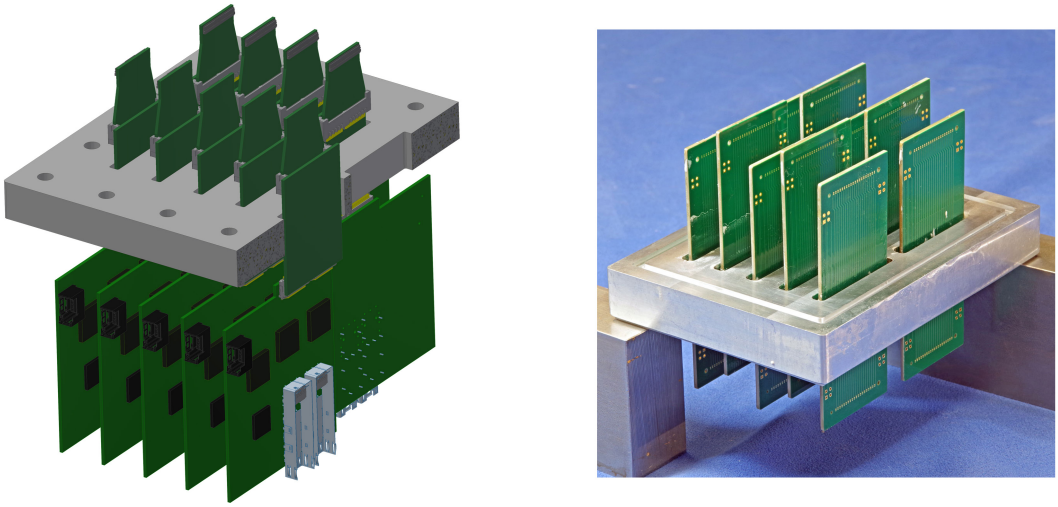

Figure 4.27: Left: Baseline PCB-feedthrough flange for electrical signals. Flexible flat cables from the MVD stations arrive from the top and are connected to a (passive) trapezoidal-shaped pitch-adapter board, housing a ZIF-connector to receive the flex cable and a block connector to plug into the PCB connector. The lower half, outside the vacuum, depicts the front-end boards (FEB), plugged from below, housing GBTx components and optical connectors. Note, in this version the FEBs are rotated by 90 degrees w.r.t. pitch-adapter boards and plugs to ease mounting. Right: Feedthrough prototype flange CNC machined in aluminium with 10 dummy PCBs assembled inside slits.

Electrical: As detailed in Sec. 4.4 the number of electrical signals[18] to be fed through the vacuum flange of the target box is about 5000 electrical connections. This does not allow to rely on industrial solutions, for both cost and signal-density reasons. During prototyping a concept based on feeding flexible flat cables through a vacuum flange has been successfully realized for PRESTO-1. However, for reasons of handling and accessibility during assembly and maintenance, this concept is not followed up. However, we are presently evaluating, assisted by CAD-based design and vacuum tests of custom flanges, a concept based on PCBs. This concept is not new, see eg. [71], but has to be adopted to the amount of electrical signals and space restrictions of the target chamber front plate. The baseline concept relies on two high-density block-connectors (*e.g.* 0.5 mm pitch, 120 lines) mounted on both sides of the target chamber front plate and connected by a (common) PCB. The PCB is glued into a slit milled in a blind flange. This flange houses 10 of these connector-to-connector PCBs, *i.e.* one of these flanges provides 1200 signal feedthroughs. Four of these flanges are envisaged for the MVD, and they are distributed across the target chamber front plate. Fig. 4.27 left depicts a detailed CAD view of such a flange housing 10 connector-to-connector PCBs.

A prototype of such a flange had been designed and a CNC machined flange was equipped with dummy PCBs, see Fig. 4.27 right. Vacuum tests will be addressed next to check tightness and out-gassing. We do not expect a principal problem, but want to reserve space-contingency

[18] The read-out concept calls for 900 data and clock links (differential plus Ground shields) between the GBTx ASICs (outside) and FEB boards (inside), in addition to lines for power (up to 30 DC/DC-FEAST converters in the vacuum), for detector control (via GBT-SCA) and dedicated sensors (*e.g.* temperature monitoring), remote positioning and grounding have to be provided.

for mounting the cables to optimize assembly and maintenance. Hence, the relative-orientation of the inner and outer block-connectors is not yet decided and will be placed by means of a mock-up. Another flavour of this concept is based on using the surfaces of PCBs glued to the flange for separating the vacuum. It offers a very attractive back-to-back mounting (and signal routing) of the block connectors. However, it eventually introduces a risk w.r.t. long-term mechanical stability due to the load introduced by the air pressure. A first pressure cycle test with a 4×4 cm^2 PCB (10 layers, 3.5 mm thick) glued in a dedicated flange did not reveal any indication of mechanical problems. However, employing 5×1 cm^2 PCBs would feature even high mechanical stability, which has to be demonstrated.

4.3.2 Procedures

4.3.2.1 Survey and alignment

The relative alignment of sensor to sensor, to carrier and to the heat sink within a given MVD module was discussed in Sec. 4.2 and will most probably rely on an optical 3D survey concept developed by the CBM STS team [62]. As a result, fiducial marks on the heat sink will allow for further aligning the module during detector integration. Due to the compactness of the system, measures of alignment are rather limited. The following options are (both) envisaged:

- **Half stations:** Once half stations are built, the alignment of the two modules relative to the C-frame supports, housing fiducial marks, can be assessed by photogrammetry [19] with an expected precision of better than 0.1 mm. The fiducial marks are supposed to be visible once the stations are in measurement position.
- **Half detectors:** Alignment of the C-frames relative to each other and to the half station base plate by means of photogrammetry, supplemented by measurement of distances along the beam axis by hand should allow for aligning the half detectors to reference points, *e.g.* positioned on the front plate, which houses both, the MVD setup and the CBM target.

In summary, for a telescope-like detector setup with co-planar stations, it is mandatory to provide redundant alignment parameter measurements along the beam (z- axis), since they are not provided with high precision by straight-track alignment, which works very reliable for lateral dimensions. Experiences from the CERN telescope-DUT alignment [63, 64], cf. Sc. 5.2.1, demonstrated, however, that our approach for detector (and sensor) alignment of a compact 4-station detector setup is sufficient in view of the envisaged spatial precision of hit and vertex reconstruction.

4.3.2.2 Quality assurance

Continuous quality assurance is mandatory during system integration, including documentation of component properties and system performance in a proper way. CBM uses a dedicated component data base complex [65], [72] for this purpose.
Starting from the commissioned and approved MVD modules, a fine-meshed QA sequence has to be applied, with a focus on (i) the electrical integrity of the sensors, and (ii) observing the mechanical tolerances. At present, the concept of QA during detector integration, like the one for module integration presented in Sec. 4.2.4.2, has still to be worked out, since prototyping

[19] We take profit of experiences made with the HADES detector, based on analyzing high-resolution photos taken from many perspectives with dedicated software tools (*e.g.* PhotoModeler).

was focusing on the integration of individual modules. As a guideline, each step of detector integration, like assembling half stations with modules, mounting them to form a half-detector, or mounting and connecting cables and pipes, has to be accompanied by standard functionality tests of the detector modules employed. These tests would for example comprise sensor control and readout tests, exemplary S-curve cycles on each sensor and assessing the grounding of the detector. It is important to note that in this stage of detector assembly tests in the vacuum at the final operation temperature and pressure are not planned, yet. To do so, a full-size CBM target box would have to be available at the detector integration site (Goethe-University), which is not in the budget. A dedicated gas-tight box attached to the original front flange with feedthroughs and flushed with (dry) nitrogen to exercise operation at low temperatures would be, however, advisable.

4.3.2.3 Maintenance and repair concept

The MVD is a highly modular detector. We will put emphasis on providing the possibility to access individual half station individually in the case of regular maintenance and repair on demand while minimizing the impact on other detector components. Hence, cabling and placing of cooling pipes have to be planned such that while removing one half station off the detector no residual forces act on the other (half) stations. To do so, detailed procedures have to be planned prior to detector installation by CAD simulations. In the case of a (urgent) repair the concept relies on the availability of a dedicated, fully tested and validated hot spare. The following steps accessing one half station are required:

- Measure the radiation level to plan the maintenance/repair, *e.g.* access times.
- Un-cabling r/o cards, LV and cooling pipes outside at the front plate.
- Pulling out the front plate, which houses the full MVD.
- Move the front plate with the MVD in a protective box (target chamber clone, made of *e.g.* plexiglass)
- Move half-stations to service (*i.e.* beam tuning) position.
- Move the protected MVD to a remote lab (clean environment) on-site, re-connect services and cables to control the sensor's temperature and to allow for and monitor sensor operation.
- Remove half-station joints and increase the clearance between the station to be serviced to the others by moving half-stations on the rails accordingly.
- Remove services and cables of the half station under service.
- Dismount the half-station and place it on a separate table (with rails/holding structures).
- Separate both modules belonging to this half station.

Having *e.g.* exchanged the module by a hot spare, the integration proceeds as defined before, comprising means of metrology and QA as well.

4.4 Detector Readout

4.4.1 On-detector electronics

Due to the restricted space available close to the detector, the FEE electronics are divided in two parts: A front-end board, mounted directly next to the detector modules inside the vacuum and a data aggregation board mounted right outside the vacuum vessel. This setup is indicated in Fig. 4.28.

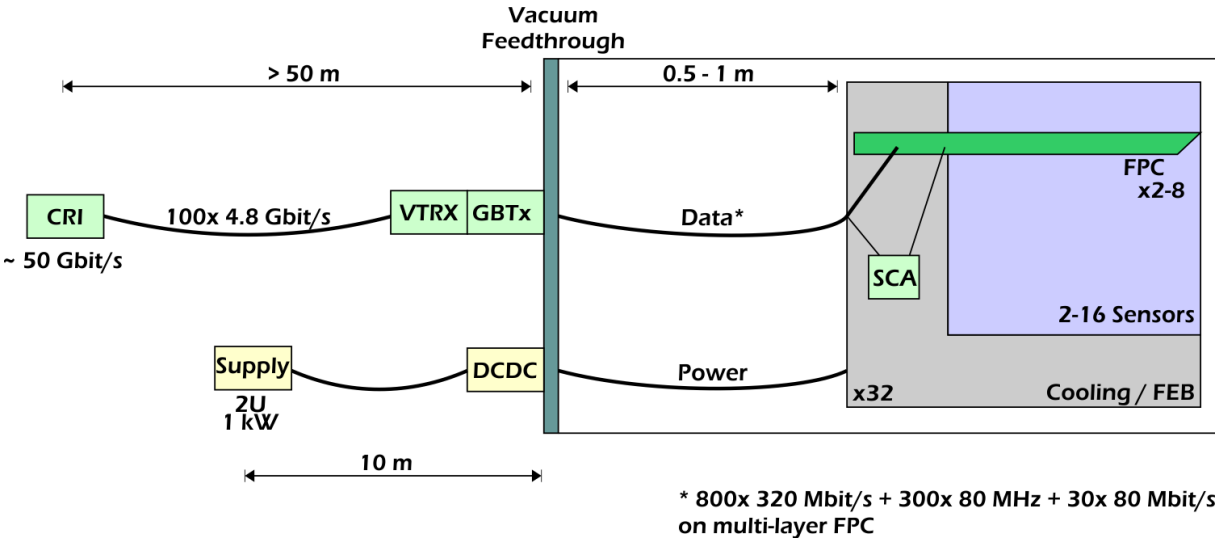

Figure 4.28: The MVD readout scheme. Right: Schematic setup inside the (vacuum-) target box. Shown is one module, with the active area assembled with sensors (blue area), flex cables (dark green) connecting sensors with passive boards mounted on the individual heat sinks (gray). Left: Boards and cabling mounted outside the target box, mounted directly on the target box flange (VTRX, GBTx, DCDC).

The front-end boards can contain a minimal set of features only due to space constraints and the environment including radiation, magnetic field and vacuum operation. Apart from connectors for the flex cables from sensors and towards the vacuum feedthrough we plan to have only passive filtering components in this location close to the sensors. GBT-SCA ASICs will provide the necessary interface for control and monitoring, *e.g.* configuration of sensors via I2C, generation of clock and synchronization signals and voltage monitoring.

The front-end boards are mounted on the moving part of each of the up to four sensor stations. Hence, connection to the vacuum feedthrough needs to be flexible to allow for lateral movement. FPC cables, preferably in a multi-layer, shielded design provide all necessary properties for a reliable data transport: Flexibility, density of signal routing and proper impedance. Further details on powering are discussed in Sec. 4.5.

4.4.2 Data transport

The MIMOSIS sensor is equipped with 320 MBit/s data links. This link design was chosen for its compatibility with existing GBTx hardware available from CERN and employed in many sub-systems of CBM. The total data rate per sensor exceeds this link bandwidth, so that each sensor is equipped with 8 data link outputs. Depending on the position in the detector and the anticipated data rates, the number of active data links can be configured between 1 and 8 links.

The total number of data links will be about 900. The exact number of links will be varying depending on the detector setup and planned event rates as detailed in a CBM note on data rates [73].

These differential data links need to be converted to optical links for transport towards the computer interfaces, located in the server room in approximately 100 m distance to the detector. This conversion is provided by data aggregation boards, equipped with GBTx ASICs and radiation hard optical transceivers (VTRX, VTTX) from CERN. The electronics will be

mounted as close to the detector as possible, which is the front-plate of the vacuum vessel.

The whole read-out chain, starting from the data aggregation boards near the detector follows the same scheme that is also used in other CBM sub-systems, like STS, cf. Ref [74]. That implies that no dedicated hardware is necessary in the data acquisition from the CRI [75] level onward. The amount of detector-specific firmware and software is likewise reduced to the absolute minimum, namely dedicated data handling and sorting routines as well as sensor control schemes.

4.4.3 Sensor controls

The sensors are designed to require a minimal amount of control. They are configured using an I2C interface, that can be controlled conveniently by GBT-SCA ASICs on the front-end boards. These chips can also provide a range of monitoring features such as voltage and current measurements and, if necessary, digital outputs to switch power to individual sensors.

The use of GBTx for data transport allows to include all control signals within the optical data links. On the data conversion boards signals are forwarded on digital links running at 80 MBit/s before the GBT-SCA provides all necessary individual control and monitoring interfaces.

The control routines will be implemented in the foreseen place inside the CRI architecture.

The operation of sensors depends on a stable power supply. On the other hand, power supplies need to be located at distance to the detector and the front-end boards don't allow for placement of active voltage regulators. These can be located only close to the vacuum feedthrough.

4.5 Services

The MVD requires services for powering and cooling. All hardware for services will be fully remote controlled and compatible to the CBM detector control standards based on EPICS tools and applications. The different services are presented in the following sections followed by a section on general aspects of detector controls.

4.5.1 Power

The MIMOSIS-0 sensors will require a bias of 1.8 V, which may potentially have to be complemented with a $\sim$ 10 V "high voltge" in case fully depleted AC-pixels are chosen. The predicted power consumption per sensor is 230 mW (corresponding to 45 mW/cm^2 active surface) at maximum load [44]. Thereof 200 mW are related to the digital data processing. This power is reduced by up to 50 mW if the sensor runs idle. A safety margin of a factor of two is added to the nominal consumption in the layout of the system. The analog and digital circuits of the sensor will be biased separately but the ground cannot be fully separated in CMOS devices.

As the power is routed through lightweight micro-cables, ohmic losses in those cables have to be considered. Those losses will vary depending on the data load and therefore ultimately on the occupancy. Occupancy fluctuations will turn into fluctuations of the digital bias and the mass potential of the sensor. This effect is alleviated by the fact that spikes in data load effectively propagate times through the different buffer stages of the chip for a period equivalent to several frames read out. Load dependent mass potential fluctuations were observed to affect the discrimination threshold in the MVD-prototype. However, the large S/N values of the MIMOSA-26 sensors left sufficient margin to compensate for this effect without dedicated optimization. It is expected that the by factors lower power consumption of MIMOSIS, as well

as complementary design measures (e.g. internal reference voltage generation) will reduce this effect further.

The total power dissipated by the MVD inside the target box amounts roughly to 150 W (assuming the TR geometry and a factor of two safety margin). This power will be supplied by a commercial low-voltage (LV) power supply and passed via one or few high-power 12 V lines into the target box. FEAST DC-DC converters [76] will transform the power to 1.8 V and regulate this voltage. The FEASTs will be mounted on a dedicated liquid-cooled shelf inside the vacuum (baseline), which is not part of the station setup. They can be controlled (on/off) by means of GBT-SCA ASICs mounted on the front-end boards.

A placement of the FEAST converters outside the target box is, however, not yet excluded, which would require routing the LV lines via the vacuum feedthroughs to the detector stations. A total of ~ 30 FEASTs will be required to handle the nominal LV currents but a higher number may be used in order to increase the granularity of the LV system and such the error tolerance of the MVD. The power will be routed via conventional cables from the FEAST converters to distribution boards located on top of the heat sinks. From this point on, it will be distributed via light, single layer flex print cables.

Employing linear voltage regulators (LDO) instead of FEAST DCDC converters and mounting them directly on the front-end boards sounds attractive, at least due to the synergy with STS as well as noise optimization. However, the LDO chips under debate are presently in conflict with space restrictions in the MVD detector. Once this conflict can be avoided, we might change the baseline concept with FEAST in favour of LDO.

The MVD has to be protected against single event latch-ups (SEL) triggered by radiation. Already early in the R&D phase the SEL protection of a MIMOSA pixel sensor has been successfully explored with a latch-up protection board, *cf.* a talk on board development in [77]. Recently, March 2021, a latch-up test with MIMOSIS-1 has been conducted at mCBM as part of the MIMOSIS-1 characterization. The sensor had been protected by a low voltage scheme, which detected the over-currents created by a SEL and initiated an automatic power cut, which was followed by a manual restart. The sensor was operated in the direct 1 *A*GeV Pb-beam of mCBM for 30 min at 10^7 ions per 13 s long spill and several minutes at 10^8 ions per spill. Multiple SEL were observed and recovered. After the mentioned exposure and likely due to the sizeable total ionizing dose, the sensor started to show an unstable behaviour but kept responding to slow control. After 1 week of room temperature annealing, the sensor was found recovered and successful calibrations of the internal DACs were carried out. While a detailed analysis is still in progress, the experiment demonstrates the robustness of the chosen SEL protection concept.

A corresponding initiative on SEL protection development is planned, using GBT-SCA together with dedicated electronics for SEL detection, once the front-end board development has started.

4.5.2 Cooling

Studies suggest a temperature window for the MIMOSIS operation between -20 and $0\,^{\circ}\mathrm{C}$, constrained by requiring a proper signal-to-noise ratio of the pixel signals, which is affected by radiation and leakage currents, motivated by sensor R&D, cf. Sec. 4.1.5.6. Since (i) the MVD is being operated in vacuum and (ii) the material budget in the geometrical acceptance has to be minimized, the current concept employs active cooling of the heat sinks positioned outside of the acceptance, preferably with mono-phase cooling. During the R&D phase, for simplicity and cost reasons, Glycol-based cooling fluids are used. However, the radiation-hard cooling fluid

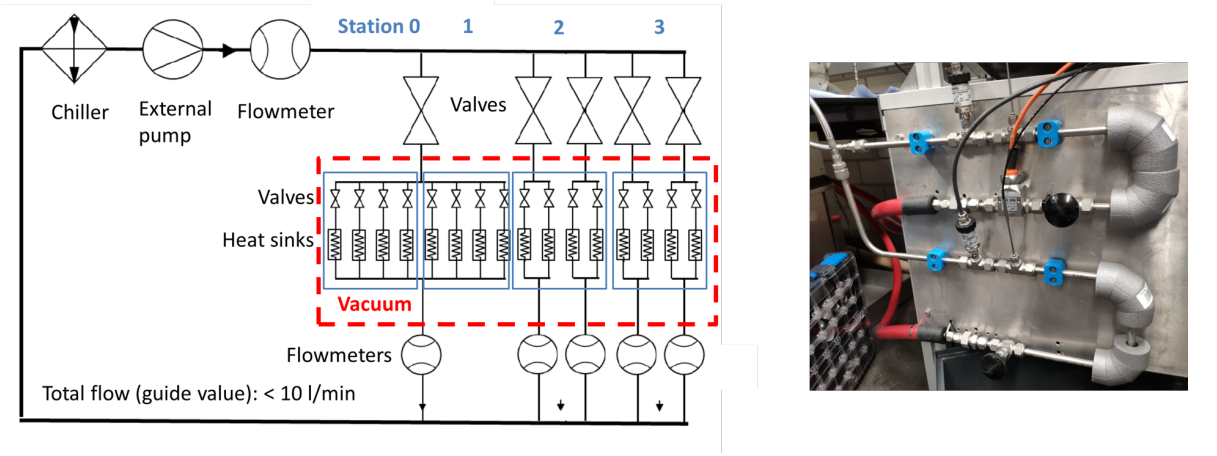

Figure 4.29: Left: The MVD cooling piping plan, supplying stations MVD 0...3, both VX and TR detector geometry. Right: Cooling piping exercised for a thermal evaluation of heat sinks, with measuring devices for flow and fluid temperature, accessible by our EPICS-based detector control system.

NOVEC-649 [20], considered also for the STS detector of CBM, represents a promising candidate for the MVD as well. It features lower (dynamical) viscosity in the interesting temperature range between -20 and −40 °C compared to Glycol-based mixtures. The proposed cooling concept critically depends on an efficient heat conduction between the sensors, which represent the main source of dissipated heat, and the heat sink. Other sources of heat inside the vacuum are traces of the flex cables attached to the sensors and the first stage of FEE mounted directly to the heat sinks. The placement of the DC-DC converters inside the vacuum requires separate cooling, which, however, is easily possible. As introduced in Sec. 4.2.5.2, the heat introduced by the VX detector geometry adds up to a grand total of 135 W for its 264 sensors. The TR detector geometry with 288 sensors yields 143 W grand total. The very different dissipated power per MVD station translates in a cooling piping plan suggested in Fig. 4.29, left side.

The temperature window for sensor operation between −20 and 0°C represents the driving baseline specification for designing the cooling system. In addition, we require a moderate temperature increase of the cooling fluid passing a MVD module of 1 K. As a consequence, cf. Sec.4.2.5.2, moderate flows between 5 and 10 l/min are required to evacuate the heat transferred to the heat exchangers. A safety margin of a factor of two is considered in the layout of the cooling system, for details see [68]. This conceptual layout represents a compromise between minimizing the number of vacuum feed throughs and flexibility in balancing the cooling power by placing manifolds, both in- and outside the target chamber housing the MVD. The layout of the cooling system and the control of the parameters have been evaluated using a demonstrator. It allowed for a careful evaluation of the dimensions of the heat sinks in vacuum as indicated in the right picture of Fig. 4.29. It also helped to identify the proper measuring devices for fluid temperature, flow and pressure, compatible to our detector control system. The same hardware has been evaluated also in our 24/7 campaign, running the prototype PRESTO-1 in vacuum over several months.

[20] NOVEC fluids manufactured by 3M are considered to replace C6F14 in cooling applications and have been positively evaluated for CERN LHCb w.r.t. radiation hardness, P. Gorbounov et al.

Cooling plant: According to [68] (employing simulations in [45] adopted to the actual MIMOSIS-1 power dissipation of 45 mW/cm^2) and NOVEC-649 as cooling fluid) the maximum temperature drop between the hottest sensor and the cooling fluid has been found to amount to less than 15 K. The heat conduction in the carrier and the heat sink–fluid interface are driving this number, cf. Fig. 4.23. For an operation temperature of the hottest sensor of 0 °C, the temperature of the cooling fluid in the heat sink has to be tuned to -15 °C. Industrial solutions (*e.g.* HUBER [78] chiller CC 405, better CC 905, both are being used with our prototypes) are available. The HUBER's CC 905 chiller (total flow of around 20 l/min) is specified to offer 1 kW cooling power at −60 °C. However, a Glycol-based cooling fluid (50% Glycol, 50% water) used during the last years of prototyping becomes quite viscous below −20 °C. This is why the installation of an external pump for an additional pressure step is being considered. Consequently, and as mentioned above, systematic studies are being conducted exploring NOVEC-649 as effective heat transfer fluid to replace Glycol-based mixtures as baseline cooling fluid. Calling for 1 K temperature increase of the coolant inside a MVD module, as stated above, and with NOVEC-649 as coolant, the heat transfer between the heat sink and the coolant increases by about a factor of two with only about 30 % increased flow. However, employing NOVEC-649 calls for a closed cooling circuit since the medium is highly hydrophilic and any contamination with water has to be avoided. In 2020, our vacuum test stand was instrumented with a JULABO [79] PRESTO A40 chiller. During TDR submission, routine operation of a MVD module in vacuum at below-0^{0}C temperatures with NOVEC-649 has been started to further evaluate our cooling concept.

In summary, with the current layout of the MVD cooling system employing cutting-edge technologies is not needed owing to the expected moderate heat dissipation inside the target chamber. We will further take profit of parallel developments for the CBM-STS detector system and aim at sharing a common concept and primary chiller.

4.5.3 Controls

The MVD will be operated via EPICS [80], a highly regarded control software framework used and maintained by accelerator and physics research groups worldwide. EPICS is available as free software and has a proven track record regarding reliability & back end performance for ten thousands of control parameters. It is selected by the CBM experiment for its controls and it is also the control system of choice for other current or future experiments at the host lab GSI/FAIR, such as HADES or PANDA. To take profit of the synergies with those other experiments on site and to integrate properly into the CBM controls framework, EPICS is the natural choice for the MVD.

Note, the activities presented in the following describe our developments for the MVD prototype PRESTO-1, *i.e.* employing the state-of-the-art EPICS packages for detector control. The controls of the final MVD system, adopted to the then available developments of EPICS will certainly profit from the results achieved.

4.5.3.1 Objectives of the Control System

Operating complex and delicate scientific instruments requires experienced detector physicists. The task of the control system is to make their life easier by providing the necessary control over the components, by showing the current and past system state, and by constraining the parameter space in a zone of safe operation. By asserting to run the detector at a proper operating point, systematic errors in the measurement will be reduced resulting in a constantly

high quality of the recorded data during the data taking. Once safe and sound operational sequences for the detector are established, simplified control user interfaces will be in place to enable operators with limited training to run the experiment during experiments. From the perspective of those "end-users" of the system, the control system should allow to:

- switch on/off devices necessary to run the detector,
- transition between different detector states (eg. "off", "idle", "standby", "running"),
- modify operational parameters such as pixel thresholds, and to
- monitor vital detector parameters.

Desirably, this should be done in a way that:

- warns operators before setting unusual values,
- brings to the operators' attention when a problematic state occurs,
- allows to quickly understand the severity of any problem,
- guides towards possible sources of failure and provides contact information when an issue needs to be escalated,
- notifies the operator of any actions automatically taken and decisions autonomously made by the system,
- highlights the root cause of a problems (if identified) while also indicating any resulting problems,

When considering those (non conclusive) lists of *what* the control system should allow to do and *how* it should fulfil its role, the **how** appears to be at least of similar importance in order for the operator to safely and effectively control the experiment.

4.5.3.2 Experience from prototyping with PRESTO

A lot of experience was gained by running the PRESTO (2nd prototype introduced in detail in sec. 5.2.2) continuously for multiple years in the IKF laboratory under realistic conditions with cooling and vacuum operation (pressure cycles). Most component categories required for the final detector in the CBM cave were already present when running the prototype. Those categories comprise cooling, low voltage, vacuum, as well as higher-level control entities such as system state logging (i.e. "archiver" component in EPICS terminology) or detector-level alarms. Several hardware components such as a 4-channel 16-bit ADC board and an 8-channel Pt100 temperature sensor board were developed in-house specifically to operate the prototype and are fully integrated into the EPICS system.

Fig. 4.30 shows an illustration of the system used to run PRESTO for the development of the EPICS control system. The prototype is operated inside a voluminous vacuum chamber pumped by a dual-stage scheme with a turbomolecular pump (Leybold) backed by a rotary vane roughing pump and monitored by vacuum gauges (MKS DualTrans 910). Furthermore, the system comprises a cooling system with heat bath (Huber CC-405), flow sensors (Kobold DPM), pressure sensors (Swagelok PTI-S-AC3-22AS), a high-quality LV power supply (R&S HMP4030), an FPGA board for data taking (TRB3), front-end electronics for a total of 8 sensors, temperature monitoring in the vacuum and outside, a single-board computer (Raspberry Pi 3) with battery-backed power supply, a VLAN-capable managed switch (D-Link DGS-1610-20), servers for data taking and control value archiving, environmental monitoring of the lab conditions (Lufft Opus-20) and more.

After implementing the EPICS support for the individual device to be controlled and

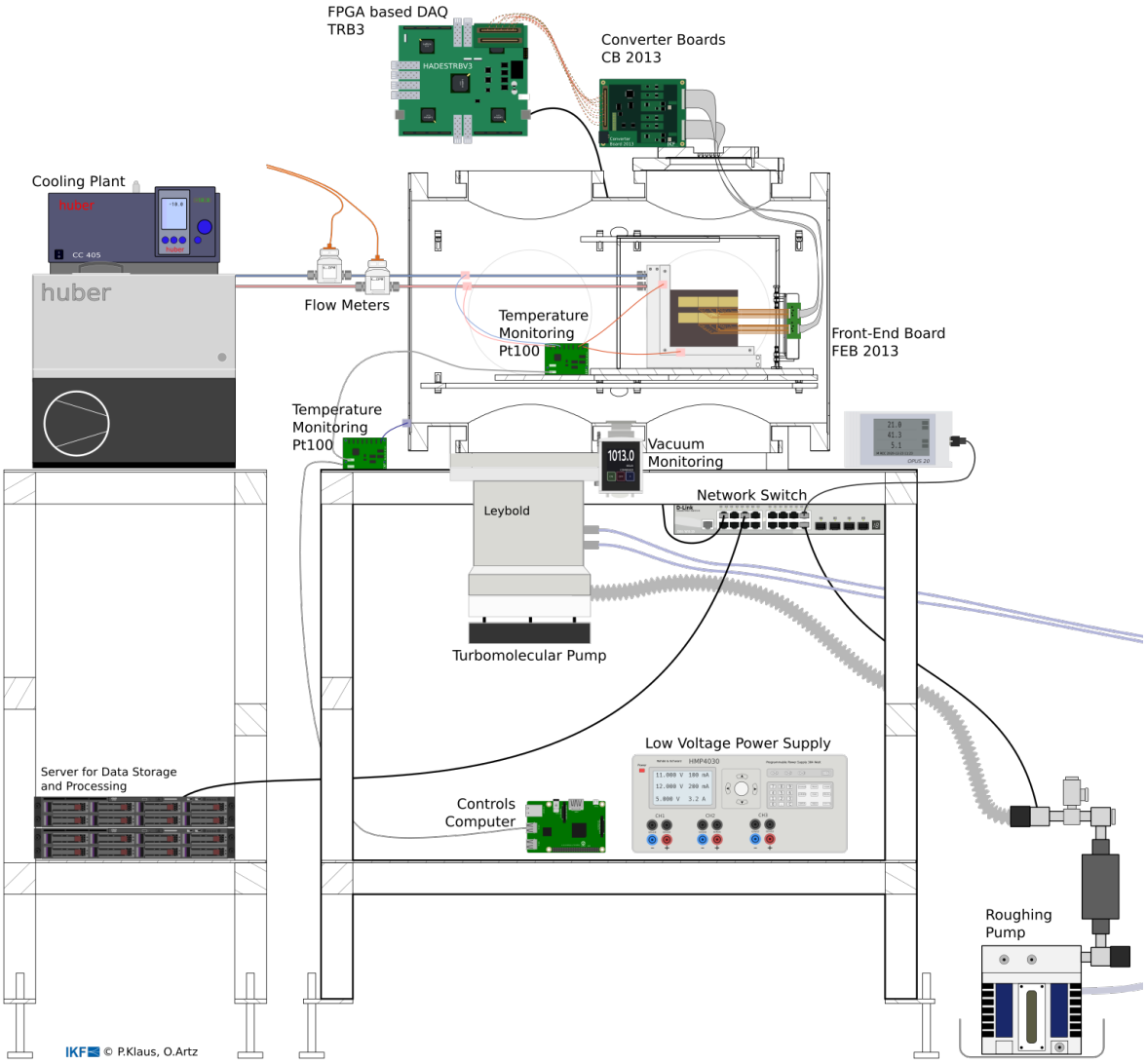

Figure 4.30: Illustration of the device topology for the operation of the prototype "PRESTO". Taken from [81].

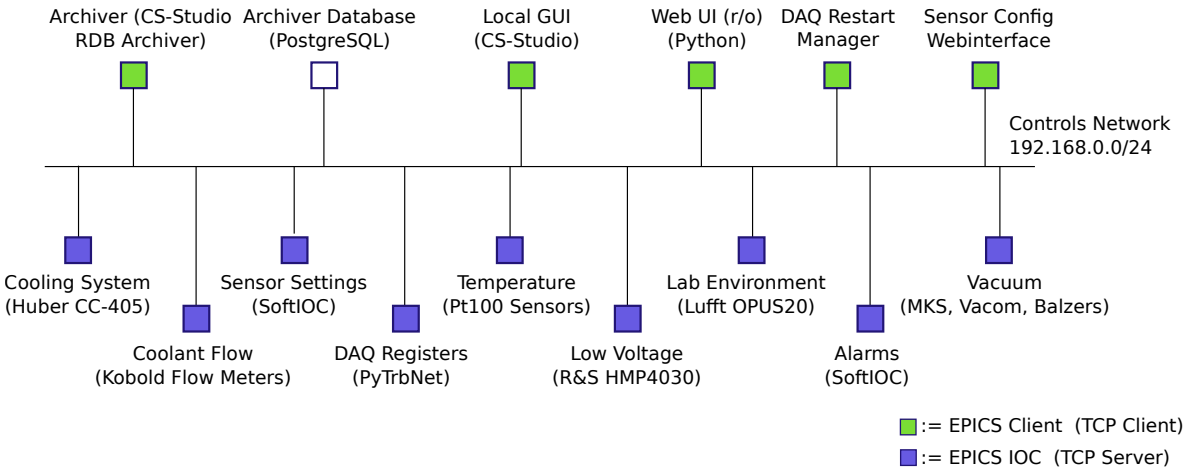

Figure 4.31: Client and server view of the EPICS control system implementation for PRESTO. Taken from [81].

monitored, all relevant process variables were added to the archiver (CS-Studio RDB Archiver w/ PostgreSQL database), keeping track of their evolution over time. With all vital parameters available for monitoring and control within EPICS, automated actions were set-up to react to malfunctions such as DAQ lockups, over-temperature conditions, risk of condensation and similar. A graphical user interface was created to control the entire detector (using CS-Studio 4.5).

PRESTO was operated over a long period of time with the described control system in place. During that time, cooling and pressure cycles took place, the prototype was operated with and without a radioactive source in vacuum with the read-out enabled most of the time. In addition to the shifter and expert GUIs, a tool to create graphs from the archived data was created. Fig. 5.10 shows an example of such a plot.

An EPICS system consists of client and server applications typically operating on a single network (i.e. broadcast domain). An illustration of the clients and servers implemented for the controls network for PRESTO is provided in fig. 4.31.

In summary, the lessons taken away from operating PRESTO 24/7 in the laboratory for the MVD project are dealing, so far, with the stand-alone operation of the MVD. It takes into account aspects of integrating and controlling different hardware and guaranteeing safe (remote) operation. Hence, the selection of tools employed has been driven by MVD constraints only. However, the choice of EPICS as control software framework to provide full compatibility and well defined interfaces to the CBM controls was a central guide line. As example, the anticipated sharing of the cooling system with STS, including *e.g.* all aspects of safe operation and alarm handling, will certainly challenge and drive the further developments on controls while integrating MVD in CBM, eventually being demonstrated during the future participation of MVD at mCBM.

4.5.3.3 Control System for the MVD in CBM

In the light of the upcoming control system for the full CBM detector, additional aspects are important. An example of this is how it fits into the context of the whole experiment, where the MVD controls network needs to become part of the overall control system. Fig. 4.32 shows how the MVD controls network could be connected to the CBM control system, with a consolidated

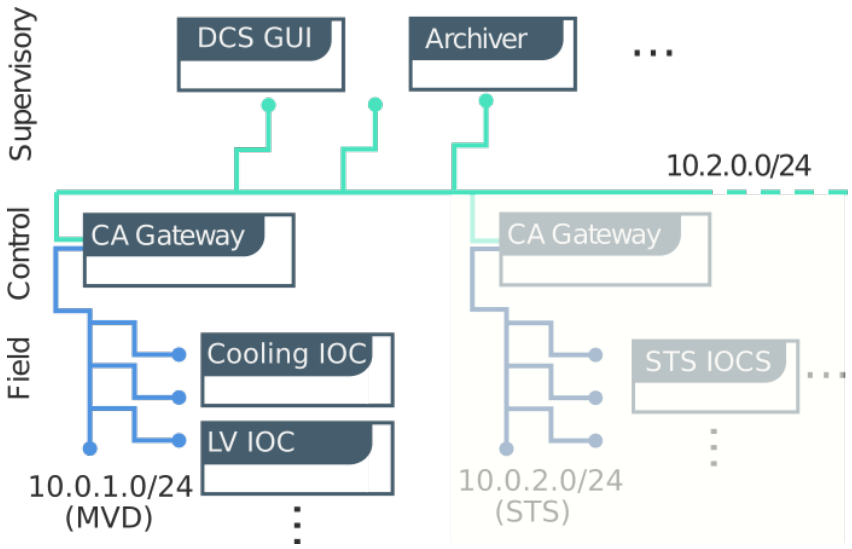

Figure 4.32: Anticipated network topology of the EPICS-based control system for CBM, where the MVD has its own subnet on the field layer.

supervisory layer on the experiment level and Channel Access gateways establishing the links between the supervisory and the field networks.

Additional aspects are how to

- keep up with the upstream EPICS development,
- ease deployment,
- strengthen the system performance,
- implement the system on a more scalable architecture.

The shift from the classic CS-Studio [82] to the renewed "phoebus" CS-Studio is an example of upstream developments to keep up with. Packaging the individual controls components in application containers (*e.g.* Docker) is a powerful trend and was in parts already used for PRESTO. It will certainly be elaborated in the next years. Furthermore, the use of higher performance archivers such as the EPICS Archiver Appliance or the Cassandra PV Archiver seems desirable as the number of process variables are going to increase with a full-size detector. Potentially, deploying the EPICS software components in a Kubernetes cluster can be investigated as a further option for a scalable architecture. More aspects concerning these topics are described in an upcoming thesis [81].

5 Prototyping and System Performance

5.1 Prototyping pixel sensors

Sensor prototyping is extensively being conducted at IPHC Strasbourg. There, long-standing developments focus on applying the CMOS monolithic pixel technology to challenges required by tracking detectors used in high energy physics applications, like e.g. providing thin, large-area and radiation-hard sensors featuring small pixel pitch. Meanwhile, read-out speed became another important challenge. The MIMOSIS sensor, developed for the CBM-MVD, represents the present culmination point in this line of development, which already has produced prominent sensors to the community, such as MIMOSA-26 (*e.g.* EUDET-type beam telescopes [83]) and ULTIMATE-2 (Star HFT-upgrade, the first MAPS used in a heavy ion experiment [84, 85]). Further details on CBM-MVD related sensor development and prototyping can be found in Sec. 4.1.

5.2 Prototyping MVD sensor modules

To date, prototyping of MVD modules relied on integrating MIMOSA-26 sensors on different carrier types, comprising the two materials considered for efficiently evacuating heat out of the active volume, as discussed in Sec. 4.2. Both materials, CVD diamond and TPG, provide sufficient conduction cooling, low material budget and sufficient mechanical support for the MVD sensors. To prove that the MVD stations based on these materials meet the experiment requirements, a prototyping campaign was started, aiming at creating a fully working CBM-MVD quadrant of Station 0 (based on a CVD diamond) and of Station 2 (based on TPG). Two projects have been accomplished:

- **Prototype 1** [64] aimed at solving all integration challenges related to the production of a fully operational, double-sided module based on CVD diamond carriers holding a layer of 50 µm thin MAPS on each side. This module was intended as representative precursor for a quarter of the particularly challenging first MVD station. Realizing the CBM-MVD prototype included the development of handling procedures for the ultra-thin sensors and carriers, the design of readout cables with the focus on low material budget as well as the construction of a scalable and reliable data acquisition system.
- **Prototype 2** (called also PRESTO = PREcursor of the Second sTatiOn of the CBM-MVD). It was to establish an assembly procedure, which guarantees vacuum compatible integration of the sensors on both sides of the carrier with a placing precision of better than 100 µm. Moreover, we study the feasibility of operating the sensors with an ultra light FPC based on industrial technologies. Note, PRESTO refers to a series of TPG-based prototypes, only the first one, PRESTO-1 (integrating MIMOSA-26 sensors) is discussed here. PRESTO-3 will for the first time integrate full-size MIMOSIS-1 sensors applying our latest techniques to build a MVD module, with the option to study an optional way of double-sided sensor integration. PRESTO (-1) comprises 15 thinned probe-tested MIMOSA-26 sensors [86, 87], which were developed at the IPHC-Strasbourg. Nine of them

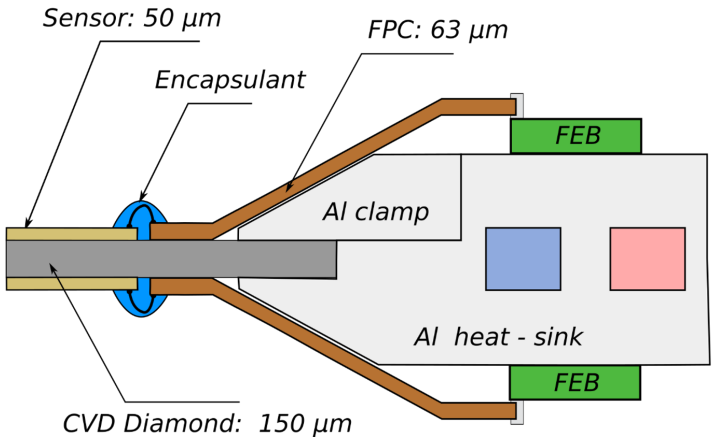

Figure 5.1: Simplified cross-section of the prototype of the CBM-MVD. In the final MVD, the sensors will be staggered to cover the insensitive area of one sensor with the sensitive area of the opposite sensor. Y-axis not to scale, thicknesses indicated.

are glued on the front, and six on the back side of PRESTO. The sensors are wire bonded to a total of 10 FPCs, which provide the necessary bias lines and data links. PRESTO has the size of a quadrant of the MVD station #1. However, since MIMOSA-26 has a size of $21.5 \times 13.8\,\mathrm{mm}^2$ while the final sensor (MIMOSIS) will presumably have a size of about $30 \times 13\,\mathrm{mm}^2$, its complexity is equivalent to the one of station #2, see [45]. The sensors and FPCs of PRESTO were integrated on a 380 µm thin carrier of the highly heat conductive Thermal Pyrolytic Graphite TPG [51].

It is worth noting that many procedures and techniques, developed during prototyping of MVD modules, have been successfully applied to the NA61 [88] Small Acceptance Vertex Detector [89, 90], as described below in the appendix.

5.2.1 The prototype 1 - CVD Diamond-based prototype

The sketch of the module realized within this project is shown in Fig.5.1. The prototype was based on the MAPS version MIMOSA-26 AHR, which was developed by the PICSEL group of IPHC Strasbourg [86]. MIMOSA-26 AHR features a radiation tolerance of > 500 krad and 10^{13} $\mathrm{n_{eq}/cm^2}$, a column-parallel readout architecture with binary charge encoded data output and a frame rate of about 10 kHz. The internal control registers defining the operation mode of the sensor, e.g., threshold voltages, are programmed by means of a JTAG interface. The data are sent via two digital output lines at the rate of 80 Mbps each. The power consumption of MIMOSA-26 AHR is about 750 mW per sensor. Despite it does not yet fully meet the requirements of the final MVD with respect to the radiation tolerance and readout time, MIMOSA-26 AHR provided the opportunity to test key aspects of the sensor integration. Due to its size of 21.5×13.8 mm^2 and its thickness of 50 µm, the device is perfectly suited for integration studies including questions of handling and bonding of such ultra-thin sensors.

5.2.1.1 Sensor integration

During the prototyping phase, the integration of 50 µm thick sensors on 200 µm thin diamond supports was investigated. The thickness of the CVD diamond was chosen as a compromise

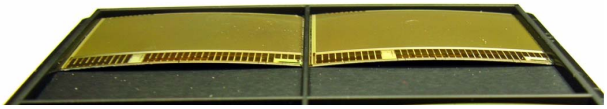

Figure 5.2: Two thinned MIMOSA-26 AHR sensors (21.5×13.8 mm^2 each). The 50 µm thin sensors bend due to inner stress. The bending radius is 20-30 cm.

Figure 5.3: Assembled "core module" comprising the two thinned MAPS wire-bonded (with encapsulation) to a standard FPC, glued on a CVD diamond carrier.

accounting for the need to minimize both, the temperature gradient along the sensor[1] and the the material budget.

The positioning and handling of the sensors was complicated due to their mechanical properties: After thinning, the devices were flexible and bent due to inner tensions (see Fig. 5.2). Therefore, custom made positioning devices and vacuum holders were fabricated to integrate the sensor onto both sides of the CVD diamond plate. Two sensors and one FPC per side were glued onto both sides of the CVD diamond plate[2]. The sensors were wire-bonded to the flex print cable and the bonds were protected against mechanical damage by encapsulating them with the silicon-based elastometer Sylgard 186 from "Dow Corning". The so-called "core module" obtained is shown in Fig. 5.3.

The full prototype module was formed by adding another set of sensors and FPCs to the backside of the carrier. The ambitious material budget for the prototype module - 0.3% X_0 in the active area- was achieved. About 55% of the material budget originates from the 200 µm thin CVD diamond carrier, 36% from the two sensor layers and 9% from the glue.

To ensure the cooling of the double-sided station, the CVD diamond support was clamped into the aluminum heat sink. The surface available for heat transfer between heat sink and the CVD diamond support is 44×11 mm^2 at each side of the carrier. A thermally-conductive grease was used to increase the heat transfer.

To test the validity of our cooling concept, the temperatures of the sensors were constantly monitored with an infrared camera[3]. The temperature of the heat sink was obtained by means of a MAXIM DS18B20 temperature sensor mounted directly on the heat sink. The tests, so far, were carried out in air, which added some heat load to the cooling system. In case the MAPS were switched off, the observed temperature difference between the heat sink and sensor amounted to 4.7±0.5 °C for each of the three temperatures applied to the heat sink, i.e. (-5.5 °C, 6.7 °C and 17.0 °C). In case the sensors were running, this temperature difference rose by additional

[1] The pixels of MIMOSA-26 AHR are grouped into four sub-matrices. All pixels of one sub-matrix share the same discriminator level. A small temperature gradient is ambitious to exclude potential, temperature driven non-uniformities in the response of the pixels, which would turn into an unwanted fixed pattern noise.

[2] We used an Epotecny E501 epoxy resin featuring the following properties: Viscosity = 0.1-0.2 Pa·s at 25 °C, density = 1.1 g/cm^3, thermal conductivity = 0.05 Wm^{-1}K^{-1}.

[3] Infratec VarioCAM hr, head 720, temperature resolution: 0.03 °C.

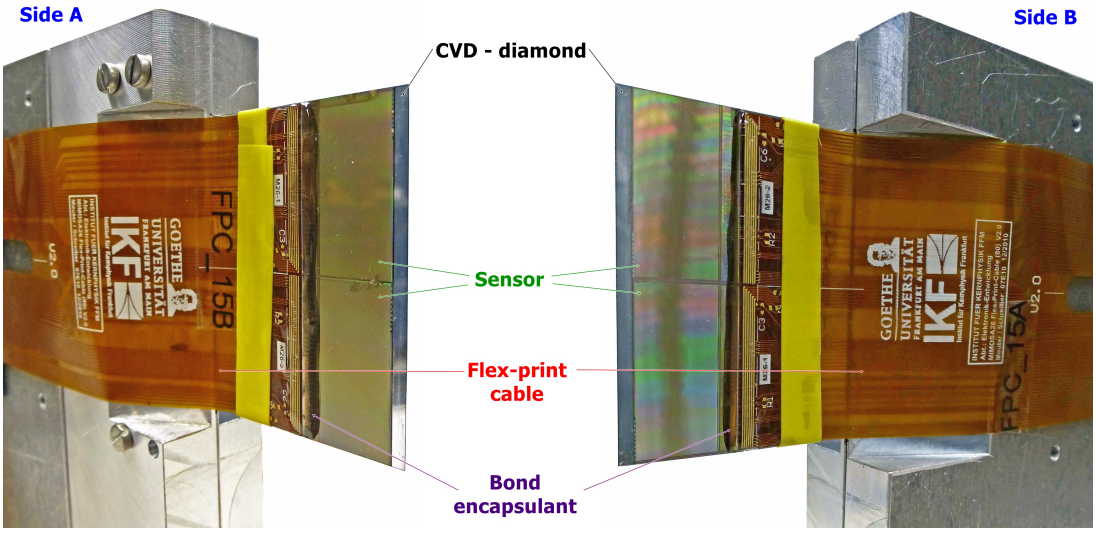

Figure 5.4: Fully assembled CVD diamond based prototype of station "0". Both sides, each comprising two identical CPS, are shown together with flex-print cables, bond encapsulation and aluminum-based heat-sinks.

4.0±0.5 °C. We conclude that the temperature gradient is dominated by the limited heat transfer between the heat sink and the CVD diamond support of the prototype. The temperature gradient along the sensor was found to be less than 1 °C. These encouraging results validate our cooling concept. Moreover, they leaf a substantial margin for cooling the final MVD-sensors, which is expected to dissipate two to three times more power than MIMOSA-26 AHR.

To test the performance of the prototype as well as the associated electronics and dedicated DAQ based on TRBv2 FPGA boards, the system was brought to a test facility at CERN-SPS. The system was composed of (i) the previously mentioned double-sided prototype station demonstrating sensor integration on both sides and providing the full cooling power required for the future MVD and (ii) four ultra-thin, single-sided stations with reduced cooling power, which were used as reference detectors for the prototype station. Alltogether, six sensors were read out. The setup was mounted at the CREN-SPS T4-H6 beam line providing negative pions with energies of 20-120 GeV, cf. Fig. 5.5, left side.

During the beam tests, the readout system operated very reliably: No network errors and data losses were observed during five days of continuous tests. All sensors of the prototype were synchronized within one 10 ns clock cycle of the FPGA-TRBv2 control unit. This synchronization remained stable during all our production runs, which lasted up to several hours each. To test the readout system, the data rates were varied from some MB/s up to 25 MB/s by changing the beam luminosity. The peak fluence reached was limited by the beam line. It used about 25% of the bandwidth of our prototype sensors. The data rate recorded did not use the full bandwidth of our DAQ. To test its limits, the thresholds of some sensors were intentionally tuned down to create more data from additional fake hits. Once saturated (100 MB/s) the DAQ remained in stable operation and kept collecting useful data by following a controlled data rejection scheme.

The data were analyzed in two steps using a customized software based on ROOT. First, a cluster analysis, an alignment, and a track selection with the four-plane beam reference system were performed. Then, the response of the prototype to the reconstructed particle

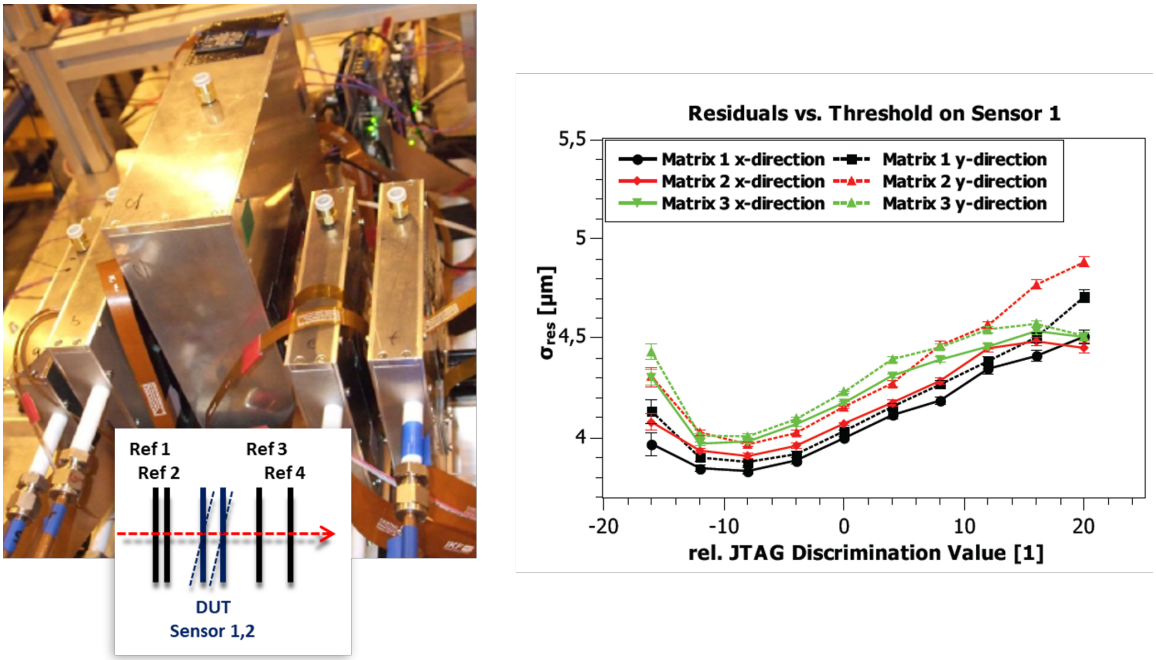

Figure 5.5: Left: Setup at CERN-SPS with the prototype 1 (DUT) sandwiched by 2 MIMOSA-26 telescope stations, respectively. Right: Spatial hit precision in different DUT sensors areas (matrix) vs. the sensors threshold, both in x- and y-direction.

tracks was evaluated. The analysis aims to re-measure the characteristics of MIMOSA-26 AHR, namely the fake hit rate, the detection efficiency and the spatial precision. The results are compatible with expectations from dedicated test campaigns validating the sensor, e.g. for the EUDET telescope. The re-measured spatial precision (σ) of about 3.8-4 µm is achieved for both coordinates, cf. right side of Fig. 5.5. More information about the setup and beam test can be found in [64, 63]. It is interesting to note that we found a relative change of the sensor-to-sensor (front and back side of the Prototype 1) alignment in time, in the order of (only, but significant) 3 nm/min. Since both sensors are glued to the same carrier, and the prototype was subject to systematic studies on the operation temperature during the course of the test run, we suspect residual effects due to not matching coefficients of expansion of the sensors, glue and pCVD diamond carrier.

5.2.1.2 Lessons learned from the Prototype 1:

Characterizing Prototype 1 yielded the following lessons:

- Thinned CPS can be integrated on 200 µm CVD diamond.
- Power of 350 mW/cm^2 can be evacuated from the most demanding sensors composing the CBM-MVD.
- Assembly jigs based on Polyoxymethylene (POM) were designed and proved to work. The design should be upgraded to improve the sensor placing precision and allow for about 100 µm sensor-to-sensor spacing. Aluminum should become the material of choice for the final jigs.
- Due to its viscosity, the Epotecny E501 adhesive met the expectation with respect to creating a low material budget link between the sensor and its carrier. However, since this

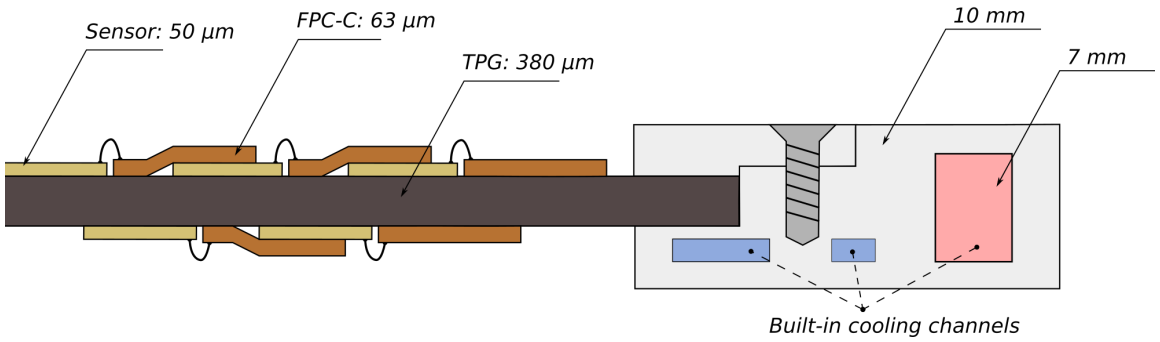

Figure 5.6: Simplified cross-sectional view of the PRESTO module. Note that the Y axis is not to scale, the material thickness is indicated.

adhesive layer is not flexible after curing, we conclude that a search for a different low viscosity glue with residual flexibility after curing and at possible operational temperature of about -20 °C) is advised. The need for a slightly flexible adhesive is due to the different thermal expansion coefficients of materials integrated in the module.

5.2.2 Prototype 2 - TPG-based prototype

In the following, selected aspects and results of the PRESTO assembly are presented and discussed w.r.t. to their relevance for the final MVD.

5.2.2.1 TPG as a sensor carrier

The Prototype 2 aimed at employing a TPG plates as a carrier material. The TPG was purchased at the Momentive Performance Materials [51]. We ordered several TPG plates with the following dimensions: 80×80×0.5 mm, 80×80×0.38 mm, 143×127×0.38 mm, 143×127×0.25 mm. The vendor provides the following tolerances: ±0.03 mm for a thickness, ± 0.05 mm for width and length. The tolerances were not cross-checked as the standard tools do not offer the required precision and moreover, the measurement process itself was considered as possibly destructive for the fragile TPG material.

The plates were inspected for respecting close to 90° angle between the neighboring edges with a precision square tool. The results are acceptable and we are in touch with the vendor to discuss possible improvements.

The visual inspection performed under microscope for each sample did not revealed any visible problems at the material surface (detached flakes, dents, lines that could suggest cracks). However, about every fourth TPG plate had one of the following problems at the corners: missing material or broken corner. The failures were attributed to the production and packaging quality. After reporting the issues to Momentive, we are still not sure if any improvement could be made in both mentioned domains. Therefore, we should assume that any future orders of this particular material should be made with excess.

5.2.2.2 Sensor quality assurance

The Prototype 1 (CVD diamond prototype), described in the section above, was based on MIMOSA-26 sensor that were not probe-tested prior to integration. One of the goals of the PRESTO project was to establish a setup and procedures to evaluate thin sensors. The tests

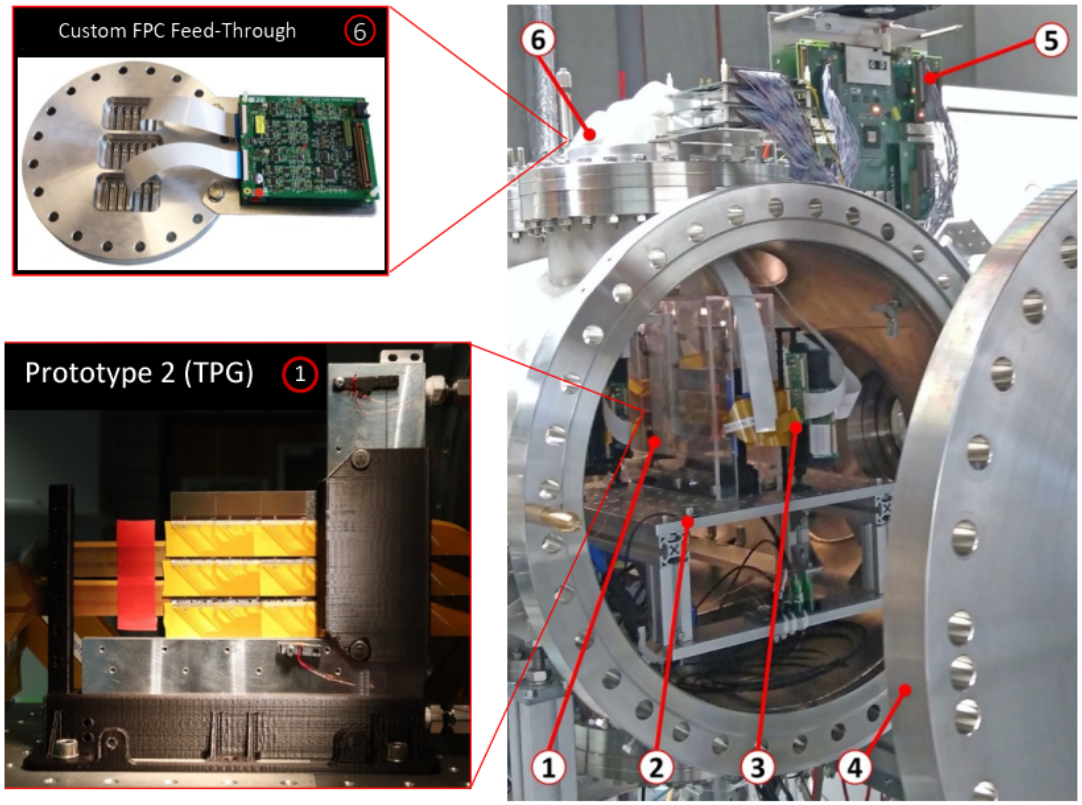

Figure 5.7: Picture shows the setup for 24/7 prototype 24/7 measurements. 1) The prototype clamped into its heat-sink, 2) support table, 3) passive front-end electronics, 4) vacuum flange, 5) TRBv3-based readout, 6) custom made flange for FPC cables and PCBs providing power and rooting the steering signals to/from the sensors. Taken from [81].

were performed with a Suss-Microtech PA-200 probe bench and a standard industrial probe card hosting 65 tungsten needles with a minimum pitch of 120 µm. The sensors were held by a chuck adapter with micro-vacuum channels. The adapter was CNC machined out of Polyoxymethylene material and fixed on the top of the original chuck. The sensor pads were contacted with the needles and their signals were routed through the probe card to a readout system based on TRBv3 [91]. The probe tests included testing of the standard operation modes of the sensor and of measuring its fixed pattern and temporal noise by the means of a transfer function scan. The temporal noise measured with the probe test setup was found to exceed the known noise of MIMOSA-26 by a factor of two to three on average. This effect can be tolerated for the selection of working sensors. It is caused by noise picked up by the long and unprotected lines used for steering and powering the sensor. The noise is injected in the sensor via a well-identified, vulnerable node. This issue is specific to MIMOSA-26 and has already been eliminated in further generations of the sensor.

It was further observed that an over-drive of about 100 µm was needed for achieving a good contact between the needle card and the sensors. This is beyond the limits of standard tungsten test cards. Therefore, the needles had to be routinely re-aligned after testing $\sim$ 50 sensors. The observed yield of thinned MIMOSA-26 sensors was about 65 %, which is in agreement with expectations for this type of sensors.

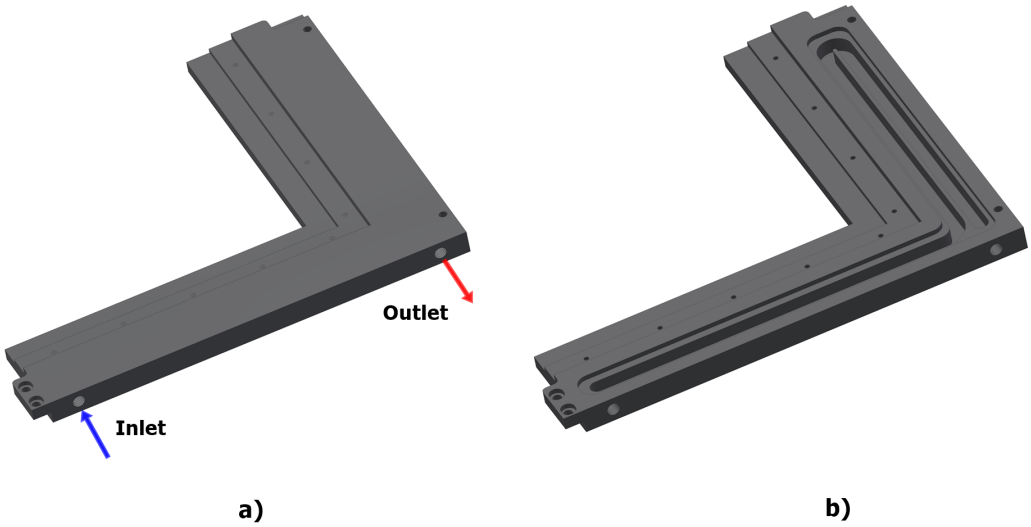

Figure 5.8: Heat-sink used at Prototype 2. a) heat-sink with the top lid welded, b) CNC machined channel for cooling liquid.

Up to now, about 300 pieces of MIOMSA-26 sensors, all thinned to 50 µm, were successfully tested with a simplified probe card and chuck adapter. To test the final MVD sensors, several modifications to the system are planned. This concerns:

- **Chuck adapter:** Should be able to host multiple thinned CPS to allow for some level of automation during probe tests. Also, the material of choice should be CNC machined aluminum. Since aluminum is electrically conductive, the chuck adapter can be grounded to prevent electrostatic charge build-up that could be the source of reduced sensor yield after probe-testing.
- **Probe card design:** It should accommodate more on-board electronics , e.g. noise filters, signal buffers and also detection of established contact between a needle and a pad to allow for automated probe tests.

5.2.2.3 The heat sink

In order to reduce the leakage currents and the shot noise found in irradiated sensors, the MVD will be operated at about −20 °C. The material budget of the related cooling system is optimized by integrating the sensors on a thin and highly heat conductive carrier, which leads the dissipated power towards the actively liquid-cooled heat sinks located outside the acceptance of the MVD. To minimize conversion, the heat sinks will be made of aluminium alloy. Within the Prototype 2 project, such a heat-sink was manufactured (quadrant size) at CoolTec GmbH, Germany, see Fig. 5.8. The heat-sink features a simple CNC machined channel. The top lid is then welded to close the channel.Thermal simulations carried-out by the vendor demonstrated that they reach the required cooling power including a safety factor of four.

The in-vacuum heat evacuation of the bare TPG was systematically explored within the PRESTO project. For this purpose, we integrated a 500 µm thin TPG carrier of $8 \times 8\,\mathrm{cm}^2$ on one side with a grid of PT-100 temperature sensors and on the other side with flexible OMEGA Engineering INC Kapton heaters ($4.5 \times 4.5\,\mathrm{cm}^2$). The latter mimic the heat dissipation of sensors. Tests were performed up to a dissipated power of 15.5 W (about $600\,\mathrm{mW/cm}^2$), which

Layer	$f \cdot d$ [µm]	x/X_0	Si-equiv [µm]
Coverlay	$100\% \cdot 26$	0.009 %	8.6
Copper	$40\% \cdot 12$	0.033 %	31.3
Polyimide	$100\% \cdot 25$	0.009 %	8.2
Sum	63	0.051 %	48.1

Table 5.1: Specification of the PRESTO flex-print cable.

is by a factor of four more than expected from the final MVD sensors. The carrier was clamped with vacuum grease as interfacing medium into the heat sink. The temperature of the heat sink input node was kept at −40 °C. An average temperature gradient of less than 2 °C/cm was observed and therefore will not contribute to non-uniform sensor operation after irradiation. The interface temperature gradient (TPG – heat sink) was found to be of about 15 °C and should become smaller for MIMOSIS sensors.

5.2.2.4 Flex print cables

The design aimed to explore the limits of commercial copper-based flex print cable technology as provided by ILFA Feinstleitertechnik GmbH, Germany. The previous generation flex cable, comprising two copper layers of 25 µm thickness each and used for the MVD-prototype project [64], was not optimized for ultra-low material budget. The improved Cu-based cables for PRESTO were designed to significantly reduce the number and thickness of the FPC layers. This turned into a single layer cable with a particularly low material budget of $x/X_0 \sim 0.051\,\%$, see Tab. 5.1 and reference [92]. The use of a smaller feature size (80 µm) allowed for reducing the total width of the cable. The measured FPCs parameters, *e.g.* trace dimensions and resistivity, are in agreement with the specification delivered by the vendor. The signal transmission quality at the range up to 80 MHz (the fastest LVDS line in case of the MIMOSA-26 sensor family) is very good, as assessed based on eye-diagram measurements. The measured signal rise time t_r of 1.7 ns and fall time t_f of 1.6 ns of the signal exceed the needs of 80 MHz transmission of MIMOSA-26 and should be appropriate for 320 Mbit/s data links considered for the final MVD sensor.

Since one flex cable provides services for two sensors, two cables are required to read out one row of the PRESTO module. We tested, if potential cross-talks between the nearby cables might have a negative impact on the sensor operation. We did not observe any significant cross talk.

5.2.2.5 Assembly tools and final material budget

For the assembly of the PRESTO module, dedicated adhesive RAL-247 (see Sec. 4.2) and appropriate tools for positioning the sensors and cables with respect to the carrier were designed and manufactured [45]. To evaluate them, a mock-up PRESTO module composed from 50 µm silicon pieces featuring the form-factor of the MIMOSA-26 sensor and a 200 µm thin glass plate, which serves as sensor carrier, was assembled. We found that 5 µL of the RAL-247 glue are suited to cover the gap between a sensor and carrier with a "bubble-free" and 15 µm thin adhesive layer, avoiding at the same time unwanted leftovers around/on a sensor. The horizontal sensor-to-sensor distance variations were measured to less than 5 µm. The vertical variation in the distances between the sensor edges were measured to be of about 20 µm. Both numbers are substantially better than our goal of 100 µm placing precision. The same technique but with increased amount of glue (9 µL) under each sensor, to compensate for the surface imperfections of

the TPG material, was applied for assembly of the MIMOSA-26 sensors onto the PRESTO-TPG carrier.

The material budget of the third MVD station was estimated accounting for the thickness and geometries of the components used for PRESTO assembly, and it is shown in Fig.4.19. One can see that it exceeded the targeted value only outside of the geometrical acceptance. Further improvements can be made by replacing the copper traces with aluminium which has a smaller electrical conductivity ($3.50 \cdot 10^7$ S/m vs. $5.96 \cdot 10^7$ S/m) but a much longer radiation length than copper (88.97 mm vs. 14.36 mm). This allows for reaching the same electrical resistance with a material budget reduced by a factor of 3.6, see also [84].

After assembly, five out of the six sensors put onto the back side of PRESTO were functional. One half of the sixth sensor worked well while the remaining half did not produced any output data. After some time, an additional sensor started to exhibit malfunctioning. Optical inspection did not reveal problems with the sensors or the wire bonding. We consider that the sensors were affected by a specific vulnerability of MIMOSA-26 to electrostatic discharges, which was recognized and accounted for with some delay only.

5.2.2.6 Long-term stability tests

The Prototype 2 was not only built to prove the double-sided integration on a fragile TPG plate but also to verify its vacuum-compatibility and ability to run under conditions close to the one expected at the CBM experiment. The conditions that will have an impact on mechanical stability of the assembled MVD modules are mostly temperature and pressure changes. They are mechanically challenging and pose a risk when air is still contained in pockets or bubbles, which might expand. In addition, vibrations caused by the gas flow or from valves and pumps might cause mechanical stress (e.g., the bonding wires might be ripped off). Therefore, a dedicated setup for 24/7 Prototype 2 tests was built. It composes of a vacuum chamber packed with temperature sensors and vacuum gauges, where the prototype was installed together with passive front-end electronics. A chiller running with glycol-water mixture (50:50) was connected to the Prototype 2 heat-sink to provide temperature control. Also, readout system was based on the TRBv3 standard was constantly taking data from the prototype's sensors. The temperature from multiple Pt100 sensors connected to the prototype at different locations, pressure, as well as sensor main life parameters (power consumption, supply voltages and return CLK signal) were constantly monitored by the mean of the EPICS control system.

In total, 130 vacuum cycles were performed. Fig. 5.9 shows the temporal and fixed-pattern noise evolution for the first six vacuum cycles. We did not investigated the noise for each run after pressure cycle since we consider this task as too much time consuming and also results are not so straight forward to interpret. The noise can change independently on the sensor performance but, for example, due to an environmental conditions imposed by other running equipment, also the one running in the neighbouring laboratories [4]. Therefore we focused on constant power consumption and sensor return clock signals monitoring (see Fig. 5.10) as the parameters reflecting the sensor' status. The Prototype 2 was tested from November 2018 till March 2020. The events where the return clock signals were at "0" are associated to sensor

[4] MIMOSA-26 uses an externally supplied reference voltage for settings the thresholds. This line should be well filtered to provide stable sensor operation. The about 30 cm FPC cables were designed for minimum material budget and therefore did not feature any screening feature that could eliminate the influence of the external noise sources. The noise of the sensors connected to the FPC cables was observed to be by factor of three higher than tested by the sensor provider. The latter tested the sensors assembled on the PCBs packed with many filtering capacitors.

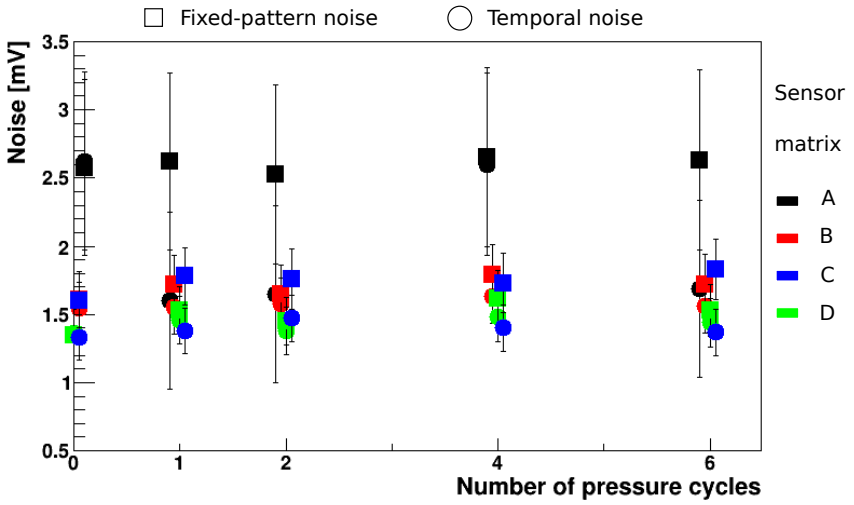

Figure 5.9: Temporal and fixed-pattern noise measured after six cycles from atmosphere pressure to the 10^{-3} mbar*. Error bars correspond to systematic measurements uncertainties.*

reprogramming, power cycles, and other actions triggered by the operator, thus, not due to any sensor malfunctioning. Consequently, we considered that all the sensors were working stable and did not undergo any sever electrical or mechanical damages during the test period considered.

5.2.2.7 Lessons learned from the Prototype 2

There were several interesting lessons learned during and after the construction of the Prototype 2. These lessons will impact the integration of the CBM-MVD and are summarized shortly as following:

- The yield after assembly did not exceed 70% for the Prototype 2., despite all the sensors were tested prior to assembly. Investigating possible yield issues, we found that our bonding machine was malfunctioning during assembly. Also, despite all ESD precautions, there might have been an accidental charge build-up on the assembly tools made of POM material.
- The TPG can be used as a carrier material. However, more adhesive is needed to form an uniform layer between sensor and TPG. The latter was concluded as unstable and hard to work with at the thicknesses around 250 µm and less. Also graphite particles are loosely bonded and can easily detach from the main plate. The TPG is electrically conductive, which may lead improper sensor operation due to the fact that the bulk material of the sensor is polarized with a potential as high as few volts. To overcome this obstacles, the TPG should be coated first with a thin layer of mechanically stable and electrically non-conductive material, that is parylene and epoxy adhesive.
- The assembly jigs designed and manufactured for the Prototype 2 allowed for assembly the prototype with the precision of about 100 µm. However, the jigs made of polyoxymethylens should be avoided as a possible source of ESD. In addition, the jigs has to be adapted to provide the controlled horizontal sensor-to-sensor spacing of about 100 µm.
- Vacuum compatibility - during commissioning and operation of PRESTO we could not identify problems imposed by vacuum operation. The key issue is to avoid any (air-filled) cavities during assembly, which during pumping and in vacuum would trigger *e.g.* residual

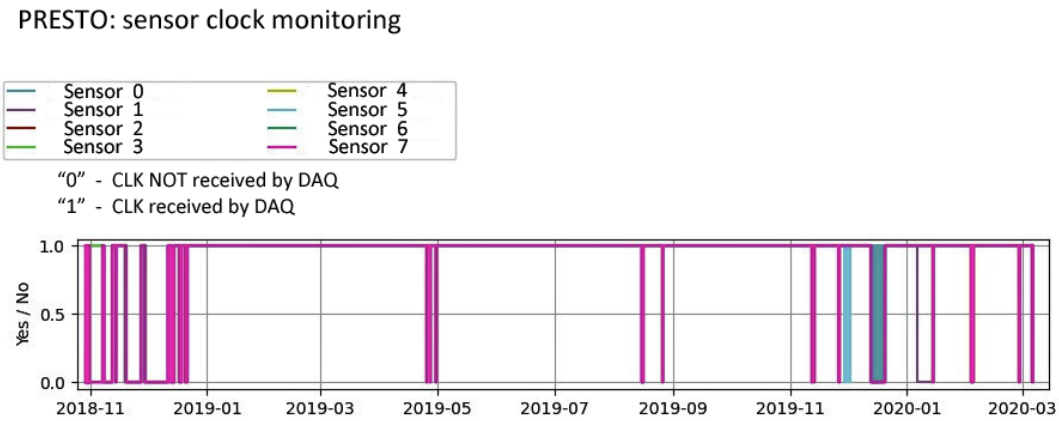

Figure 5.10: PRESTO 24/7 - sensor life function monitoring: return clock signal was monitored from November 2018 till March 2020. The clock equal "1" means that the readout system was receiving the return clock from the sensor. The events where the return clock signals were at "0" are associated to sensor reprogramming, power cycles, and other actions triggered by the operator, so not due to any sensor malfunctioning.

mechanical forces on the components. Long-term operation in vacuum did not reveal any incidents pointing to such problems.

5.2.3 Issues to be addressed before production readiness

Thinned to 50 µm CMOS sensors MIMOSA-26 have been successfully used for many integration related activities. We have learned how to probe test, handle and integrate this particular sensor as well as selected materials and adhesives that would fit the MVD requirements. We can assume that, despite its different form-factor, mechanical handling of the MIMOSIS sensor will be addressed in the similar manner as in case of MIMOSA-26. However, there are still a number of issues that have to be addressed when moving to integrate the MIMOSIS sensors:

- Design and produce assembly jigs and tools. Since the procedure of moving a double-sided integrated MVD modules are considered as a high-risk operation, we need to design, prototype and put into operation dedicated heat-sinks which can be also used during integration phase as mechanical jigs.
- Sensors need to be electrically insulated from the support and from each other. This is because the sensor bulk is polarized to a given potential. While diamond-based carriers are electric insulators, the problem has to be solved for carbon-based materials required to build the large acceptance modules. The way to go is Parylene or epoxy coating. Unfortunately, objects covered with Parylene becomes strongly hydrophobic and dispensing any adhesive layer under control is impossible. Plasma activation options needs to be addressed together with Fraunhofer Institute for Interfacial Engineering and Biotechnology (IGB). We need also to find an industrial or academic partner where coating with a 10-15 epoxy layer could be routinely performed. Despite, the 10-15 µm of thermally less conductive coating layer added to each side of the assembly should not significantly affect the heat evacuation from the MVD sensors - the quantitatively verification needs to be addressed. In addition, together with Rutherford Appleton Laboratory, we are in process to develop a resin that, by wetting additives, could be Parylene-compatible.

- Adapt the probe station setup to test the MIMOSIS sensor and it prototypes prior to any assembly. This concerns development of a chuck adapter holding multiple sensors, a new probe card and MIMOSIS-compatible readout.
- Identify an alternative adhesive for sensor mounting. The RAL-247 adhesive is a custom made resin that was developed at Rutherford Appleton Laboratory, United Kingdom. This resin is supposed to be provided to the CBM-MVD (and also groups in Mainz and Bochum) for next several years. However, to avoid a single point of failure, we are presently actively looking for alternative adhesives that could meet the CBM-MVD requirements.
- Study the susceptibility of MIMOSIS sensor prototypes to environmental conditions, e.g., electromagnetic noise, while running the sensor with dedicated, long and low-mass flex-print cables. When operating MIMOSA-26 sensors in laboratory conditions, we have observed an influence of the flex-print cable length on the sensor performance, mainly w.r.t. the signal-to-noise ratio. This aspect has to be followed up with MIMOSIS sensors, in two stages. First, we will design a single layer PCB (emulating a flex-print-cable) with many options of filtering the noise to reveal potentially noise-sensitive weak points of MIMOSIS. The lessons learned will in a second step be applied to design a low-mass single layer flex print cable. In parallel, a two-layer flex-cable will be designed to compare the MIMOSIS performance.

6 Physics Performance

This chapter describes the anticipated physics performance of the MVD, based on the detector designs discussed in Sec. 3.3. Studies were performed for beam energies delivered by SIS100 only. By the time the stretcher synchrotron with higher rigidity will become available, the MVD will likely be rebuilt using advanced sensor technology. We will first summarize the experimental conditions in Sec. 6.1 and then present the details of the simulation and analysis tools used for the performance studies in Sec. 6.2 as well as the relevant event reconstruction algorithms in brief (Sec 6.3). The remaining Sec. 6.4 is dedicated to the intrinsic detector performance and the physics performance with the MVD. Full simulations for three selected cases, dielectron background rejection, missing mass analysis for hyperon decays and open charm detection in proton induced reactions will be presented. It should be noted that the physical performance studies with the CBM silicon tracking system (STS & CBM) will need to be consolidated in the near future, as the TR and VX detector configurations have only recently been revised to incorporate the sensor geometries and heat dissipation of the MIMOSIS. It is advisable to extend the simulation studies to lower beam energies, now with a magnetic field setting adapted accordingly. The focus would be on the track reconstruction efficiency for momenta below 1 GeV/c, taking into account the most recent material budget of the tracking system and vacuum window. The MVD software package is ready to allow for detailed simulations to elaborate on detector operation aspects, such as *e.g.* sensor misalignment, fake hits or redundancy.

6.1 Experimental conditions

According to the conceptual design studies [13], the MVD will be operated in Au+Au experiments at interaction rates of up to 100 kHz and p+Au experiments at interaction rates of up to 1 MHz. In this chapter we will report on performance studies related to key observables addressed in the CBM physics program. To provide a realistic assessment of such cases, it is important to consider as well detector activity which is not directly related to the nuclear reaction in the target. Due to the comparatively long integration of the detector of about 5 µs the occupancy of the detector is strongly influenced by such "background" particles. Moreover, the additional load due to such particles also effects the stability and lifetime of the detectors. In case of heavy-ion collisions, substantial additional detector activity will occur due to δ-electrons emerging from the solid target placed only a few centimeters upstream. Yet, most of the δ-electrons will be curling up around the field lines of the magnetic dipole field present in target area. However, certain regions in the MVD stations are dominated by δ-electrons, as discussed in Sec. 3. A second source of particles to consider are light nuclear clusters originating from the break-up of target light residues.

In the following we will first discuss the simulation environment used for the performance studies and then address various key performance parameters.

6.2 Simulation environment and tools

Simulations on the performances of the MVD were performed with the CBMROOT simulation framework. This framework is extended with dedicated detector response models (digitizer) and a data analysis package. For the MVD, the digitizer packages simulates a realistic sensor response in terms of signal charge amplitude and signal charge sharing between neighboring pixels. Moreover, the thermal noise and the threshold circuits are taken into account. The material budget of the two considered detector geometries (TR and VX, see Sec. 4) is inherited from the related CAD drawings of the stations. In the active area, it includes the sensor and support materials, glue and cables. The material outside the active area is represented by a simplified model of the cooling supports. Ideal vacuum is assumed for the target chamber. The simulation package is at this stage not supposed to simulate the in-chip digital data processing of the sensors as the details of this processing are not expected to affect the physics performance and as the underlying technological solution is not yet finally implemented.

Typical simulations embed signal signatures into UrQMD-events and transport the entire final-state particles with GEANT through the detector geometry. The simulation provides `CbmMvdMCPoints`, which contain time-of-flight information as well as the ideal coordinates at which a particle enters and leaves the sensor volume. From this information, the digitizer generates `CbmMvdMCPoints`, which reflect the response of the individual pixels. In MAPS, typically more than one pixel receives signal charge (charge sharing) and each (detection efficiency significantly above 99 %, see Sec. 4.1) impinging particle generates clusters of active pixels. Those clusters are reconstructed by a dedicated cluster finder. Next, a `CbmMvdHit` is built from the cluster and the position information is refined by means of the center-of-charge of the individual clusters. The `CbmMvdHit` serves as input for the track finding and track fitting algorithms of CBMROOT.
For this report, the physics performance of the MVD was evaluated with an event-by-event based simulation but with the option to include a number of underlying events in addition to the event containing the physics (signal). Those are events containing the δ-electrons derived from a GEANT simulation for Au ions traversing the target material w/o interaction and up to a few minimum bias Au+Au events, simulated with UrQMD, to mimic local (in time) rate fluctuations immanent to the slow-extracted beam of a synchrotron. All particles of the combined event are treated and contained in one "image" of the MVD (*cf.* 6.2.2).

6.2.1 Charge generation, charge collection and noise

The simulation model underlying the MVD digitizer [93] relies on parametrizing measured sensor responses. The motivation of this solution as much as the details of the model are discussed in [25]. The model was initially tested for MAPS with low resistivity epitaxial layer. Its validity for non-irradiated and irradiated sensors with high resistivity epitaxial layer (such as MIMOSIS with DC pixels and conventional epitaxial layer) was shown in [94]. In both works, an excellent accordance of the simulated with measured detector response is reported. For example, the number of active pixels per cluster and the signal charge collected by the pixels is reproduced within 10%. The aging of detectors due to radiation can be considered by the software as well. However, this feature was so far not exploited as the differences in response between new and aged sensors is by definition to remain small during the working lifetime of the sensors.

The noise of the pixels is set by the user and is represented as Gaussian noise of the individual pixels. The noise is added to the signal amplitude of all active pixels and may move them below threshold. Optionally, noise as caused by random telegraph signal (RTS) and respective hot

pixels are simulated by generating false positive hit indications to random pixels.

6.2.2 Event overlay

Given the relatively long integration time of MIMOSIS, an image, *i.e.* the information obtained from one scan of all pixel arrays, can contain signals from a number of different events. In the most general case, an image processed in combination with the response to the signal event of all other detector system of a given CBM configuration, contains the following events in total:

Signal event: This is the event under consideration, *i.e.* it contains the signal to be investigated. This can be a central Au+Au event generated with UrQMD, or such an event including a particular rare signal like a dilepton or open charm obtained from the PLUTO event generator and included to the CBMROOT particle list.

Minimum bias event: At high interaction rates of 1 MHz and beyond, several interactions can fall within the "integration time" (time span referring to one frame) of MIMOSIS. To test the performance loss in case of high interaction rates, several UrQMD minimum bias events are randomly picked from an event stream and overlaid to the signal event.

δ-electron event: An important performance aspect of the MVD are the abundant δ-electrons impinging on the detector. The generation of δ-electrons is simulated with GEANT3 by "sending" Au ions to the target of CBM. Also, such events can be sampled from a stream and added to the list of charged particle impacts in the MVD (`MCpoint`).

In that way flexibility is given to tune the simulation such as to investigate the intrinsic performance of the detector system, like *e.g.* the pointing accuracy or the full track reconstruction performance, under realistic experiment conditions.

6.3 Reconstruction Tools

For the evaluation of the intrinsic and physics performance of the MVD the standard track reconstruction package of CBM is employed as implemented in the CBMROOT framework. While a detailed account can be found in [95], a short description of it will follow below. The track finding and reconstruction package reads the list of all `Hit` objects for a given event. It uses the magnetic field map and tables, describing the material budget of each tracking station as 2-dimensional arrays with fine granularity. In a first step, hit candidates forming a possible track segments are found using a cellular automaton. For that, all tracking station, 4 MVD and 8 STS stations are treated on equal footing. In a second step, the hits contributing to a track candidate are fitted with a Kalman Filter (KF). To improve performance of the processing, track fitting is carried out along a priority scheme. Tracks are fitted starting from the rear stations and selecting track candidates with a reduced momentum of $p/q \geq 1\,\mathrm{GV}/c$. Also it is assumed that the tracks emerge from the the event origin (this is the expected position of the event, *i.e.* the primary vertex[1]). Such tracks are called *reference tracks* and typically feature best reconstruction performance. The quality of a track can be characterized by inspecting Monte Carlo information and quantifying the fraction of true `MCpoints` used in the fit and also the number of fake `MCpoints` connected to the fits (purity). Tracks which generate at least three `Hit` objects in three different tracking stations are considered to be reconstructable. In a second

[1] In the case of simulations this is taken from GEANT information and refers to the location where the reaction products start to propagate through the setup.

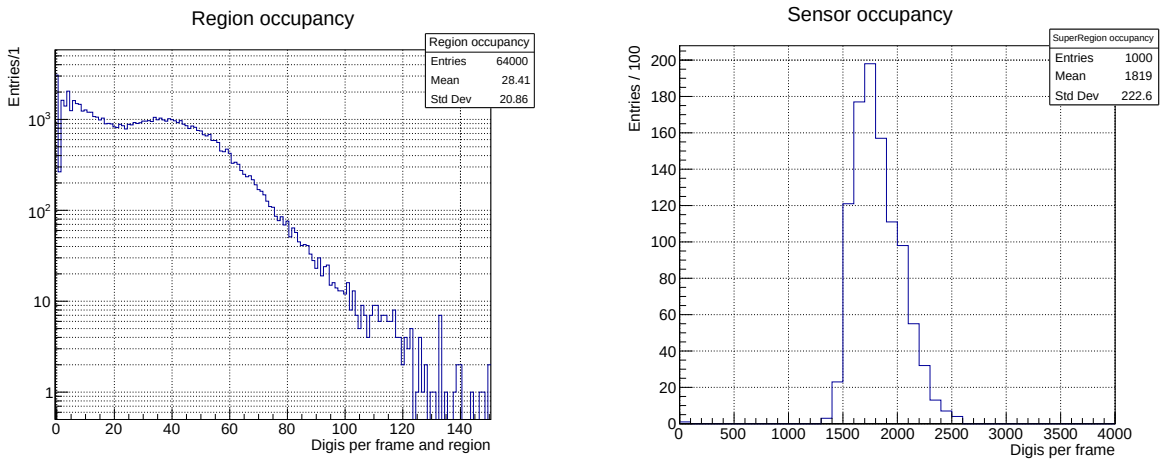

Figure 6.1: Simulated data load (fired pixels per frame) for the regions (left) and at the input of the elastic buffer (right) of the most illuminated MVD-sensor at peak occupancy. See text.

and third round tracks not originating from the event origin and softer tracks, *i.e.* $p/q < 1\,\mathrm{GV}c$ are fitted, respectively. `Hit` objects not used in previous fits are given back to the pool, while sharing of hits is not allowed.

6.4 Simulation results

6.4.1 Validation of the MIMOSIS on-chip data transmission system

The requirements on the counting rate of the MIMOSIS sensor were simulated down to the level of the load on the 64 individual regions of the sensor. The detailed simulation was carried out based on the most exposed vertex geometry (VX) and assuming that the beam intensity would fluctuate by up to a factor of three from its nominal average value.

The simulations assume an average 12 A GeV Au+Au reaction rate of 100 kHz and a frame time of 5 µs for MIMOSIS. The occupancy of the sensor during this time was simulated by superimposing the tracks generated by one minimum bias 12 A GeV UrQMD-collision and the δ-electrons generated by 50 gold ions penetrating the target. For the peak occupancy, one central and one minimum bias collision were superimposed with δ-electrons from 150 gold ions. Both assumptions are conservative as the average number of nuclear collisions amounts to 0.5 and 1.5 collisions with random impact parameter, respectively. Similar simulations were carried out with 30 GeV p+Au collisions at a rate of 10 MHz but the system requirements were found to be driven by the heavy-ion case.

The requirements for the sensor geometry are laid down by the peak beam intensity reached in a few individual sensors located in the occupancy hot-spot created by deflected δ-electrons. To confirm the validity of the current sensor design, the occupancy in the sensor regions and the load on the respective event buffers were simulated with CBMROOT at peak beam intensity and for the most illuminated sensor of the vertex geometry. Results are shown in Fig. 6.1. The left panel of this figure displays the number of fired pixels for the 64 regions of the MIMOSIS-sensor and for 1000 simulated frames. One observes that at a 90-electron threshold, the average number of active pixels amounts to 28 and only a marginal number of overflows beyond the

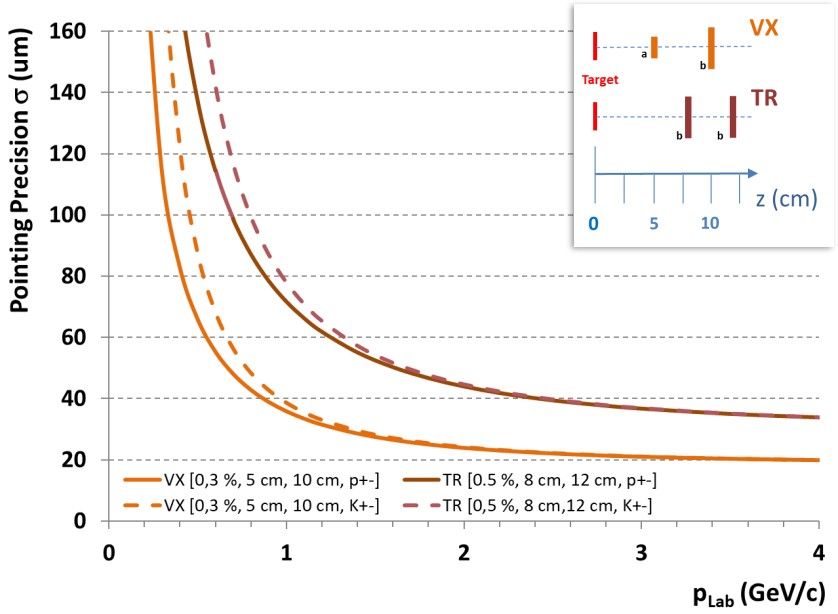

Figure 6.2: Pointing precision σ (Eq. 6.3) vs. the pion (kaon) momentum, for two detector geometries VX and TR, respectively, shown as insert. The calculation is based on assuming two planar detector stations with a given distances to the target, spatial precisions and material budgets, see equation 6.3.

100 pixels/frame bandwidth of the region are seen. In about 14 % of frames, at least one region will loose the information on at least one fired pixel. However, even in the hypothetical scenario that this most exposed sensor was continuously operated at peak data rates, the data loss would be restricted to 1.2 %.

The input data stream of the elastic buffer is shown in the right panel of the Fig. 6.1. One observes that the buffer will face an average input data stream of slightly above 1800 fired pixels per frame and its bandwidth of up to 3200 words per frame is not challenged. Accounting for the output bandwidth of 800 words per frame of this buffer, the sensor may withstand beam peaks of a duration of above 80 µs.

It should be mentioned that the above presented results might become more relaxed once the on-chip cluster finding is accounted for, which will presumably turn into a data stream of substantially less than one data word per fired pixel. This will reduce the load on the elastic buffer and the output data streams of the sensors. The compression factor for highly illuminated sensors may approach a factor of two but the detailed value remains to be evaluated based on beam test data.

6.4.2 Generic Single Track Pointing Capability

The pointing capability of a vertex detector can be analytically assessed, only based on the distance of the first two stations from the interaction point (target, primary vertex), their intrinsic spatial precision to locate a track, and the material budget of the first station closest to the target. In the case of the MVD no additional material, *e.g.* beam pipe or air, has to be considered. Outlined in reference [66], the single straight track pointing precision σ_D in two

dimensions due to only geometrical properties of the detector setup can be described as:

$$\sigma_D^2 = \frac{\sigma_1^2 r_2^2 + \sigma_2^2 r_1^2}{(r_2 - r_1)^2}, \tag{6.1}$$

with r_i the distance between target and station and σ_i the spatial precision of the sensor plane i to locate a track. As expected, maximizing the distance between both stations optimizes the pointing precision. To set the stage, the pointing precision solely due to the detector geometry results in 18.4 (29.7) µm for the detector geometry VX (TR). The sensor pitch of MIMOSIS was plugged in, x–y averaged 28.5 µm, with a spatial precision of $pitch/\sqrt{12}$. This pointing precision is blurred by the multiple scattering in the first station ($x/X_0 = 0.3$ (0.5) % for the VX (TR) detector geometry). This contribution σ_{MS} can be described as:

$$\sigma_{MS}^2 = \frac{\Theta_{MS}^2 r_1^2}{sin^2\Theta}, \tag{6.2}$$

with Θ_{MS} being the (standard) multiple Coulomb scattering angular rms width (in plane) $\propto \sqrt{x/X_0}/p/\beta$ (with p the particle's lab momentum, β the velocity), and Θ the hit angle of the track with respect to the detector plane. We assume an average value of 72^o, derived from boosting particles (pions, kaons) created in a fireball (temperature of 100 MeV, 10 A GeV projectile on a fixed target) into the lab frame. Fig. 6.2 depicts the pointing precision, *i.e.* the square-root of the quadratic sum of both contributions, as a function of the particle's lab momentum:

$$\sigma_{Pointing}^2 = \sigma_D^2 + \sigma_{MS}^2 \tag{6.3}$$

Obviously, the VX detector geometry performs almost a factor of two better compared to the TR geometry. This is expected since due to both, reduced material budget as well as the shorter distance of the first station to the target entail higher pointing precision. Also, the station-to-station distance is unfavorable for the TR detector geometry. One can evaluate two scenarios:

- **Geometry VX:** Pions with lab momenta above 2 GeV/c feature a pointing precision of about 20 µm dictated by the geometrical part of the pointing performance. Assuming, hypothetically, a D^o meson decaying in the fireball (T = 100 MeV, 10 A GeV projectile energy) in a kaon and pion, lab momenta well above 2 GeV/c would result due to the decay Q value, and the boost. Here, the pointing precision would be more and more driven by the detector's geometrical properties (pixel pitch, position of the stations).
- **Geometry TR:** Pions and kaons featuring a Boltzmann energy distribution with T = 100 MeV and emitted from the fireball (10 A GeV projectile energy) have lab momenta well below 2 GeV/c and hence their single track pointing precision in the MVD is dominated by multiple scattering, eventually exceeding 100 µm.

Due to the forward boost in the fixed-target setup, introducing a parallax w.r.t. the beam axis, the single track pointing precision in z (along the beam axis) is typically a factor 3 worse compared to the x or y coordinate.

In conclusion, the MVD would, in the case of a (secondary) vertex detector for open charm identification in the SIS100 energy range, feature a pointing precision along the beam axis of significantly below 100 µm. It should be noted that the maximum beam energy provided by SIS100 for Au beam is just at the NN threshold for charm production. Reliable calculations for charm production exist only for much higher beam energies, where perturbative calculations

Beam momentum	System	Geometry	All	> 800 MeV/c	> 1 GeV/c
10 AGeV/c	Au+Au	TR	250 µm	180 µm	160 µm
10 AGeV/c	Au+Au	VX	140 µm	110 µm	100 µm
28.3 GeV/c	p+Au	TR	260 µm	170 µm	140 µm
28.3 GeV/c	p+Au	VX	170 µm	110 µm	110 µm

Table 6.1: Precision of secondary vertex reconstruction (σ) in the coordinate along the beam axis for the tracking (TR) and vertexing (VX) geometry, different collision systems and as function of the particle momentum.

are applicable. This is the reason why we do not press the performance parameters towards utmost pointing precision in favor of giving up design criteria which enable stable and reliable operation.

Formula 6.3 employed here, motivated by similar assessments of the STAR HFT tracker [84][2], suggest a pointing precision in z of around 60 µm (VX geometry). However, the single track pointing precision of particles with momenta well below 2 GeV/c is noticeably dominated by multiple scattering and exceeds 100 µm along the beam-axis, strongly depending on the lab momentum and emission angle. Since the material budget[3] is already challenging for vacuum operation, and its impact on vertexing is attenuated by its square root, only moving the first station close to the target would gain pointing precision. However, this is excluded due to limits regarding the local hit density and radiation damage.

6.4.3 Vertex Reconstruction Capability

The decay vertex reconstruction precision achievable with MVD was studied with reconstructed tracks from a simulation using 10 A GeV Au+Au UrQMD collisions. The events were transported, digitized and track finding and track fitting was performed with the L1 and KF reconstruction packages included in CBMROOT. A representative result of the study is shown in Fig. 6.3, which depicts the reconstructed primary vertex position along the z-axis (beam axis) as measured by CBM with the MVD (tracking geometry TR) and as measured based on STS-data. The true interaction point is located at the origin of the coordinate system. The primary vertex precision as reconstructed with the MVD is given with $\sigma_{PvZ} = 4.1$ µm and as such far more than an order of magnitude better than the vertex precision of the stand-alone STS. Due to the distance of the STS to the target and its segmentation this is no surprise.

The precision for secondary vertex reconstruction along the z-axis is shown in Tab. 6.1 for different collision systems and the tracking and vertexing geometry. The results were obtained by reconstructing simulated UrQMD-collisions and by determining the distance of closest approach for two randomly chosen primary tracks. The center point of the respective distance is used to derive the z-coordinate. The distance between the reconstructed and the true intersection point (at the origin of the coordinate system) was fitted with a Gaussian, which introduces some uncertainties due to the tails of distributions obtained. The variance of the Gaussian is shown in Tab. 6.1. The procedure was repeated with tracks with a momentum of $p > 0.8$ GeV/c and $p > 1$ GeV/c as tracks fulfilling those requirements are the ones selected for charm reconstruction.

[2]The STAR technical design reports points out the overall agreement between results derived with equation 6.3 and more sophisticated calculations and simulations.

[3]Note, we do not discuss here the impact of *e.g.* thermal stability, alignment precision or residual vibration caused by vacuum pumps.

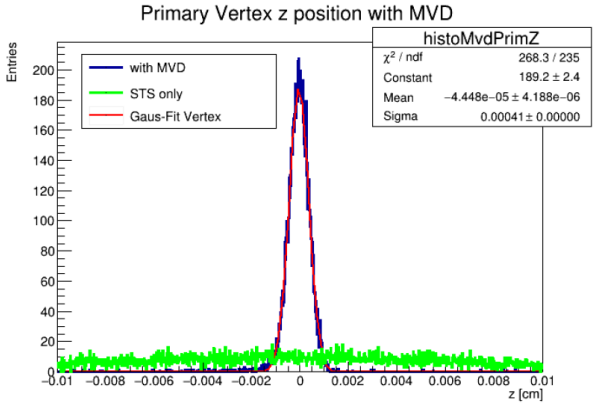

Figure 6.3: Comparison of the reconstructed z-coordinate of the primary vertex position in the presence and absence of the vertex detector, employing 10 A GeV Au+Au UrQMD collisions. One observes that the vertex detector (VX detector geometry) improves the primary vertex reconstruction to a precision of σ_{PvZ} =4.1 µm along the beam axis, i.e. by about one order of magnitude better.

Over all it is found that the precision of the secondary vertex reconstruction reaches 250 µm for the most unfavorable and about 100 µm for the most favorable conditions.

6.4.4 Dielectron Background Rejection

Dielectron continuum spectroscopy requires sophisticated strategies to reduce contributions to the spectrum originating from combinatorial pairs, *i.e.* opposite sign pairs of electrons which do not originating from one and the same (virtual) photon. Three different contributions to such combinatorial pairs can be identified: (1) single leptons from two different pairs for which each two daughters were fully reconstructed, (2) lepton pairs which contain at least one electron which originates from an incompletely reconstructed pair, and (3) lepton pairs which contain at least one falsely reconstructed electron (fake). And, of course, mixtures of these cases. Such combinatorial background grows quadratically with the mean charged particle multiplicity in a given centrality class.

One of the important characteristics of conversion and Dalitz pairs is a small opening angle. However, in the CBM configuration the target is placed in a strong magnetic dipole field. Consequently, pairs with small opening angle, indicative for conversion and π^0 Dalitz pairs, will immediately bend apart. A further feature of conversion pairs and Dalitz-pairs with small invariant mass is a high probability to observe one of the daughters with comparatively low momentum. In a proof of principle study it has been shown [96] that such reducible background pairs can effectively be rejected, if the soft partner of an fully reconstructed partner electron is reconstructed, even if the soft lepton did only traverse a few tracking stations (track segment). Such incomplete tracks (track segments) will not be reconstructed as lepton candidates and would normally be rejected in the analysis. An extreme implementation of such a "tagging" of single electron tracks would be to require a next neighbor hit in the first tracking station traversed by the fully reconstructed lepton, not attached to any reconstructed charged particle track or track segment.

With MVD positioned near to the target, the probability for track segment reconstruction is substantially enhanced. Hence, the strategy pursued to reduce background is to search, for each

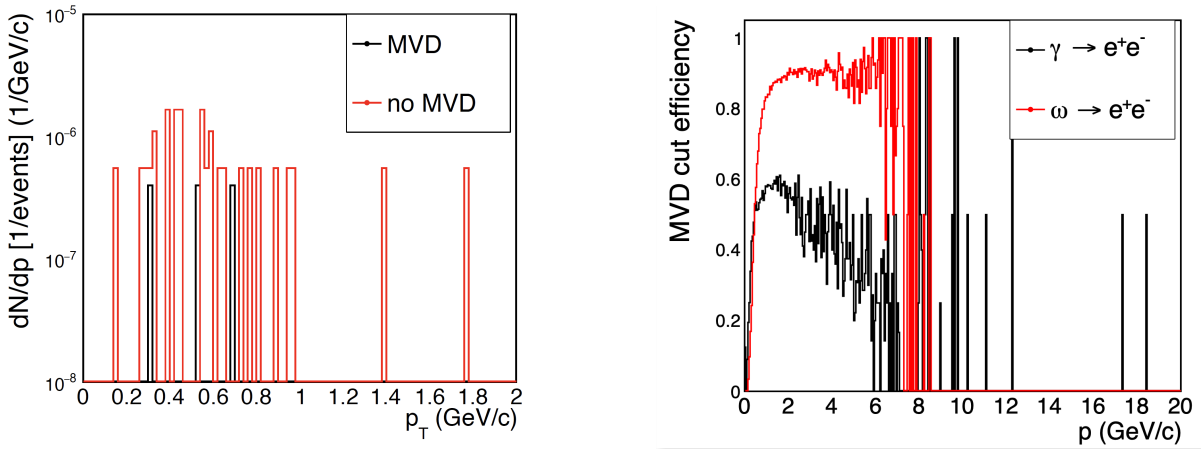

Figure 6.4: (left panel): Momentum distribution of remaining single lepton tracks originating from conversion processes of π^0 decay photons. Two simulations are compared: (MVD) full set-up including the MVD TR detector geometry configuration and (no MVD) simulation, for which the MVD had been taken out. The data refers to 2.5 M 8 A GeV Au+Au events of the 10% most central event class. (Right panel): Signal efficiency for to sources, photon conversion in the target (γ), and dielectron decay of ω mesons.

fully reconstructed electron or positron candidate, for a track segment with opposite charge polarity, forming a small opening angle with the fully reconstructed track. In an process of trading signal efficiency vs background rejection capability, cuts can be placed on quantities like opening angle and/or invariant of that pair. For this it is assumed that the track segment is due to an electron.

Background rejection capability has been evaluated performing a complete GEANT simulation, but without δ-electrons mixed in. In total 2.5 M UrQMD events for the collision system Au+Au at 8 A GeV have been used. The centrality class was selected by requiring the charged tracks in the detector acceptance to be above a given threshold so that the 10% most central collisions are selected (most difficult case). The dielectron signal has been embedded and artificially enriched as to acquire sufficient statistics of these rare events. In the analysis, respective down-scale factors have been used. This procedure was found to provide exact results concerning the multiplicities in the final spectra.

To have a realistic assessment of the relevance of the MVD for dielectron continuum spectroscopy, two simulation setups have been compared. In one simulation, the MVD has been entirely removed from the GEANT detector configuration. Hence, there is no extra material budget enhancing the conversion probability for photons. This simulation represents the reference. The second simulation has been performed with exactly the same UrQMD input events, but including the MVD-TR configuration in the GEANT detector setup. Evidently, in the analysis of these events the respective digitizer of MVD has been included and all MVD hits used in the track finding and fitting.

The pair analysis has been carried out in the so-called PAPA framework[4]. The standard scope of the framework has been expanded only in respect of the kind of track which selected for a given event, which now included also the track segments. The simulation studies revealed

[4]This framework was originally developed for the ALICE experiment and has been ported to CBMROOT.

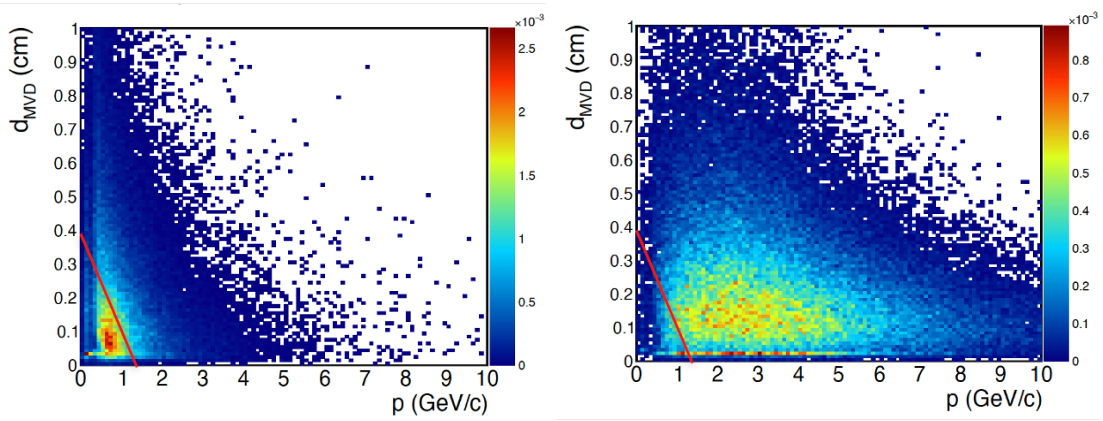

Figure 6.5: Correlation between the momentum of a fully reconstructed electron/positron track of a γ conversion processes in the target and the distance to the closest by track segment found in the MVD (left panel). The red line in the lower left corner marks a rejection criterion to suppress background from such γ conversion processes. The right panel shows the same correlation but this time for fully reconstructed electron/positron tracks from ρ meson decay, 8 A GeV Au+Au.

that the additional conversion processes in the MVD detector material could be identified and efficiently rejected to a large extent. Moreover, the signal efficiency in the simulation with the MVD is, within errors, identical to the simulation w/o MVD. We take this as evidence that additional rings produced in the RICH do not hamper the track-ring matching quality.

In Fig. 6.4 (left panel) the remaining background tracks from conversion processes, *i.e.* single electron/positron tracks are shown in correlation with their closet distance to the next neighbor track segment reconstructed in the MVD. For most of such conversion tracks the partner is identified as track segment (*i.e.* w/o particle identification). The conversion pairs can partially be rejected by allowing only tracks above the right line in the further analysis. In the right panel, the same correlation is shown but for electron(positron tacks originating from ρ decay. Respective signal pairs have large opening angles and only in a few cases a random track segment is found as close to the signal track that the rejection criteria would apply. This loss in signal is acceptable because of the much stronger effect in the mitigation of combinatorial background. It should be noted that this capability of rejecting conversion singles originating from the target, *i.e.* from the primary vertex, also means that respective track-pair topologies originating from π^0 Dalitz decay can also be identified and rejected.

The latter aspect is implicitly demonstrated in Fig. 6.5. Shown in the left panel is the remaining combinatorial background in the dielectron signal reconstruction in the simulation environment outlined above, after all background rejection cuts have been applied. Evidently, a substantial reduction of the combinatorial background is achieved, which, over the invariant mass range from the π^0 Dalitz region to the vector meson mass region, amounts to about 40% (*cf.* right panel). It should be noted that for this study no particular further background rejection cuts where applied. We expect, that after a fine tuning and the implementation of a dedicated track segment reconstruction algorithm, the background rejection capability of the MVD will even increase.

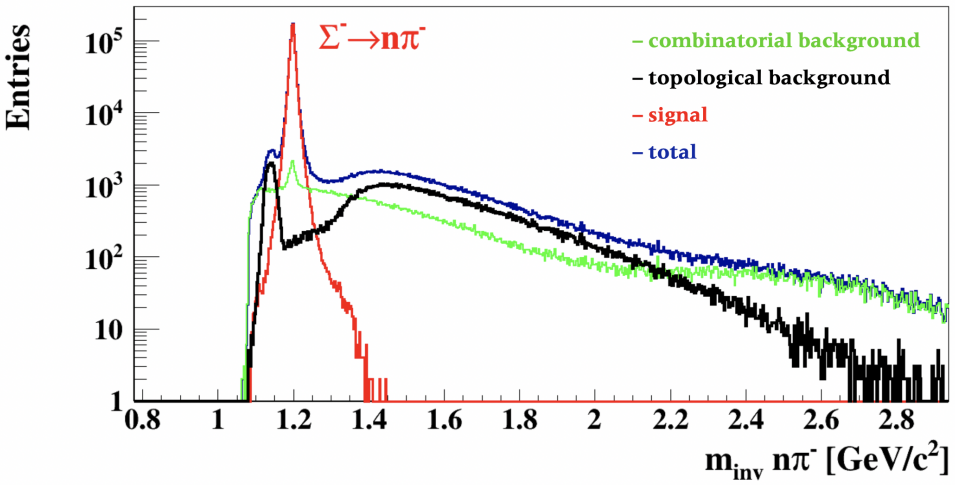

Figure 6.6: Reconstructed invariant mass distribution for weak decay topologies of a negative particle decaying into a charged (negative) and a neutral particle, for central Au+Au collisions at a beam energy of 12 AGeV. While the blue curve represents the reconstructed distribution, also the Monte Carlo identified composition (cocktail) is shown: (red) true signal, (black) contributions from Monte Carlo true decays of any other type, mainly weak decays of π^- and K^-, (green) all combinations, where the Monte Carlo PID assignment to the included tracks resulted in combinatorial pairs (charged secondary track is not a daughter of the primary track). This part contains true pairs but with an ambiguous Monte Carlo assignment (ghost track).

6.4.5 Charged Hyperon Reconstruction with Missing Mass Method

The MVD in tracking geometry together with STS feature 12 individual planar tracking stations each providing high-accuracy track position measurements. With MVD in the TR configuration, first track position measurement will be as close as 8cm to the target. Such a configuration enables the reconstruction of charged particles decaying into one charged and one neutral daughter particle. The detection and reconstruction of such decay topologies requires that the charged mother particle traverses at least three stations before it decays. The secondary charged track then needs a minimum of four individual position measurements as it is not originating from the primary vertex. Since the four MVD station are close to the target and with a distance of only 4 cm between the stations (TR detector geometry), weakly decaying hadrons can be reconstructed with significant efficiency.

As test case for such a measurement we use the hyperon decay $\Sigma^- \rightarrow n + \pi^-$ with the neutron escaping undetected. The Q-value of this decay is 110.3 MeV. The track topology investigated here is a charged track exhibiting a kink. The simulation environment is the complete final state of a heavy-ion event simulated with UrQMD or pHSD. The final state particles are transported through the detector (GEANT3) and the detector response is simulated in each detector module. Finally, track reconstruction and fitting is performed using the CBM standard Cellular Automaton and Kalman Filter algorithms, respectively. The simulation is done on an event-by-event basis.

The weak decay topologies are searched for using `KfParticleFinder`, an automated procedure performing kinematical refits of tracks forming a certain decay topology. For that, the position and momentum vectors of the reconstructed tracks assigned to the decay are varied within error

bands applying a particular event hypothesis. Here it is assumed that the primary track is a Σ^-, the secondary charged track a π^- and that the missing mass is that of a neutron. The result of this procedure is shown in Fig. 6.6 for central Au+Au collisions at a beam energy of 12 AGeV. The invariant mass distribution exhibits a very significant peak around the nominal mass of the Σ^- sitting on a somewhat wavy background. The signal to background ratio is > 10. Inspection of the Monte Carlo information assigned to the reconstructed tracks allows to separate the cocktail into two categories. The first case includes charged tracks which originate from a true weak decay, other than the decay of a Σ^-. This contribution is labelled "topological background" in Fig. 6.6 and is made up essentially from weak decays of π^- and K^-. Note, the algorithm assigns the mass of a Σ to the meson track and a mass of a π to the muon track. Yet, it includes only case where the falsely reconstructed missing mass amounts to the neutron mass (the neutrino mass in the true decay). The second case, labelled "combinatorial background" includes all combinations where the Monte Carlo PID assignment to the tracks included in the decay topology resulted in combinatorial pairs. This means that the charged secondary track was not identified as the daughter of the particle assigned to the primary track. Among these cases are true combinations from a Σ^- decay but with an ambiguous Monte Carlo PID assignment obtained in the track reconstruction. This occurs with finite likelihood if the secondary track was reconstructed from very few position measurements and in a high track density environment.

6.4.6 Open charm reconstruction

The occurrence of open charm particles in heavy-ion collisions at SIS100 energies is questionable as the energy threshold for charm production is hardly reached in a binary nucleon-nucleon collision. However, some models [98] predict a sizeable "sub-threshold" production, which may reach a production multiplicity of $\sim 10^{-4}$ $(D + \bar{D})$ per Au+Au collision and such the production multiplicities initially predicted for SIS300 energies. The capability of the MVD to reconstruct open charm particles at SIS300 energies has frequently been confirmed [19, 25].

More recently [99], the reconstruction of $(D^0 + \bar{D}^0 \rightarrow K + \pi)$ was studied for a Ni+Ni collision system of 15 A GeV. The beam energy was motivated by the consideration that the beneficial Z/A-value of Ni and applying mild over-currents to the SIS100 magnets[5] might allow for exceeding the charm production threshold. The study assumed a pile-up of three minimum bias collisions within the frame time of the sensor and included δ-electrons, which corresponds to a collision rate of 600 kHz if scaled to the frame readout time of the MIMOSIS sensor. The segmented MVD simulation geometry *v14b* was employed, which is the precursor of the VX geometry. The results (S/N >0.4, efficiency=1.7%) suggest that a yield measurement of $D^0 + \bar{D}^0$ would be possible down to a production rate of $\lesssim 10^{-6}$ per central Ni+Ni collision if a beam statistics of $\sim 2 \times 10^{11}$ collisions was recorded within 40 days beam on target. The statistical uncertainties of the simulation were estimated to amount less than a factor of three. In the left panel of Fig. 6.7 invariant mass spectra for off-vertex $K^-\pi^+$ and $K^+\pi^-$ pairs are shown. The spectra are obtained after optimization of the topological cuts and applying a kinematic refit using the KF-particle package. In the simulation, central Ni+Ni collisions have been assumed and a multiplicity of $\bar{D}^0$ and D^0 of $3.8 \cdot 10^{-6}$ and $6.57 \cdot 10^{-7}$, respectively. This relates to a N+N cross section for $\bar{D}^0$ production of about 0.7 nb. This value is indicated on the right panel where the excitation function for total inclusive charm production is shown. The original figure taken from [97] has been extended to the "threshold region" to put this hypothetical cross section in

[5] By today, it is considered that operating the SIS100 beyond its nominal beam momentum is not possible.

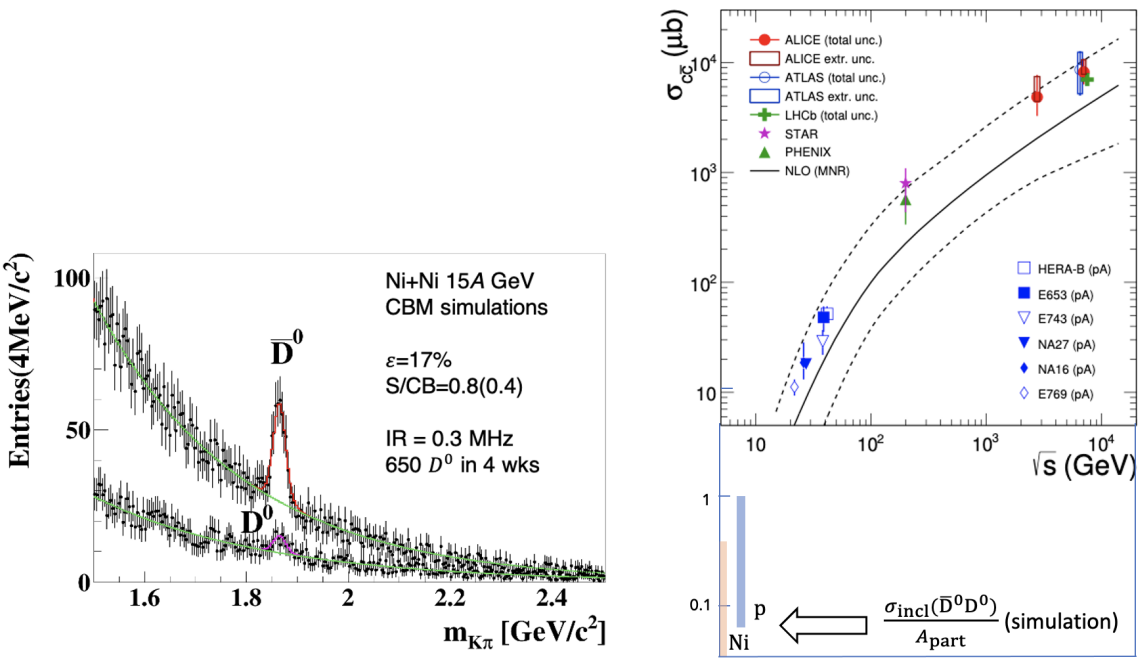

Figure 6.7: Reconstructed neutral open charm mesons of a simulation of Ni+Ni reactions at 15 A GeV (left panel). The assumed cross section for $\bar{D}^0 D^0$ production per A_{part} is indicated as arrow in the right panel. The figure is from [97] and is extended to lower energies in the bottom part. It shows measured cross sections for total inclusive charm production in p+N collisions ($\sigma_{c\bar{c}}$) as function of the nucleon nucleon center of mass energy ($\sqrt{s}$). The blue and red areas indicated the conjectured cross sections for measurements with proton beam at 29 GeV and Ni beam at 15 A GeV, respectively.

context. The colored areas are meant to guide the eye in respect to the assumed uncertainty and location of the total charm cross section at "threshold" energies. For the simulation, the charm decays have been embedded in central UrQMD background reactions.

An important program in the focus of CBM is charm production in proton induced reactions. At a maximum beam energy of 29 GeV the total inclusive cross sections are expected to be larger compared to the Ni+Ni case by at least a factor of 5. Due the the lower charged particle multiplicity, a maximum interaction rate of 1 MHz is anticipated. A measurement of open charm channels, in combination with the J/ψ measurements in the dilepton channel, would add substantially to the understanding of charm production and propagation in cold matter. Among such topics are the excitation function of charm production in the non-perturbative regime, the effects of shadowing and anti-shadowing, and the formation time of open and hidden charm mesons. A high statistics measurement would allow to study the production as function of rapidity, i.e. investigating different relative momenta relative to the cold medium. As mentioned in section 3.2.2, the limiting factor for the MVD in case of p+A collisions are charged particle scattered under small polar angles. The feasibility of reconstructing open charm particles generated in a p+C collision system at a beam energy of 30 GeV [100] was studied with a meanwhile out-dated MVD geometry, which relied on two stations only. However, this geometry, which was abandoned due to its poor MVD-to-STS track matching performance later, anticipated a yet realistic material budget and spatial precision of the detector. A frame time

of 30 µs of the sensors and a collision rate of 1.5 MHz was anticipated, which corresponds to a collision rate of 9 MHz after scaling to MIMOSIS frame times. As the identification of a primary decay vertex is hard in p+A systems due to the small number of charged particles created, the reconstruction strategy aimed to reconstruct decay vertices located significantly outside but nearby the target. The study suggests that CBM being operated with the MVD might reconstruct $D^{\pm} \to K^{\mp} + \pi^{\pm} + \pi^{\pm}$ and $D^0 \to K^{\mp} + \pi^{\mp} + \pi^{\pm} + \pi^{\pm}$ with a $S/B \gtrsim 1$. Assuming a production multiplicity of 3×10^{-8} per central collision, as suggested by HSD model calculations, and an efficiency for $D^{\pm}$ detection of $\gtrsim 10\%$, a beam time of less than one week might be sufficient for obtaining first yield information. This also holds at a lower total number of reconstructed particles for the D^0 channel, as this channel shows lower detection efficiency $\sim 2\%$ but also lower background.

While updated simulations would be required to obtain quantitative predictions on the sensitivity threshold of CBM with MVD for open charm particles, the results provide a solid indication that those particles could be detected at a beam energy of 30 GeV in the p+A collision system. Moreover, it appears possible to spot open charm production in Au+Au collisions at the SIS100 top energy in the event of the existence of an efficient sub-threshold production mechanism.

7 Project Organization and Costs

The MVD is part of the start version of CBM at SIS100, realized in the TR detector geometry, which comprises only two different station geometries (versions)[1] and four stations equidistantly arranged between $z = 8$ and 20 cm downstream the target, respectively. Building the detector is shared between the participating institutions and coordinated by a project leader and project technical coordinator. The project is split into work packages, which are coordinated by working group coordinators. The participating institutes comprise:

- Goethe-University Frankfurt (GUF, Inst. f. Kernphysik IKF), Germany, team leader Prof. Dr. Joachim Stroth (project leader), Dr. Christian Müntz (project technical coordinator)
- IPHC Strasbourg, France, team leader Dr. Marc Winter
- GSI Darmstadt, Germany, Dr. Michael Deveaux
- Pusan National University (PNU), South Korea, team leader Prof. Dr. In-Kwon Yoo*
- Institute of Modern Physics (IMP) of the Chinese Academy of Sciences, Lanzhou, China, Prof. Dr. Nu Xu*
- Czech Technical University (CTU), Prague, Dr. P. Chaloupka*[2]

The R&D phase was conducted by IPHC Strasbourg (sensor development and validation) and Goethe-University Frankfurt (physics simulation, detector design, sensor integration, R/O and DAQ, services, quality assessment, studies on radiation hard sensors), according to the institution's expertise and technical infrastructure. The production of the MVD will be organized accordingly, as outlined in the following section.

7.1 Work Packages

An overview of the MVD work packages and projected responsibilities are listed in Tab. 7.1. The third column depicts the presently assigned work package coordinators, motivated by their leading role in the given field during the R&D phase of the project. The WP 6 (Software) coordinator is presently not assigned and will be appointed in accordance with new groups joining MVD and the CBM software project in future.

- **WP 1: Sensor development MIMOSIS family** This WP continues the R&D activities of IPHC, GSI and IKF/GUF on CMOS Pixel Sensors towards future upgrades of the detector. It points towards improving the bandwidth and R/O time (frame time) of future CPS, and it explores options to further increase the radiation hardness. It depends on the expertise on sensor design of IPHC, complemented by the expertise of GSI and IKF/GUF to characterize and validate prototype sensors for CBM.

[1] The VX detector geometry would only require to exchange the first station by a low material budget one, based on CVD diamond, positioned at 5 cm, and increasing the station-to-station distance by 1 cm accordingly.

[2] *) expressed interest to formally join the MVD project.

- **WP 2: Sensor production** This WP covers the full logistics behind organizing submissions, producing and post-process wafers up to the point that fully tested sensors are available for sensor integration. A major part represents the quality management, depending on a close-meshed assessment and control of the wafers and diced sensors, both visually and electrically. Hence, dedicated tools, test benches and procedures have to be developed, based on both, the experiences with the sensor during R&D, and experience gained during (large-scale) sensor production in other experiments. Here we would depend on new partners, *e.g.* PNU, IMP and CTU.

- **WP 3: R/O, DAQ** This WP comprises the full R/O line ending at the CRI board level, which translated into the development and production of the dedicated boards, optical and electrical cables, and the development of the detector-specific firmware. It requires the input of experts from IKF/GUF and GSI to meet the specific requirements *w.r.t.* detector and CBM-DAQ, especially during development. The production (providing technical specifications and organization of the procurement) and, even more relevant for outsourcing, the related quality management can be shared with more partners, which have to be identified.

- **WP 4: Mechanics, Integration** This WP covers all activities related to the mechanical components of the detector, and it relies on the engineering designs developed during R&D, and sharpened during pre-production. It also covers the interfaces of the MVD to the target box and its main flange, which requires input from CBM (GSI). Due to the comparatively low number of items to be produced, procurement and quality management is assumed to be promoted by IKF and GSI alone.

- **WP 5: Services** This WP covers the procurement and commissioning of power and cooling supplies and associated infrastructure, as well as of the vacuum-related infrastructure. The close cooperation between IKF/GUF and GSI (CBM) guaranties the high quality standards enforced by CBM and FAIR and the embedding of items to the detector control (DCS).

- **WP 6: Software** Software development represents a continues activity during planning, engineering and conducting the CBM experiment. It comprises the detailed technical CAD drawings to be provided for production and input for (GEANT) simulation, detector-specific response functions (*i.e.* digitizer), (online) code for data processing and unpacking, as well as detector-specific routines regarding detector alignment and hit finding. The activity is part of the respective CBM work areas and hence requires the cooperation with CB (GSI). By definition, activities in this WP can be easily conducted remotely and off-site, and hence, future partners are invited to participate, nominating a coordinator who will further shape this WP.

- **WP 7: General** This WP comprises the coordination of the MVD detector project, which is taken over by IKF/GUF (project leader and technical project coordination). Besides coordination the different WPs, this WP coordinates the final commissioning of the detector and its operation.

Note, the MVD production will be accompanied by R&D studies on sensor radiation hardness and readout speed to get ready for possible future upgrades.

Work package & tasks	Responsibility	Coordinator
WP 1 Sensor development MIMOSIS family	IPHC, GSI, IKF	M. Deveaux
R&D: radiation hardness, speed, characterization		
Test beams		
WP 2 Sensor production	IKF, GSI, (PNU, IMP, CTU)*	M. Deveaux
Production flow		
QA (wafer, sensors)		
WP 3 R/O, DAQ	IKF, GSI	J. Michel
Flex cables		
Boards: FEE, R&O (GBTx)		
QA (flex, boards)		
DAQ integration		
Firmware		
WP 4 Mechanics & Integration	IKF, GSI	M. Koziel
Production, QA of carriers, heat sinks, C-frame		
Module integration (sensors, carriers, tooling)		
Module QA (commissioning, metrology)		
Detector integration (half stations/detector)		
Detector QA (Commissioning, metrology)		
WP 5 Services	IKF, GSI	M. Koziel
Power (distribution, controls, with prototype)		
Cooling (distribution, controls, with prototype)		
Vacuum feed throughs (coolant, electrical signals)		
DCS integration		
WP 6 Software	IKF, GSI	N.N.
Physics performance		
Digitizer, Data reduction		
Geometry & CAD		
WP 7 General		C. Müntz
Detector commissioning and operation	All	
Coordination	IKF	

Table 7.1: MVD work packages, projected responsibilities, shared by IKF (Goethe University Frankfurt), GSI Darmstadt, IPHC Strasbourg, PNU Pusan, IMP Lanzhou*, CTU Prague*, and designated coordinators during production. *): Expressed interest to formally join the MVD project.*

7.2 Production Time line

Figure 7.1 depicts a rough time line of the MVD production organized based on Tab. 7.1. Note, work package WP 1 is not core part of the MVD production for day-1, but considers activities required to follow up a possible future upgrade of the detector.

7.3 Infrastructure needed at FAIR

The MVD will be fully assembled and commissioned off-site FAIR, e.g. at Frankfurt University. The detector will then be delivered to FAIR, mounted to the front flange of the CBM target chamber an attached to a protective shielding. On-site FAIR a clean temporary storage (10-15 m^2) preferably near the CBM setup is required, to host the MVD before inserting it into CBM. Cooling, detector biasing and DAQ, to conduct final tests before insertion, will be provided by the MVD/CBM team. During STS maintenance periods the MVD might reside at this place as well.

7.4 Safety

The design and construction of the MVD including the infrastructure for operation will be done according to the safety requirements of FAIR and the European and German safety regulations. All electrical equipment and cooling will comply with the legally required safety code and concur to standards for large scientific installations to ensure the protection of all personnel working at or close to the components of the CBM experimental facility. Hazardous voltage supplies and lines will be marked visibly and protected from damage by any equipment which may cause forces to act on them. All supplies will be protected against over-current and over-voltage and have appropriate safety circuits and fuses. All cabling and connections will use non- flammable halogen-free materials according to up-to-date standards and will be designed with proper safety margins to prevent overheating. A safe ground scheme will be employed throughout all electrical installations of the experiment. Appropriate measures will be taken during installation and maintenance to avoid damage to or by the MVD.

7.5 Risk assessment

Assessing the risk in this phase of R&D will result in preliminary and rough statements, driven by experiences we made preparing the submissions of MIMOSIS-0 and MIMOSIS-1 as well as designing, producing and commissioning various PRESTO module (quadrant) prototypes. However, we will not further comment on level of detailing simulation studies *w.r.t.* optimizing the detector geometry or its contribution to the CBM physics performance with MVD, outlined in Sec. 6.

The following main risk of the MVD project are identified:

- **Sensor radiation hardness** First preliminary results from MIMOSIS-1 generate confidence in full-filling the specified specifications *w.r.t.* the sensor radiation hardness regarding ionizing and non-ionizing radiation by CBM. The robustness concerning the large gradient in hit occupancy over a sensor (matrix) has still to be confirmed, despite of the dedicated and flexible readout scheme of the sensor, optimizing its bandwidth according to varying hit density depending on the mounting position, *e.g.* due to δ-electrons. It is

important to emphasize the importance of the SIS100 beam quality *w.r.t.* the beam halo for the sensor life time and intensity fluctuations for the sensor performance in the experiment, *cf.* [18].

- **Sensor production yield** Based on the low number of processed wafers of the MIMOSIS-1 submission a solid estimation on the sensor (post-) production yield in not yet possible. We hope to finally scrutinize this aspect with MIMOSIS-2 in order to fix the number of wafers to be produced for MIMOSIS-3, and consequently to pin down the investment costs associated with the sensor production.
- **Sensor integration yield** As for the sensor, the production yield of modules (quadrants) is hard to assess based on the produced PRESTO prototypes during R&D. However, within the running CREMLINplus project and ongoing PRESTO prototyping activities we are conducting studies to reduce the risk of double-sided sensor integration on large-area TPG carriers. By conducting these projects we will defined a close-meshed QA ready for (pre-) production, relying on a minimum number of different modules and station geometries.
- **Funding** The current funding solely depends on the German BMBF, which presently defines a narrow funding corridor for CBM in general, and specifically the MVD. Hence, the project's current funding plan might have to be adopted to *e.g.* more realistic production yields and new sources of funding might have to be identified.

Figure 7.1: The MVD production time line, condensed and according to the CBM project planning as of February 2021.

Bibliography

[1] S. Borsanyi et al. "Is there still any T_c mystery in lattice QCD? Results with physical masses in the continuum limit III". In: *JHEP* 09 (2010), p. 073. DOI: 10.1007/JHEP09(2010)073. arXiv: 1005.3508 [hep-lat].

[2] A. Bazavov et al. "The chiral and deconfinement aspects of the QCD transition". In: *Phys. Rev.* D85 (2012), p. 054503. DOI: 10.1103/PhysRevD.85.054503. arXiv: 1111.1710 [hep-lat].

[3] Y. Aoki et al. "The order of the quantum chromodynamics transition predicted by the standard model of particle physics". In: *Nature* 443 (2006), pp. 675–678. DOI: 10.1038/nature05120. arXiv: hep-lat/0611014 [hep-lat].

[4] Z. Fodor and S. D. Katz. "Critical point of QCD at finite T and μ_B, lattice results for physical quark masses". In: *JHEP* 04 (2004), p. 050. DOI: 10.1088/1126-6708/2004/04/050. arXiv: hep-lat/0402006 [hep-lat].

[5] A. Andronic et al. "Hadron production in ultra-relativistic nuclear collisions: quarkyonic matter and a triple point in the phase diagram of QCD". In: *Nucl. Phys.* A837 (2010), pp. 65–86. DOI: 10.1016/j.nuclphysa.2010.02.005. arXiv: 0911.4806 [hep-ph].

[6] K. Fukushima and T. Hatsuda. "The phase diagram of dense QCD". In: *Rept. Prog. Phys.* 74 (2011), p. 014001. DOI: 10.1088/0034-4885/74/1/014001. arXiv: 1005.4814 [hep-ph].

[7] A. Schmah et al. "Highlights of the beam energy scan from STAR". In: *Central Eur. J. Phys.* 10 (2012), pp. 1238–1241. DOI: 10.2478/s11534-012-0149-1. arXiv: 1202.2389 [nucl-ex].

[8] A. Aduszkiewicz et al. "NA61/SHINE at the CERN SPS: plans, status and first results". In: *Acta Phys. Polon.* B43 (2012), p. 635. DOI: 10.5506/APhysPolB.43.635. arXiv: 1201.5879 [nucl-ex].

[9] D. Blaschke et al. "Topical issue on exploring strongly interacting matter at high densities - NICA white paper". In: *Eur. Phys. J. A* 52.8 (2016), p. 1. ISSN: 1434-601X. DOI: 10.1140/epja/i2016-16267-x.

[10] W. Ehehalt and W. Cassing. "Relativistic transport approach for nucleus nucleus collisions from SIS to SPS energies". In: *Nucl. Phys.* A602 (1996), pp. 449–486. DOI: 10.1016/0375-9474(96)00097-8.

[11] S.A. Bass et al. "Microscopic models for ultrarelativistic heavy ion collisions". In: *Prog. Part. Nucl. Phys.* 41 (1998), pp. 255–369. DOI: 10.1016/S0146-6410(98)00058-1. arXiv: nucl-th/9803035.

[12] A. Andronic et al. "Hadron production in central nucleus-nucleus collisions at chemical freeze-out". In: *Nucl. Phys.* A772 (2006), pp. 167–199. DOI: 10.1016/j.nuclphysa.2006.03.012. arXiv: nucl-th/0511071 [nucl-th].

[13] T. Ablyazimov et al. "Challenges in QCD matter physics –The scientific program of the Compressed Baryonic Matter experiment at FAIR". In: *Eur. Phys. J. A* 53.3 (2017), p. 60. DOI: 10.1140/epja/i2017-12248-y. arXiv: 1607.01487 [nucl-ex].

[14] P. Senger, V. Friese, et al. *Nuclear matter physics at SIS-100*. CBM Report 2012-01. 2011.

[15] B. Friman et al. "The CBM physics book: Compressed baryonic matter in laboratory experiments". In: *Lect. Notes Phys.* 814 (2011), pp.1–980. DOI: 10.1007/978-3-642-13293-3.

[16] H. Gutbrod et al. *FAIR baseline technical report*. ISBN 3-9811298-0-6 and ISBN 978-3-9811298-0-9. Darmstadt, 2006.

[17] J. Pietraszko. *CBM+HADES in FAIR Beam Parameter Booklet*. CBM Technical Board, 4th Sept. 2018. 2018.

[18] P. Schuett et al. *FAIR Operation Modes - Reference Modes for the Modularized Start Version (MSV)*. EDMS 2374493 v.2 status Released access Restricted, FAIR_Operation_Modes_V6-20200915.pdf. 2020.

[19] Michael Deveaux. "Development of fast and radiation hard Monolithic Active Pixel Sensors (MAPS) optimized for open charm meson detection with the CBM - vertex detector". PhD thesis. Universite Louis Pasteur Strasbourg and Goethe University Frankfurt, 2008.

[20] et al. M. A. Xapsos. "NIEL calculations for high-energy heavy ions". In: *IEEE TNS* 51 (2004), pp. 3250–3254.

[21] The NA61 collaboration. *Status report to the proposal SPSC-P-330 Report from the NA61/SHINE experiment at the CERN SPS*. CERN-SPSC-2016-038. Oct. 2016.

[22] F. A. Cucinotta et al. *Heavy Ion Track-Structure Calculations for Radial Dose in Arbitrary Materials*. NASA Technical Memorandum 3497. 1995.

[23] P. Forck et al. *Influence of Sextupole Strength on Spill micro-Structure*. Presentation given at GSI Beam Time Retreat. unpublished. Jan. 2019.

[24] P. Klaus et al. *The MVD simulation geometry models*. CBM Computing Note: CBM-TN-20007. Aug. 2020.

[25] Christina A. Dritsa. "Design of the Micro Vertex Detector of the CBM experiment: Development of a detector response model and feasibility studies of open charm measurement". PhD thesis. Goethe University Frankfurt and Universite de Strasbourg, 2011.

[26] Christian Trageser. "Systematische Untersuchung zur Auswirkung der Detektorgeometrie auf die Spurrekonstruktionseffizienz und Stossparameteraufloesung des CBM Mikro-Vertex-Detektors". MA thesis. Goethe-University Frankfurt, 2012. URL: https://www.gsi.de/documents/DOC-2012-Dec-56.html.

[27] R. Turchetta et al. "A monolithic active pixel sensor for charged particle tracking and imaging using standard VLSI CMOS technology". In: *Nucl. Instrum. Meth. A* 458 (2001), pp. 677–689. DOI: 10.1016/S0168-9002(00)00893-7.

[28] G. Deptuch et al. "Development of monolithic active pixel sensors for charged particle tracking". In: *Nucl. Instrum. Meth. A* 511 (2003). Ed. by S.L. Olsen and D. Bortoletto, pp. 240–249. DOI: 10.1016/S0168-9002(03)01801-1.

[29] D. Contarato et al. "Beam-test of CMOS pixel sensors with 6-GeV electrons". In: *Nucl. Instrum. Meth. A* 565 (2006). Ed. by J. Grosse-Knetter, H. Krueger, and N. Wermes, pp. 119–125. DOI: 10.1016/j.nima.2006.04.068.

[30] M. Deveaux. "Progress on the radiation tolerance of CMOS Monolithic Active Pixel Sensors". In: *JINST* 14.11 (2019), R11001. DOI: 10.1088/1748-0221/14/11/r11001. arXiv: 1909.05715 [physics.ins-det].

[31] Giacomo Contin et al. "The STAR MAPS-based PiXeL detector". In: *Nucl. Instrum. Meth. A* 907 (2018), pp. 60–80. DOI: 10.1016/j.nima.2018.03.003. arXiv: 1710.02176 [physics.ins-det].

[32] M. Suljic. "ALPIDE: the Monolithic Active Pixel Sensor for the ALICE ITS upgrade". In: *JINST* 11.11 (2016). Ed. by Claudia Gemme and Leonardo Rossi, p. C11025. DOI: 10.1088/1748-0221/11/11/C11025.

[33] The ALICE collaboration. *Technical Design Report for the Upgrade of the ALICE Inner Tracking System*. Nucl. Part. Phys. 41 087002. 2014.

[34] D. Kim et al. "Front end optimization for the monolithic active pixel sensor of the ALICE Inner Tracking System upgrade". In: *JINST* 11.02 (2016), p. C02042. DOI: 10.1088/1748-0221/11/02/C02042.

[35] J. Heymes et al. "Study of the depletion depth in a frontside biased CMOS pixel sensors". In: *JINST* 14.01 (2019), P01018. DOI: 10.1088/1748-0221/14/01/P01018.

[36] M. Deveaux et al. "Observations on MIMOSIS-0, the first dedicated CPS prototype for the CBM MVD". In: *Nucl. Instrum. Meth. A* 958 (2020). Ed. by Manfred Krammer et al., p. 162653. DOI: 10.1016/j.nima.2019.162653. arXiv: 1909.05614 [physics.ins-det].

[37] Heinz Pernegger et al. "First tests of a novel radiation hard CMOS sensor process for Depleted Monolithic Active Pixel Sensors". In: *JINST* 12.06 (2017), P06008. DOI: 10.1088/1748-0221/12/06/P06008.

[38] Magdalena Munker et al. "Simulations of CMOS pixel sensors with a small collection electrode, improved for a faster charge collection and increased radiation tolerance". In: *JINST* 14.05 (2019), p. C05013. DOI: 10.1088/1748-0221/14/05/C05013. arXiv: 1903.10190 [physics.ins-det].

[39] M. Deveaux et al. "Observations on MIMOSIS-0, the first dedicated CPS prototype for the CBM MVD". In: *Nucl. Instrum. Meth. A* 958 (2020). Ed. by Manfred Krammer et al., p. 162653. DOI: 10.1016/j.nima.2019.162653. arXiv: 1909.05614 [physics.ins-det].

[40] T. Dyndal et al. "Mini-MALTA: radiation hard pixel designs for small-electrode monolithic CMOS sensors for the High Luminosity LHC". In: *Journal of Instrumentation* 15.02 (Feb. 2020), P02005–P02005. DOI: 10.1088/1748-0221/15/02/p02005. URL: https://iopscience.iop.org/article/10.1088/1748-0221/15/02/P02005.

[41] G. Lindstrom. "Radiation damage in silicon detectors". In: *Nucl. Instrum. Meth. A* 512 (2003). Ed. by P. Holl et al., pp. 30–43. DOI: 10.1016/S0168-9002(03)01874-6.

[42] D Doering et al. "Noise performance and ionizing radiation tolerance of CMOS Monolithic Active Pixel Sensors using the 0.18µm CMOS process". In: *Journal of Instrumentation* 9.05 (May 2014), pp. C05051–C05051. DOI: 10.1088/1748-0221/9/05/c05051. URL: https://doi.org/10.1088%2F1748-0221%2F9%2F05%2Fc05051.

[43] Frederic Morel et al. "MISTRAL & ASTRAL: two CMOS Pixel Sensor architectures suited to the Inner Tracking System of the ALICE experiment". In: *JINST* 9.01 (2014), p. C01026. DOI: 10.1088/1748-0221/9/01/C01026.

[44] F. Morel. *The MIMOSIS-1 Architecture*. presentation shown at the MIMOSIS Design Review, IPHC Strasbourg. unpublished. June 2019.

[45] Tobias Tischler. "Mechanical Integration of the Micro Vertex Detector for the CBM Experiment". PhD thesis. Goethe-University Frankfurt, 2015. URL: http://publikationen.ub.uni-frankfurt.de/frontdoor/index/index/docId/38679.

[46] Diamond Materials. vendor. URL: www.diamond-materials.com/downloads/cvd_diamond_booklet.pdf.

[47] M. Tanabashi et al. "Review of Particle Physics". In: *Phys. Rev. D* 98.3 (2018), p. 030001. DOI: 10.1103/PhysRevD.98.030001.

[48] URL: http://www.e6.com/wps/wcm/connect/E6_Content_EN/Home (visited on 2020).

[49] URL: https://didco.com (visited on 2020).

[50] S. Gonzalez-Sevilla et al. "A double-sided silicon micro-strip Super-Module for the ATLAS Inner Detector upgrade in the High-Luminosity LHC". In: *JINST* 9 (2014), P02003. DOI: 10.1088/1748-0221/9/02/P02003.

[51] Momentive. vendor. URL: www.momentive.com.

[52] Optigraph. vendor. URL: http://www.optigraph.eu/optigraph.html.

[53] Fraunhofer IGB Stuttgart. URL: www.igb.fraunhofer.de.

[54] Panasonic. vendor. URL: https://na.industrial.panasonic.com/.

[55] Epotecny. URL: http://www.epotecny.com/ (visited on 2020).

[56] S. Canfer. *private communication, SFC - Advanced Material Group (UK), Glue development: Rutherford Appleton Laboratory (UK).*

[57] now LOCTITE ABLESTIK 45 poxy glue Hysol Eccobond 45 - Catalyst 15. URL: http://na.henkel-adhesives.com/product-search-1554.htm?nodeid=8797827760129 (visited on 2020).

[58] 3M. *3M thermal management fluids: NOVEC 649 engineering fluid.* https://indico.cern.ch/event/639798/. vendor. 2017.

[59] CollTec. URL: www.cooltec.de (visited on 2020).

[60] CTX Thermal Solutions. URL: www.ctx.eu (visited on 2020).

[61] Volker Blobel and Claus Kleinwort. "A New method for the high precision alignment of track detectors". In: *Conference on Advanced Statistical Techniques in Particle Physics.* June 2002. arXiv: hep-ex/0208021.

[62] E. Lavrik. "Advanced optical quality assurance of silicon micro-strip sensors for the CBM Silicon Tracking System". In: *Nucl. Instrum. Meth. A* 936 (2019). Ed. by Giovanni Batignani et al., pp. 640–641. DOI: 10.1016/j.nima.2018.09.131.

[63] S. Youcef et al. *MVD: Results from the 2012 Test Beam Campaign at CERN SPS.* CBM Technical Note: CBM-TN-14001. Jan. 2014.

[64] Michal Koziel et al. "The prototype of the Micro Vertex Detector of the CBM Experiment". In: *Nucl. Instrum. Meth. A* 732 (2013). Ed. by T. Bergauer et al., pp. 515–518. DOI: 10.1016/j.nima.2013.07.041.

[65] E.P Akishina et al. "Development of database complex for the CBMexperiment". In: *CEUR Workshop Proceedings* 1787 (2016), p. 85. URL: http://ceur-ws.org/Vol-1787/.

[66] Norbert Wermes. "Pixel vertex detectors". In: *34th SLAC Summer Institute on Particle Physics: The Next Frontier: Exploring with the LHC*. Nov. 2006. arXiv: physics/0611075.

[67] P. Klaus et al. *The MVD CAD Geometry Models*. CBM Technical Note: CBM-TN-20005. Aug. 2020.

[68] C. Muentz. *MVD: Assessing the thermal performance*. CBM Technical Note: CBM-TN-19007. June 2019.

[69] *ThSim - Temperature Simulator*. http://thsim.sourceforge.net/. (Visited on 2020).

[70] P. Klaus et al. *MVD Keep-Out Volumes*. CBM Technical Note: CBM-TN-19004. July 2019.

[71] LHCb collaboration. *LHCb VELO Upgrade Technical Design Report*. CERN-LHCC-2013-021. 2013.

[72] E.P. Akishina et al. "Development of the geometry database for the CBM experiment". In: *Phys. Part. Nucl. Lett.* 15.1 (2018), pp. 97–106. DOI: 10.1134/S1547477118010028.

[73] J Michel and Qyian Li. *MVD: Hit Rates, Link Bandwidth and Interaction Rate*. CBM Technical Note: CBM-TN-19002. Jan. 2019.

[74] J. Lehnert et al. "GBT based readout in the CBM experiment". In: *JINST* 12.02 (2017), p. C02061. DOI: 10.1088/1748-0221/12/02/C02061.

[75] Wojciech M. et al. "CRI board for CBM experiment: preliminary studies". In: *Photonics Applications in Astronomy, Communications, Industry, and High-Energy Physics Experiments 2018*. Ed. by Ryszard S. Romaniuk and Maciej Linczuk. Vol. 10808. International Society for Optics and Photonics. SPIE, 2018, pp. 1184–1191. DOI: 10.1117/12.2501415. URL: https://doi.org/10.1117/12.2501415.

[76] *Radiation tolerant 10W Synchronous Step-Down Buck DC/DC converter*. URL: https://project-dcdc.web.cern.ch/public/Documents/FEAST%20datasheet.pdf.

[77] Michal Koziel. *Workshop on system integration of highly granular and thin vertex detectors*. URL: https://indico.cern.ch/event/144152/overview.

[78] Huber. vendor. URL: www.huber-online.com/en.

[79] Julabo. vendor. URL: www.julabo.com/en.

[80] the Experimental Physics EPICS and Industrial Control System. URL: https://epics-controls.org/.

[81] "The PRESTO. Concept and Operation". in preparation. PhD thesis. Goethe-University Frankfurt.

[82] Control System Studio CSS. URL: http://controlsystemstudio.org/.

[83] Hendrik Jansen et al. "Performance of the EUDET-type beam telescopes". In: *EPJ Tech. Instrum.* 3.1 (2016), p. 7. DOI: 10.1140/epjti/s40485-016-0033-2. arXiv: 1603.09669 [physics.ins-det].

[84] C Chasman et al. "A Heavy Flavor Tracker for STAR". In: (2008). DOI: 10.2172/939892. URL: https://www.osti.gov/biblio/939892.

[85] L. Greiner et al. "A MAPS based vertex detector for the STAR experiment at RHIC". In: *Nucl. Instrum. Meth. A* 650 (2011). Ed. by Roland Horisberger, Danek Kotlinski, and Andrey Starodumov, pp. 68–72. DOI: 10.1016/j.nima.2010.12.006.

[86] C. Hu-Guo et al. "First reticule size MAPS with digital output and integrated zero suppression for the EUDET-JRA1 beam telescope". In: *Nucl. Instrum. Meth. A* 623 (2010). Ed. by Hiroyuki Iwasaki, Takeshi K. Komatsubara, and Yasuhiro Sugimoto, pp. 480–482. DOI: 10.1016/j.nima.2010.03.043.

[87] A. Dorokhov et al. "High resistivity CMOS pixel sensors and their application to the STAR PXL detector". In: *Nucl. Instrum. Meth. A* 650 (2011). Ed. by Roland Horisberger, Danek Kotlinski, and Andrey Starodumov, pp. 174–177. DOI: 10.1016/j.nima.2010.12.112.

[88] N. Abgrall et al. "NA61/SHINE facility at the CERN SPS: beams and detector system". In: *JINST* 9 (2014), P06005.

[89] P. Staszel et al. "Open charm measurements in NA61/SHINE at CERN SPS". In: *Nucl. Instrum. Meth. A* 982 (2019), pp. 879–882. DOI: 10.1016/j.nuclphysa.2018.12.018.

[90] Deveaux, M. et al. "The Small Acceptance Vertex Detector of NA61/SHINE". In: *EPJ Web Conf.* 171 (2018), p. 21001. DOI: 10.1051/epjconf/201817121001. URL: https://doi.org/10.1051/epjconf/201817121001.

[91] C. Ugur et al. "Field programmable gate array based data digitisation with commercial elements". In: *JINST* 8 (2013), p. C01035. DOI: 10.1088/1748-0221/8/01/C01035.

[92] P. Klaus et al. "Prototyping the read-out chain of the CBM Microvertex Detector". In: *JINST* 11.03 (2016), p. C03046. DOI: 10.1088/1748-0221/11/03/C03046.

[93] P. Sitzmann et al. *The Digitizer for the MVD Detector*. CBM Computing Note: CBM-CN-20005. July 2019.

[94] M. Domachowski. "Ein Simulationsmodell zur Darstellung von nicht-ionisierenden Strahlenschaeden an Monolithic Active Pixel Sensoren mit CBM-Root". MA thesis. Goethe University, 2012.

[95] I. Kisel. "Event reconstruction in the CBM experiment". In: *Nucl. Instrum. Meth. A* 566 (2006). Ed. by R. Bernhard et al., pp. 85–88. DOI: 10.1016/j.nima.2006.05.040.

[96] T. Galaytuk. "Dielectron spectroscopy in HADES and CBM: from p+p and n+p collisions at SIS to Au+Au collisions at FAIR". PhD thesis. PhD thesis: Goethe University, 2009.

[97] Jaroslav Adam et al. "D-meson production in p-Pb collisions at $\sqrt{s_{\mathrm{NN}}}$ =5.02 TeV and in pp collisions at $\sqrt{s}$ =7 TeV". In: *Phys. Rev. C* 94.5 (2016), p. 054908. DOI: 10.1103/PhysRevC.94.054908. arXiv: 1605.07569 [nucl-ex].

[98] J. Steinheimer, A. Botvina, and M. Bleicher. "Sub-threshold charm production in nuclear collisions". In: *Phys. Rev. C* 95 (1 Jan. 2017), p. 014911. DOI: 10.1103/PhysRevC.95.014911. URL: https://link.aps.org/doi/10.1103/PhysRevC.95.014911.

[99] I. Vassiliev. *Status of the open charm simulations at GSI*. presented at the 26th CBM Collaboration Meeting, Prague. 14 Sept., 2015.

[100] I. Vassiliev. *CBM Benchmark Observables*. presented at the 20th CBM Collaboration Meeting, Kolkata, India. 26 Sept., 2012.

[101] Grigory Feofilov. "NA61/SHINE vertex detector for open charm measurements". In: *J. Phys. Conf. Ser.* 668.1 (2016). Ed. by David Alvarez-Castillo et al., p. 012012. DOI: 10.1088/1742-6596/668/1/012012.

[102] B Abelev et al. "Technical Design Report for the Upgrade of the ALICE Inner Tracking System". In: *J. Phys. G* 41 (2014), p. 087002. DOI: 10.1088/0954-3899/41/8/087002.

A Appendices

A.1 Contribution to the Small Acceptance Vertex Detector of NA61

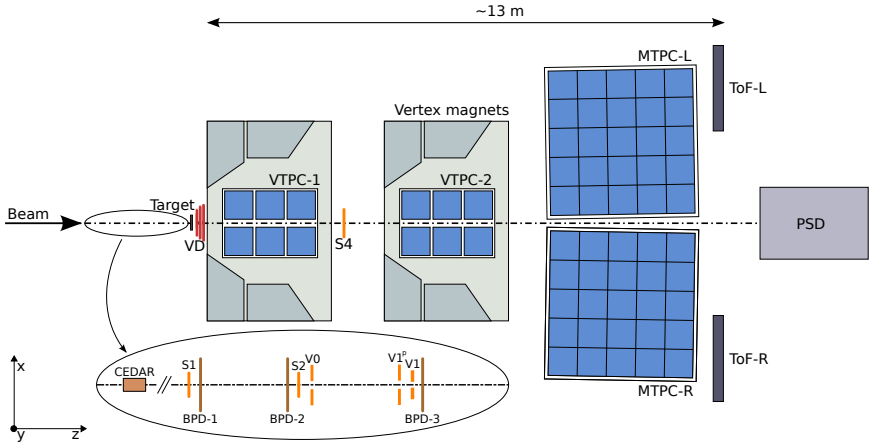

Figure A.1: Layout of the NA61/SHINE experimental set-up (top view, not to scale).

The Small Acceptance Vertex Detector SAVD of NA61 [88] at CERN is positioned between the target and the first TPC (VTPC1, *cf.* Fig. A.1) in the in-homogeneous and weak (0.13 - 0.25 T) fringe field of the VTPC-1 magnet[89, 101, 90]. The SAVD (shown in Fig. A.2) is composed of four detector planes (stations) equipped with position-sensitive MIMOSA-26 AHR [1]. CMOS Monolithic Active Pixel Sensors (MAPS) provided by the PICSEL group of IPHC Strasbourg. The arms are horizontally movable and allow to put the sensors into a save position during beam tuning. They consist of four sensor planes (stations), which are located 5, 10, 15 and 20 cm downstream the target. The sensors are held and water-cooled by vertically oriented ALICE-ITS carbon fibre support "ladders" [102] developed by the St. Petersburg State University and CERN. The ladders are mounted in C-frames made from aluminum. The four C-frames of each arm share a movable support plate. The first station of one arm consists of a ladders holding each one sensor, the second and third station each of a ladder holding two sensors and the last station of two ladders with two sensors each. A holder for targets was placed on an additional, movable support.

The whole structure is installed on a thick aluminum base plate, which provides mechanical stability. Four brass screws serve as legs for the plate and enable fine adjustment of the vertical position when installed on the beam line. The pink color box-structure visible on the photography is a made of Plexiglas covered with conducting paint. The base plate together with the Plexiglas structure and front and back Mylar windows (dismounted on the photograph) served as a gas tight detector box. During data taking, the detector box is filled with helium gas

[1] To increase non-ionizing radiation tolerance of MIMOSA-26 sensor generation, some of these sensors were manufactured at austriamicrosystems AG (A) using wafers featuring a High Resistivity (HR) epitaxial layer.

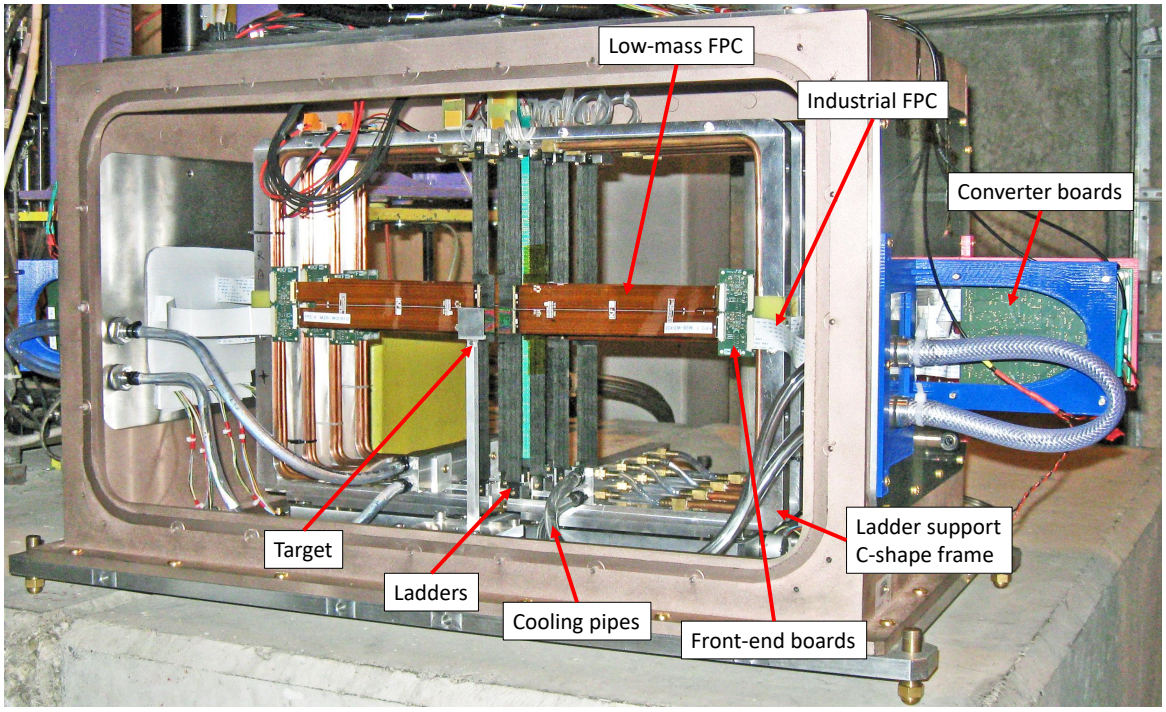

Figure A.2: Photograph of the SAVD setup before closing the detector with the front and exit windows. The detector elements are indicated.

at atmospheric pressure, which reduces beam-gas interactions and unwanted multiple Coulomb scatterings between target and sensors.

The readout of the sensors was done via 20 cm long, copper based single layer Flex Print Cables (FPC). The non-shielded cables were chosen to minimize the material budget in the acceptance of the TPC, being aware that they may inject pick-up noise to the sensors.

The (IKF) MVD-team has contributed to the NA61-SAVD project on the following topics:

- Probe-testing of thinned MIMOSA-26 sensors: Prior to integration, all MIMOSA-26 sensors were probe-tested using the same system as already described in Sec. 5.2.2.2. In total, 50 sensors were tested to verify their basic quality parameters: power consumption, digital readout test with known pattern, pixel to pixel uniformity, reaction to a light source. The best 16 sensors have been selected for integration.
- Sensor and detector integration, using methods developed for Prototype 1 and Prototype 2. The main task for the IKF group was to provide sensor ladders for the NA61-SAVD, as shown in Fig. A.3.
- Quality assessment: The quality control was addressed by verifying the sensor performance almost after every integration step. Consequently, the senor behaviour was tested during probe testing phase, after assembly of the sensor and FPC onto a extension plate, after joining the extension plate with the ALICE-ITS stave frame. The focus was directed to search for changes in digital and analog current consumption, number of dead and noisy pixels and reaction of the on-chip data processing unit to a defined pixel pattern. After the full NA61-SAVD ladder had been finally assembled, tests with Fe-55 radioactive source were carried out to identify the best set of steering signals for each of the sensors.

- Provide sensor readout based on the readout developed for the Prototype 2.
- Detector installation at the experiment site.
- Know-how transfer and documentation.

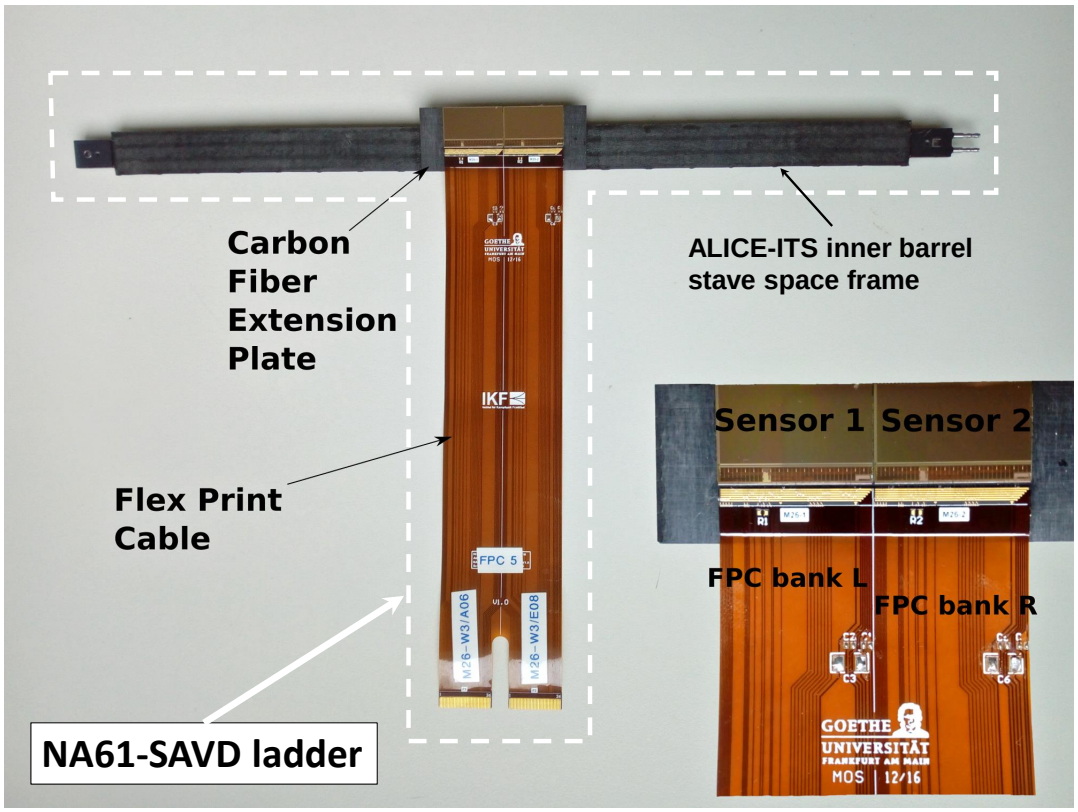

Figure A.3: The NA61-SAVD ladder composed of an ALICE-ITS inner barrel stave space frame, carbon fiber extension plate, low-mass flex-print circuit cable and two MIMOSA-26 AHR sensors.

A.2 The CBM Collaboration

List generated October 2020

- **Aligarh, India, Department of Physics, Aligarh Muslim University**

  N. Ahmad, M.D. Azmi, M.M. Khan, O. Singh

- **Beijing, China, Department of Engineering Physics, Tsinghua University**

  Zhi Deng, Dong Han, Yuanjing Li, Botan Wang, Yi Wang, Xianglei Zhu

- **Berlin, Germany, Konrad-Zuse-Zentrum für Informationstechnik Berlin (ZIB)**

  A. Reinefeld, F. Salem, F. Schintke

- **Bhubaneswar, India, Institute of Physics**

  B. Mallick, P.K. Sahu, S.K. Sahu

- **Bhubaneswar, India, National Institute of Science Education and Research (NISER)**

  V.K.S. Kashyap, B. Mohanty, R. Singh

- **Bucharest, Romania, Horia Hulubei National Institute of Physics and Nuclear Engineering (IFIN-HH)**

  A. Bercuci, M. Petriş, M. Petrovici, L. Radulescu, C. Schiaua

- **Bucharest, Romania, Atomic and Nuclear Physics Department, University of Bucharest**

  D. Argintaru, V. Baban, M. Cãlin, T. Eşanu, A. Jipa, I. Lazanu, C. Ristea, O. Ristea, N.G. Tuturas

- **Budapest, Hungary, Eötvös Loránd University (ELTE)**

  M. Csanád

- **Budapest, Hungary, Institute for Particle and Nuclear Physics, Wigner Research Centre for Physics, Hungarian Academy of Sciences**

  G. Balassa, Gy. Wolf

- **Chandigarh, India, Department of Physics, Panjab University**

  L. Kumar, N. Sharma

- **Chongqing, China, Chongqing University**

  Liang-ming Pan, Qiqi Wu, Wenxiong Zhou

- **Darmstadt, Germany, Facility for Antiproton and Ion Research in Europe GmbH (FAIR)**

  E. Clerkin, J. Eschke[1], P. Gasik[1], E. Lavrik, P.-A. Loizeau, W.F.J. Müller, A. Rost[2], A. Senger, P. Senger[3], D. Smith

- **Darmstadt, Germany, GSI Helmholtzzentrum für Schwerionenforschung GmbH (GSI)**

  M. Al-Turany, M. Bajdel, D. Bertini, O. Bertini, P. Dahm, H. Deppe, M. Deveaux[3], A. Dubla, D. Emschermann, H. Flemming, P. Foka, U. Frankenfeld, V. Friese, J. Frühauf, Xin Gao, S. Gorbunov, J. Hehner, J.M. Heuser, R. Holzmann, R. Kapell, R. Karabowicz, M. Kiš, K. Koch, P. Koczoń, D. Kresan, P. Kuhl, A. Lebedev[4], J. Lehnert, S. Löchner, O. Lubynets[3], A. Lymanets, O. Maragoto Rodriguez[3], A.M. Marin Garcia, J. Markert, D. Miskowiec, T. Morhardt, F. Nickels, W. Niebur, J. Pietraszko, A. Rustamov, C.J. Schmidt, I. Selyuzhenkov[5], M. Shiroya[3], C. Simons, C. Sturm, A. Toia[3], M. Träger, M. Traxler, F. Uhlig, I. Vassiliev, O. Vasylyev, R. Visinka, A. Wilms, P. Zumbruch

- **Darmstadt, Germany, Institut für Kernphysik, Technische Universität Darmstadt**

  T. Galatyuk[1], F. Seck

- **Dresden, Germany, Institut für Strahlenphysik, Helmholtz-Zentrum Dresden-Rossendorf (HZDR)**

  Xingming Fan[11], B. Kämpfer[11], R. Kotte, L. Naumann, D. Stach

- **Dubna, Russia, Laboratory of Information Technologies, Joint Institute for Nuclear Research (JINR-LIT)**

  P. Akishin, E. Alexandrov, I. Alexandrov, S. Belogurov[5], O. Derenovskaya, Victor Ivanov[5], A.V. Kryanev[5]

- **Dubna, Russia, Veksler and Baldin Laboratory of High Energy Physics, Joint Institute for Nuclear Research (JINR-VBLHEP)**

  A. Bychkov, D. Dementiev, V.V. Elsha, O. Fateev, Yu. Gusakov, G. Kekelidze, A. Kolozhvari, V. Ladygin, A. Malakhov, Yu. Murin, S. Parzhitskiy, A. Shabunov, A.D. Sheremetiev, M. Shitenkow, N. Sukhov, N.I. Zamiatin, A. Zinchenko

- **Frankfurt, Germany, Frankfurt Institute for Advanced Studies, Goethe-Universität Frankfurt (FIAS)**

  A. Belousov, J. de Cuveland, H. Hartmann, D. Hutter, I. Kisel, P. Kisel[1,4], G. Kozlov[4], V. Lindenstruth[1], A. Redelbach, F. Weiglhofer

- **Frankfurt, Germany, Institut für Kernphysik, Goethe-Universität Frankfurt**

  V. Akishina[1], H. Appelshäuser, B. Arnoldi-Meadows, E. Bechtel, C. Blume[1], T. Bus, H. Cherif[1], M. Esen, I. Fröhlich[1], D. Giang, S. Gläßel, P. Klaus, M. Koziel, J. Michel, C. Müntz, P. Raisig, A. Rodriguez Rodriguez[1], F. Roether, D. Spicker, J. Stroth[1]

- **Frankfurt, Germany, Institute for Computer Science, Goethe-Universität Frankfurt**

  A. Adler, T. Janson, U. Kebschull, D. Schmidt

- **Gatchina, Russia, Petersburg Nuclear Physics Institute named by B.P.Konstantinov of National Research Centre "Kurchatov Institute" (PNPI)**

  D. Ivanishchev, Vladimir Ivanov[5], A. Khanzadeev[5], L. Kochenda[5], B. Komkov, V. Kozlov, P. Kravtsov[5], E. Kryshen, L. Kudin, V. Nikulin, E. Rostchin[5], Yu. Ryabov, V. Samsonov[5,12], O. Tarassenkova, M. Zhalov

- **Gießen, Germany, Justus-Liebig-Universität Gießen**

  M. Becker, M. Beyer, M. Dürr, C. Feier-Riesen, T. Geßler, R. Haas, C. Höhne, L. Koch, S. Lebedev[4], E. Lebedeva, J.H. Otto, A.A. Weber, F. Zorn

- **Guwahati, India, Nuclear and Radiation Physics Research Laboratory, Department of Physics, Gauhati University**

  B. Bhattacharjee, S. Gope

- **Hefei, China, Department of Modern Physics, University of Science & Technology of China (USTC)**

  Dongdong Hu[6], Chao Li, Yuan Su, Yongjie Sun, Zhengyang Sun, Kaiyang Wang, Tianxing Wang, Xinjian Wang, Junfeng Yang, Jianhui Yuan, Jian Zhou

- **Heidelberg, Germany, Physikalisches Institut, Universität Heidelberg**

  I. Deppner, D. Gottschalk, N. Herrmann[1], R. Kolb, E. Rubio, C. Simon, Y. Söhngen, P. Weidenkaff, Qiunan Zhang[7]

- **Heidelberg, Germany, Institut für Technische Informatik, Universität Heidelberg**

  P. Fischer

- **Indore, India, Indian Institute of Technology Indore**

  S.K. Kundu, A. Roy, R. Sahoo

- **Jammu, India, Department of Physics, University of Jammu**

  A. Bhasin, A. Gupta, S. Mahajan, S.S. Sambyal

- **Karlsruhe, Germany, Karlsruhe Institute of Technology (KIT)**

  S. Bähr, M. Balzer, J. Becker, T. Blank, M. Caselle, P. Pfistner, V. Sidorenko, E. Trifonova, K.L. Unger, M. Weber

- **Kharagpur, India, Indian Institute of Technology Kharagpur**

  A.K. Singh

- **Kolkata, India, Department of Physics, Bose Institute**

  S. Biswas, S. Chatterjee, Supriya Das, S.K. Ghosh, S. Mukherjee, S.K. Prasad, S. Raha, R. Ray, S. Roy, A. Sen

- **Kolkata, India, Department of Physics and Department of Electronic Science, University of Calcutta**

  A. Bhattacharyya, A. Chakrabarti, R. Ganai, G. Gangopadhyay

- **Kolkata, India, Variable Energy Cyclotron Centre (VECC)**

  A. Agarwal, Z. Ahammed, P.P. Bhaduri, S. Chattopadhyay[8], A.K. Dubey, C. Ghosh, Ajit Kumar, M. Mandal, E. Nandy, J. Saini, V. Singhal

- **Kraków, Poland, AGH University of Science and Technology (AGH)**

  M. Baszczyk, P. Dorosz, K. Kasiński, R. Kłeczek, W. Kucewicz, P. Otfinowski, R. Szczygieł, W. Zubrzycka

- **Kraków, Poland, Marian Smoluchowski Institute of Physics, Jagiellonian University**

  J. Brzychczyk, K. Łojek, Z. Majka, R. Płaneta, P. Staszel, A. Wieloch

- **Kyiv, Ukraine, High Energy Physics Department, Kiev Institute for Nuclear Research (KINR)**

  V. Kyva, V. Militsija, I. Momot[3], M. Pugach, V. Pugatch, D. Storozhyk

- **Kyiv, Ukraine, Department of Nuclear Physics, Taras Shevchenko National University of Kyiv**

  O. Bezshyyko, L. Golinka-Bezshyyko, I. Kadenko, V. Plujko

- **Moscow, Russia, Institute for Nuclear Research (INR)**

  D. Finogeev, M. Golubeva, F. Guber, A. Ivashkin, A. Izvestnyy, N. Karpushkin, S. Morozov, O. Petukhov, A. Reshetin, A. Shabanov

- **Moscow, Russia, Institute for Theoretical and Experimental Physics named by A.I. Alikhanov of National Research Centre "Kurchatov Institute" (ITEP) in Moscow, Russia (ITEP)**

  A. Akindinov, I. Alekseev, E. Dorenskaya, D. Golubkov, F. Khasanov, S. Kiselev, I. Korolko, N. Lyublev, D. Malkevich, K. Mikhailov, V. Plotnikov, M. Prokudin, A. Semennikov, S. Shirinkin, R. Sultanov, D. Svirida, Yu. Zaitsev, I. Zivko

- **Moscow, Russia, National Research Nuclear University MEPhI (Moscow Engineering Physics Institute)**

  E. Atkin, A. Demanov, O. Golosov, P. Ivanov, N. Kargin, E. Kashirin, O. Malyatina, D. Normanov, P. Parfenov, I. Segal, V. Shumikhin, M. Strikhanov, A. Taranenko

- **Moscow, Russia, National Research Centre "Kurchatov Institute"**

  D. Blau[5], A. Kazantsev, V. Manko, I. Sibiryak, I. Yushmanov

- **Moscow, Russia, Skobeltsyn Institute of Nuclear Phyiscs, Lomonosov Moscow State University (SINP-MSU)**

  N. Baranova, D. Karmanov, M. Korolev, I. Kudryashov, M. Merkin, A. Voronin

- **Münster, Germany, Institut für Kernphysik, Westfälische Wilhelms-Universität Münster**

  A. Andronic, R. Berendes, F. Fidorra, N. Heine, P. Kähler, Ch. Klein-Bösing, M. Kohn, A. Meyer-Ahrens, H. Morgenweck, D. Mühlheim, P. Munkes, A. Puntke, P.M. Schneider, L. Wahmes, J.P. Wessels

- **Prague, Czech Republic, Czech Technical University (CTU)**

  V. Petráček, L. Škoda

- **Protvino, Russia, Institute for High Energy Physics (IHEP)**

  S. Golovnya, S. Gorokhov, A. Kiryakov, I. Lobanov, E. Lobanova, Yu. Tsyupa, A. Vorobiev

- **Pusan, Korea, Pusan National University (PNU)**

  In-Kwon Yoo

- **Řež, Czech Republic, Nuclear Physics Institute of the Czech Academy of Sciences**

  P. Chudoba, A. Kugler, V. Mikhaylov, A. Prozorov

- **Srinagar, India, Department of Physics, University of Kashmir**

  A. Ahmad, S.A. Bhat, W.A. Bhat, M.F. Mir, T. Rehman

- **Tübingen, Germany, Physikalisches Institut, Eberhard Karls Universität Tübingen**

  K. Agarwal, Susovan Das, S. Khan, V. Klochkov, S. Mehta, I. Panasenko[9], H.R. Schmidt[1], E. Volkova

- **Varanasi, India, Department of Physics, Banaras Hindu University (BHU)**

  Ajay Kumar, S. Pandey, B.K. Singh, C.P. Singh

- **Warsaw, Poland, Faculty of Physics, Warsaw University of Technology**

  J. Pluta, D. Wielanek, H. Zbroszczyk

- **Warsaw, Poland, Institute of Electronic Systems, Warsaw University of Technology**

  M. Gumiński, M. Kruszewski, P. Miedzik, K. Poźniak[10], R. Romaniuk, W. Zabołotny[10]

- **Warsaw, Poland, Faculty of Physics, University of Warsaw**

  T. Matulewicz, K. Piasecki

- **Wuhan, China, College of Physical Science and Technology, Central China Normal University (CCNU)**

  Sheng Dong[6], Shu He, Guangming Huang, Feng Liu, Xiaofeng Luo, Shusu Shi, Dong Wang, Zhongbao Yin, Xiaoming Zhang, Yu Zhang, Daicui Zhou, Nu Xu

- **Wuppertal, Germany, Fakultät für Mathematik und Naturwissenschaften, Bergische Universität Wuppertal**

  K.-H. Becker, J. Förtsch, K.-H. Kampert, I. Kres, V. Patel, C. Pauly, D. Pfeifer

- **Yichang, China, College of Science, China Three Gorges University (CTGU)**

  Sheng-Qin Feng, Jian-Hao Ma, Ke-Jun Wu, Sheng Zheng

Additional affiliations:

[1] GSI Helmholtzzentrum für Schwerionenforschung GmbH (GSI), Darmstadt, Germany

[2] Institut für Kernphysik, Technische Universität Darmstadt, Darmstadt, Germany

[3] Institut für Kernphysik, Goethe-Universität Frankfurt, Frankfurt, Germany

[4] Laboratory of Information Technologies, Joint Institute for Nuclear Research (JINR-LIT), Dubna, Russia

[5] National Research Nuclear University MEPhI (Moscow Engineering Physics Institute), Moscow, Russia

[6] Physikalisches Institut, Universität Heidelberg, Heidelberg, Germany

[7] Department of Engineering Physics, Tsinghua University, Beijing, China
[8] Department of Physics, Bose Institute, Kolkata, India
[9] High Energy Physics Department, Kiev Institute for Nuclear Research (KINR), Kyiv, Ukraine
[10] Faculty of Physics, University of Warsaw, Warsaw, Poland
[11] also: Technische Universität Dresden, Dresden, Germany
[12] also: St. Petersburg Polytechnic University (SPbPU), St. Petersburg, Russia

Abbreviations (selected)

AHR Austriamicrosystems AG process offering a High Resistivity epitaxial layer.

ALICE A Large Ion Collider Experiment at CERN.

ASIC Application-Specific Integrated Circuit.

BMBF Bundesminsisterium für Bildung und Forschung.

CAD Computer-Aided Design.

CBM Compressed Baryonic Matter Experiment.

CBMROOT Version of the ROOT software adapted for the Compressed Baryonic Matter (CBM) experiment. ROOT is an object-oriented program and library developed by CERN. It was originally designed for particle physics data analysis and contains several features specific to this field, but it is also used in other applications such as astronomy and data mining.

CERN The European Organization for Nuclear Research.

CERN-SPS CERN's Super Proton Synchrotron.

CMOS Complementary Metal - Oxide - Semiconductor.

CPS CMOS Pixel Sensor.

CRI Common Readout Interface, a PCIe card used by all CBM subsystems as connection from front-ends to the server farm.

CTE Coefficient of Thermal Expansion.

CVD diamond Chemical Vapour Deposited diamond.

DAQ Data Acquisition System.

DCS Detector Control System.

DEPFET DEPleted Field Effect Transistors.

EPICS The Experimental Physics and Industrial Control System (EPICS) is a set of software tools and applications used to develop and implement distributed control systems to operate devices such as particle accelerators, telescopes and other large experiments.

FAIR Facility for Antiproton and Ion Research.

FEB Front-End Board.

FEE Front-End Electronics.

FPC Flexible Printed Circuit.

FPGA Field Programmable Gate Array.

GBT-SCA CERN GigaBit Transceiver Slow Control Adapter. A custom, radiation hardened chip used to provide control and monitoring for front-end electronic.

GBTx GigaBit Transceiver ASIC. A custom, radiation-hard chip developed by CERN for upgrades of LHC experiments that allows to send several slow data streams from sensors over one fast optical link.

GEANT GEANT is the name of a series of simulation software designed to describe the passage of elementary particles through matter, using Monte Carlo methods. The name is an acronym formed from "GEometry ANd Tracking". Originally developed at CERN for high energy physics experiments.

GEANT3 GEANT is the name of a series of simulation software designed to describe the passage of elementary particles through matter, using Monte Carlo methods. The name is an acronym formed from "GEometry ANd Tracking". Originally developed at CERN for high energy physics experiments.

GEANT4 Revised version of GEANT3 with modified geometry handling.

HADES High-Acceptance Di-Electron Spectrometer.

HERA-B The HERA-B detector was a particle physics experiment at the HERA accelerator at Deutsches Elektronen-Synchrotron (DESY).

HFT Heavy Flavour Tracker.

HSD Hadron String Dynamics.

IKF Institut für Kernphysik Frankfurt.

IPHC Institut Pluridisciplinaire Hubert CURIEN.

IR Infra-Red.

ITS Inner Tracking System.

KF Kalman Filter.

L1 Dedicated Software package for track finding in the CBM silicon tracking stations (STS, MVD).

LHC Large Hadron Collider.

LHCb The LHCb (Large Hadron Collider beauty) experiment is one of eight particle physics detector experiments collecting data at the Large Hadron Collider at CERN.

LV Low Voltage.

MAPS Monolithic Active Pixel Sensor.

mCBM mini-CBM setup at SIS18.

MIMOSA Minimum Ionizing particle MOS Active pixel sensor.

MIMOSIS The CMOS Pixel Sensor developed for the CBM Micro-Vertex Detector installed at SIS Schwer-Ionen-Synchrotron (SIS).

MVD Micro Vertex Detector.

NA61/SHINE The e Super Proton Synchrotron (CERN) Heavy Ion and Neutrino Experiment to study the properties of hadrons in collisions of beam particles with fixed targets.

pCVDD poly-crystalline Chemical Vavour Deposited Diamond.

PHENIX Pioneering High Energy Nuclear Interaction eXperiment.

PLUTO PLUTO is an object oriented C++ library to simulate multi-step hadronic process and decays. It is a free software developed and maintained by Ingo Froehlich.

POM Polyoxymethylene, also known as acetal polyacetal, and polyformaldehyde, is an engineering thermoplastic used in precision parts requiring high stiffness, low friction, and excellent dimensional stability.

PRESTO PREcursor of the Second sTatiOn of the CBM-MVD.

QA Quality Assurance, the way it is used here it also includes the assessment of quality.

RAL Rutherford Appleton Laboratory.

RTS Random Telegraph Signal.

SAVD Small Acceptance Vertex Detector.

STS Silicon Tracking Station.

TPG Thermal Pyrolytic Graphite.

TR TRacking detector geometry.

TRBv3 Trigger and Readout Board version 3.

UrQMD Ultra-relativistic Quantum Molecular Dynamics.

VTRX CERN Versatile link Transceiver and Receiver module, radiation and magnetic field tolerant optical module.

VTTX CERN Versatile link double Transceiver module, radiation and magnetic field tolerant optical module.

VX VerteXing detector geometry.